ELECTROCHEMICAL SYNTHESIS OF NANOENGINEERED MATERIALS AND THEIR APPLICATIONS

EDITED BY: Nosang Vincent Myung, Jae-Hong Lim, James Rohan, Syed Mubeen Jawahar Hussaini and Bongyoung Yoo

PUBLISHED IN: Frontiers in Chemistry

frontiers Research Topics

ISSN 1664-8714
ISBN 978-2-88963-192-6
DOI 10.3389/978-2-88963-192-6

About Frontiers

Frontiers is more than just an open-access publisher of scholarly articles: it is a pioneering approach to the world of academia, radically improving the way scholarly research is managed. The grand vision of Frontiers is a world where all people have an equal opportunity to seek, share and generate knowledge. Frontiers provides immediate and permanent online open access to all its publications, but this alone is not enough to realize our grand goals.

Frontiers Journal Series

The Frontiers Journal Series is a multi-tier and interdisciplinary set of open-access, online journals, promising a paradigm shift from the current review, selection and dissemination processes in academic publishing. All Frontiers journals are driven by researchers for researchers; therefore, they constitute a service to the scholarly community. At the same time, the Frontiers Journal Series operates on a revolutionary invention, the tiered publishing system, initially addressing specific communities of scholars, and gradually climbing up to broader public understanding, thus serving the interests of the lay society, too.

Dedication to Quality

Each Frontiers article is a landmark of the highest quality, thanks to genuinely collaborative interactions between authors and review editors, who include some of the world's best academicians. Research must be certified by peers before entering a stream of knowledge that may eventually reach the public - and shape society; therefore, Frontiers only applies the most rigorous and unbiased reviews.
Frontiers revolutionizes research publishing by freely delivering the most outstanding research, evaluated with no bias from both the academic and social point of view. By applying the most advanced information technologies, Frontiers is catapulting scholarly publishing into a new generation.

What are Frontiers Research Topics?

Frontiers Research Topics are very popular trademarks of the Frontiers Journals Series: they are collections of at least ten articles, all centered on a particular subject. With their unique mix of varied contributions from Original Research to Review Articles, Frontiers Research Topics unify the most influential researchers, the latest key findings and historical advances in a hot research area! Find out more on how to host your own Frontiers Research Topic or contribute to one as an author by contacting the Frontiers Editorial Office: researchtopics@frontiersin.org

ELECTROCHEMICAL SYNTHESIS OF NANOENGINEERED MATERIALS AND THEIR APPLICATIONS

Topic Editors:
Nosang Vincent Myung, University of California, Riverside, United States
Jae-Hong Lim, Gachon University, South Korea
James Rohan, University College Cork, Ireland
Syed Mubeen Jawahar Hussaini, The University of Iowa, United States
Bongyoung Yoo, Hanyang University, South Korea

Citation: Myung, N. V., Lim, J.-H., Rohan, J., Hussaini, S. M. J., Yoo, B., eds. (2019). Electrochemical Synthesis of Nanoengineered Materials and Their Applications. Lausanne: Frontiers Media. doi: 10.3389/978-2-88963-192-6

Table of Contents

frontiers in Chemistry

ORIGINAL RESEARCH
published: 24 September 2018
doi: 10.3389/fchem.2018.00436

Synthesis and Thermoelectric Characterization of Lead Telluride Hollow Nanofibers

*Miluo Zhang[1], Su-Dong Park[2], Jiwon Kim[3], Michael Nalbandian[4], Seil Kim[3,5], Yongho Choa[5], Jaehong Lim[3] and Nosang V. Myung[1]**

[1] Department of Chemical and Environmental Engineering and UC KIMS Center for Innovation Materials for Energy and Environment, University of California, Riverside, Riverside, CA, United States, [2] Advanced Materials and Application Research Division, Korea Electrotechnology Research Institute, Changwon, South Korea, [3] Department of Electrochemistry, Korea Institute of Materials Science, Changwon, South Korea, [4] Department of Civil Engineering and Construction Management, California Baptist University, Riverside, CA, United States, [5] Department of Materials Science and Chemical Engineering, Hanyang University, Ansan, South Korea

Lead telluride (PbTe) nanofibers were fabricated by galvanic displacement of electrospun cobalt nanofibers where their composition and morphology were altered by adjusting the electrolyte composition and diameter of sacrificial cobalt nanofibers. By employing Co instead of Ni as the sacrificial material, residue-free PbTe nanofibers were synthesized. The Pb content of the PbTe nanofibers was slightly affected by the Pb^{2+} concentration in the electrolyte, while the average outer diameter increased with Pb^{2+} concentration. The surface morphology of PbTe nanofibers was strongly dependent on the diameter of sacrificial nanofibers where it altered from smooth to rough surface as the Pb^{2+} concentration increased. Some of thermoelectric properties [i.e., thermopower (S) and electrical conductivity(σ)] were systematically measured as a function of temperature. Energy barrier height (E_b) was found to be one of the key factors affecting the thermoelectric properties–that is, higher energy barrier heights increased the Seebeck coefficient, but lowered the electrical conductivity.

Keywords: lead telluride, electrospinning, galvanic displacement reaction, thermoelectrics, hollow nanofiber, energy barrier height

OPEN ACCESS

Edited by:
Elizabeth J. Podlaha, Clarkson University, United States

Reviewed by:
Avinash Raj Kola, Applied Materials, United States
Edward Gillan, University of Iowa, United States
Despina Davis, Raytheon, United States

***Correspondence:**
Nosang V. Myung
myung@engr.ucr.edu

Specialty section:
This article was submitted to Electrochemistry, a section of the journal Frontiers in Chemistry

Received: *31 July 2018*
Accepted: *03 September 2018*
Published: *24 September 2018*

Citation:
Zhang M, Park S-D, Kim J, Nalbandian M, Kim S, Choa Y, Lim J and Myung NV (2018) Synthesis and Thermoelectric Characterization of Lead Telluride Hollow Nanofibers. Front. Chem. 6:436. doi: 10.3389/fchem.2018.00436

INTRODUCTION

The restriction of non-renewable resources along with the threat of environmental and ecological degradation is a key driver for improving energy generation and efficiency. Various renewable energy technologies including solar cells (Oregan and Gratzel, 1991; Miles et al., 2007), biomasses (Huber et al., 2006), fuel cells (Aricò et al., 2005), and thermoelectrics (Snyder and Toberer, 2008) are considered to achieve the goal. Solid-state thermoelectric generators convert waste thermal energy into useful electric energy to improve the efficient of system. They have many advantages such as long operating time without maintenance, easy scalability, and zero-emission (Pichanusakorn and Bandaru, 2010). The conversion efficiency of the thermoelectric device can be described by the thermoelectric figure-of-merit ($ZT = S^2\sigma T/\kappa$), which consists of thermopower (Seebeck Coefficient, S), electrical conductivity (σ), and thermal conductivity (κ), and absolute temperature (T). In order to maximize the ZT, there parameters must be independently optimized. However, the interdependence of S, σ, and κ make difficult to further enhance ZT (Szczech et al., 2011). One-dimensional (1-D) nanostructures can offer several advantages in enhancing ZT over

bulk materials, such as increasing the power factor, ($S^2\sigma$), by means of quantum confinement and/or the energy filtering effect or reducing lattice thermal conductivity (κ_L) by enhanced phonon scattering (Hochbaum et al., 2008; Chen et al., 2010). Furthermore, both quantum confinement and surface scattering effects are expected to display an added degree of control and enhancement within tubular/hollow nanostructures (*vs.* solid nanowires and nanobelts) (Chen et al., 2010; Zhou et al., 2010, 2014), as wall thickness and fiber diameter can be controlled independently. Thus, tubular nanostructures offer the possibility of decoupling $S^2\sigma$ and κ, which allows for independent control over the $S^2\sigma$/ κ ratio, thereby increasing the overall thermoelectric performance (Chen et al., 2010; Zhou et al., 2010, 2014).

Lead telluride (PbTe) is a V-VI semiconductor with a narrow band-gap energy of 0.31 eV at room temperature with a rock-salt crystal structure. By adjusting the composition, PbTe can be either an n- or p-type semiconductor. For example, Te-rich PbTe results in p-type semiconductor whereas Pb-rich PbTe results in n-type semiconductor (Dughaish, 2002). The commercially available PbTe-based thermoelectric devices show ZT of ∼0.8 around 600 K, which makes them suitable for the middle-high temperature range. Additionally, the enhancement of the thermoelectric properties of PbTe has already been realized by band-gap engineering. Enhancement in the thermoelectric efficiency of PbTe was also achieved by doping the material with potassium (K) or sodium (Na) (Androulakis et al., 2010). Furthermore, improvement of ZT was achieved via nanoengineering of the Se alloyed PbTe quantum dot superlattice (Harman et al., 2002). The enhancement of ZT (∼1.6 at 300 K and ∼3.5 at 570 K) in this system is caused by reduction in κ_L meanwhile an increase in ($S^2\sigma$) (Venkatasubramanian, 2000; Harman et al., 2002, 2005).

Various methods including chemical deposition (Lokhande, 1991; Tai et al., 2008), stress-induced method (Dedi et al., 2013), electrodeposition (Xiao et al., 2006, 2007a; Jung et al., 2011; Yang et al., 2011), galvanic displacement reaction (Chang et al., 2014), CVD (Fardy et al., 2007) have been used to fabricate PbTe nanostructures. The thermoelectric properties of these nanostructures are normally characterized in the form of nanowire arrays or highly-packed nanowire films (pellets). This is due to the difficulties in maintaining the single nanowire's structural and chemical composition during the lithographic contacting (Tai et al., 2008; Yang et al., 2011; Dedi et al., 2013). For example, p-type PbTe nanowires were fabricated using hydrothermal method. The sample were then hot pressed into a pellet for measuring thermoelectric properties, yielding the highest Seebeck coefficient of 628 μV/K (Tai et al., 2008). N-type PbTe nanoribbon arrays with a diameter of 60 nm were synthesized by lithographically patterned nanowire electrodeposition (LPNE), which showed S of −445 μV/K and σ of 0.63 S/cm, respectively (Yang et al., 2011).

Electrospinning is a technique that can produce ultra-long nanofibers by continuously stretching and whipping viscoelastic jets in a high electric field. Various nanofibers of polymer (Xiao et al., 2007a), metal (Xiao et al., 2006), and metal oxide (Yang et al., 2011) materials have been fabricated by electrospinning with controllable morphology, diameter, composition, and orientation. However, limited works are reported on the synthesis of metal chalcongenide nanofibers because of difficulty to prepare solutions. Therefore, synthesis of a few millimeter chalcogenide nanofibers has been realized by combining electrospinning with an additional process called the galvanic displacement reaction (Xiao et al., 2007b; Chang et al., 2010a,b, 2014; Hangarter et al., 2010; Jung et al., 2010, 2012; Park et al., 2010, 2013; Rheem et al., 2010; Suh et al., 2012, 2013; Elazem et al., 2013; Jeong et al., 2013; Liu et al., 2013; Wu et al., 2014, 2015; Zhang et al., 2014), by which the electrospun nanofibers can be converted to desired hollow metal chalcogenides spontaneously. Several hollow nanofibers of chalcogens and metal chalcogenides [e.g., Te (Lee et al., 2011; Jeong et al., 2013), Ag_2Te (Park et al., 2015; Zhang et al., 2015), and $Pb_xSe_yNi_z$ (Zhang et al., 2014)] have been successfully synthesized by this method in our group.

In this paper, hollow PbTe nanofibers with controlled dimension and morphology were synthesized for the first time. Electrospinning was exploited to fabricate sacrificial cobalt nanofibers. Various dimensions and morphologies of the PbTe hollow nanofibers were synthesized by tuning the electrolyte concentrations in the galvanic displacement reactions. Additionally, thermoelectric properties were characterized and correlated to their materials properties.

MATERIALS AND METHODS

Electrospinning of Co Nanofibers

The procedure of electrospinning of cobalt nanofibers is based on previous reported nickel nanofibers (Park et al., 2013). Citric acid ($C_6H_8O_7$, anhydrous, enzyme grade, Fisher Chemical) and cobalt acetate [$Co(C_4H_6O_4).4H_2O$, 98%, Sigma-Aldrich] at a molar ratio of 1 were dissolved in 6.3 g of water followed by mixing with 3.34 g of anhydrous ethanol solution (Fisher Scientific, PA) containing 5.2 wt. % of polyvinylpyrrolidone (PVP). MW of PVP was 1,300,000 g/mol. The concentration of the precursor solution was varied to electrospin the Co sacrificial nanofibers with two different diameters. The concentration of cobalt acetate was chosen to be 1.0 M (solution 1) and 1.6 M (solution 2) based on the spinnability of the solution and the solubility of the salt. A 0.25 mm inner diameter metallic needle was used as the spinneret. The applied voltage and the distance between spinneret and collector (i.e., 3 × 3 cm Si/SiO_2 wafer) were fixed at 10 kV and 10 cm, respectively. The flow rate was fixed at 0.5 mL/h using a peristaltic pump. The electrospinning time was fixed at approximately 15 min to keep the thickness of collected nanofiber mats consistent. The temperature and relative humidity were 40 ± 2°C and 8 ± 1%, respectively. The collected nanofibers were first aged at 60°C in air overnight and then calcined at 500°C in pure H_2 for 5 h to obtain Co nanofibers.

Synthesis of PbTe Nanofiber Mats by Galvanic Displacement

The galvanic displacement of cobalt to PbTe nanofiber mat was conducted at room temperature for 30 min by dipping a freestanding Co nanofiber mat of the desired amount into 10 ml solution. The solution consisted of X mM lead nitrate

(Pb(NO3)2, Fisher Chemical), 0.1 mM tellurium oxide (TeO_2, 99+%, Acros Organic) and 0.1 M nitric acid (HNO_3, Certified ACS Plus, Fisher Chemical) The pH of solution was controlled to be 2 by adding nitric acid (HNO_3, Certified ACS Plus, Fisher Chemical). The effects of Pb^{+2} concentration on the morphology and dimension of the nanofiber were conducted by altering the Pb^{2+}concentrations from 10 to 100 mM. After galvanic displacement, the mats were rinsed with de-ionized water five times follow by air dried.

Solution and Material Characterization

Various solution properties including electrical conductivity, solution viscosity, and surface tension were measured with Accumet AB-200 benchtop electrical conductivity meter, Brookfield DV-I Prime viscometer, and Interfacial tensiometer (CSC-Denouy 70545), respectively.

Transmission electron microscopy (TEM), selected area electron diffraction (SAED), field emission-scanning electron microscopy (FE-SEM, FEG-Philips XL30), energy-dispersive X-ray spectroscopy (EDS), and X-ray diffraction (XRD, D8 Advance Diffractometer, Bruker) were used to characterize morphologies, compositions, crystal structures and crystallinity of the nanofiber mats.

Electrical and Thermopower Characterizations

Single fiber-based devices were fabricated by a standard photolithography process with a gap size of 3 μm between two Au pads. Nanofiber mats based devices were formed by sputtering Pt to form electrodes using shadow mask technique with the fixed electrode gap distance of 1 mm.

Temperature-dependent electrical properties including current-voltage (I-V) and field-effect transient (FET) measurements were characterized based on the single fiber-based devices at a temperature ranging from 293 to 353 K, while thermopower (S) was measured based on mats by a home-built instrument. The temperature range was varied from 300 to 360 K.

RESULTS AND DISCUSSIONS

Electrospinning of Co Nanofibers as Sacrificial Materials

Table 1 shows the solution properties of two electrospinning solutions which were investigated. As listed in the table, higher loadings of citric acid and cobalt acetate significantly increased electrical conductivity and viscosity. However, the surface tension of both solutions were almost the same, as expected, since this parameter would mainly depend on the properties of the solvent. Smooth, cylindrical $CoAc_2$/citric acid/PVP nanofibers were electrospun from both solutions, as shown in **Figures 1A,C**. Their average diameters were 519 ± 168 nm and 161 ± 47 nm, respectively. The large standard deviations were likely due to the inhomogeneous electrical bending instability of the fibers as well as the formation of branched fibers, which originated from the nonuniform charge density distribution on the surface of the jet (Reneker and Yarin, 2008). Compared to **Figure 1A**, the nanofibers in **Figure 1C** are more curled due to their smaller average diameter. Annealing of the as-spun fibers at 500°C for 5 h in H_2 environment led to a complete decomposition of the polymer and acid as well as the formation of continuous Co nanofibers (**Figures 1B,D**). The average diameter of the Co nanofibers was 124 ± 30 nm and 52 ± 12 nm. The smaller Co nanofibers (**Figure 1D**) seemed to have a rougher surface than the larger ones (**Figure 1B**). Both nanofibers exhibited a similar volume shrink ratio of approximately 60%.

TABLE 1 | Solution properties of electrospinning precursors.

Solution property	Viscosity (cP)	Electrical conductivity (mS/cm)	Surface tension (dyne/cm)
Solution 1 (Resulted in smaller Co nanofiber)	82.5	1.0	37
Solution 2 (Resulted in larger Co nanofiber)	130.3	1.1	37

Fabrication of PbTe Hollow Nanofibers and Their Material Characteristics

Co was chosen as the sacrificial material for galvanic displacement reaction for the synthesis of PbTe due to its ability to provide an appropriate electrochemical driving force (difference in materials' redox potential) for the metal chalcogenide displacement. Since the redox potential of Co^{2+}/Co pair (-0.28 V vs. SHE) is more cathodic than that of the Pb^{2+}/Pb (−0.13 V vs. SHE) and $HTeO_2^+$/Te (0.551 V vs. SHE) pairs, the formation of PbTe from Co was thermodynamically favorable. A suitable dissolution rate of the sacrificial materials was also a key parameter for a successful displacement. Sacrificial materials with a dissolution rate comparable to the deposition rate of the target materials are required to achieve high deposition efficiency and a low sacrificial material residual. Dipping the Co nanofiber mats into the acidic electrolytes containing Pb^{2+} and $HTeO_2^+$ would lead to the dissolution of Co to Co^{2+} (Equation 1) as well as the formation of PbTe. Here, Co nanofibers served as both the electron source and the template for the PbTe deposition. The deposition would initiate with overpotential deposition of Te nuclei on the surface of the Co nanofibers (Equation 2), due to a more negative standard reduction potential of Co than Te. Pb spontaneously deposited on Te by underpotential deposition (UPD) mechanism, which resulted in the formation of PbTe. PbTe compound is formed instead of Pb and Te due to the negative ΔG of PbTe formation (Equation 3) (Xiao et al., 2006). Galvanic displacement of PbTe from Co can be described in the Equations 1–4:

$$Co(s) \rightarrow Co^{2+}(aq) + 2e^- \qquad E^0 = -0.28\ V\ vs.SHE \quad (1)$$

$$HTeO_2^+(aq) + 4e^- + 3H^+(aq) \rightarrow Te(s) + 2H_2O \qquad E^0 = 0.551\ V\ vs.SHE \quad (2)$$

$$Pb^{2+}(aq) + Te(s) + 2e^- \rightarrow PbTe(s) \qquad \Delta G_f^0 = -69.5\ kJ/mol \quad (3)$$

$$Pb^{2+}(aq) + HTeO_2^+(aq) + 3Co(s) + 3H^+(aq) \rightarrow PbTe(s) + 3Co^{2+}(aq) + 2H_2O \quad (4)$$

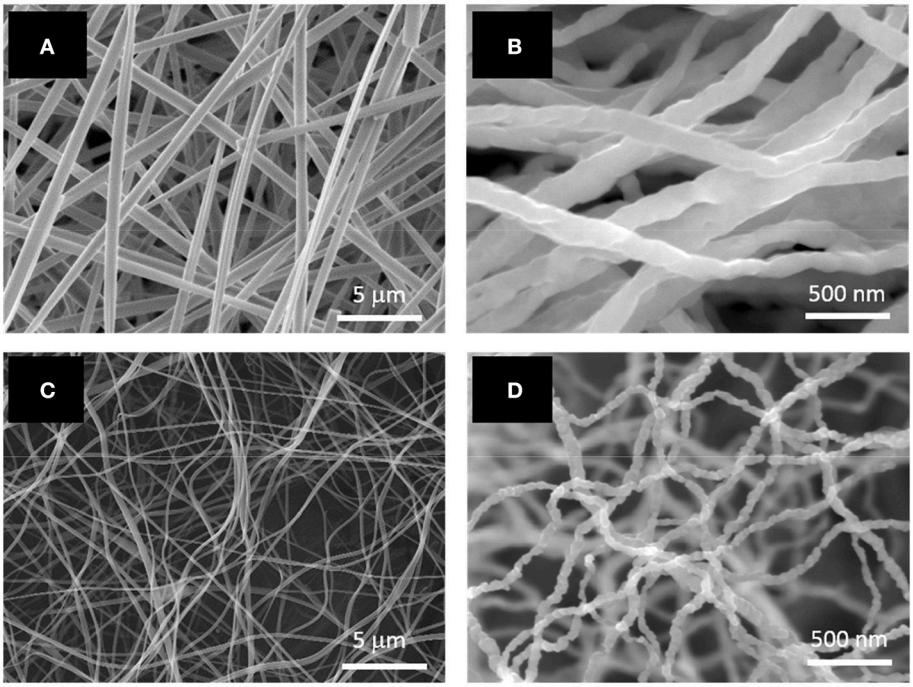

FIGURE 1 | SEM images of electrospun PVP/acetic acid/Co acetate nanofibers with average diameters of **(A)** 394 nm and **(C)** 161 nm; SEM images of Co nanofibers with average diameters of **(B)** 124 nm and **(D)** 52 nm.

Control over the dimension and morphology of the PbTe nanofibers was achieved by varying the diameter of Co nanofibers (*i.e.*, 52 and 124 nm) and the concentrations of Pb^{2+} (i.e., 10, 50, and 100 mM) in the electrolytes and, while maintaining the concentrations of HNO_3 and $HTeO_2^+$ at 0.1 M and 0.1 mM, respectively. Compared to the GDR of PbSeNi, the concentration of HNO_3 in the PbTe's electrolytes was ten times lower (i.e., 0.1 M) to reduce the dissolution rate of Co, which is much faster than that of Ni (Jung et al., 2012).

Figure 2 shows the SEM images of PbTe produced from Co nanofibers with average diameters of 124 nm (top row) and 52 nm (bottom row). The concentration of Pb^{2+} was varied from 10 mM (left column), to 50 mM (middle column), and to 100 mM (right column). All three conditions produced nanofibers, some of them with clear hollow structures (**Figures 2A,C**). Most of the nanofibers in the top row were consistently larger than that in the bottom row, as the diameter of the sacrificial nanofiber was larger. For the larger PbTe nanofibers (top row of **Figure 2**), hollow and smooth nanofibers were synthesized in the electrolytes containing low concentrations of Pb^{2+}, while nanofibers with rough surfaces were observed from the concentrated electrolytes. For smaller PbTe nanofibers (bottom row of **Figure 2**), no clear morphology difference was observed with varied Pb^{2+} concentration. A closer look at the low magnification images (**Figure S1**) showed that these larger fibers were smoother than the smaller fibers. This might be attributed to the smoother surface of the larger sacrificial nanofibers, providing less local nucleation sites for the chalcogenide deposition. The formation of hetero-structures in the smaller PbTe nanofibers might be due to the greater mass transfer limitation resulting from the higher fiber pack density. Opened nanotubes or porous tubes were observed in **Figures 2B,C**, which might be caused by the incomplete coverage of the deposits on the sacrificial material or the dissolution of the as-deposited materials along the reaction. Fibers merged together with adjacent ones as shown in **Figures 2D–F**, which might be due to the linking of sacrificial nanofibers as well as the dissolution of the as-deposited PbTe.

The synthesized PbTe nanofiber mats were then sonicated and dispersed in IPA to obtain single nanofiber-based suspension solutions. These solutions were drop-casted on Si/SiO_2 chips for the EDS characterization. The composition of over six individual fibers were measured and averaged for each condition. The composition of PbTe as a function of Pb^{2+} concentration (**Table 2**). For the smaller PbTe nanofibers, the Pb content stayed at 42 at.% as the concentration of Pb^{2+} increased from 10 mM to 50 mM, then decreased to 37 at. % at a higher level of Pb^{2+} concentration. However, for the larger PbTe nanofibers, a slight decrease in the Pb content at the low Pb^{2+} concentration region [*i.e.*, $(Pb^{2+}) = 10$ mM and 50 mM] was first observed, followed by a slight increase in the Pb content when the concentration of Pb^{2+} was increased to 100 mM. Variations in the ion concentration had minor effects on the fibers' composition because the Pb content maintained at around 42 at.% and only a 7 at. % (from 37 at.% to 44 at.%) change was observed corresponding to a one order of magnitude change in the electrolyte concentration. The insignificant effect of a high Pb^{2+} concentration ($[Pb^{2+}] \geq 50$ mM) on the composition of PbTe has been suggested in our previous work (Xiao et al., 2006).

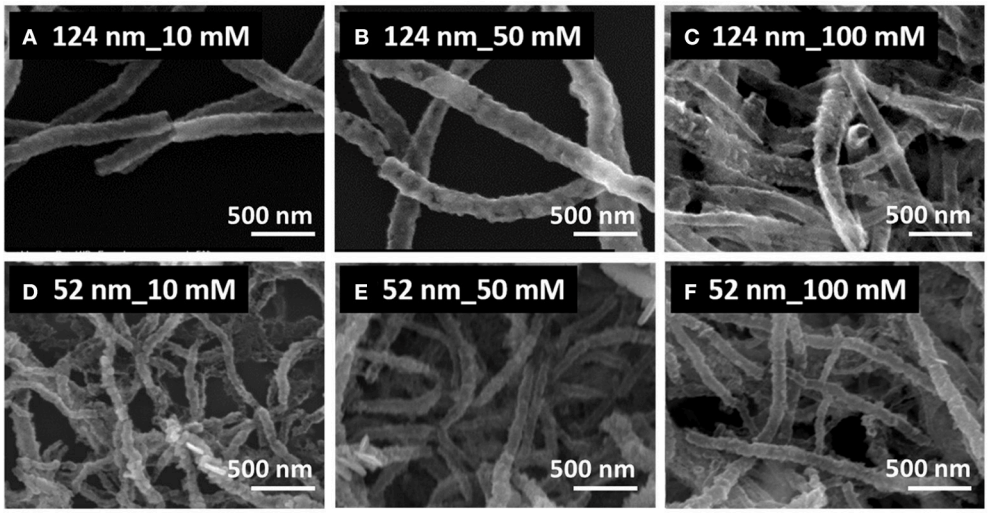

FIGURE 2 | SEM images of synthesized PbTe hollow nanofibers using 124-nm (top row, **A–C**) and 52-nm (bottom row, **D–F**) Co nanofibers as sacrificial materials. The electrolytes contained a fixed concentration of 0.1 mM $HTeO_2^+$ and 0.1 M HNO_3 with various concentration of Pb^{2+} of 10 mM (left column, **A,D**), 50 mM (middle column, **B,E**), and 100 mM (right column, **C,F**). All reactions were conducted at room temperature for 30 min.

Large error bars were observed for all the conditions, which might be attributed to the inhomogeneity in the reactions due to the mass transfer limitation. The highest Pb content in the lead chalcogenide nanofibers (i.e., PbSe and PbTe) galvanically displaced from the sacrificial materials that have a similar redox potential (*i.e.*, Ni and Co) (Zhang et al., 2014) was around 45 at.%. GDR of PbTe from Co has been studied by Chang et al. (2014). In their system, electrodeposited Co thin film was used as sacrificial anode. The electrolytes consisted of 50 mM to 500 mM Pb^{+2} while fixing $HTeO_2^+$ concentration at 10 mM. These electrolytes allowed them to study the deposition in the $[Pb^{2+}]/[HTeO_2^+]$ system ranging from 5 to 50. In our case, however, the deposition occurred in a much higher $[Pb^{2+}]/[HTeO_2^+]$ range of 100 to 1000 due to the 100-fold lower $HTeO_2^+$ concentration (*i.e.*, 0.1 mM). In Chang's thin film system, Te-rich PbTe films were obtained at $[Pb^{2+}]/[HTeO_2^+] \leq 20$, while Pb-rich PbTe films were synthesized at $[Pb^{2+}]/[HTeO_2^+] \geq 50$ (Chang et al., 2014). However, only Te-rich PbTe were obtained in the nanofiber system, even with a higher $[Pb^{2+}]/[HTeO_2^+]$ of 1,000. The difference in the composition might be due to the different geometry of the sacrificial material leading to growth of heterostructures in the thin film system, or the difference in the crystal orientation of Co film (hcp) and nanofibers (fcc) that provided different activation energies for the Pb overpotential deposition (OPD) (Oviedo et al., 2006).

A quantitative assessment of the effect of the Pb^{2+} concentrations on the average outer diameter of the Pb_xTe_y nanofibers is shown in **Figure 3**. Pb^{2+} concentration was kept significantly higher than $HTeO_4^+$ concentration since the PbTe deposition mechanism follows overpotential deposition (OPD) of Te, followed by underpotential deposition (UPD) of Pb. Nanofibers displaced in the electrolytes with a higher Pb^{2+} concentration exhibited larger outer diameter. As the concentration of Pb^{2+} was increased from 10 mM to 100 mM, the outer diameters increased from 141 to 193 nm for smaller PbTe nanofibers and 193 to 297 nm for larger PbTe nanofibers. Owing to the faster deposition rate, greater outer diameters were expected in the electrolytes containing higher concentrations of Pb^{2+}. In addition, the large disparity in the size of the larger fiber diameter may cause the larger error bars in the fiber diameters. The same phenomenon has been observed in previous work (Zhang et al., 2014). The wall thickness of the PbTe nanofibers were estimated assuming the inner diameters of hollow PbTe nanofibers were the same as the outer diameter of Co nanofibers. As the Pb^{2+} concentration was increased from 10 to 50 to 100 mM, the wall thickness increased from 45 to 56 to 70 nm for the smaller nanofibers, and from 35 to 59 to 86 nm for the larger nanofibers. Given that the Bohr radius of PbTe is 46 nm, the quantum confinement effect may occur in the thin nanofibers.

TABLE 2 | Effect of $[Pb^{2+}]$ on the Pb content in the PbTe nanofibers using two different Co nanofibers (i.e., 52 nm and 124 nm).

$[Pb^{+2}]$	Pb content (at. %)	
	52 nm Co nanofiber	124 nm Co nanofiber
10	42 ± 4.1	42 ± 6.3
50	42 ± 5.9	38 ± 6.2
100	37 ± 6.8	44 ± 3.3

Figure 4 shows XRD patterns of the Co nanofibers and the $Pb_{43}Te_{57}$ nanofibers. Co nanofibers (**Figure 4A**) had a diffraction pattern of a fcc structure with <1 1 1> and <2 0 0> orientations. All the peaks in the PbTe (**Figure 4B**) matched with PbTe (JCPDS 38-1435) except for the peak that belonged to the Pt electrodes that were sputtered on top of the nanofiber mats,

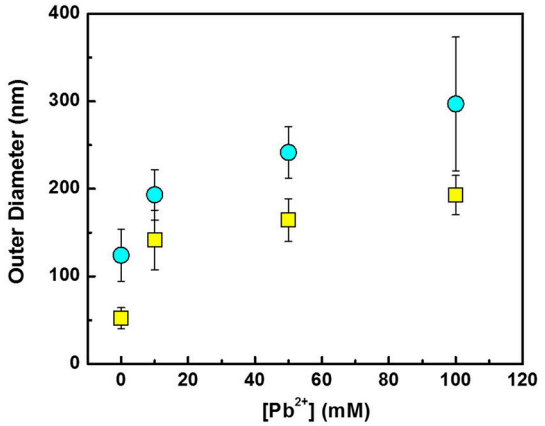

FIGURE 3 | Effect of $[Pb^{2+}]$ on the outer diameter of PbTe nanofibers. The outer diameters of Co nanofibers are shown in Figure at $[Pb^{2+}] = 0$. Yellow squares and blue circles indicate PbTe nanofibers from Co nanofibers with the average diameter of 52 and 124 nm, respectively.

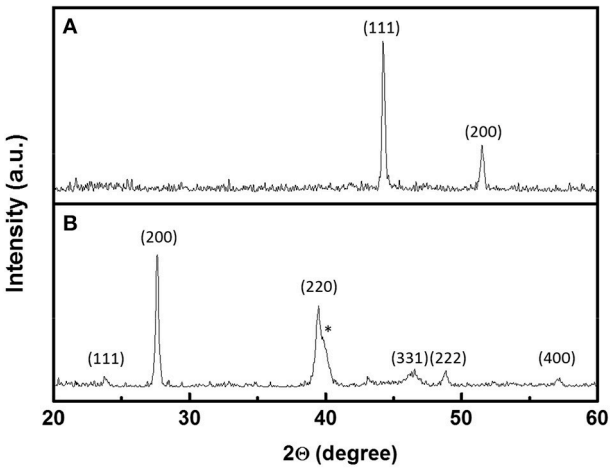

FIGURE 4 | XRD pattern of **(A)** 124-nm Co nanofibers and **(B)** $Pb_{43}Te_{57}$ hollow nanofibers from **Figure 2A**. The peaks with * belong to Pt electrodes.

which was marked with an asterisk. The asymmetric peaks at 39.5°C were contributed from both the <2 2 0> orientation of PbTe as well as the <1 1 1> plane of the sputtered Pt electrodes. The PbTe nanofibers showed no preferred orientation. The average grain size was calculated to be 60 nm, based on the intensity of the X-ray peak. No peak from elemental Te was observed. **Figure S2** shows XRD patterns of Pb_xTe_y nanofibers synthesized from various concentrations of Pb^{2+} and dimensions of Co nanofibers. Similar to the $Pb_{43}Te_{57}$ sample shown in **Figure 4B**, all of the samples showed random crystal orientation. The average grain size of the larger PbTe nanofibers were approximately the same (i.e., around 60 nm), while that of the smaller fibers was about 44 nm. This might be due to the smaller diameter of Co nanofibers, which provided limited sacrificial material source for the deposition of PbTe. Compared to larger PbTe nanofibers (**Figure S2A**), smaller nanofibers (**Figure S2B**) possessed a much lower peak intensity, which indicated a lower degree of crystallinity. No Te peak was observed in either of the nanofiber mats.

High-resolution transmission electron microscopy (HR-TEM) with EDS and SAED were utilized to characterize the morphology, composition, and crystal structure of nanofibers (**Figure 5**). As shown in the figure, the as-prepared nanofiber showed a nodular and hollow structure (**Figure 5A**) with Pb content of 43 at. %. The line-scan EDS (**Figure 5D**) analysis showed that the composition of nanofibers was uniform throughout the fiber. The fast Fourier transform (FFT)-converted SAED patterns indicated that the diffraction pattern came from (222), (220), and (200) orientation of PbTe.

Temperature-dependent I-V characterizations were carried out based on single nanofibers where the temperature was varied from 295 to 360 K (**Figure 6A**). In this temperature range, all the samples show linear I-V characteristics which indicate that the contact between nanofiber and electrodes were ohmic. **Figure 6B** shows σ as a function of temperature with the insert plot of ln $(\sigma T^{0.5})$ as a function of 1/kT. Here, k is the Boltzmann's constant. The electrical conductivity of single nanofiber was estimated from conductance of nanofiber, the estimated cross sectional area and length of hollow nanofiber. The sample showed an increase in σ with increased temperature, suggesting that the sample is semiconductor which has an energy barrier (E_b). By fitting the inserted figure in **Figure 6B**, E_b was calculated (Scheele et al., 2011). **Figures 6C,D** show σ and E_b as a function of their Pb content. The electrical conductivity increased by almost an order of magnitude when the Pb content increased by 66% in both sizes of nanofibers, whereas the energy barrier height decreased with the Pb content. The lower electrical conductivity in the lower Pb-content nanofibers might be due to the higher amount of Te, which may have created a larger energy barrier along the sample due to its amorphous phase. A more sensitive effect of Pb content on E_b was found in the larger PbTe nanofibers, shown by its steeper slope than the smaller PbTe fibers. This might be due to the larger grain size in the larger nanofibers, to which the electrical conductivity is also proportional (Seto, 1975). As shown in **Figure 6E**, the electrical conductivity was plotted as a function of E_b, which showed a monotonically decreasing trend. σ increased one order of magnitude by decreasing in E_b of 0.1 eV. A similar trend has been predicted by Faleev in a Pb nanoinclusion embedded PbTe bulk material due to the energy filtering effect (Faleev and Leonard, 2008). However, a much more significant dependence of electrical conductivity on E_b was observed in our case, since only a maximum of a 2-fold reduction was suggested in Faleev's model. This may be due to the improved charge carrier movement via non-planar radial transport as compared to 3-D planar transport in bulk materials. The effect of outer diameter of nanofibers on the electrical conductivity and E_b is shown in **Figure S3**. As no clear trend was observed, it could be concluded that the electrical conductivity and energy barrier height of PbTe nanofibers mainly depended on the composition rather than the dimension.

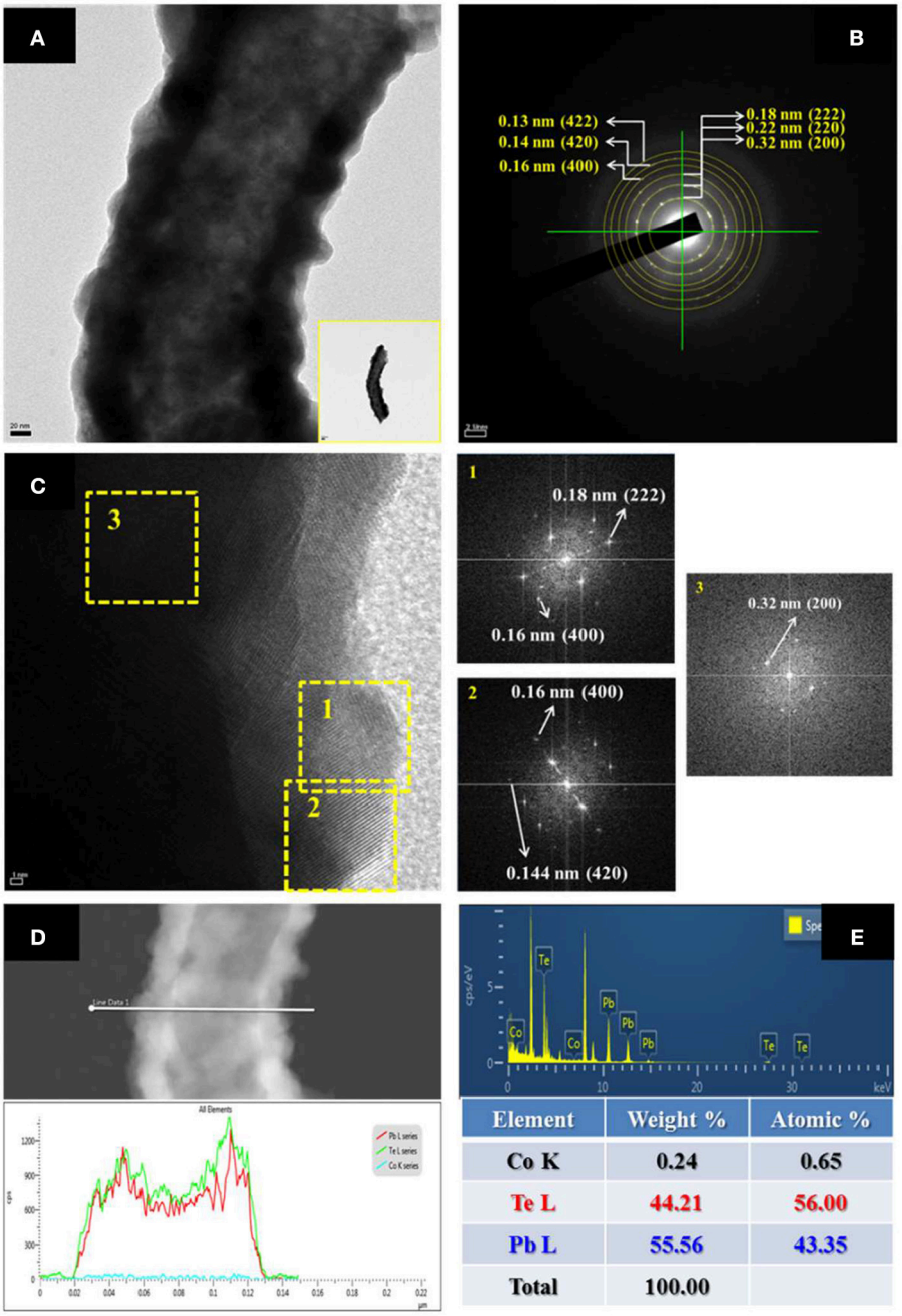

FIGURE 5 | (A) HRTEM image (inset: TEM image of low magnification); **(B)** SAED pattern; **(C)** FTT images; **(D)** Line-scan EDS; and **(E)** EDS analysis of $Pb_{43}Te_{56}$ hollow nanofibers. The electrolyte consisted of 50 mM Pb^{2+}, 0.1 mM $HTeO_2^+$, and 0.1 M HNO_3 at room temperature.

Figure 7A shows the temperature dependent ΔV-ΔT of the $Pb_{43}Te_{57}$ nanofiber mat where the temperature was varied from 300 K to 360 K. Thermopower (Seebeck Coefficient, S) were determined from the slope of ΔV-ΔT. The temperature-dependent Seebeck coefficients were plotted in **Figure 7B**. Positive thermopower (S) indicated that the samples are p-type semiconductors. Additionally, lower S with increasing temperature indicating that the sample are closed to intrinsic semiconductor (i.e., low carrier concentration). The highest S of 366 μV/K was observed at 308 K, which was higher than bulk counterpart (Abrams and Tauber, 1969). For a bulk, the maximum Seebeck coefficient (S_{max}) is a function of effective band gap energy (i.e., $S_{max} = E_g/2eT_{max}$) (Goldsmid and Sharp, 1999). Therefore, S_{max} of PbTe was predicted as shown in the dashed line in **Figure 7B**, knowing that the band gap of PbTe bulk material would follow the equation $E_g = 0.0004T$

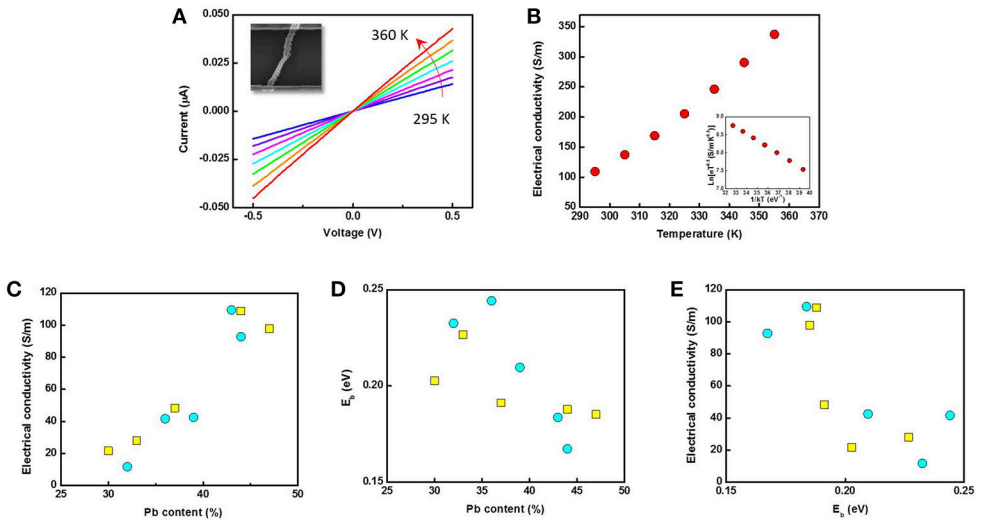

FIGURE 6 | Temperature-dependent **(A)** I-V characterization and **(B)** electrical conductivity of a single $Pb_{43}Te_{57}$ nanofiber (inset: $Ln(\sigma T^{0.5})$ as a function of 1/kT). **(C)** Electrical conductivity and **(D)** energy barrier height E_b as a function of Pb content. **(E)** Electrical conductivity of PbTe single nanofibers as functions of energy barrier height, E_b. In Figure c, d and e, yellow squares and blue circles indicate PbTe nanofibers from Co nanofibers with the average diameter of 52 nm and 124 nm, respectively.

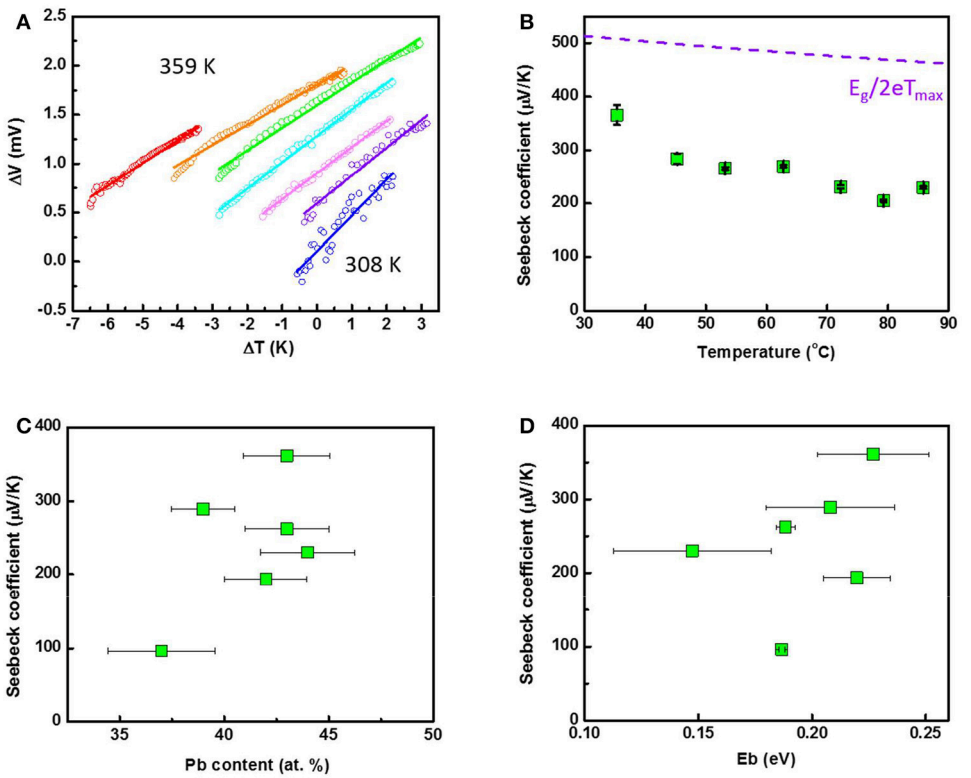

FIGURE 7 | Temperature-dependent **(A)** ΔV-ΔT characterization and **(B)** Seebeck coefficient of $Pb_{43}Te_{57}$ nanofiber mat. The maximum Seebeck coefficient $S_{max} = E_g/2eT_{max}$ was predicted and plotted as the purple dotted line. Seebeck coefficient of PbTe as functions of **(C)** Pb content and **(D)** energy barrier height, E_b.

+ 0.19. Because no optimum Seebeck coefficient was achieved in our temperature-dependent study, no comparison was made between the theoretical prediction and our experimental data.

Temperature-dependent Seebeck coefficient of Pb_xTe_y nanofiber mats with various x are shown in **Figure S4**. Smaller PbTe (i.e., $Pb_{43}Te_{57}$, $Pb_{42}Te_{58}$, and $Pb_{37}Te_{63}$) nanofibers that were reacted from 52-nm Co nanofiber mats are shown in **Figure S4a**, while larger PbTe (i.e., $Pb_{43}Te_{57}$, $Pb_{39}Te_{61}$, and $Pb_{44}Te_{56}$) nanofibers that were reacted from 124-nm Co nanofiber mats (**Figure S4B**). The thermopowers, S, were positive in all samples, indicating that they are p-type semiconductors. It is known that the thermopowere consists of partial thermopowers that are contributed by holes and electrons (Goldsmid and Sharp, 1999). Thus, thermopower of instinsic or near-instinsic semiconductor increases with increasing temperature due to greater carrier mobility at high temperature whereas thermopower of highly doped/degraded semiconductor initially increases with temperature upto onset temperature followed by decreasing thereafter (Abrams and Tauber, 1969). The enhancement of the thermopower with temperature is caused by change of Fermi level from the band edge. After onset temperature, the decrease in the thermopower is due to biopolar effects (Dow et al., 2009).

In our experiments, higher Pb content (i.e., $Pb_{43}Te_{57}$ and $Pb_{42}Te_{58}$) smaller nanofibers show the thermopower increased with temperature (**Figure S4A**). This was a typical behavior of near-intrinsic semiconductors. However, for fibers with relatively lower Pb content (i.e., $Pb_{37}Te_{63}$), the thermopower has an onset temperature at 320 K. Unfortunately, the almost plateauing tendancy of the thermopower cannot be explained at this stage. For the larger PbTe nanofibers (**Figure S4B**), the thermopower decreased with temperature for all samples. The difference behaviors require further investigation.

Figure 7C shows the thermopower as a function of the Pb content. As expected, higher thermopower were observed when the composition in near stoichiometric due to lower carrier concentration. The Seebeck coefficient describes the ability of the carrier transport from the Fermi level to the conduction band corresponding to a temperature difference. Therefore, a lower Seebeck coefficient is expected in a Te-rich PbTe nanofibers since its Fermi level has been pushed into the conduction band.

Figure 7D shows the thermopower as a function of E_b. Boundaries and interfaces can acted as an energy filter for the charge carriers, which would enable the transport only from the high charge carriers: a phenomenon known as the energy filtering effect. By doing so, the average energy of the charge carriers increases, which resulted in enhancement of the thermopower. As shown in **Figure 7D**, the thermopowers increased with the E_b of the nanofibers, which was consistent with the prediction (Faleev and Leonard, 2008). The thermopower was also plotted against the average grain size of the nanofiber mats (**Figure S5**). The smaller PbTe nanofibers had an average grain size of around 45 nm, while the larger PbTe fibers' grain size was approximately 60 nm.

CONCLUSIONS

PbTe nanofiber mats were fabricating using electrospun cobalt nanofibers as the sacrificial materials. Control over the dimension and morphology of the nanofibers were achieved by applying sacrificial material with various diameters and tuning the concentration of Pb^{2+} in the electrolytes during galvanic displacement reaction. Hollow PbTe nanofibers were synthesized in all the conditions. The fibers with larger outer diameter were obtained from thicker Co nanofibers. For the larger PbTe nanofibers, hollow and smooth surfaces were achieved using electrolytes containing low concentrations of Pb^{2+}, whereas rough surfaces were observed from using concentrated electrolytes. The formation of rough surface in the latter case may be due to the faster reaction rate. On the other hand, for the smaller PbTe nanofibers, no clear differences in morphology were observed with various [Pb^{2+}]. The smaller PbTe nanofibers were rougher than the larger PbTe nanofibers, which might be due to the rougher surface of small Co nanofibers. The Pb^{2+} concentration had negligible effects on the fibers' composition in the studied range. No residue of Co was observed in the fibers after the galvanic displacement reactions, which indicated a complete reaction. The outer diameter of PbTe nanofibers increased with the Pb^{2+} concentration. XRD analysis showed that all synthesized PbTe samples were polycrystalline in nature.

The temperature-dependent I-V characterization was conducted based on single PbTe nanofibers. The electrical conductivity decreased as the Pb content in the nanofibers decreased. It could be suggested that the excess Te created barriers in the nanofibers, increasing the barrier height while decreasing the electrical conductivity.

AUTHOR CONTRIBUTIONS

MZ, JK, and MN conducted the experiments. SK conducted TEM analysis. S-DP, YC, JL, and NM provided funding and inputs to the manuscript.

FUNDING

This research was supported by the Global Frontier Program through the Global Frontier Hybrid Interface Materials (GFHIM) project of the National Research Foundation of Korea (NRF), funded by the Ministry of Science, ICT, & Future Planning (2013M3A6B1078870). This research was also partially supported by Future Materials Discovery Program through the National Research Foundation of Korea (NRF) funded by the Ministry of Science, ICT & Future Planning(NRF-2016M3D1A1027836) and Korea Electrotechnology Research Institute (KERI).

SUPPLEMENTARY MATERIAL

The Supplementary Material for this article can be found online at: https://www.frontiersin.org/articles/10.3389/fchem.2018.00436/full#supplementary-material

REFERENCES

Abrams, H., and Tauber, R. N. (1969). Thermoelectric power of single-crystal p-Type PbSe. *J. Appl. Phys*. 40, 3868–3870.

Androulakis, J., Todorov, I., Chung, D. Y., Ballikaya, S., Wang, G, Uher, C. et al. (2010). Thermoelectric enhancement in PbTe with K or Na codoping from tuning the interaction of the light- and heavy-hole valence bands. *Phys. Rev. B*. 82:115209. doi: 10.1103/PhysRevB.82.115209

Aricò, A. S., Bruce, P., Scrosati, B., Tarascon, J. M., and Van Schalkwijk, W. (2005). Nanostructured materials for advanced energy conversion and storage devices. *Nat. Mater*. 4, 366–377. doi: 10.1038/nmat1368

Chang, C. H., Rheem, Y., Choa, Y. H., Park, D. Y., and Myung, N. V. (2010a). Galvanic displacement of BixTey thin films from sacrificial iron group thin films. *Electrochim Acta* 55, 1072–1080. doi: 10.1016/j.electacta.2009.09.066

Chang, C. H., Rheem, Y., Choa, Y. H., Shin, D. H., Park, D. Y., and Myung, N. V. (2010b). Bi and Te thin films synthesized by galvanic displacement from acidic nitric baths. *Electrochim Acta* 55, 743–752. doi: 10.1016/j.electacta.2009.09.038

Chang, C. H., Zhang, M. L., Lim, J., Choa, Y., Park, S., and Myung, N. V. (2014). Synthesis of PbTe and PbTe/Te nanostructures by galvanic displacement of cobalt thin films. *Electrochim Acta* 138, 334–340. doi: 10.1016/j.electacta.2014.06.088

Chen, J., Zhang, G., and Li, B. W. (2010). Remarkable reduction of thermal conductivity in silicon nanotubes. *Nano. Lett*. 10, 3978–3983. doi: 10.1021/nl101836z

Dedi, D., Lee, P. C., Chien, C. H., Dong, G. P., Huang, W. C., Chen, C. L., et al. (2013). Stress-induced growth of single-crystalline lead telluride nanowires and their thermoelectric transport properties. *Appl. Phys. Lett.* 103:023115. doi: 10.1063/1.4813606

Dow, H. S., Oh, M. W., Park, S. D., Kim, B. S., Min, B. K., Lee, H. W., et al. (2009). Thermoelectric properties of $AgPb_mSbTe_{m+2}$ ($12 \leq m \leq 26$) at elevated temperature. *J. Appl. Phys.* 105:113703. doi: 10.1063/1.3138803

Dughaish, Z. H. (2002). Lead telluride as a thermoelectric material for thermoelectric power generation. *Physica B*. 322, 205–223. doi: 10.1016/S0921-4526(02)01187-0

Elazem, D., Jung, H., Wu, T. J., Lim, J. H., Lee, K. H., and Myung, N. V. (2013). Morphology change of galvanically displaced one-dimensional tellurium nanostructures via controlling the microstructure of sacrificial Ni thin films. *Electrochim Acta*, 106, 447–452. doi: 10.1016/j.electacta.2013.05.117

Faleev, S. V., and Leonard, F. (2008). Theory of enhancement of thermoelectric properties of materials with nanoinclusions. *Phys. Rev. B*. 77:214304. doi: 10.1103/PhysRevB.77.214304

Fardy, M., Hochbaum, A. I., Goldberger, J., Zhang, M. M., and Yang, P. D. (2007). Synthesis and thermoelectrical characterization of lead chalcogenide nanowires. *Adv. Mater*. 19, 3047–3051. doi: 10.1002/adma.200602674

Goldsmid, H. J., and Sharp, J. W. (1999). Estimation of the thermal band gap of a semiconductor from Seebeck measurements. *J. Electron. Mater*. 28, 869–872.

Hangarter, C. M., Lee, Y. I., Hernandez, S. C., Choa, Y. H., and Myung, N. V. (2010). Nanopeapods by galvanic displacement reaction. *Angew. Chem. Int. Edit*. 49, 7081–7085. doi: 10.1002/anie.201001559

Harman, T. C., Taylor, P. J., Walsh, M. P., and LaForge, B. E. (2002). Quantum dot superlattice thermoelectric materials and devices. *Science* 297, 2229–2232. doi: 10.1126/science.1072886

Harman, T. C., Walsh, M. P., Laforge, B. E., and Turner, G. W. (2005). Nanostructured thermoelectric materials. *J. Electron. Mater*. 34, L19–L22. doi: 10.1007/s11664-005-0083-8

Hochbaum, A. I., Chen, R. K., Delgado, R. D., Liang, W. J., Garnett, E. C., Najarian, M. et al. (2008). Enhanced thermoelectric performance of rough silicon nanowires. *Nature* 451, 163–U5. doi: 10.1038/nature06381

Huber, G. W., Iborra, S., and Corma, A. (2006). Synthesis of transportation fuels from biomass: chemistry, catalysts, and engineering. *Chem. Rev*. 106, 4044–4098. doi: 10.1021/cr068360d

Jeong, D. B., Lim, J. H., Lee, J., Park, H., Zhang, M. L., Lee, Y. I. et al. (2013). Template-free synthesis of vertically oriented tellurium nanowires via a galvanic displacement reaction. *Electrochim Acta* 111, 200–205. doi: 10.1016/j.electacta.2013.07.228

Jung, H., Park, D. Y., Xiao, F., Lee, K. H., Choa, Y. H., Yoo, B. et al. (2011). Electrodeposited single crystalline PbTe nanowires and their transport properties. *J. Phys. Chem. C*. 115, 2993–2998. doi: 10.1021/jp110739v

Jung, H., Rheem, Y., Chartuprayoon, N., Lim, J. H., Lee, K. H., Yoo, B. et al. (2010). Ultra-long bismuth telluride nanoribbons synthesis by lithographically patterned galvanic displacement. *J. Mater. Chem*. 20, 9982–9987. doi: 10.1039/c0jm02058c

Jung, H., Suh, H., Hangarter, C. M., Lim, J. H., Lee, Y. I., Choa, Y. H., et al. (2012). Programmable synthesis of shape-, structure-, and composition-modulated one-dimensional heterostructures by galvanic displacement reaction. *Appl. Phys. Lett*. 100:223105. doi: 10.1063/1.4722919

Lee, K.-J., Song, H., Lee, Y.-I., Jung, H., Zhang, M., Choa, Y-H. et al. (2011). Synthesis of ultra-long hollow chalcogenide nanofibers. *Chem. Commun*. 47, 9107–9109. doi: 10.1039/C1CC12312B

Liu, J. F., Uprety, B., Gyawali, S., Woolley, A. T., Myung, N. V., and Harb, J. N. (2013). Fabrication of DNA-templated Te and Bi_2Te_3 nnowires by galvanic displacement. *Langmuir* 29, 11176–11184. doi: 10.1021/la402678j

Lokhande, C. D. (1991). Chemical deposition of metal chalcogenide thin films. *Mater. Chem. Phys*. 27, 1–43. doi: 10.1016/0254-0584(91)90158-Q

Miles, R. W., Zoppi, G., and Forbes, I. (2007). Inorganic photovoltaic cells: the inorganic semiconductor materials used to make photovoltaic cells. *Materials Today* 10, 20–27. doi: 10.1016/S1369-7021(07)70275-4

Oregan, B., and Gratzel, M. (1991). A low-cost, high-efficiency solar-cell based on dye-sensitized colloidal TiO_2 films. *Nature* 353, 737–740.

Oviedo, O. A., Leiva, E. P. M., and Rojas, M. I. (2006). Energetic and entropic contributions to the underpotential/overpotential deposition shifts on single crystal surfaces from lattice dynamics. *Electrochim Acta* 51, 3526–3536. doi: 10.1016/j.electacta.2005.10.008

Park, D. Y., Jung, H. S., Rheem, Y., Hangarter, C. M., Lee, Y. I., Ko, J. M. et al. (2010). Morphology controlled 1D Pt nanostructures synthesized by galvanic displacement of Cu nanowires in chloroplatinic acid. *Electrochim Acta* 55, 4212–4216. doi: 10.1016/j.electacta.2010.02.054

Park, H., Jung, H., Zhang, M., Chang, C. H., Ndifor-Angwafor, N. G., Choa, Y. et al. (2013). Branched tellurium hollow nanofibers by galvanic displacement reaction and their sensing performance toward nitrogen dioxide. *Nanoscale* 5, 3058–3062. doi: 10.1039/c3nr00060e

Park, K. R., Kim, S., Myung, N. V., Kang, S. O., and Choa, Y. H. (2015). Simple electrochemical synthesis of ultra-long silver telluride nanotubes. *RSC. Adv*. 5, 29782–29785. doi: 10.1039/C4RA15688A

Pichanusakorn, P., and Bandaru, P. (2010). Nanostructured thermoelectrics. *Mat. Sci. Eng. R*. 67, 19–63. doi: 10.1016/j.mser.2009.10.001

Reneker, D. H., and Yarin, A. L. (2008). Electrospinning jets and polymer nanofibers. *Polymer* 49, 2387–2425. doi: 10.1016/j.polymer.2008.02.002

Rheem, Y., Chang, C. H., Hangarter, C. M., Park, D. Y., Lee, K. H., Jeong, Y. S. et al. (2010). Synthesis of tellurium nanotubes by galvanic displacement. *Electrochim Acta* 55, 2472–2476. doi: 10.1016/j.electacta.2009.12.002

Scheele, M., Oeschler, N., Veremchuk, I., Peters, S. O., Littig, A., Kornowski, A. et al. (2011). Thermoelectric properties of lead chalcogenide core-shell nanostructures. *ACS Nano*. 5, 8541–8551. doi: 10.1021/nn2017183

Seto, J. Y. W. (1975). Electrical properties of polycrystalline silicon films. *J. Appl. Phys*. 46, 5247–5254.

Snyder, G. J., and Toberer, E. S. (2008). Complex thermoelectric materials. *Nat. Mater*. 7, 105–114. doi: 10.1038/nmat2090

Suh, H., Jung, H., Hangarter, C. M., Park, H., Lee, Y., Choa, Y. et al. (2012). Diameter and composition modulated bismuth telluride nanowires by galvanic displacement reaction of segmented NiFe nanowires. *Electrochim Acta* 75, 201–207. doi: 10.1016/j.electacta.2012.04.090

Suh, H., Nam, K. H., Jung, H., Kim, C. Y., Kim, J. G., Kim, C. S. et al. (2013). Tapered BiTe nanowires synthesis by galvanic displacement reaction of compositionally modulated NiFe nanowires. *Electrochim Acta* 90, 582–588. doi: 10.1016/j.electacta.2012.12.011

Szczech, J. R., Higgins, J. M., and Jin, S. (2011). Enhancement of the thermoelectric properties in nanoscale and nanostructured materials. *J. Mater. Chem*. 21, 4037–4055. doi: 10.1039/C0JM02755C

Tai, G., Zhou, B., and Guo, W. L. (2008). Structural characterization and thermoelectric transport properties of uniform single-crystalline lead telluride nanowires. *J. Phys. Chem. C*. 112, 11314–11318. doi: 10.1021/jp8041318

Venkatasubramanian, R. (2000). Lattice thermal conductivity reduction and phonon localizationlike behavior in superlattice structures. *Phys. Rev. B* 61, 3091–3097. doi: 10.1103/PhysRevB.61.3091

Wu, T. J., Myung, L. Y., Zhang, M. L., Lee, K. H., Lee, Y. L., Lim, H. R. et al. (2015). Size controlled synthesis of tellurium nanorices by galvanic displacement reaction of aluminum. *Electrochim Acta* 176, 1382–1392. doi: 10.1016/j.electacta.2015.07.088

Wu, T. J., Zhang, M. L., Lee, K. H., Kim, S. I., Choa, Y., and Myung, N. V. (2014). Synthesis of tellurium heterostructures by galvanic displacement reaction of zinc in alkaline baths. *Electrochim Acta* 150, 298–307. doi: 10.1016/j.electacta.2014.10.099

Xiao, F., Yoo, B., Bozhilov, K. N., Lee, K. H., and Myung, N. V. (2007a). Electrodeposition of single-crystal cubes of lead telluride on polycrystalline gold substrate. *J. Phys. Chem. C.* 111, 11397–11402. doi: 10.1021/jp072584y

Xiao, F., Yoo, B., Lee, K. H., and Myung, N. V. (2007b). Synthesis of Bi2Te3 nanotubes by galvanic displacement. *J. Am. Chem. Soc.* 129, 10068–10069. doi: 10.1021/ja073032w

Xiao, F., Yoo, B., Ryan, M. A., Lee, K. H., and Myung, N. V. (2006). Electrodeposition of PbTe thin films from acidic nitrate baths. *Electrochim Acta* 52, 1101–1107. doi: 10.1016/j.electacta.2006.06.044

Yang, Y. A., Taggart, D. K., Cheng, M. H., Hemminger, J. C., and Penner, R. M. (2011). High-throughput measurement of the Seebeck coefficient and the electrical conductivity of lithographically patterned polycrystalline PbTe nanowires *J. Phys. Chem. Lett. 2*, 944–944. doi: 10.1021/jz200449s

Zhang, M. L., Kim, J., Kim, S., Park, H., Jung, H., Ndifor-Angwafor, N. G. et al. (2014). Galvanically displaced ultralong PbxSeyNiz hollow nanofibers with high thermopower. *Chem. Mater*. 26, 2557–2566. doi**:** 10.1021/cm4041067

Zhang, M. L., Park, H., Kim, J., Park, H., Wu, T. J., Kim, S. et al. (2015). Thermoelectric properties of ultra long silver telluride hollow nanofibers. *Chem. Mater*. 27, 5189–5197. doi: 10.1021/acs.chemmater.5b00960

Zhou, G., Li, L., and Li, G. H. (2010). Enhancement of thermoelectric figure of merit in bismuth nanotubes. *Appl. Phys. Lett.* 97:023112. doi: 10.1063/1.3463473

Zhou, W. X., Tan, S. H., Chen, K. Q., and Hu, W. P. (2014). Enhancement of thermoelectric performance in InAs nanotubes by tuning quantum confinement effect. *J. Appl. Phys.* 115:124308. doi: 10.1063/1.4869745

Conflict of Interest Statement: The authors declare that the research was conducted in the absence of any commercial or financial relationships that could be construed as a potential conflict of interest.

frontiers in Chemistry

ORIGINAL RESEARCH
published: 14 January 2019
doi: 10.3389/fchem.2018.00600

Kerf-Less Exfoliated Thin Silicon Wafer Prepared by Nickel Electrodeposition for Solar Cells

Hyun-Seock Yang[1,2], Jiwon Kim[1], Seil Kim[1], Nu Si A. Eom[1], Sangmuk Kang[3], Chang-Soon Han[4], Sung Hae Kim[5], Donggun Lim[3], Jung-Ho Lee[5], Sung Heum Park[2], Jin Woo Choi[6], Chang-Lyoul Lee[6], Bongyoung Yoo[5] and Jae-Hong Lim[1]**

[1] Electrochemistry Department, Korea Institute of Materials Science, Changwon, South Korea, [2] Department of Physics, Pukyong National University, Busan, South Korea, [3] Department of IT Convergence, Korea National University of Transportation, Chungju, South Korea, [4] Laser Advanced System Industrialization Center, Mam-myeun, South Korea, [5] Department of Materials Engineering, Hanyang University, Ansan, South Korea, [6] Advanced Photonics Research Institute, Gwangju Institute of Science and Technology, Gwangju, South Korea

Ultra-thin and large-area silicon wafers with a thickness in the range of 20–70 μm, were produced by spalling using a nickel stressor layer. A new equation for predicting the thickness of the spalled silicon was derived from the Suo–Hutchinson mechanical model and the kinking mechanism. To confirm the reliability of the new equation, the proportional factor of stress induced by the nickel on the silicon wafer, was calculated. The calculated proportional factor of $\lambda = 0.99$ indicates that the thickness of the spalled silicon wafer is proportional to that of the nickel layer. A similar relationship was observed in the experimental data obtained in this study. In addition, the thickness of the stressor layer was converted to a value of stress as a guide when using other deposition conditions and materials. A silicon wafer with a predicted thickness of 50 μm was exfoliated for further analysis. In order to spall a large-area (150 × 150 mm^2 or 6 × 6 in^2) silicon wafer without kerf loss, initial cracks were formed by a laser pretreatment at a proper depth (50 μm) inside the exfoliated silicon wafer, which reduced the area of edge slope (kerf loss) from 33 to 3 mm^2. The variations in thickness of the spalled wafer remained under 4%. Moreover, we checked the probability of degradation of the spalled wafers by using them to fabricate solar cells; the efficiency and ideality factor of the spalled silicon wafers were found to be 14.23%and 1.35, respectively.

Keywords: ultra-thin silicon wafer, spalling, stressor layer, kerf loss, edge slope, electrodeposition

OPEN ACCESS

Edited by:
Juchen Guo,
University of California, Riverside, United States

Reviewed by:
Abhishek Lahiri,
Clausthal University of Technology, Germany
Young-In Lee,
Seoul National University of Science and Technology, South Korea

***Correspondence:**
Bongyoung Yoo
byyoo@hanyang.ac.kr
Jae-Hong Lim
lim@kims.re.kr

Specialty section:
This article was submitted to Electrochemistry, a section of the journal Frontiers in Chemistry

Received: *22 September 2018*
Accepted: *20 November 2018*
Published: *14 January 2019*

Citation:
Yang H-S, Kim J, Kim S, Eom NSA, Kang S, Han C-S, Kim SH, Lim D, Lee J-H, Park SH, Choi JW, Lee C-L, Yoo B and Lim J-H (2019) Kerf-Less Exfoliated Thin Silicon Wafer Prepared by Nickel Electrodeposition for Solar Cells. Front. Chem. 6:600. doi: 10.3389/fchem.2018.00600

INTRODUCTION

Silicon solar cells are the focus of considerable research efforts because of their high energy-conversion efficiency (∼25%) (Green et al., 2015), stability, and so on (Bruel, 1995; Dross, 2008; Shahrjerdi et al., 2012; Radhakrishnan et al., 2014; Kobayashi et al., 2015; Lee et al., 2016; Green et al., 2017; Wang et al., 2017). Ultra-thin silicon wafers with thickness in the range of 40–60 μm are particularly suitable for high-efficiency solar cells because of their high light absorption and flexibility (Dross, 2008). However, the >100% kerf loss during the fabrication of ultra-thin silicon wafers (thickness: <100 μm) using conventional sawing technology is a critical problem (Green et al., 2017) that increases material cost and requires additional post-sawing processes. Therefore, it is important to minimize the waste associated with wafer losses during sawing. Several methods

are available for fabricating kerf-less thin silicon wafers, such as the stress-inducing process (Shahrjerdi et al., 2012; Wang et al., 2017), ion implantation (Bruel, 1995; Lee et al., 2016), and epitaxial growth (Radhakrishnan et al., 2014; Kobayashi et al., 2015). Since it is difficult to form a stable trajectory during the ion-implantation process, the resulting wafers tend to have high surface roughness (Suo, 1989). The process of inducing stress through by mismatching the thermal coefficients of silicon and a deposited polymer requires a high temperature, which causes degradation of the carrier lifetime (Suo and Hutchinson, 1989). Slim-cut and epitaxial-growth processes require complex equipment and procedures (Radhakrishnan et al., 2014). On the other hand, the electrochemical process is quite suitable because of the low production cost, easy scale-up, stress control, and high material yield (Drory et al., 1988). However, it is difficult to predict the propagation and initial depth inside a silicon wafer, creating problems in the thickness control of spalled silicon wafers, which represent a major disadvantage of the electrochemical process when compared with other methods. In addition, the general electrochemical process causes edge sloping up through the threshold of steady-state crack depth during spalling (Suo, 1989), which causes problems such as kerf loss at the edge of the wafer and high roughness which can cause fractures in the spalled silicon wafer. The fractures induced by kerf loss can be a critical problem for the large-scale production of spalled silicon wafers with areas over 150 × 150 mm^2 (6 × 6 in^2). It is therefore necessary to reduce the edge slope and predict the thickness of the spalled silicon wafer.

In the study reported here, we combined the process of laser pretreatment at the edge of a silicon wafer and electrodeposition of nickel, with high internal stress, on top of the substrate. This structure was designed to reduce the edge slope and enhance the uniformity of the silicon wafer after spalling. In addition, a relationship was proposed for predicting the thickness of the spalled silicon wafer. The long-wavelength laser process formed cracks without damaging the surface of the sample, which served as the initial cracks that extended along the interface, deviated into the substrate, and subsequently propagated in a direction parallel to the interface at a steady-state crack depth beneath the interface (Suo and Hutchinson, 1990). We confirmed the effect of the initial crack formed by the laser process on the kerf-less silicon wafer. A new equation for predicting the spalling silicon thickness was proposed, based on the prediction of the initial crack depth and the calculation of the steady-state crack depth from the Suo–Hutchinson (S&H) model (Suo and Hutchinson, 1990). The validity of the proposed equation was evaluated by comparing the calculated results with the experimental data.

EXPERIMENTAL

The spalling process can be divided into three successive steps: (1) pretreatment with a laser to form cracks at the edge of the wafer; (2) electrodeposition of the metal stressor layer; and (3) spalling of the silicon wafer. A schematic diagram of the process is shown in **Figure 1**.

In our study, p-type monocrystalline 150 × 150 mm^2 (6 × 6 in^2) silicon wafers with <100> orientation and 1–10 Ω resistance were utilized because their low roughness was suitable for crack propagation. In order to reduce the edge slope after spalling, pretreatment was carried out using a laser (Lumera Hyper Rapid 50, Coherent, USA). The laser wavelength was set at 1,064, 532 or 355 nm, the generation capacity was selectable with a power of 50, 20, or 16 W, and the frequency was 400 KHz. The laser was focused at a point in an area that had the same steady-state crack depth, to form initial cracks all around the edge of the silicon wafer at a periodic distance of 100 μm. After the laser treatment, an electron-beam (e-beam) evaporator (Super High Speed Evaporator System, Daedong Hightec, Korea) was used to deposit Ti as an adhesion layer (thickness: 20 nm) and nickel as a seed layer (thickness: 100 nm) on the silicon wafer. The nickel seed layer had much higher conductivity than the silicon wafer. Prior to electrodeposition, the wafer was degreased in an alkaline bath (5% NaOH) to increase the hydrophilicity of its surface, followed by pickling in a 10% HCl bath to remove any metal oxide.

After the wafer was cleaned and treated, nickel(II) chloride ($NiCl_2$; concentration: 1 mol/L, purity: 98.5%, SAMCHUN, Korea) and sodium citrate (concentration: 0.1 mol/L, purity:

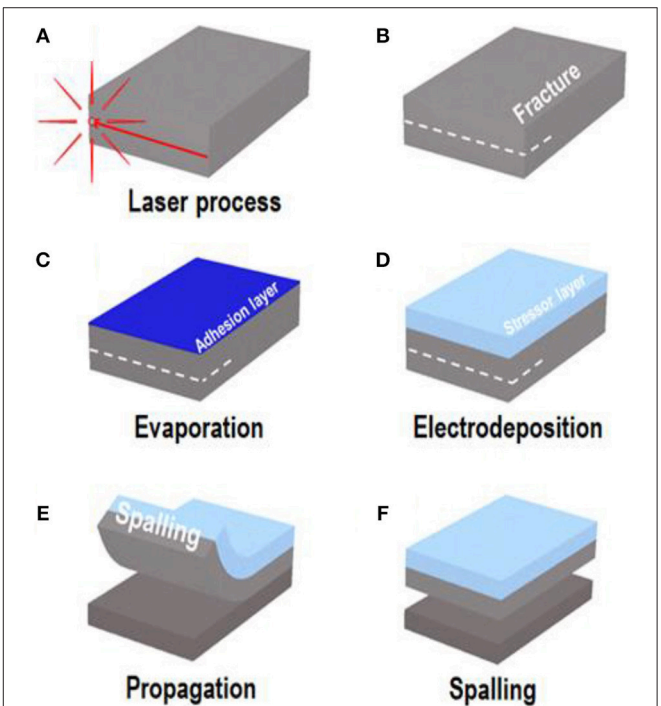

FIGURE 1 | Schematic of the laser-based spalling process: **(A)** laser process at the edge of silicon wafer; **(B)** formation of a fracture at the wafer edge; **(C)** e-beam evaporation for adhesion layer and seed layer; **(D)** electrodeposition to grow stressor layer; **(E)** spontaneous crack and propagation of the tip; **(F)** spalled kerf-less silicon wafer.

Abbreviations: ALD, atomic layer deposition; DI, deionized; IPA, isopropyl alcohol; ITO, indium–tin oxide; PL, photoluminescence; S&H, Suo and Hutchinson; SEM, scanning electron microscopy; SIMS, secondary ion mass spectroscopy; XRD, X-ray diffraction.

99%, Sigma Aldrich, USA) were mixed together to form the electrodeposition bath; a sufficient amount of HCl was added to adjust the pH of the mixture to 3.5. $NiCl_2$ was the main supplier of nickel ions, and sodium citrate served as a buffer to maintain the pH and carry the electrons in the bath. The nickel stressor layer was deposited on the silicon wafer by immersing it in the all-chloride bath. This was done because a higher internal stress could be obtained than in an all-chloride bath, than in a non-chloride bath (Bedell et al., 2017). A low voltage (1.2–2.8 V) was applied by a power supply with a direct current, and a nickel stressor layer with a thickness of 50 μm was obtained after 250 min. The current density used for the nickel electrodeposition was 5 mA/cm^2, and the bath temperature was maintained at 50. The thickness and variations in thickness of the deposited nickel stressor layer, were measured by analyzing scanning electron microscope (SEM; SU-6000, Hitachi, Japan) cross-sectional images and using an X-ray fluorescence thickness analyzer (D/MAX-2500, Rigaku, Japan). In addition, the elemental detection and crystal structure of the spalled silicon wafer were measured by secondary ion mass spectroscopy (SIMS; IMS 7f, CAMECA, France) and a X-ray diffraction (XRD; D/Max-2500VL, Rigaku, Japan), *respectively*. Steady-state photoluminescence (PL) spectra were measured using a monochromator (Acton Series SP-2150i, Princeton Instruments, USA) equipped with a photomultiplier tube (PMT; ID-441 for Acton Series, Princeton Instruments, USA) and a Ti:sapphire excitation laser with a wavelength of 860 nm (Mira 900, Coherent, USA).

A wafer sample, which did not have spontaneous cracks formed during nickel electrodeposition, was removed from the electrodeposition bath. If there was sufficient breaking stress within the silicon wafer, the fracture formed by laser treatment would have propagated through the sample itself. After spalling, the nickel layer was etched by a mixed solution consisting of nitric acid (mixing ratio of 1:1), deionized water, and 25 mL/L HF. The etching of the Ni layer and Ti adhesion layer and the diffusion of the impurities into the silicon wafer were measured by SIMS.

The stress induced in the nickel layer was measured by a stress strip test (B975, Specialty Testing, USA). The stress depended on the grain size of the nickel particles, deposition rate, and potential difference. Moreover, the most critical factor of stress control was the thickness of the nickel layer. The edge slope of the spalled silicon wafer was measured with an optical microscope (RH-2000, Hirox, Japan) and by thickness profiling (RH-2000, Hirox, Japan).

Prior to the fabrication of the solar cell, the spalled silicon wafer was sequentially cleaned as follows: (1) a short dip in 5 M hydrofluoric (HF) acid; (2) immersion in 50 wt% potassium hydroxide (KOH) at a temperature of 80°C for 1 min; (3) immersion in a piranha solution (H_2SO_4/H_2O_2 volume ratio = 3:1) for 15 min; and (4) a short dip in HF to remove unwanted contaminants from the spalling process. To increase light absorption, pyramid textures were formed on the front side of the wafer by treating it with 700 mL of a 2 wt% KOH solution mixed with 45 mL of isopropyl alcohol (IPA) at a temperature of 80°C for 1 h.

A silicon solar cell with a dopant-free heterojunction was fabricated using the cleaned and textured spalled silicon wafer. First, an ultra-thin Al_2O_3 layer (thickness: 0.5 nm) was deposited using an atomic layer deposition (ALD) system (D100, NCD Tech, Korea) at a temperature of 150°C to lightly passivate the surface. Next, a layer of lithium fluoride (LiF_x; purity: 99.98%, LTS chemical, USA) (thickness: 1 nm) was deposited by evaporation as an electron-transporting layer and an Al layer (thickness: 100 nm) was deposited without a vacuum break on the rear side of the wafer. A vanadium oxide (V_2O_x; purity: 99.99%, LTS Chemical, USA) layer (thickness: 15 nm) was deposited in the same manner as a hole-transporting layer on the front side of the wafer. Subsequently, a layer of indium–tin oxide (ITO; 10% SnO_2, 90% In_2O_3, purity: 99.99%) (thickness: 80 nm) was sputtered onto the V_2O_x surface in an Ar flow at room temperature under a pressure of 8.0×10^{-7} Torr for 1070 s. Finally, an Ag layer (thickness: 1 μm) was deposited by evaporation as the electrode on the front side.

The current density vs. voltage (J–V) data of the solar-cell performance was obtained with a solar simulator (XES-502S, San-El Electric, Japan) under one sun irradiation (100 mW/cm^2, AM 1.5 spectrum, 25°C). The ideality factor (η) and series resistance (R_S) were extracted from the dark J–V curve. The spectral response measurements were obtained as the incident-photon-to-current conversion efficiency (IPCE; k3100, PV Measurements, USA) using a 150 W arc lamp with a wavelength range of 350–1,100 nm.

RESULTS AND DISCUSSIONS

Stress Induced Stress by Nickel Stressor Layer

For delivery of uniform stress on a large silicon wafer, the nickel stressor layer must be uniformly deposited. Since the trajectory of spalling propagation was parallel to the nickel surface, the control of uniform deposition of the nickel stressor layer was a critical factor of large-area spalling (Suo and Hutchinson, 1990). **Figure 2** shows a shield, with dimensions of 12.48 × 12.48 cm^2, used for the nickel deposition. It was placed 2 cm from the substrate to reduce the thickness variation (Drory et al., 1988). **Figure 2B** shows the thickness of the nickel layer at different points in the diagonal direction. Without a shield, the thickness of the deposited nickel film at the edge and center, and the mean thickness were approximately 9.5, 5, and 6 μm, respectively. On the other hand, the nickel film deposited with a shield had a uniform thickness of about 7 μm, which demonstrates that the shield assisted uniform growth of the nickel stressor layer, when it was deposited by controlling the electric field in the bath.

Figure 3 shows the stress of different nickel layers formed under various deposition conditions. Tensile stress was induced on the silicon wafer because the nickel layer had a smaller lattice constant (3.520 Å) than the silicon wafer (5.430 Å for Si<100>) (Bilby and Eschelby, 1968). **Figure 3A** shows the intrinsic stress of the deposited nickel stressor layers, with a thickness of 45 and 55 μm, as a function of the current density (3, 5, and 10 mA/cm^2). The intrinsic stress decreased with increasing current

density, indicating that higher intrinsic stress was induced in the thinner silicon substrate. Although all the stressor layers had the same thickness, the amount of induced stress changed with the current density, which meant that an optimized current density was necessary (Durney, 1984). To optimize the current density, the stress induced by the intrinsic stress in the nickel stressor layer, was measured by a stress strip test; the results are shown in **Figure 3B**. The stress induced by the nickel layer decreased with increasing nickel-layer thickness, because the stress was transferred from the nickel layer to the silicon wafer. When a high level of intrinsic stress (1,260 mA/cm^2) was induced, a spontaneous crack emerged at the edge of the sample and caused high roughness on the spalled silicon wafer. On the other hand, when a lower level of induced stress (1,600 mA/cm^2) was not enough to cause spalling, the initial crack at the edge of the silicon wafer did not cause any breakage (**Supplementary Figure 1**). If the external force for spalling was applied to the silicon wafer's edge, the nickel layer would be torn because of low induced stress. The optimized current density for spalling a 50 μm silicon wafer was 5 mA/cm^2. The stress induced in the silicon wafer, was calculated from the shift in the XRD peak. The main peak of the silicon wafer was shifted from 2θ of 68.88° to 69.28° by the stress of the silicon wafer, indicating that the silicon wafer was under compressive stress. However, the scale of the peak shift was too small to allow an accurate calculation of the stress in the silicon wafer (**Figure 3C**).

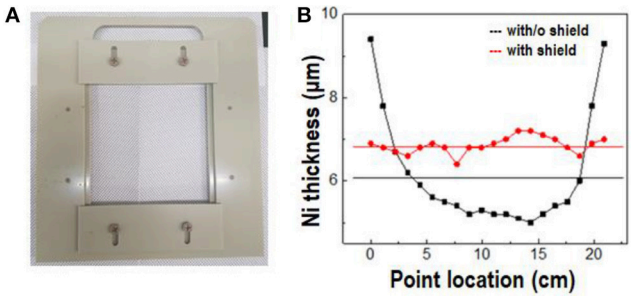

FIGURE 2 | (A) Image of shield for uniform deposition of the nickel stressor layer. **(B)** Variations in thickness of nickel stressor layers, deposited without the shield (black line), and with the shield (red line).

Initial Crack Formed in Silicon Wafer by Laser Process

Based on our findings, we suggest fabricating kerf-less silicon wafers via a laser process to decrease the kerf-loss area. **Figure 4** shows the edge slope image of spalled silicon wafers prepared with and without laser pretreatment. The edge of the spalled silicon wafer without the laser pretreatment had non-uniform roughness and an edge-slope width of 5,500 μm. The edge-slope width of all samples prepared without the laser treatment had the same area, regardless of the sample size. On the other hand, the laser-treated spalled silicon wafer had an edge-slope width of 500 μm, as shown in **Figure 4B**. The area of the edge slope was <10% than that of the sample without the laser pretreatment because of the trajectory formed at the edge slope of the spalled silicon wafer. A spalled silicon wafer generally exhibits an unstable trajectory toward the fracture threshold before the steady-state crack depth. To reach the steady-state crack depth for a stable-state trajectory, crack propagation must be initiated at the interface between the silicon wafer and the nickel stressor layer. The depth of the initial cracks could be controlled by focusing on the edge, as shown in **Figure 4C.** By adjusting the laser focus, the initial cracks were produced at points that had the same depth and the steady-state crack depth. These initial cracks led to a stable-state trajectory, and crack propagation was initiated at the steady-state crack depth. The trajectory initiated from the silicon wafer edge by the laser process, was parallel to the interface between the silicon wafer and the nickel stressor film with biaxial tensile stress (Rice, 1988). Consequently, we confirmed that the initial crack formed by the laser process led to a decrease in the kerf-loss area of the silicon wafer.

Spalled Kerf-Less Silicon Wafer

Figure 5A shows the thickness of spalled thin silicon wafers and the induced stress as functions of the nickel thickness. The induced stress in the silicon wafer decreased with increasing nickel thickness, resulting in increased thickness of the spalled silicon wafer. Because the induced stress in the silicon wafer caused crack propagation inside the silicon wafer at a steady-state crack depth, the thickness of the spalled silicon wafer was higher when the internal stress of the nickel stressor layer was lower. As shown in **Figures 5A,C**, the thickness of the spalled silicon wafers was in the range of 20 to 70 μm. Once a crack was initiated

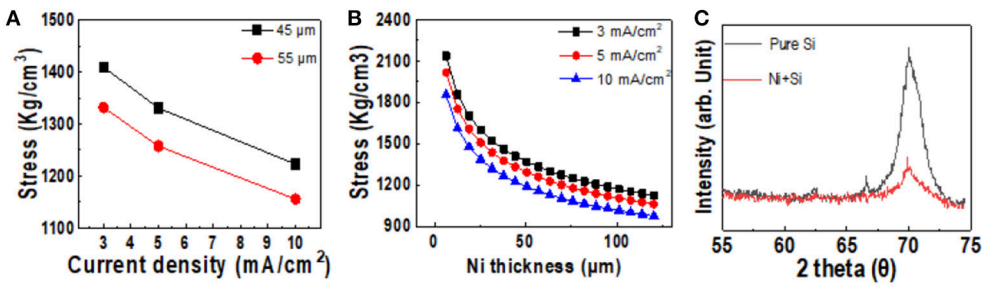

FIGURE 3 | Stress induced by the nickel stressor layer as a function of the **(A)** current density and **(B)** thickness of nickel layer. **(C)** Shift in XRD peak caused by the stressor layer.

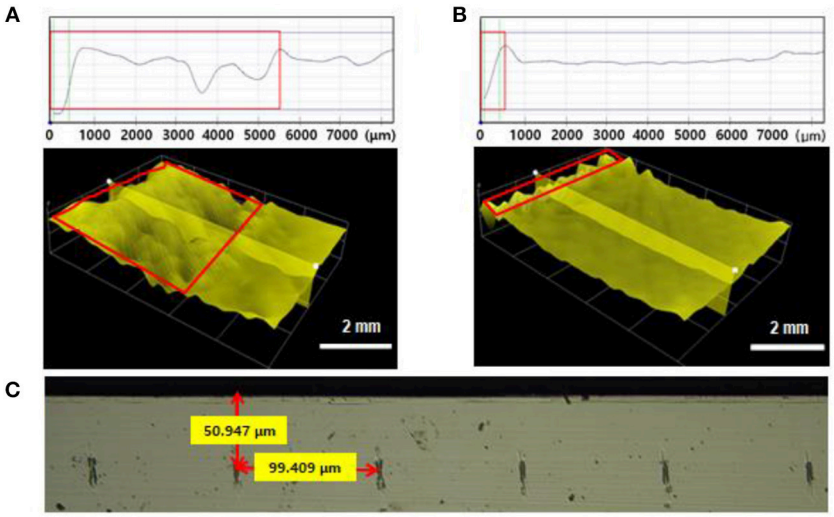

FIGURE 4 | Surface profiling (top) and 3D optical microscope image (bottom) of the edge slope of spalled silicon wafers: **(A)** without laser pretreatment; **(B)** with laser pretreatment. **(C)** Image of initial cracks (50 μm).

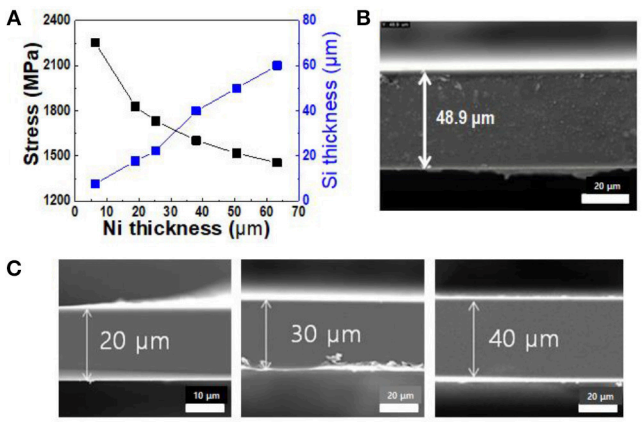

FIGURE 5 | Thickness of spalled silicon wafers corresponding to nickel stressor layers of various thickness: **(A)** variations in thickness of spalled silicon wafer with changes in stress and nickel layer thickness; **(B)** SEM cross-sectional image of spalled silicon wafer (156 × 157 mm^2); **(C)** spalled silicon wafers of various thickness.

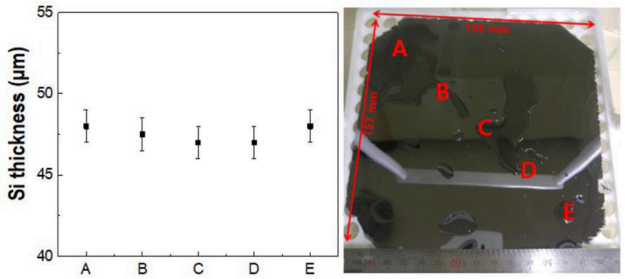

FIGURE 6 | Thickness distribution on a 150 × 150 mm^2 (6 × 6 in^2) large-area spalled silicon wafer; image of a kerf-less ultra-thin silicon wafer.

in a silicon wafer, it could propagate in a direction parallel to the surface at a depth proportional to the thickness of the nickel layer at the center of the wafer. **Figure 5B** shows an SEM cross-sectional image of a spalled silicon wafer with a 50 μm nickel stressor layer. It should be noted that this nickel stressor layer was removed by wet etching, leaving a spalled silicon wafer with a flat surface and a thickness of 50 μm.

To verify the thickness distribution of the spalled silicon wafer with a large area, the spalling process was carried out on a 150 × 150 mm^2 (6 × 6 in^2) silicon wafer. **Figure 6** shows that a thin silicon wafer with a large area was obtained. The thickness was measured at five points on the silicon wafer, and each point on the same line was plotted at intervals of 220 mm. The spalled silicon wafer in **Figure 6** exhibited a uniform thickness of approximately 50 μm, and the deviation of the silicon wafer thickness remained under 2 μm (4%). This uniform thickness resulted from the induced homogenous stress, and we believe that the approach can be used to provide significant performance improvements in large-scale silicon production.

For the successful application of spalled wafers in silicon-based solar cells, impurities that diffused into the silicon wafer during evaporation or electrodeposition, must be monitored as they could affect the mechanical and optical properties of the silicon, thus compromising the efficiency of the solar cell. **Figure 7** shows the physical and optical properties of a spalled silicon wafer after each etching process. There were no impurities on the bare silicon wafer, as shown in **Figure 7A.** In general, the detection limit of most instruments is in the range of 10^{13}-10^{15} atom/cm^3[1]. As shown in **Figure 7A**, 10^{17} atoms of Ti were detected in 1 cm^3 of the pure silicon wafer. Therefore,

[1]Evans Analytical Group. Available online at: http://www.nanoscience.co.jp/industry_analysis/pdf/AN339.pdf

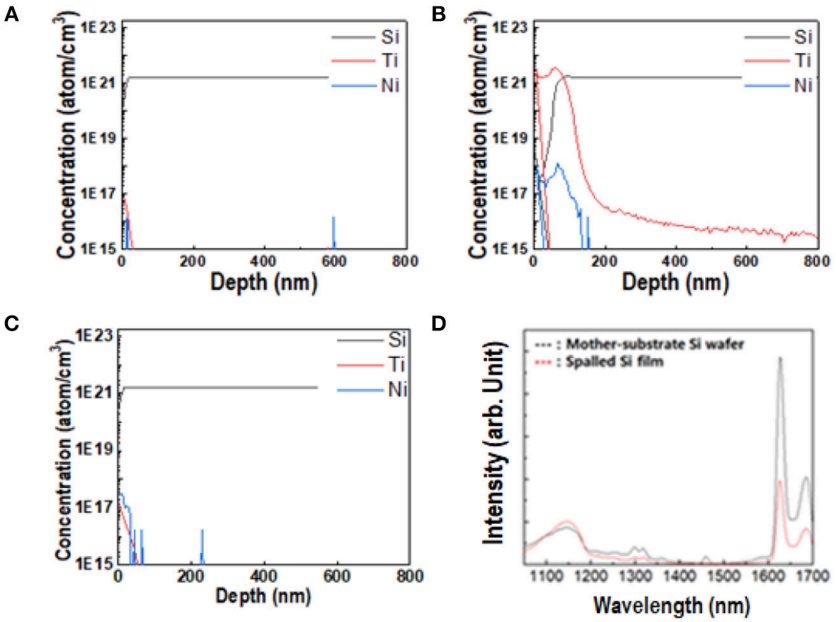

FIGURE 7 | Physical properties of spalled Si wafer. **(A–C)** Atomic concentration of Si, Ti, and Ni at various vertical positions in different samples: **(A)** pure Si mother substrate; **(B)** spalled Si wafer after etching without HF; **(C)** spalled Si wafer after etching with 25 mL/L HF. **(D)** Comparison of PL of spalled Si wafer (red line) with that of pure Si mother substrate (black line).

in this study, the detection limit of Ti and Ni atoms was assumed to be 10^{17} atom/cm^3. After the nickel etching process without the HF solution, a Ti layer and a small Ni peak was detected on the spalled silicon wafer (**Figure 7B).** The Ni ions were expected to penetrate the Ti layer during the evaporation or electrodeposition. To eliminate Ni-based impurities, the Ti layer must be etched. **Figure 7C** shows no impurities on the spalled silicon wafer after it was etched with a HF solution. **Figure 7D** shows the PL spectra of both the pure silicon wafer and the spalled silicon wafer. The spalled silicon wafer showed no obvious PL spectrum shift, when compared to the spectrum of the pure silicon wafer, indicating that the band structure related to PL of the spalled silicon wafer remained unchanged by spalling.

Analysis of Steady-State Crack Depth

According to the S&H model, the thickness of a spalled silicon wafer can be predicted when the initial crack can be calculated from the stress induced by the electrodeposited layer. There, internal stress of electrodeposited materials during the spalling process, can be traced to two origins. The first source is the misfit stress resulting from the lattice mismatch between the substrate and the metal film (Sun and Jih, 1987; Saitou, 2008). The induced misfit stress in the substrate tends to reduce the potential energy and causes its own curvature and fracture (Richardson, 2014). This phenomenon manifests as changes in the energy release rate (Kim et al., 1996), which is the energy dissipated per unit of a newly created fracture surface area (i.e., the tip) during a fracture[2]. A fracture causes free-state stress on the upper side, which is the opposite side of the mother substrate.

This energy release rate, G, is defined as

$$G = \frac{\partial (U - V)}{\partial A}, \tag{1}$$

where U is the potential energy available for crack propagation, V is the work associated with any external forces acting on the system, and A is the crack area (linear for two-dimensional cracks). The crack direction is along the direction of the tip. When the fracture energy, G_c, is higher than G ($G_c > G$), the crack begins to propagate. G_c is considered to be a material property that is independent of the applied load and the geometry of the body. In order to apply the stress needed for spalling, the external force must be zero, i.e., $V = 0$, which means that the crack propagation occurs on its own. If the external force is not zero, the spalled wafer will have high roughness.

Internal stress can also be induced when coalescence occurs in a single material. The intrinsic stress of the coalescence of metal grains (He and Hutchinson, 1989) is caused by the nucleation of isolated states that grow and approach other grains. When a grain encounters other grains, recrystallization occurs at the grain boundary (Sun and Jih, 1987) This recrystallization area has a different crystal direction when compared with the original grains (Rachwal, 2010), resulting in stress in the metal film. To induce stress inside a silicon substrate in our study,

[2]DEAS Harvard University. Available online at: http://www.mrsec.harvard.Edu/education/ap298r2004/Vlassak%20AP298presentation.pdf

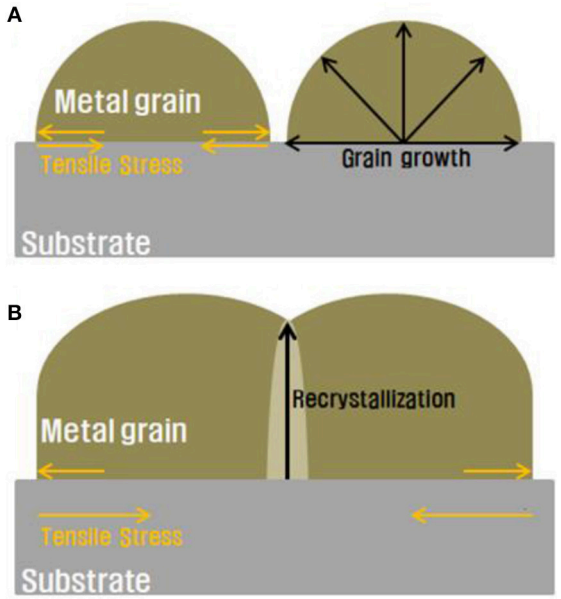

FIGURE 8 | Schematic of residual stress induced by **(A)** isolated metal particles and **(B)** coalescence of metal particles on the substrate.

an electrodeposited nickel layer was used as the stressor layer. At the initial stage, isolated nickel grains were formed on the silicon substrate and each grain grew at the same rate to form the nickel stressor layer. Because the nickel layer had a smaller lattice constant than that of the silicon substrate, tensile stress was induced in the silicon substrate (Indenbom and Kaganer, 1990). Because the deposited nickel particles on the silicon substrate had different crystal growth directions, there was a lattice mismatch between the silicon wafer and every grain with a single-crystalline structure (**Figure 8**). Consequently, spalling stress was formed in the silicon wafer (Moridi et al., 2013). Because the stress of the nickel layer can be controlled as a function of the layer thickness, we expected to be able to predict the steady-state crack depth of the silicon wafer from the stress induced by the nickel layer.

To estimate the growth of the initial crack depth to the steady-state value, the steady-state crack depth must be calculated before the formation of the nickel stressor layer. Since the initial crack depth was determined by material properties such as Dundurs' elastic parameter and the stress intensity factor, it could be calculated using the Ni/Si thin-film system and any other material in the system. The calculation proposed here is based on the S&H model (Evans and Hutchinson, 1984; Suo and Hutchinson, 1990; DEAS Harvard University) and the kinking mechanism (Rice, 1988; Martini et al., 2012; Kwon et al., 2013). The starting point for calculating the steady-state depth is the energy-release rate, G, which is determined by the strain value of the beam (P, M, d) and the trajectory of propagation with stress intensity factors, K_{I} and K_{II}:

$$G = \left[P^2 + 12\left(\frac{M}{d}\right)^2\right]/2\hat{E}d = \frac{\left(K_I^2 + K_{II}^2\right)}{\hat{E}}, \tag{2}$$

where d and h are the spalled silicon wafer thickness and electrodeposited nickel thickness, respectively; P is the edge load; M is the momentum of the beam; and $\hat{E}$ is the strain or stress (**Figure 9**). The factor K_{I} is the minimum condition for the propagation of a crack caused by the nickel stressor layer. Otherwise, K_{II} expresses the direction of propagation. Since the spalling method is based on an existing crack, the K_{I} value is positive and will change with K_{II} values. Otherwise, if there are no external forces, the direction of crack propagation is parallel to the interface between the silicon wafer and the nickel stressor layer. For multilayered thin-film systems, individual stress intensity factors can be assigned to each film layer and solved separately.

$$K_I = c_1\frac{P}{\sqrt{d}} + c_2\frac{M}{\sqrt{d^3}}, \tag{3}$$

$$K_{II} = c_3\frac{P}{\sqrt{d}} + c_4\frac{M}{\sqrt{d^3}}, \tag{4}$$

where c_1, c_2, c_3, and c_4 are dimensionless constants. These constants can be calculated using the loading conditions as follows:

$$c_1^2 + c_3^2 = \frac{1}{2}, \tag{5}$$

$$c_1c_2 + c_3c_4 = 0, \tag{6}$$

$$c_2^2 + c_4^2 = 6. \tag{7}$$

To satisfy these loading conditions, $c_1 = 0.434$, $c_2 = 1.934$, $c_3 = 0.558$, and $c_4 = -1.503$ were used (Evans and Hutchinson, 1984), with c_4 being a negative value. Because K_{II} is a complex number, d can be obtained from

$$K_I = 0.434\frac{P}{\sqrt{d}} + 1.934\frac{M}{\sqrt{d^3}}, \tag{8}$$

$$K_{II} = 0.558\frac{P}{\sqrt{d}} - 1.503\frac{M}{\sqrt{d^3}}. \tag{9}$$

Because the trajectory of the tip in a spalling process is parallel to the interface between the nickel layer and the silicon wafer, K_{II} must be zero. Therefore, the P/M ratio has the same shape as the function for d.

The h formation can be represented as

$$K_I = \frac{P}{\sqrt{2h}}\cos w + \frac{2\sqrt{3}M}{\sqrt{2h^3}}\sin w, \tag{10}$$

$$K_{II} = \frac{P}{\sqrt{2h}}\sin w - \frac{2\sqrt{3}M}{\sqrt{2h^3}}\cos w, \tag{11}$$

where w is the mode mixity for a complex number of the stress intensity factor (Suo and Hutchinson, 1990). To obtain the value of w, Dundurs' elastic parameter (α) is needed. It can be calculated as follows (Suo and Hutchinson, 1990):

$$\alpha = \frac{\Gamma(\kappa_2 + 1) - (\kappa_1 + 1)}{\Gamma(\kappa_2 + 1) + (\kappa_1 + 1)}, \tag{12}$$

where Γ is the shear modulus ratio, $\kappa_1 = 3 - 4\nu_1$, $\kappa_2 = 3 - 4\nu_2$, ν_1 is Poisson's ratio of nickel, and ν_2 is Poisson's ratio of silicon. Dundurs' elastic parameter has various values ranging from 0 to 1, and it only depends on the intrinsic properties of the material. This theoretical approach can be applied to various materials. For a silicon wafer with a nickel stressor layer, w is 52 when α is 0.4 (obtained from the mode mixity table of the S&H model) (Suo, 1989). The term h can also be represented as $P/M = g(h)$ when $K_{II} = 0$. As a result, we have the equation $d = \lambda h$, where λ is a proportional factor. For the Ni/Si thin-film system, $\lambda = 0.99$, which means that the thickness of the spalled silicon layer was proportional to that of the nickel layer. This proportional relationship originates from the standard properties (from modulus ratio to elastic parameter) of nickel. Moreover, h can be expressed in terms of stress. Therefore, the thickness of a spalled silicon wafer can be calculated regardless of the unstable factors. d is expressed in terms of stress as

$$d = \frac{\mu\lambda}{S} U_{(h)}, \tag{13}$$

where μ is a constant originating from the ratio between the modulus of the substrate and that of the film, $U_{(h)}$ is the curvature of the beam, and S is the intrinsic stress. Furthermore, $U_{(h)}$ can be calculated using the equation

$$U_{(h)} = \text{Curvature rate} \times \left(\frac{h - h_e}{\text{Deposition rate}}\right)^{\text{Degradation of curvature}}, \tag{14}$$

where h_e is the initial thickness of the nickel layer (adhesion layer). In this equation, the curvature rate shows the amount of the upper beam that has been curved, while the degradation of curvature shows changes in the curvature rate as a function of the thickness of the nickel stressor layer. As a result, a new equation can be obtained for predicting the thickness of a spalled silicon wafer. To confirm the reliability of the new equation, the calculated value was carefully compared with the experimental result.

Figure 10 shows a comparison of the theoretical and experimental values of thickness of the spalled silicon wafer as functions of the nickel layer thickness and stress. The red line shows the fitted line based on the calculated value, while the black dots represent the experimental results. As shown in **Figure 10A**, the thickness of the silicon layer increased proportionately with the thickness of the deposited nickel layer. A calculated value of $\lambda = 0.99$ was obtained from the red line, which nearly coincides with the experimental value. **Figure 10B** shows the calculated and experimental values of the silicon wafer thickness as functions of the stress induced by the intrinsic stress in the nickel layer. The results show that the thickness of the spalled silicon wafer was inversely proportional to the stress, which means that the induced stress in the silicon wafer increased with decreasing internal stress in the nickel layer. The discrepancy between the calculated and experimental results is under 1.1%; this low error may have originated from the roughness of the nickel layer and K_{II} not being a perfect zero during the spalling process because of external forces. Kerf-less silicon wafers of the desired thickness were successfully fabricated from the calculated value of the steady-state crack depth and initial crack depth predicted by the new equation, providing a noticeable enhancement in the performance of the kerf-less silicon device.

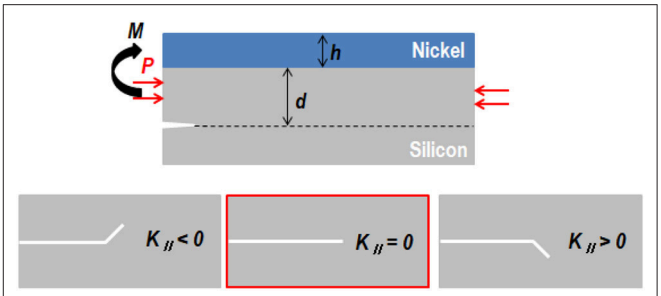

FIGURE 9 | (A) Edge load and momentum of the Ni/Si thin-film system. **(B)** Trajectory of crack propagation in terms of K_{II} value.

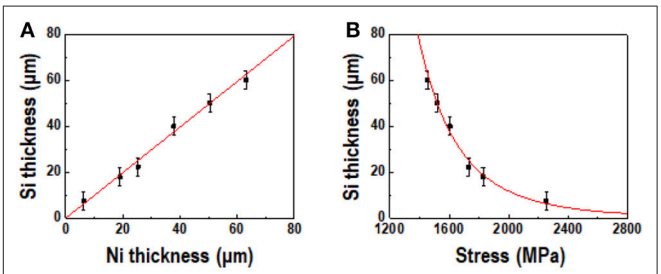

FIGURE 10 | Comparison of theoretical (red line) and experimental (black dots) values of silicon thickness as functions of **(A)** Ni layer thickness and **(B)** stress induced by Ni layer.

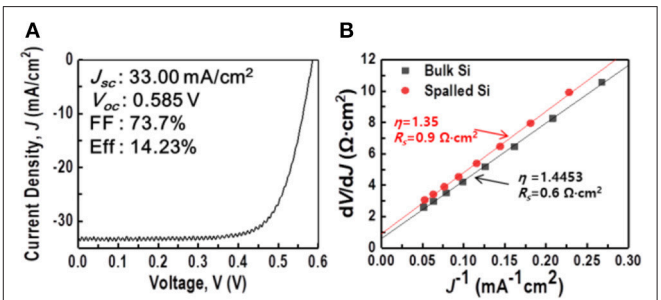

FIGURE 11 | *J–V* characteristics of spalled-silicon solar cell: **(A)** standard *J–V* curve; **(B)** *r*(*J*) with fitted results used to determine *R* and *A* at room temperature.

Fabrication of Solar Cells Using the Spalled Si Wafer

Several parameters such as the ideality factor (η), quantum efficiency (EQE), and conversion efficiency (Eff) were evaluated to determine the applicability of the spalled silicon wafer. The results are shown in **Figures 11**, **12**.

As shown in **Figure 11A,** the efficiency of the resulting solar cell was 14.23%. The short-circuit current density, J_{sc}, which was determined by the light absorption and quantum efficiency, was

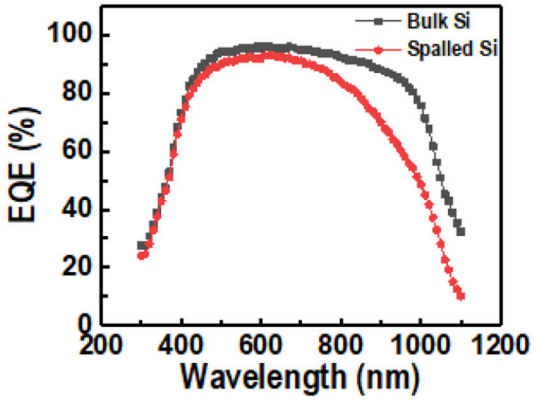

FIGURE 12 | External quantum efficiency (EQE) of both spalled silicon wafer and bulk silicon wafer.

33 mA/cm^2. It is well known that the performance of a silicon-based solar cell is affected by defects originating from impurities in the materials. These impurities can lead to shallower- and deeper-energy defect levels in the band structure, which can create recombination paths that are different from band-to-band recombination. This means that if there were defects on the spalled silicon wafer, degradation of performance could be measured from the defects in the band structure. In order to check the degradation of performance, the ideality factor of the spalled silicon wafer was compared with that of a bulk silicon wafer (obtained from the Shockley diode equation Hegedus and Shafarman, 2004 and the general single-exponential diode equation), as shown in **Figure 11B.** The plot of the derivative dV/dJ vs. J^{-1} was obtained from the dark J–V curve to identify differences in the device characteristics, ideality factor η, and the series resistance R_S between the solar cells, fabricated utilizing a bulk Si wafer and a spalled Si wafer according to the following equation (Hegedus and Shafarman, 2004):

$$J = J_0 \exp\left[\frac{q}{\eta kT}(V - R_s J)\right] + G'V, \tag{15}$$

where J_0 is the dark saturation current, q is the electrical charge, η is the ideality factor, k is the Boltzmann constant, T is the temperature in Kelvin, R_S is the series resistance, and G' is the shunt conductance. Since G' is supposed to be negligible, the derivative plot could be extracted through a simplified equation without G' as follows (Hegedus and Shafarman, 2004):

$$r(J) \equiv \frac{dV}{dJ} = R_s + \frac{\eta kT}{q} J^{-1}. \tag{16}$$

Equation 16 was plotted as a linear line with a slope of ηkT/q and a y-intercept of R_S. η was calculated using the slope and a thermal voltage (kT/q) of 25.69 mV at room temperature. As shown in the comparison of device characteristics **Figure 11B** of the solar cells using a bulk silicon wafer and a spalled silicon wafer, the measured values of R_S were 0.6 and 0.9 $\Omega \cdot$cm^2, respectively, and the measured values of η were 1.45 and 1.35, respectively. Even though the same fabrication processes were used, the calculated results of R_S and η for the solar cell using a spalled wafer, were higher than those for the solar cell using a bulk wafer. This increase was attributed to the wafer thickness because the thinner the wafer, the larger the effect of rear-side recombination. The ideality factor η of the solar cell using a spalled silicon wafer was 1.35, which is closer to 1 when compared with η of the solar cell using a bulk silicon wafer. This means that the spalling process for preparing thin silicon solar cells did not form cracks and defects in the band structure. It also appears that the lower ideality factor was due to the shunt resistance during the fabrication of the solar cell. Moreover, the EQE of the cells using a spalled silicon wafer and a bulk silicon wafer (mother substrate) was measured; the results are shown in **Figure 12**. The absorption of light in the wavelength range of 400–550 nm was the same for both cells. In the wavelength range above 550 nm, the difference in light absorption by both cells was more distinct, because the light-absorption efficiency was related to the silicon thickness (Green and Keevers, 1995). The lower EQE was also affected by the rear-side recombination in the spalled silicon film, which had a thickness of 50 μm.

CONCLUSIONS

A kerf-less thin silicon wafer with a large area was successfully fabricated by spalling, and its thickness was calculated from the steady-state crack depth, using the proposed equation based on the Suo–Hutchinson model and the kinking mechanism. A nickel stressor layer was uniformly deposited on the silicon wafer with the assistance of a shield. It displayed a uniform thickness of about 7 μm and exhibited excellent electric properties. In order to create the initial crack for decreasing kerf-loss in a large-area thin silicon, the silicon wafer was pretreated with a laser before the spalling process. We confirmed that the kerf-loss area of a laser-treated silicon wafer, was <10% of the kerf-loss area of a spalled silicon wafer without pretreatment. The thickness of the spalled silicon wafer varied from 20 to 70 μm. The silicon layer thickness increased proportionately with the nickel layer thickness, while it was inversely proportional to the stress. The predicted thickness calculated using the proposed equation is in agreement with the experimental value. Finally, the solar cell fabricated with a spalled silicon wafer had an efficiency of 14.23% and an ideality factor of 1.35.

AUTHOR CONTRIBUTIONS

All authors assisted in the development and writing of the paper. In addition, H-SY, JK, SeK, NE, SP, BY, and J-HL were involved in designing and doing the experiment. C-SH, SHK, and DL did laser process at the edge of silicon wafer. SaK and J-HL made the solar cell using the exfoliated silicon wafer and measured the solar cell efficiency. JC and C-LL measured and analyzed the optical properties of the exfoliated silicon wafer.

ACKNOWLEDGMENTS

This work was mainly supported by the Global Frontier Program through the Global Frontier Hybrid Interface Materials (GFHIM) project of the National Research Foundation of Korea (NRF), which was funded by the Ministry of Science, ICT, & Future Planning (2018010003). The work was also supported by the New & Renewable Energy Core Technology Program of the Korea Institute of Energy Technology Evaluation and Planning (KETEP), a granted financial resource from the Ministry of Trade, Industry & Energy, Republic of Korea (No. 20153030013200). Additional sources of support included the Korea Institute of Materials Science (CAP-16-10-KIMS) and MSIT (Ministry of Science and ICT), Korea, under the ITRC (Information Technology Research Center) program (IITP-2018-0-01426).

SUPPLEMENTARY MATERIAL

The Supplementary Material for this article can be found online at: https://www.frontiersin.org/articles/10.3389/fchem.2018.00600/full#supplementary-material

REFERENCES

Bedell, S., Lauro, P., Ott, J., Fogel, K., and Sadana, D. (2017). Layer transfer of bulk gallium nitride by controlled spalling. *J. Appl. Phys.* 122:025103. doi: 10.1063/1.4986646

Bilby, B., and Eschelby, J. D. (1968). "Testing electrodeposited coating", In *Fracture: An Advanced Treatise,* Vol. 1, ed H. Liebowitz (New York, NY: Academic Press), 99–182.

Bruel, M. (1995). Silicon on insulator material technology. *Electron. Lett.* 31, 1201–1202. doi: 10.1049/el:19950805

Drory, M. D., Thouless, M. D., and Evans, A. G. (1988). On the decohesion of residually stressed thin films. *Acta Metall.* 36, 2019–2028. doi: 10.1016/0001-6160(88)90303-3

Dross, F. (2008). *Presented in Part at Photovoltaic Specialists Conference 11–16 May 2008.* San Diego, CA.

Durney, L. J. (ed.). (1984). *Graham's Electroplating Engineering Handbook*. Springer New York, NY: Science & Business Media.

Evans, A. G., and Hutchinson, J. W. (1984). On the mechanics of delamination and spalling in compressed films. *Int. J. Solids Struct.* 20, 455–466. doi: 10.1016/0020-7683(84)90012-X

Green, M. A., Emery, K., Hishikawa, Y., Warta, W., and Dunlop, E. D. (2015). Solar cell efficiency tables (version 46). *Prog. Photovoltaics* 23, 805–812. doi: 10.1002/pip.2637

Green, M. A., Hishikawa, Y., Warta, W., Dunlop, E. D., Levi, D. H., Hohl-Ebinger, J., et al. (2017). Solar cell efficiency tables (version 50). Prog. *Photovoltaics* 25, 668–676. doi: 10.1002/pip.2909

Green, M. A., and Keevers, M. J. (1995). Optical properties of intrinsic silicon at 300 K. *Prog. Photovoltaics* 3, 189–192. doi: 10.1002/pip.4670030303

He, M.-Y., and Hutchinson, J. W. (1989). Kinking of a crack out of an interface. *J. Appl. Mech.* 56, 270–278. doi: 10.1115/1.3176078

Hegedus, S. S., and Shafarman, W. N. (2004). Thin-film solar cells: device measurements and analysis. *Prog. Photovoltaics* 12, 155–176. doi: 10.1002/pip.518

Indenbom, V. L., and Kaganer, V. M. (1990). X-ray analysis of internal stresses in crystals II. Lattice distortions due to residual strains in crystals grown from melts. *Phys. Status Solidi A* 122, 97–109. doi: 10.1002/pssa.2211220109

Kim, J.-D., Pyun, S.-I., and Oriani, R. A. (1996). Effects of chloride ion and applied current density on the stress generation during anodic oxidation of tungsten in 0.1 M H2SO4 solution. *Electrochim. Acta* 4, 57–62. doi: 10.1016/0013-4686(95)00284-L

Kobayashi, E., Watabe, Y., Hao, R., and Ravi, T. S. (2015). High efficiency heterojunction solar cells on n-type kerfless mono crystalline silicon wafers by epitaxial growth. *Appl. Phys. Lett.* 106:223504. doi: 10.1063/1.4922196

Kwon, Y., Yang, C., Yoon, S.-H., Um, H.-D., Lee, J.-H., and Yoo, B. (2013). Spalling of a thin Si layer by electrodeposit-assisted stripping. *Appl. Phys. Exp.* 6:116502. doi: 10.7567/APEX.6.116502

Lee, C., Lee, J., Kim, J., Jang, B.-Y., and Yoon, W. (2016). Kerf-less layer transfer of monocrystalline silicon used by hydrogen implantation. *J. Nanosci. Nanotechnol.* 16, 10620–10624. doi: 10.1166/jnn.2016.13206

Martini, R., Gonzalez, M., Dross, F., Masolin, A., Vaes, J., Frederickx, D., et al. (2012). Epoxy-induced spalling of silicon. *Energy Procedia* 27, 567–572. doi: 10.1016/j.egypro.2012.07.111

Moridi, A., Zhang, L. C., and Liu, M. (2013). Residual stresses in thin film systems: effects of lattice mismatch, thermal mismatch and interface dislocations. *Int. J. Solids Struct* 50, 3562–3569. doi: 10.1016/j.ijsolstr.2013.06.022

Rachwal, J. D. (2010). *X-ray Diffraction Applications in Thin Films and (100) Silicon Substrate Stress Analysis.* Master's Thesis, University of South Florida.

Radhakrishnan, H. S., Martini, R., Depauw, V., Van Nieuwenhuysen, K., Debucquoy, M., Govaerts, J., et al. (2014). Improving the quality of epitaxial foils produced using a porous silicon-based layer transfer process for high-efficiency thin-film crystalline silicon solar cells. *IEEE J. Photovoltaics* 4, 70–77, doi: 10.1109/JPHOTOV.2013.2282740

Rice, J. R. (1988). Elastic fracture mechanics concepts for interfacial cracks. *J. Appl. Mech.* 55, 98–103. doi: 10.1115/1.3173668

Richardson, G. (2014). *RIT Scholar Works.* Rochester, NY: Rochester Institute of Technology.

Saitou, M. (2008). Scaling behavior of internal stress in electrodeposited nickel thin films. *J. Appl. Phys.* 104:093518. doi: 10.1063/1.3009336

Shahrjerdi, D., Bedell, S. W., Ebert, C., Bayram, C., Hekmatshoar, B., Fogel, K., et al. (2012). High-efficiency thin-film InGaP/InGaAs/Ge tandem solar cells enabled by controlled spalling technology. *Appl. Phys. Lett.* 100:053901. doi: 10.1063/1.3681397

Sun, C. T., and Jih, C. J. (1987). On strain energy release rates for interfacial cracks in bi-material media. *Eng. Fract. Mech.* 28, 13–20. doi: 10.1016/0013-7944(87)90115-9

Suo, Z. (1989). Singularities interacting with interfaces and cracks. *Int. J. Solids Struct.* 25, 1133–1142. doi: 10.1016/0020-7683(89)90072-3

Suo, Z., and Hutchinson, J. W. (1989). Steady-state cracking in brittle substrates beneath adherent films. *Int. J. Solids Struct.* 25, 1337–1353. doi: 10.1016/0020-7683(89)90096-6

Suo, Z., and Hutchinson, J. W. (1990). Interface crack between two elastic layers. *Int. J. Fracture* 43, 1–18. doi: 10.1007/BF00018123

Wang, T.-Y., Chen, C.-H., Shiao, J.-C., Chen, S.-Y., and Du, C.-H. (2017). Fabricating 40 μm-thin silicon solar cells with different orientations by using SLiM-cut method. *J. Micromech. Microeng.* 27:105017. doi: 10.1088/1361-6439/aa8a38

Conflict of Interest Statement: The authors declare that the research was conducted in the absence of any commercial or financial relationships that could be construed as a potential conflict of interest.

frontiers in Chemistry

ORIGINAL RESEARCH
published: 10 April 2019
doi: 10.3389/fchem.2019.00216

Nanopore-Templated Silver Nanoparticle Arrays Photopolymerized in Zero-Mode Waveguides

Donghoon Han[1†], *Garrison M. Crouch*[2†], *Zhongmou Chao*[3†], *Susan K. Fullerton-Shirey*[3†], *David B. Go*[2,4†] *and Paul W. Bohn*[2,5*]

[1] Department of Chemistry, The Catholic University of Korea, Bucheon, South Korea, [2] Department of Chemical and Biomolecular Engineering, University of Notre Dame, Notre Dame, IN, United States, [3] Department of Chemical and Petroleum Engineering, University of Pittsburgh, Pittsburgh, PA, United States, [4] Department of Aerospace and Mechanical Engineering, University of Notre Dame, Notre Dame, IN, United States, [5] Department of Chemistry and Biochemistry, University of Notre Dame, Notre Dame, IN, United States

In situ fabrication of nanostructures within a solid-polymer electrolyte confined to subwavelength-diameter nanoapertures is a promising approach for producing nanomaterials for nanophotonic and chemical sensing applications. The solid-polymer electrolyte can be patterned by lithographic photopolymerization of poly(ethylene glycol) diacrylate (PEGDA)-based silver cation (Ag^+)-containing polyelectrolyte. Here, we present a new method for fabricating nanopore-templated Ag nanoparticle (AgNP) arrays by *in situ* photopolymerization using a zero-mode waveguide (ZMW) array to simultaneously template embedded AgNPs and control the spatial distribution of the optical field used for photopolymerization. The approach starts with an array of nanopores fabricated by sequential layer-by-layer deposition and focused ion beam milling. These structures have an optically transparent bottom, allowing access of the optical radiation to the attoliter-volume ZMW region to photopolymerize a PEGDA monomer solution containing AgNPs and Ag^+. The electric field intensity distribution is calculated for various ZMW optical cladding layer thicknesses using finite-element simulations, closely following the light-blocking efficiency of the optical cladding layer. The fidelity of the polyelectrolyte nanopillar pattern was optimized with respect to experimental conditions, including the presence or absence of Ag^+ and AgNPs and the concentrations of PEGDA and Ag^+. The self-templated approach for photopatterning high-resolution photolabile polyelectrolyte nanostructures directly within a ZMW array could lead to a new class of metamaterials formed by embedding metal nanoparticles within a dielectric in a well-defined spatial array.

Keywords: zero-mode waveguide, photopolymerization, solid-polymer electrolyte, recessed Ag ring electrode, nanopore array

OPEN ACCESS

Edited by:
James Rohan,
University College Cork, Ireland

Reviewed by:
Wook Ahn,
Soonchunhyang University, South Korea
Zheng Chen,
University of California, San Diego, United States

***Correspondence:**
Paul W. Bohn
pbohn@nd.edu
orcid.org/0000-0001-9052-0349

†Donghoon Han
orcid.org/0000-0003-1870-3006
Garrison M. Crouch
orcid.org/0000-0002-0056-5269
Zhongmou Chao
orcid.org/0000-0002-9882-4440
Susan K. Fullerton-Shirey
orcid.org/0000-0003-2720-0400
David B. Go
orcid.org/0000-0001-8948-1442

Specialty section:
This article was submitted to Electrochemistry, a section of the journal Frontiers in Chemistry

Received: *22 January 2019*
Accepted: *19 March 2019*
Published: *10 April 2019*

Citation:
Han D, Crouch GM, Chao Z, Fullerton-Shirey SK, Go DB and Bohn PW (2019) Nanopore-Templated Silver Nanoparticle Arrays Photopolymerized in Zero-Mode Waveguides. Front. Chem. 7:216. doi: 10.3389/fchem.2019.00216

INTRODUCTION

The increasing utilization of micro- and nanostructured devices in chemical sensing and nanophotonic applications has created a need for precise spatial, temporal, and geometric control over the formation of nanoscale systems. For example, solid-polymer electrolytes, a particularly interesting class of materials due to potential applications in batteries and actively configurable systems, have been utilized in memory devices based on resistive switching (Lin et al., 2014). Further, active control of conductive filament formation and dissolution in solid electrolytes may provide the foundation for a new class of metamaterials with reconfigurable optical properties, especially when combined with arrays of metal nanoparticles embedded in the dielectric host. Previously, we demonstrated actively reconfigurable constructs based on solid-polymer electrolyte-based nanoelectrochemical systems for the formation and dissolution of metal conductive filaments in polyethylene oxide (PEO)-based (Wu et al., 2011; Crouch et al., 2017) and poly(ethylene glycol) diacrylate (PEGDA)-based (Chao et al., 2018) electrolytes. In addition, polymer electrolytes formed by photopolymerization of polyethylene glycol (PEG)-based electrolyte have been utilized for various biomaterials and biomedical applications (Mellott et al., 2001; Burdick and Anseth, 2002; Aimetti et al., 2009; Huebsch et al., 2014; DeForest and Tirrell, 2015). Several methods have been introduced to fabricate miniaturized polymer electrolyte features, including molding (Terray et al., 2002; Fairbanks et al., 2009), printing (DeForest and Anseth, 2012), and lithography (Jang et al., 2007). Combined with patterning of polymer electrolyte composites, *in situ* polymer electrolyte photolithography can be used to determine the spatial composition pattern, e.g., molecular weight, degree of cross-linking, in a polymer electrolyte, in addition to physical shape (Bong et al., 2010; Wu et al., 2015). All of these techniques provide degrees of micro- and nanoscale control over polymer electrolyte's physical/chemical properties, and geometric resolution of micro- and nanostructures on multiple length scales.

Photopolymerization is an attractive technique as it provides unparalleled spatial and temporal control over polymer electrolyte spatial composition patterns and fabrication characteristics. Diacrylate-based polymers are particularly appealing in this context, since they exhibit exceptional transparency, color variation, robust mechanical properties, and elasticity (Mark, 2013). Acrylates can be chemically cross-linked to form polymer electrolytes for a variety of applications and are widely used in industrial chemical processes as adhesives, sealant composites, and protective coatings (Mark, 2013). In contrast to other monomers, acrylates are attractive due to their biocompatibility, semi-permeability, and chemical versatility, allowing modification with a range of mono- or multifunctional moieties (Burkoth and Anseth, 2000; Metters et al., 2000). Of specific importance to the current studies, acrylate-based polymers can controllably produce cross-linked networks *via* photopolymerization (Yu et al., 2001). To exploit these useful characteristics, polyethylene glycol (PEG)-based photo-crosslinkable polymers, based upon acrylate polymerization chemistries, have been developed (Sawhney et al., 1993; Nguyen and West, 2002).

Photoinitiated polymerization of acrylates is typically performed in the presence of a photo-initiator (PI) which generates free radicals upon exposure to UV light. Photopolymerizable acrylates are typified by poly(ethylene glycol) diacrylate (PEGDA), an ion-conducting polymer (Yang et al., 2006) frequently used in biological applications (Shu et al., 2004). It provides design flexibility, because the material can start at low-viscosity and be converted to a high-viscosity solid simply by exposing it to light. In the current work, this property could support the precise positioning of metal nanoparticles, by first placing them in a liquid-like environment, after which the metal nanoparticles are locked into place by simple UV exposure.

Placement of well-defined metallic nanostructures within a dielectric material allows the optical properties of the composite material to be tailored, potentially achieving responses not possible in a single-component material (Oldenburg et al., 1998; Prasad, 2004; Rill et al., 2008; Shukla et al., 2010a,b). This capability is most notably exploited in the rapidly advancing field of metamaterials—composite materials that exhibit unusual optical and electromagnetic properties such as a negative refractive index (Smith et al., 2004; Kuwata-Gonokami et al., 2005; Furlani and Baev, 2009b). The unique properties of metamaterials arise from the engineered electromagnetic/optical response of subwavelength structures, for example well-defined nanoporous metallic arrays, rather than the intrinsic properties of the constituent materials. These metamaterials hold promise for various applications such as far-field subwavelength imaging, nanoscale optical trapping, ultracompact waveguides, and optical power limiting (Baev et al., 2007; Furlani and Baev, 2009a). Most experimentally-realized metamaterials have been fabricated by "top-down" lithography techniques, usually either e-beam lithography (EBL) or focused-ion-beam lithography (FIBL) (Kuwata-Gonokami et al., 2005; Lee et al., 2008; Rill et al., 2008; Henzie et al., 2009). Although powerful, these serial, direct-write approaches are not amenable to large-area patterning. Another approach to metamaterials involves laser direct-writing in a polymeric structure followed by metal deposition onto the fabricated surface (Shukla et al., 2010b). Although this method is promising, full metal coverage is challenging. Thus, new fabrication methods are needed.

Here we present a new approach for the fabrication of PEGDA-based solid-polymer electrolyte nanopillars constructed from silver nanoparticles (AgNPs) templated within recessed Ag ring electrode arrays. Importantly, the Ag ring electrodes are bifunctional, serving as the optical cladding layer in zero-mode waveguides (ZMWs) during fabrication while retaining the capability to serve as working electrodes for electrochemical tuning of the array in future applications. As ZMWs, the metal layers control the spatial distribution of optical radiation used in photopolymerization and, consequently, the distribution of cross-linked PEGDA photopolymer. This approach can significantly simplify the fabrication of PEGDA solid-polymer electrolyte arrays and provide a viable route to the fabrication of three-dimensional metamaterials by photopolymerization.

Metamaterials can be realized by embedding AgNPs in a well-defined dielectric-embedded nanopore array, where the optical properties can be tuned by adjusting the number of AgNPs, the inter-pore spacing, or both. Here, we explore the controlled fabrication of ZMW nanopore-templated photopolymerization of AgNP-containing PEGDA polymeric structures. This study indicates that: (1) metal ZMW arrays may be used to template the nanopillars for the polymerization process; (2) the ZMW can be tuned to control the spatial distribution of the confined optical field and, thus, of the photopolymerization process; and (3) these properties can be realized in the presence of nanopore-embedded AgNPs and Ag^+ ions in the electrolyte.

MATERIALS AND METHODS

Chemicals

Anhydrous acetonitrile (ACN), silver nitrate ($AgNO_3$), sulfuric acid (95%), hydrogen peroxide (30%), fluorescein 5(6)-isothiocyanate (FITC), and 2-hydroxy-4′-(2-hydroxyethoxy)-2-methylpropiophenone photoinitiator (PI) were obtained from Sigma-Aldrich. Silver nanoparticles (AgNPs, 50 nm size, 5 kDa PEG capped) were purchased from nanoComposix. Poly(ethylene glycol) diacrylate (PEGDA) with number average molecular weight $M_N = 700$ was purchased from Sigma-Aldrich. Cleanroom-cleaned glass coverslips (Glass D, 75 x 25 mm, 1.0 mm thick) were obtained from Schott Nexterion. All reagents were used as received.

Fabrication of ZMW Arrays

The nanopore arrays were fabricated via a combination of standard photolithography, layer-by-layer deposition, and focused ion beam (FIB) milling. The primary processing steps are shown in **Figure 1A**. Glass slides were cleaned in piranha solution (3:1 sulfuric acid (95%):hydrogen peroxide (30%)—*Caution—Strong oxidizer, use with extreme care*), rinsed with deionized (DI) water, and dried at 120°C. A 5 nm thick Au layer was deposited by electron-beam evaporation (UNIVEX 450B, Oerlikon) after deposition of a 5 nm Ti adhesion layer. Then, a 20 nm Ag film was e-beam evaporated onto the same glass slide, after which a 150 nm thick SiN_x layer was deposited by plasma-enhanced chemical vapor deposition (PECVD 790, Plasma-Therm). Finally, an additional 50 nm thick Cr layer was deposited on the substrate. A dual-source FIB instrument (Helios Nanolab 600, FEI Corp.) was used for milling and characterization. Nanopore arrays were patterned in a 20 × 20 μm square array with a lattice spacing of 500 nm, shown in **Figures 1B,C**. FIB milling was performed at 30 kV acceleration, 0.28 nA ion aperture, and 0.1 ms dwell time to produce the recessed dual-ring electrode (RDRE) array. These FIB-milled pores exhibit a conical frustum shape with typical top diameter, d_{top}∼140–160 nm, and bottom diameter, d_{bottom}∼60–80 nm. Although milled under nominally identical conditions, small sample-to-sample variations in pore geometry were observed.

Photopolymerization of PEGDA Solution

In an argon-filled glovebox with oxygen and water concentrations controlled to <0.1 ppm, 10 and 20 mM solutions of $AgNO_3$ in anhydrous ACN were prepared. Similarly, PEGDA was dissolved in ACN to make 0.5, 1, 2, and 3 wt% PEGDA solutions, each adjusted to 1 mM of PI. To purify the AgNPs, 1,000 μL of 50 nm AgNPs was centrifuged at 10,000 rpm for 30 min (microcentrifuge RS-200, REVSCI); then the solvent was decanted, and the AgNPs were resuspended in 100 μL ACN. The AgNPs and $AgNO_3$ solution were added to the PEGDA + PI solutions in a 1:1:8 volume ratio, yielding final solutions of $AgNO_3$ in ACN with concentrations of 1 and 2 mM for PEGDA concentrations of 0.5, 1, 2, and 3 wt%, respectively. Fifty microliter of each solution was then dropcast onto the nanopore array inside the glovebox. The PEGDA-coated nanopore array was exposed to UV light (405 nm) with an intensity of 14 mW cm^{-2} for 30 min in the cleanroom. Next, the nanopore array was washed with ACN and dried in filtered air.

Fluorescence Measurements

Fluorescence measurements were performed on an Olympus IX71 wide-field epi-illumination microscope. Radiation from a 488 nm laser was passed through an excitation filter (Chroma Z488/10X), and defocused to illuminate an area *ca*. 100 × 100 μm on the Cr side of the sample to directly excite fluorescence of FITC molecules in the nanopores. The fluorescence was collected by a 100× NA 1.4 oil-immersion objective, and projected onto a 512 × 512 pixel CCD camera (Andor Technology Ltd). A dichroic mirror (Chroma Z488RDC) and emission filter (Chroma HQ525/50 m) were used to separate excitation from emission radiation.

Modeling and Calculations

Finite element simulations were performed using COMSOL Multiphysics version 5.3. The simulations were performed over a two-dimensional domain representing the geometry and dimensions of the zero-mode waveguides employed in our experiments (Han et al., 2017). We used the "Electromagnetic Waves" physics of COMSOL in a frequency domain mode to obtain the excitation field inside a ZMW. A free triangular mesh was used with "Extremely fine" resolution and refinement applied to the ZMW layer. The ZMW was represented by a single pore, consisting of an adhesion layer (Ti, $h = 5$ nm), a second adhesion layer (Au, $h = 5$ nm), an optical cladding layer (Ag, $h = 20$, 50, and 100 nm), a dielectric layer (SiN_x, $h = 150$ nm), and a top layer (Cr, $h = 50$ nm). A perfectly matched layer was incorporated in the glass substrate component to cancel any reflection artifacts from the simulation boundaries. The complex refractive indices of Ti (Werner et al., 2009), Au (Olmon et al., 2012), Ag (Werner et al., 2009), and Cr (Johnson and Christy, 1974) were taken as $n = -5.74 + i4.4$, $-1.14 + i6.1$, $-4.70 + i2.5$, and $-4.13 + i11.8$, respectively. The refractive indices of water, glass, and SiN_x were taken to be 1.33, 1.45, and 2.016, respectively. Excitation radiation at 405 nm wavelength, consistent with the UV aligner, was simulated to irradiate the bottom of the glass module, arriving perpendicular to the plane of the structure.

RESULTS AND DISCUSSION

Characterization of ZMW Devices

ZMW arrays with 500 nm inter-pore spacing were fabricated to form square arrays consisting of annular apertures of sacrificial

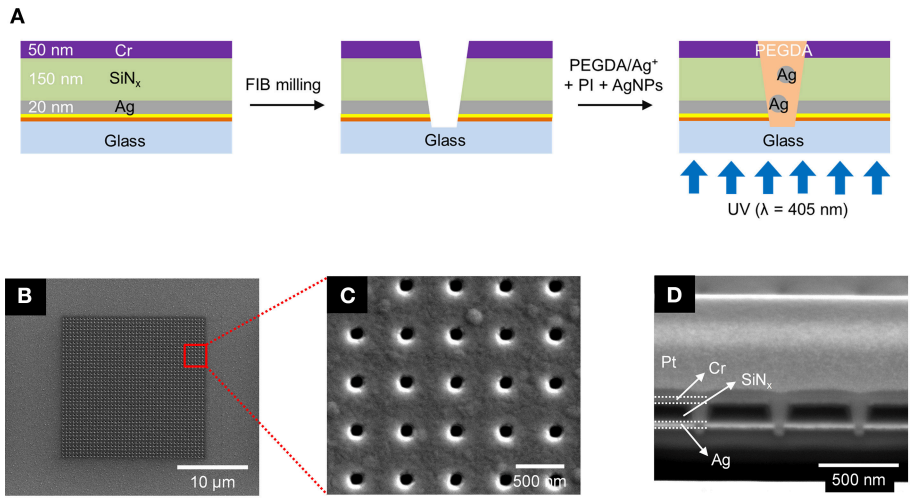

FIGURE 1 | (A) Schematics of the fabrication process for the photopolymerized ZMW array. **(B–D)** Scanning electron micrographs of a nanopore array at different magnifications and perspectives. **(B)** Top-down view of the entire 20 × 20 μm nanopore array. **(C)** Top-down view of a 5 × 5 subset of the same array. **(D)** Cross sectional SEM image of the nanopores taken at 52° tilt.

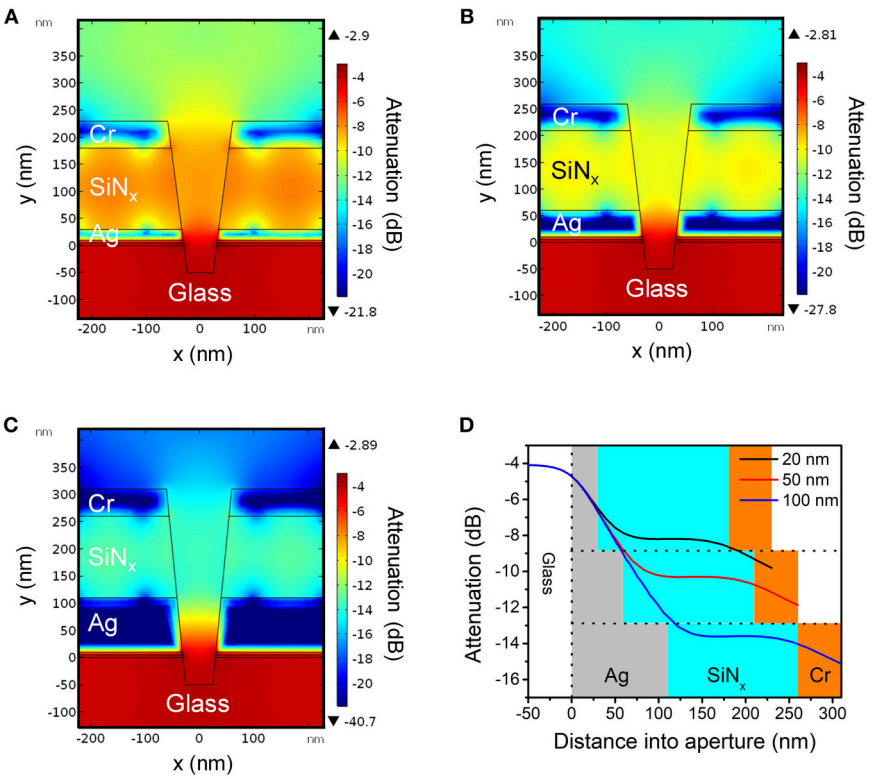

FIGURE 2 | Cross-sectional heat maps of evanescent field amplitudes in conical nanopores obtained by finite element simulations for Ag layer thicknesses of **(A)** 20 nm, **(B)** 50 nm, and **(C)** 100 nm, respectively. For all cases, bottom aperture of the nanopore structure had a diameter of d_{bottom} = 70 nm and the top aperture was determined by the ratio d_{top}/d_{bottom} = 2. **(D)** Simulated attenuation of energy density along the central axis of the ZMW for different thicknesses of Ag as indicated in the legend. Area shading corresponds to the material surrounding the opening: gray (Ag), blue (SiN_x), orange (Cr).

layer(Cr)-insulator(SiN_x)-metal layer(Ag). In these recessed Ag ring electrode nanopore stacks, the Ag layer can be electrically connected and used as an electrode for electrochemical experiments. **Figure 1A** illustrates the fabrication process using standard photolithography, layer-by-layer deposition, and FIB milling to produce nanopore recessed Ag ring electrode arrays.

This simple direct-write approach enables direct fabrication of precise nanopore structures exhibiting conical frustum shapes in contrast to the cylindrical nanopores obtained using electron beam (Dawson et al., 2012; Kleijn et al., 2012) or nanosphere lithography (Fu et al., 2018). Cylindrical pore shapes would likely result in minor alterations to the concentration parameters required for optimal pore filling due to changing in polymer wetting behavior, and the extent to which the photocrosslinking radiation can penetrate the pore. **Figures 1B,C** show SEM images of the entire array with an interpore distance 500 nm, and **Figure 1D** shows a corresponding cross-section SEM image of typical pores produced by FIB milling. The overetched region below the Ag/glass interface typically decreases with pore diameter, and well-controlled milling processes yield pores overetched by ≤50 nm. From bottom to top, the cross-section image in **Figure 1D** shows the bottom Ag layer (bright), silicon nitride (black), and the sacrificial Cr layer (bright). The nanopore ZMWs exhibit a conical shape with a larger aperture at the top than at the bottom electrode. The typical diameter of the top of the pore (d_{top}) is ∼140–160 nm, while the bottom diameter (d_{bottom}) is ∼60–80 nm.

Effect of the Thickness of Ag Layer on UV Irradiation

The spatial distribution of the optical field, both within and external to the ZMWs, is important in determining the extent of photopolymerization that will occur within the nanopores. For wavelengths above the cutoff wavelength of the nanoaperture, λ_c, where $\lambda_c \sim 1.7\ d$ and d is the pore diameter, the evanescent field decays exponentially with distance at a rate that depends on the radius and diameter (Crouch et al., 2018). In addition, the light-blocking efficiency of the Ag optical cladding layer also depends on the thickness of Ag. Experimentally, photopolymerization of PEGDA within nanopores was accomplished with collimated UV radiation from a UV aligner irradiating the bottom (Ag ring) surface of the ZMW array, as shown schematically in **Figure 1A**. To assess the effectiveness of this strategy in the ZMW nanopores studied here, finite element simulations were performed for various Ag thicknesses.

Figures 2A–C show the electric field amplitudes in a series of conical frustum pores each having different Ag layer thicknesses (20, 50, and 100 nm, respectively), but with constant ratio $d_{top}/d_{bottom} = 2$. As **Figures 2A–C** illustrate, the field decays exponentially within the nanopore, and the nanostructures provide attenuation primarily determined by the thickness of the Ag optical cladding layer, with thinner Ag thicknesses leading to less attenuation. **Figure 2D** shows the attenuation of electromagnetic energy density inside apertures with different Ag layer thicknesses, where for the 20 nm Ag thickness (black line), the smallest energy attenuation is predicted, confirming the thickness-dependent attenuation. These results indicate that thinner Ag thicknesses provide less optical field confinement and, thus, should lead to more

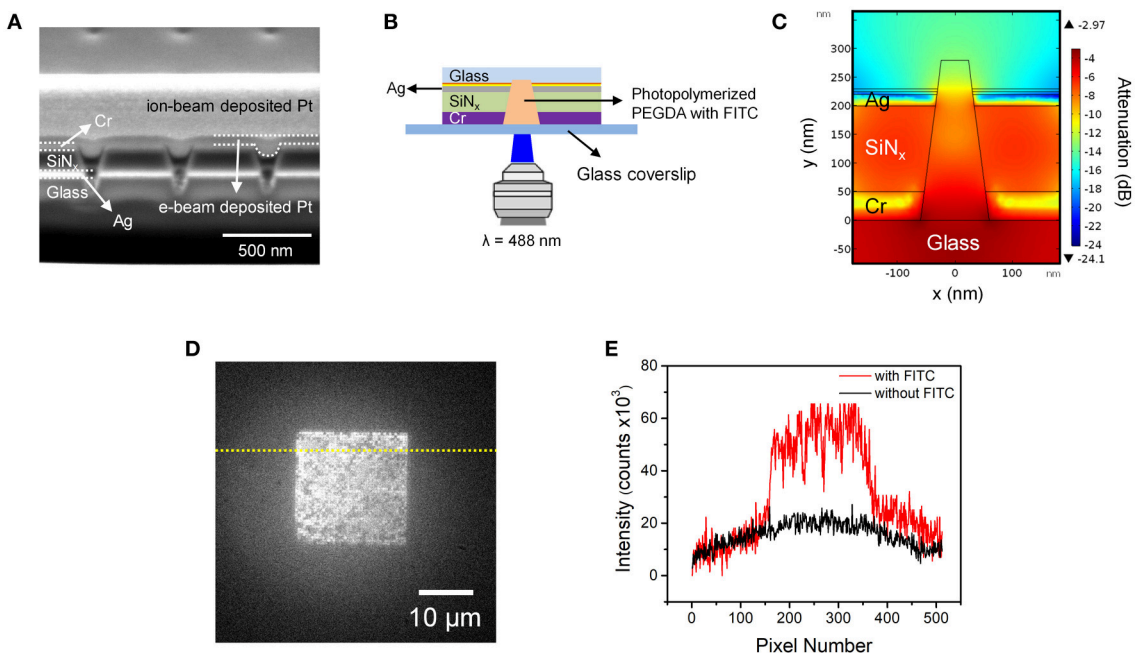

FIGURE 3 | (A) Cross-sectional SEM image of photopolymerized PEGDA-FITC in nanopores. Positions and identities of functional layers are indicated on the left, while positions of e-beam and ion-beam deposited Pt structural layers, used to obtain cross-sectional images, are indicated on the right. **(B)** Schematic diagram of the fluorescence epi-illumination geometry. In this geometry the ZMW region is distal from the illumination plane. **(C)** Cross-sectional heat map of optical field amplitude in a conical nanopore obtained from a finite element simulation. **(D)** Fluorescence micrograph of a nanopore array containing photopolymerized FITC-PEGDA in the nanopores. **(E)** Fluorescence intensity profiles obtained along the dotted lines shown in **(D)** with (red) and without (black) FITC.

spatially-extended PEGDA photopolymerization within the ZMW nanopores.

Characterization of Photopolymerized PEGDA in ZMW Devices

To further characterize the photopolymerization of PEGDA in ZMW nanopores, a fluorescent probe was added to the PEGDA monomer, and fluorescence was measured after photopolymerization. A 2.0 wt% solution of PEGDA monomer in ACN was prepared with 1 mM PI and 10 μM fluorescein isothiocyanate (FITC). The average number of fluorescent molecules occupying a single nanopore is given by $\langle n \rangle_{pore} = CVN_A$, where C is the FITC concentration, N_A is Avogadro's number, and V is the volume of the conical frustum of a single nanopore. For the 2.2 aL volume of the conical frustum nanopores used in these experiments, single molecule occupancy, $\langle n \rangle_{pore} = 1$ is expected at 0.75 μM, meaning that under the conditions of this experiment, $\langle n \rangle_{pore} \sim 13$. Before photopolymerization, the ZMW nanopores were filled with the PEDGA solution and allowed to equilibrate at room temperature for 10 min, after which the PEGDA-filled nanopore array was exposed to UV radiation from the aligner for 30 min. **Figure 3A** shows a cross-section SEM image of adjacent nanopores containing FITC.

Importantly, in this experiment the array was irradiated from the large diameter side of the conical nanopores, in the fluorescence epi-illumination geometry illustrated in **Figure 3B**. To confirm that the FITC can be effectively excited once inside the nanopore, finite element simulations were conducted for this inverted configuration. **Figure 3C** shows a cross-sectional heat map of energy intensity obtained from a simulation of a single conical nanopore, confirming its ZMW behavior. Importantly, there is little attenuation of energy intensity inside the nanopore and nearly the entire volume of the nanopore can be excited. The simulation provided confidence that fluorescent radiation can be collected from the upper (Cr) surface of the ZMW array in order to characterize the fluorescence response of the FITC within the photopolymerized PEGDA-filled nanopores.

Figure 3D shows a low magnification, wide-area fluorescence micrograph of the ZMW array. Although there is some variation in intensity among the individual nanopores, the overall image indicates significant incorporation of FITC-impregnated photopolymerized PEGDA in the individual nanopores. **Figure 3E** shows a fluorescence intensity line profile obtained along the dotted line in **Figure 3D**, both with and without FITC. This result clearly shows isolation and photoactivation of the polyelectrolyte with fluorescent probes in each pore.

Formation and Optimization of AgNPs Embedded in Polyelectrolyte Nanopore Array

Encouraged by the subwavelength control of the radial and axial field distributions provided by the ZMWs, we extended the fabrication of recessed Ag ring electrode array to include AgNPs and Ag^+ embedded in the photopolymerized PEGDA. In principle, AgNPs arrayed in the dielectric PEGDA could form the basis of a metamaterial, and the presence of Ag^+ would enable the electrochemical formation of nanofilaments connecting the AgNPs (Crouch et al., 2017; Chao et al., 2018). To understand the fabrication of nanopore-templated AgNPs embedded in PEGDA nanopillars, photopolymerization experiments were undertaken to investigate the influence of PEDGA concentration, Ag^+ concentration, and the presence or absence of AgNPs on the formation of solid-polymer electrolytes within the nanopore templates.

First, we tested the effect of PEGDA concentration in the presence of 1 mM $AgNO_3$ but without AgNPs under optimized conditions. **Figures 4A,B** show cross-sectional SEM images of a recessed Ag ring electrode array obtained after photoirradiation of 1.0 wt% and 3.0 wt% PEGDA with 1 mM $AgNO_3$, respectively. These concentrations were chosen to bracket the optimal conditions for PEGDA filling determined in initial tests, in which concentrations over 2.0 wt% PEGDA with 1 mM Ag^+ were found to yield the best filling behavior in the absence of AgNPs. Photopolymerized PEGDA was observed to fill the nanopore only to the Ag ring for the

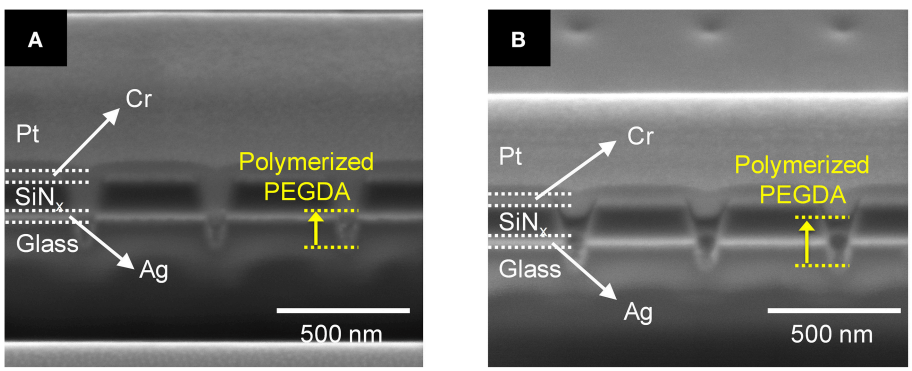

FIGURE 4 | Cross-sectional SEM images of **(A)** 1.0 wt% and **(B)** 3.0 wt% photopolymerized PEGDA with 1 mM $AgNO_3$ in a recessed Ag ring electrode array without AgNPs. The extent of the PEGDA photopolymer, after photopolymerization, is shown by the yellow dashed lines.

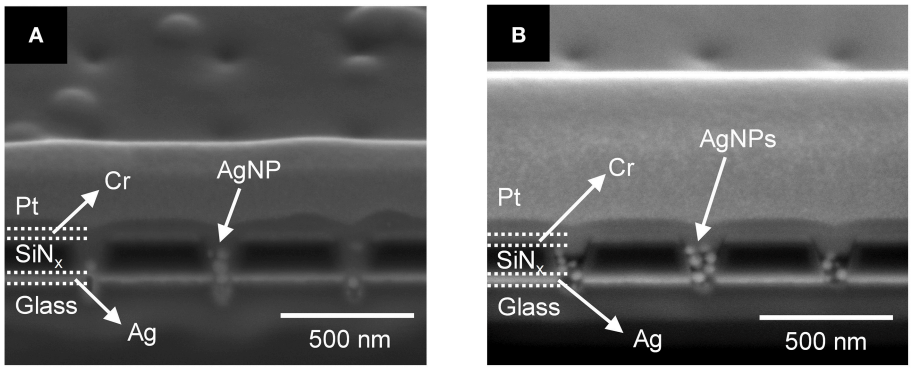

FIGURE 5 | Cross-section SEM images of 1.0 wt% photopolymerized PEGDA in a recessed Ag ring electrode array with embedded AgNPs containing **(A)** 2 mM and **(B)** 1 mM $AgNO_3$ salt.

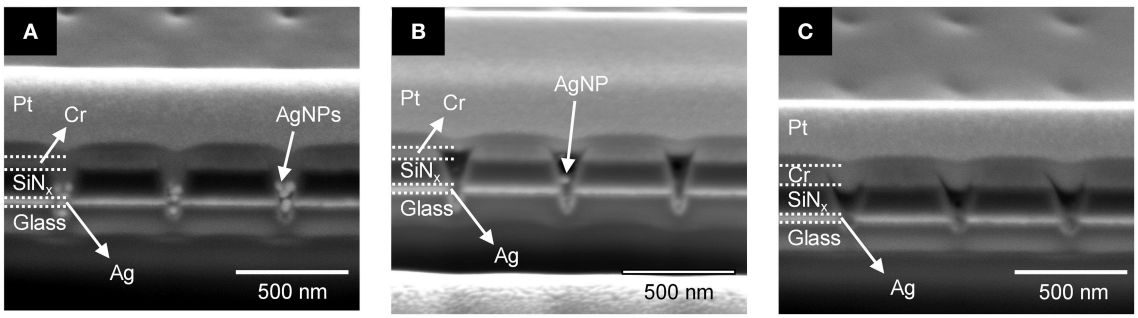

FIGURE 6 | Cross-sectional SEM images of photopolymerized polyelectrolyte in a recessed Ag ring electrode array with embedded AgNPs for different PEGDA concentrations: **(A)** 0.5 wt%, **(B)** 1.0 wt%, and **(C)** 2.0 wt%.

1.0 wt% monomer solution, but 3.0% PEGDA filled the nanopore up through the middle of the SiN_x layer, as shown in **Figure 4B**.

Silver ions in the PEGDA are required for subsequent direct-write nanofilament formation and dissolution between AgNPs (Crouch et al., 2017; Chao et al., 2018), so we also investigated how Ag^+ concentration affects the photopolymerization of PEGDA in the presence of AgNPs. **Figures 5A,B** show cross-sections of photopolymerized 1.0 wt% PEGDA with 2 mM $AgNO_3$ and 1 mM $AgNO_3$, respectively. Here, we included AgNPs in the PEGDA solution as opposed to the results in **Figure 4** with no AgNPs. At 2.0 mM, **Figure 5A**, some AgNPs can be observed in the nanopore, but there is little to no polymerized PEGDA. However, at 1 mM Ag^+ shown in **Figure 5B**, not only are individual stacked AgNPs observed, but they are in polymerized PEGDA. Surprisingly, comparison of **Figures 5A,B** shows that increasing the concentration of $AgNO_3$ inhibits polymer filling of the nanopores. Given the nanoscale dimensions of the pores, an electrostatic screening effect is plausible, however understanding the mechanism giving rise to this effect will require further detailed studies in which polymer electrolyte characteristics and nanopore surface charge are carefully controlled. Nevertheless, this serves as experimental verification that in the presence of AgNPs, Ag-containing PEGDA monomer can be UV cross-linked to form AgNPs nanopillars embedded in the polyelectrolyte inside the nanopores.

Given the above result, in which lower Ag^+ concentrations yield better fabrication of polymerized nanopillars, the photopolymerization behavior of PEGDA with AgNPs in a ZMW was also tested as a function of PEGDA concentration in the absence of Ag^+ (i.e., no $AgNO_3$). **Figure 6** shows cross-section SEM images of PEGDA photopolymerized from solutions with various concentrations of monomer in the presence of AgNPs, but without Ag^+. At the lowest concentration, 0.5 wt% PEGDA, **Figure 6A**, AgNPs fill the nanopore to the middle of the SiN_x insulator layer. Further increasing PEGDA concentration suppresses the number of AgNPs captured in the nanopore, *cf.* **Figures 6B,C**. One possible explanation is less physical crosslinking, which will decrease the likelihood of AgNP retention in the pore, although further experiments are needed to fully explore this interpretation. Interestingly, the PEGDA concentration dependence on pore filling is switched in the absence/presence of AgNPs. Higher PEGDA concentrations promote more extensive polymerization and therefore more pore filling in the absence of AgNPs, while lower PEGDA concentrations are more effective at pore filling when AgNPs are present. We tentatively

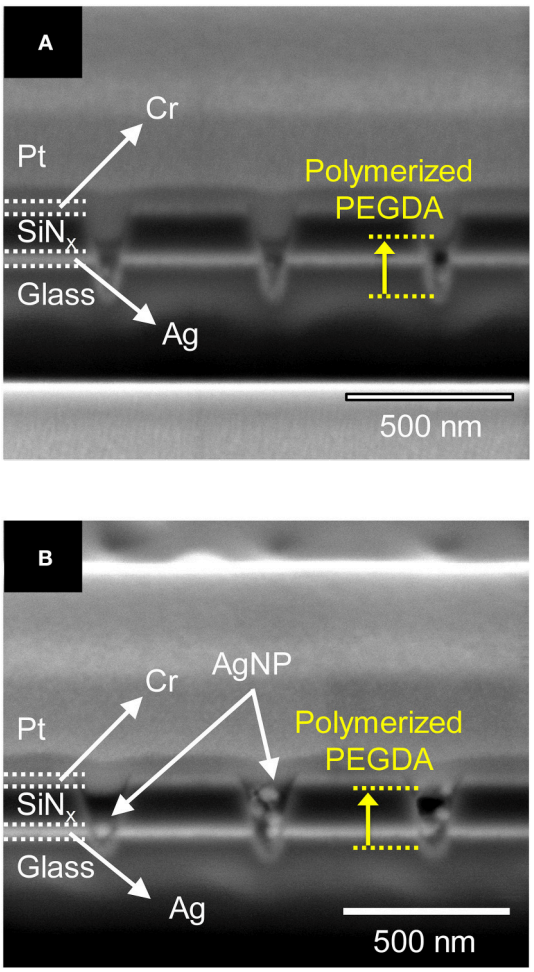

FIGURE 7 | Cross-section SEM image of 2.0 wt% photopolymerized PEGDA and 1 mM Ag^+ in a recessed Ag ring electrode array **(A)** without and **(B)** with embedded AgNPs.

assign this behavior to a volume-filling effect in the presence of AgNPs.

Based on the above parametric experiments, we asked whether it might be possible to determine a single set of conditions that would yield satisfactory PEGDA polymerization behavior both in the absence and presence of AgNPs. Thus, we experimentally tested a preparation of 2.0 wt% PEGDA monomer with 1 mM $AgNO_3$ salt in the presence and absence of AgNPs. The results shown in **Figure 7** illustrate that this formulation yields photopolymerized polyelectrolyte nanopillars inside ZMW nanopores either without, **Figure 7A**, or with, **Figure 7B**, AgNPs. The resulting structures were effectively cross-linked by UV light, thus immobilizing the polyelectrolyte in the ZMW arrays. In the presence of AgNPs, this procedure clearly yields a nanopore-templated array of AgNP-containing solid-polymer electrolyte structures that could form the basis of a reconfigurable metamaterial.

CONCLUSION

Templated pillars of AgNPs with nanometer-scale registration precision are of interest in nanophotonic and nanomanufacturing applications. Here, we describe a new fabrication strategy for producing ordered subwavelength arrays of AgNP nanopillars in PEGDA/Ag^+ polyelectrolyte, using a ZMW to control and shape the spatial distribution of the confined electromagnetic field and, therefore, the volume occupied by photopolymerized PEGDA. Both chemical and ZMW geometric effects on the fabrication process were characterized. The influence of the optical cladding layer thickness on the ZMW-directed photopolymerization predicted through finite-element simulations was found to agree with experiment. We determined that careful control of the structure was necessary and sufficient to achieve well-controlled PEGDA photopolymer volumes. In addition, we characterized the solution conditions needed to produce well-templated PEGDA either with or without AgNPs and therefore identified optimal conditions for the preparation of nanopore-templated AgNP nanopillar assemblies in PEGDA/Ag^+ polyelectrolyte. We believe that this approach employing *in situ* nanopore-templated fabrication of plasmonic and conductive nanostructures constitutes an exciting new platform for sequential formation/dissolution of nanofilaments through polyelectrolyte-confined nanopillar arrays of nanoparticles, thereby opening possible applications in actively reconfigurable metamaterials.

AUTHOR CONTRIBUTIONS

DG, SF-S, and PB designed the experiments. DH and GC performed the experiments. All authors contributed to analysis of the results, data analysis, and preparation of the final manuscript.

FUNDING

This work was supported by the Defense Advanced Research Projects Agency FA8650-15-C-7546. DH was supported by the National Research Foundation of Korea (NRF) grant funded by the Korea government (MSIT) 2018R1C1B5085888. GC was supported by NASA Space Technology Research Fellowship NNX16AM45H.

REFERENCES

Aimetti, A. A., Machen, A. J., and Anseth, K. S. (2009). Poly (ethylene glycol) hydrogels formed by thiol-ene photopolymerization for enzyme-responsive protein delivery. *Biomaterials.* 30, 6048–6054. doi: 10.1016/j.biomaterials.2009.07.043

Baev, A., Furlani, E. P., Samoc, M., and Prasad, P. N. (2007). Negative refractivity assisted optical power limiting. *J. Appl. Phys.* 102:043101. doi: 10.1063/1.2769144

Bong, K. W., Bong, K. T., Pregibon, D. C., and Doyle, P. S. (2010). Hydrodynamic focusing lithography. *Angew. Chem. Int. Ed.* 49, 87–90. doi: 10.1002/anie.200905229

Burdick, J. A., and Anseth, K. S. (2002). Photoencapsulation of osteoblasts in injectable RGD-modified PEG hydrogels for bone tissue engineering. *Biomaterials.* 23, 4315–4323. doi: 10.1016/S0142-9612(02)00176-X

Burkoth, A. K., and Anseth, K. S. (2000). A review of photocrosslinked polyanhydrides:: *in situ* forming degradable networks. *Biomaterials.* 21, 2395–2404. doi: 10.1016/S0142-9612(00)00107-1

Chao, Z., Radka, B. P., Xu, K., Crouch, G. M., Han, D., Go, D. B., et al. (2018). Direct-write formation and dissolution of silver nanofilaments in ionic liquid-polymer electrolyte composites. *Small.* 14:1802023. doi: 10.1002/smll.201802023

Crouch, G. M., Han, D., and Bohn, P. W. (2018). Zero-mode waveguide nanophotonic structures for single molecule characterization. *J. Phys. D.* 51:193001. doi: 10.1088/1361-6463/aab8be

Crouch, G. M., Han, D., Fullerton-Shirey, S. K., Go, D. B., and Bohn, P. W. (2017). Addressable direct-write nanoscale filament formation and dissolution by nanoparticle-mediated bipolar electrochemistry. *ACS Nano.* 11, 4976–4984. doi: 10.1021/acsnano.7b01657

Dawson, K., Wahl, A., Murphy, R., and O'Riordan, A. (2012). Electroanalysis at single gold nanowire electrodes. *J. Phys. Chem. C* 116, 14665–14673. doi: 10.1021/jp302967p

DeForest, C. A., and Anseth, K. S. (2012). Photoreversible patterning of biomolecules within click-based hydrogels. *Angew. Chem. Int. Ed.* 51, 1816–1819. doi: 10.1002/anie.201106463

DeForest, C. A., and Tirrell, D. A. (2015). A photoreversible protein-patterning approach for guiding stem cell fate in three-dimensional gels. *Nat. Mater.* 14:523. doi: 10.1038/nmat4219

Fairbanks, B. D., Schwartz, M. P., Halevi, A. E., Nuttelman, C. R., Bowman, C. N., and Anseth, K. S. (2009). A versatile synthetic extracellular matrix mimic via thiol-norbornene photopolymerization. *Adv. Mater.* 21, 5005–5010. doi: 10.1002/adma.200901808

Fu, K., Han, D., Kwon, S. R., and Bohn, P. W. (2018). Asymmetric nafion-coated nanopore electrode arrays as redox-cycling-based electrochemical diodes. *ACS Nano* 12, 9177–9185. doi: 10.1021/acsnano.8b03751

Furlani, E. P., and Baev, A. (2009a). Free-space excitation of resonant cavities formed from cloaking metamaterial. *J. Mod. Opt.* 56, 523–529. doi: 10.1080/09500340802582706

Furlani, E. P., and Baev, A. (2009b). Optical nanotrapping using cloaking metamaterial. *Phys. Rev. E* 79:026607. doi: 10.1103/PhysRevE.79.026607

Han, D., Crouch, G. M., Fu, K., Zaino, L. P. III., and Bohn, P. W. (2017). Single-molecule spectroelectrochemical cross-correlation during redox cycling in recessed dual ring electrode zero-mode waveguides. *Chem. Sci.* 8, 5345–5355. doi: 10.1039/C7SC02250F

Henzie, J., Lee, J., Lee, M. H., Hasan, W., and Odom, T. W. (2009). Nanofabrication of plasmonic structures. *Annu. Rev. Phys. Chem.* 60, 147–165. doi: 10.1146/annurev.physchem.040808.090352

Huebsch, N., Kearney, C. J., Zhao, X., Kim, J., Cezar, C. A., Suo, Z., et al. (2014). Ultrasound-triggered disruption and self-healing of reversibly cross-linked hydrogels for drug delivery and enhanced chemotherapy. *Proc. Natl. Acad. Sci. U.S.A.* 111, 9762–9767. doi: 10.1073/pnas.1405469111

Jang, J. H., Dendukuri, D., Hatton, T. A., Thomas, E. L., and Doyle, P. S. (2007). A route to three-dimensional structures in a microfluidic device: stop-flow interference lithography. *Angew. Chem. Int. Ed.* 46, 9027–9031. doi: 10.1002/anie.200703525

Johnson, P., and Christy, R. (1974). Optical constants of transition metals: Ti, V, Cr, Mn, Fe, Co, Ni, and Pd. *Phys. Rev. B* 9:5056. doi: 10.1103/PhysRevB.9.5056

Kleijn, S. E., Yanson, A. I., and Koper, M. T. (2012). Electrochemical characterization of nano-sized gold electrodes fabricated by nano-lithography. *J. Electroanal. Chem.* 666, 19–24. doi: 10.1016/j.jelechem.2011.11.022

Kuwata-Gonokami, M., Saito, N., Ino, Y., Kauranen, M., Jefimovs, K., Vallius, T., et al. (2005). Giant optical activity in quasi-two-dimensional planar nanostructures. *Phys. Rev. Lett.* 95:227401. doi: 10.1103/PhysRevLett.95.227401

Lee, K.-S., Kim, R. H., Yang, D.-Y., and Park, S. H. (2008). Advances in 3D nano/microfabrication using two-photon initiated polymerization. *Prog. Polym. Sci.* 33, 631–681. doi: 10.1016/j.progpolymsci.2008.01.001

Lin, W. P., Liu, S. J., Gong, T., Zhao, Q., and Huang, W. (2014). Polymer-based resistive memory materials and devices. *Adv. Mater.* 26, 570–606. doi: 10.1002/adma.201302637

Mark, H. F. (2013). *Encyclopedia of Polymer Science and Technology, Concise*. New York, NY: John Wiley and Sons.

Mellott, M. B., Searcy, K., and Pishko, M. V. (2001). Release of protein from highly cross-linked hydrogels of poly (ethylene glycol) diacrylate fabricated by UV polymerization. *Biomaterials* 22, 929–941. doi: 10.1016/S0142-9612(00)00258-1

Metters, A. T., Bowman, C. N., and Anseth, K. S. (2000). A statistical kinetic model for the bulk degradation of PLA-b-PEG-b-PLA hydrogel networks. *J. Phys. Chem. B* 104, 7043–7049. doi: 10.1021/jp000523t

Nguyen, K. T., and West, J. L. (2002). Photopolymerizable hydrogels for tissue engineering applications. *Biomaterials.* 23, 4307–4314. doi: 10.1016/S0142-9612(02)00175-8

Oldenburg, S., Averitt, R., Westcott, S., and Halas, N. (1998). Nanoengineering of optical resonances. *Chem. Phys. Lett.* 288, 243–247. doi: 10.1016/S0009-2614(98)00277-2

Olmon, R. L., Slovick, B., Johnson, T. W., Shelton, D., Oh, S.-H., Boreman, G. D., et al. (2012). Optical dielectric function of gold. *Phys. Rev. B* 86:235147. doi: 10.1103/PhysRevB.86.235147

Prasad, P. N. (2004). *Nanophotonics.* New York, NY: John Wiley and Sons. doi: 10.1002/0471670251

Rill, M. S., Plet, C., Thiel, M., Staude, I., Von Freymann, G., Linden, S., et al. (2008). Photonic metamaterials by direct laser writing and silver chemical vapour deposition. *Nat. Mater.* 7:543. doi: 10.1038/nmat2197

Sawhney, A. S., Pathak, C. P., and Hubbell, J. A. (1993). Bioerodible hydrogels based on photopolymerized poly (ethylene glycol)-co-poly (alpha.-hydroxy acid) diacrylate macromers. *Macromolecules.* 26, 581–587. doi: 10.1021/ma00056a005

Shu, X. Z., Liu, Y., Palumbo, F. S., Luo, Y., and Prestwich, G. D. (2004). *In situ* crosslinkable hyaluronan hydrogels for tissue engineering. *Biomaterials.* 25, 1339–1348. doi: 10.1016/j.biomaterials.2003.08.014

Shukla, S., Baev, A., Jee, H., Hu, R., Burzynski, R., Yoon, Y.-K., et al. (2010a). Large-area, near-infrared (IR) photonic crystals with colloidal gold nanoparticles embedding. *ACS Appl. Mater. Interfaces.* 2, 1242–1246. doi: 10.1021/am100109f

Shukla, S., Kumar, R., Baev, A., Gomes, A., and Prasad, P. (2010b). Control of spontaneous emission of CdSe nanorods in a multirefringent triangular lattice photonic crystal. *J. Phys. Chem. Lett.* 1, 1437–1441. doi: 10.1021/jz100134y

Smith, D. R., Pendry, J. B., and Wiltshire, M. C. (2004). Metamaterials and negative refractive index. *Science.* 305, 788–792. doi: 10.1126/science.1096796

Terray, A., Oakey, J., and Marr, D. W. (2002). Fabrication of linear colloidal structures for microfluidic applications. *Appl. Phys. Lett.* 81, 1555–1557. doi: 10.1063/1.1503176

Werner, W. S., Glantschnig, K., and Ambrosch-Draxl, C. (2009). Optical constants and inelastic electron-scattering data for 17 elemental metals. *J. Phys. Chem. Ref. Data.* 38, 1013–1092. doi: 10.1063/1.3243762

Wu, C. Y., Owsley, K., and Di Carlo, D. (2015). Rapid software-based design and optical transient liquid molding of microparticles. *Adv. Mater.* 27, 7970–7978. doi: 10.1002/adma.201503308

Wu, S., Tsuruoka, T., Terabe, K., Hasegawa, T., Hill, J. P., Ariga, K., et al. (2011). A polymer-electrolyte-based atomic switch. *Adv. Funct. Mater.* 21, 93–99. doi: 10.1002/adfm.201001520

Yang, C.-M., Kim, H.-S., Na, B.-K., Kum, K.-S., and Cho, B. W. (2006). Gel-type polymer electrolytes with different types of ceramic fillers and lithium salts for lithium-ion polymer batteries. *J. Power Sources* 156, 574–580. doi: 10.1016/j.jpowsour.2005.06.018

Yu, Q., Nauman, S., Santerre, J., and Zhu, S. (2001). Photopolymerization behavior of di (meth) acrylate oligomers. *J. Mater. Sci.* 36, 3599–3605. doi: 10.1023/A:1017980523677

Conflict of Interest Statement: The authors declare that the research was conducted in the absence of any commercial or financial relationships that could be construed as a potential conflict of interest.

frontiers in Chemistry

ORIGINAL RESEARCH
published: 16 April 2019
doi: 10.3389/fchem.2019.00241

Nanocrystalline Electrodeposited Fe-W/Al_2O_3 Composites: Effect of Alumina Sub-microparticles on the Mechanical, Tribological, and Corrosion Properties

Aliona Nicolenco[1,2], Antonio Mulone[3], Naroa Imaz[4], Natalia Tsyntsaru[1,2]*, Jordi Sort[5,6], Eva Pellicer[6], Uta Klement[3], Henrikas Cesiulis[1] and Eva García-Lecina[4]*

[1] Department of Physical Chemistry, Vilnius University, Vilnius, Lithuania, [2] Institute of Applied Physics, Chisinau, Moldova, [3] Department of Industrial and Materials Science, Chalmers University of Technology, Gothenburg, Sweden, [4] CIDETEC, San Sebastián, Spain, [5] Departament de Física, Universitat Autònoma de Barcelona, Bellaterra, Spain, [6] Institució Catalana de Recerca i Estudis Avançats, Barcelona, Spain

OPEN ACCESS

Edited by:
Bongyoung Yoo,
Hanyang University, South Korea

Reviewed by:
Anthony Peter O'Mullane,
Queensland University of Technology, Australia
Yang Yang,
University of Central Florida, United States

***Correspondence:**
Aliona Nicolenco
alionanicolenco@gmail.com
Natalia Tsyntsaru
ashra_nt@yahoo.com

Specialty section:
This article was submitted to Electrochemistry, a section of the journal Frontiers in Chemistry

Received: 21 January 2019
Accepted: 26 March 2019
Published: 16 April 2019

Citation:
Nicolenco A, Mulone A, Imaz N, Tsyntsaru N, Sort J, Pellicer E, Klement U, Cesiulis H and García-Lecina E (2019) Nanocrystalline Electrodeposited Fe-W/Al_2O_3 Composites: Effect of Alumina Sub-microparticles on the Mechanical, Tribological, and Corrosion Properties. Front. Chem. 7:241. doi: 10.3389/fchem.2019.00241

In this study, nanocrystalline Fe-W alloy and Fe-W/Al_2O_3 composite coatings with various contents of sub-microsized alumina particles have been obtained by electrodeposition from an environmentally friendly Fe(III)-based electrolyte with the aim to produce a novel corrosion and wear resistant material. The increase in volume fraction of Al_2O_3 in deposits from 2 to 12% leads to the grain refinement effect, so that the structure of the coatings change from nanocrystalline to amorphous-like with grain sizes below 20 nm. Nevertheless, the addition of particles to the Fe-W matrix does not prevent the development of a columnar structure revealed for all the types of studied coatings. The observed reduction in both hardness and elastic modulus of the Fe-W/Al_2O_3 composites is attributed to the apparent grain size refinement/amorphization and the nanoporosity surrounding the embedded Al_2O_3 particles. In the presence of 12 vol% of Al_2O_3 in deposits, the wear rate decreases by a factor of 10 as compared to Fe-W alloy tested under dry friction conditions due to the lowering of tribo-oxidation. The addition of alumina particles slightly increases the corrosion resistance of the coatings; however, the corrosion in neutral chloride solution occurs through the preferential dissolution of Fe from the matrix. The obtained results provide a possibility to integrate the nanocrystalline Fe-W/Al_2O_3 composite coatings into various systems working under dry friction conditions, for example, in high-temperature vacuum systems.

Keywords: iron alloys, alumina, composite coatings, columnar growth, wear resistance

INTRODUCTION

Nanocrystalline Fe-W coatings with tunable functional properties can be electrodeposited from environmentally friendly Fe(III)-based solution with a high current efficiency (up to 60–70%) (Nicolenco et al., 2017, 2018a). The W content in the alloys can be varied from a few at.% up to 25 at.% by fine control of experimental parameters. Previous studies (Nicolenco et al., 2018a)

have shown that alloys with low W content have a soft magnetic character and relatively high saturation magnetization, making such alloys suitable for the design and fabrication of MEMS, for example, read-write heads or actuators. On the other hand, Fe-W alloy coatings with high W content (>20 at.%) are characterized by outstanding thermal stability (up to 600°C), good mechanical properties in a wide range of temperatures (10 ÷ 16 GPa) (Mulone et al., 2018a), and mirror-like smooth surface (Ra < 100 nm) (Bobanova et al., 2009; Mulone et al., 2018b; Nicolenco et al., 2018a). Nevertheless, one of the drawbacks of Fe-W coatings is their rather low wear and corrosion resistance that remains an important issue for the applications of these nanoengineered materials as protective coatings and smart interfaces.

Fabrication of composite materials is one of the common approaches, which enables to combine the useful properties of the second-phase particles with those of the metallic matrix, thus rendering a novel material with the tailored characteristics. For example, the co-deposition of transition metal sulfides (MoS_2 and WS_2) in Ni-W and Ni-P coatings significantly reduced the friction coefficient of the composites due to the specific layered structure and high elasticity of the particles, which provide a self-lubricating effect (Cardinal et al., 2009; García-Lecina et al., 2013; He Y. et al., 2016). Many studies have been conducted on the electrodeposition of metallic matrix composites with oxide and carbide particles. Here, an improvement of the strength and corrosion resistance of the resulting composite coatings was obtained thanks to the high hardness, the oxidation and thermal resistance of the co-deposited particles (Hosseini et al., 2014; Anwar and Mulyadi, 2015; Bhogal et al., 2015; Bajwa et al., 2016). However, the presence of second phase particles in the coating is not a guarantee that the desired performance will be attained. Often the incorporation of particles causes porosity, bad adhesion and weak interface bonding with the matrix. All these effects can eventually reduce the overall performance of the surface, particularly, corrosion resistance (Starosta and Zielinski, 2004; Hu et al., 2009; Bajwa et al., 2016). Therefore, the appropriate design of the composite system is essential.

Composite coatings with alumina particles have been the most extensively studied among particles-reinforced composites. In addition of its cost effectiveness, alumina has high chemical stability and sufficiently high affinity to adsorb iron group metal ions on its surface, thus facilitating the co-deposition of composites with Co, Ni and their alloys (Wu et al., 2004; Man et al., 2014). Well-dispersed composites with Al_2O_3 particles typically show good corrosion resistance in the sulfate and chloride medium due to the partial blocking of corrosion pits by inert alumina nano- or microsized particles (Bajwa et al., 2016). The addition of alumina particles can also contribute to the increased hardness and strength of the coatings, as the particles restrain the grain growth and provide a dispersion strengthening effect described by Orowan mechanism (Beltowska-Lehman et al., 2012; Man et al., 2014;Bajwa et al., 2016; Wasekar et al., 2016).

Several works exist in the literature correlating the mechanical characteristics of composite coatings with their tribological properties, giving relationships between the plasticity index (or hardness) and wear (Rupert and Schuh, 2010; García-Lecina et al., 2013; Bajwa et al., 2016). The studies performed mainly on Ni-based coatings showed that nanocrystalline materials with a higher ratio between hardness and elastic modulus, so-called elastic strain to failure, should better resist the plastic deformation, hence, resulting in lower wear (Leyland and Matthews, 2000; Rupert and Schuh, 2010). Nevertheless, the wear mechanism of Fe-containing coatings was ascribed to the combination of abrasive and adhesive wear considering tribo-oxidation as the driving factor. The high wear rates of Fe-W coatings could only be overcome by applying lubrication conditions (Bobanova et al., 2009; Nicolenco et al., 2018b). The tribological study performed on Ni-Fe/Al_2O_3 composites under dry friction conditions has also shown the negative and prevalent effect of Fe content in matrix on the wear resistance of the coatings, while the content of alumina particles had a minor effect (Starosta and Zielinski, 2004).

The aim of our work is to electrodeposit nanocrystalline Fe-W/Al_2O_3 composite coatings with various contents of incorporated sub-microsized alumina particles to improve the wear and corrosion characteristics of the coatings and make them suitable for various applications where aggressive conditions can exist. The effect of alumina particles' co-deposition on the composition and structure of the coatings, and their mechanical, tribological, and corrosion behavior is investigated.

EXPERIMENTAL PART

Fe-W/Al_2O_3 composite coatings were electrodeposited from a glycolate-citrate Fe(III)-based electrolyte which contained alumina particles in suspension. The base electrolyte was composed of 1 M glycolic acid, 0.3 M citric acid, 0.1 M $Fe_2(SO_4)_3$, and 0.3 M Na_2WO_4. Bath pH was adjusted to 7.0 with NaOH at room temperature. Sub-microsized alumina particles (Alfa Aesar 42572) with the concentration of 25, 50, and 100 g L^{-1} were added to the base electrolyte and the suspensions were stirred at 300 rpm for 24 h prior to first electrodeposition in order to hydrate the particles. Before starting the electroplating, the electrolytes were placed in an ultrasonic bath for 10 min to prevent agglomeration.

Electrodeposition was performed in a typical three-electrode cell, where a brass plate with an area of 4 cm^2 was used as a working electrode, Ag/AgCl/KCl_{sat} as a reference electrode and a platinized titanium mesh as a counter electrode. The substrates were degreased in a hot commercial alkaline cleaner and activated in H_2SO_4 solution, followed by Ni-seed layer electrodeposition at 30 mA cm^{-2} for 1 min from sulfate-chloride bath operated at 65°C. The anode was placed parallel to the cathode at a distance of 4.8 cm. The electrolyte volume was kept at 200 mL. The bath temperature was maintained at 65°C. Electrodeposition was carried out at a constant cathodic current density of 40 mA cm^{-2} during 1 h, at a constant stirring rare of 200 rpm.

The morphology of the coatings was investigated by a Carl Zeiss Ultra Plus field emission scanning electron microscope (Zeiss, Jena). The chemical composition was analyzed on cross-sectional area with the energy dispersive X-ray spectroscopy

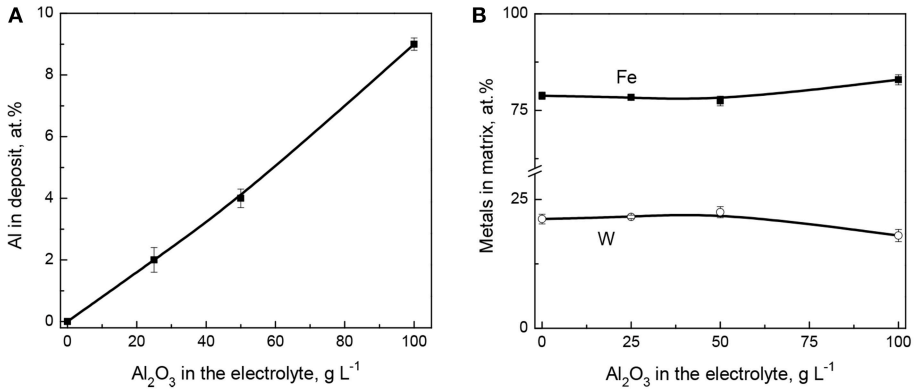

FIGURE 1 | Effect of Al_2O_3 particles' concentration in the electrolyte on Al content in deposit **(A)** and on the composition of Fe-W matrix **(B)**. The coatings were obtained at 200 rpm, 40 mA cm^{-2}, 65°C.

(EDS) analysis tool AMETEK EDAX attached to the microscope operated at 15 kV. The particles size distribution and the volume fraction of co-deposited Al_2O_3 particles in the deposits was determined by the image analysis software ImageJ. It was determined that the majority of the alumina particles have the mean diameter between 50 and 150 nm, although some of the particles were forming agglomerates with 200–250 nm (**Figure S1**), probably due to the high surface energy of the powder. The contact profilometer Surftest SJ-210 was used to determinate the roughness (R_a) of the coatings. A contact needle tip was scanning the surfaces horizontally along the 1.5 mm length. The crystallographic structure and phase composition of the obtained coatings were studied by means of X-ray diffraction (XRD), using a Rigaku MiniFlex II diffractometer with Cu Kα radiation ($\lambda = 1.54183$ Å) operated at 30 kV and 30 mA.

The crystallographic orientation of the grains in the deposited coatings was examined by the Electron Back Scattered Diffraction technique (EBSD) in a Leo 1550 Gemini Scanning Electron Microscope (SEM). The EBSD data were acquired with a Nordlys II detector (Oxford Instruments) using a step size of 25 nm. Post-processing of the acquired EBSD data was done with the HKL Channel 5 software (Oxford Instruments): noise reduction was performed by removal of wild spikes and extrapolation of non-indexed points (5 nearest neighbors required). Metallographic preparation of the samples was performed by mechanical polishing with a 50 nm finishing using OP-S silica suspension as the last step.

The mechanical properties were evaluated by means of nanoindentation using Nanoindenter XP from MTS equipped with a Berkovich pyramidal-shaped diamond tip under load-control mode on the cross-section of the coatings, previously embedded in epoxy resin and polished to mirror-like appearance. The maximum applied load was 50 mN to ensure that the lateral size of the imprint remained small compared to the total film thickness but still embraced both the matrix and the particles in the case of composite coatings. Fifty indentations were placed in the middle of the cross-section area of the coatings in order to avoid the influence from the resin. The metallographic preparation of the samples was performed by mechanical polishing with a 1 μm finishing using a diamond suspension as the last step. Both hardness (H) and reduced elastic modulus (E_r) were derived from the initial part of the unloading indentation segments using the method of Oliver and Phar (Oliver and Pharr, 2004). In order to characterize the elastic-plastic response of the coatings under external deformation, the plasticity index (U_p/U_{tot}) was calculated as a ratio between plastic and total (plastic + elastic) energy during nanoindentation. The plastic energy was derived as the area between loading and unloading curves, while the total energy was calculated as the area between the loading curve and the displacement axis. All the extracted parameters were statistically treated, and the average values are reported.

The investigation of tribological behavior of electrodeposited coatings was carried out under dry friction conditions using ball-on-disk configuration sliding tests (CSM, model THT). A corundum ball of 6 mm diameter was the counter-body that moved against rigidly fixed coated samples for 500 m with a rotation speed of 4 cm s^{-1} (rotation diameter 6 mm). The applied load was 2 N. All the tests were performed in ambient air at 20 ± 2°C and 55% relative humidity. After the sliding tests, the debris were removed from the surface with dry cold air jet, and the samples were ultrasonically cleaned in ethanol in order to remove the remaining adhered debris prior to measuring the wear track profiles. The specific wear rate was defined as wear volume per unit distance and unit load (Bajwa et al., 2016).

Corrosion resistance of the Fe-W and Fe-W/Al_2O_3 coatings was investigated by potentiodynamic polarization and electrochemical impedance spectroscopy (EIS) techniques under open circuit conditions. A 250 mL three-electrode Flat Cell Kit (Princeton Applied Research, Oak Ridge, TN, USA) with a platinized titanium mesh and Ag/AgCl/$NaCl_{(3M)}$ electrodes as counter and reference electrodes, respectively, was used to conduct the experiments. The potential of the working electrode was measured against the reference electrode with a Luggin

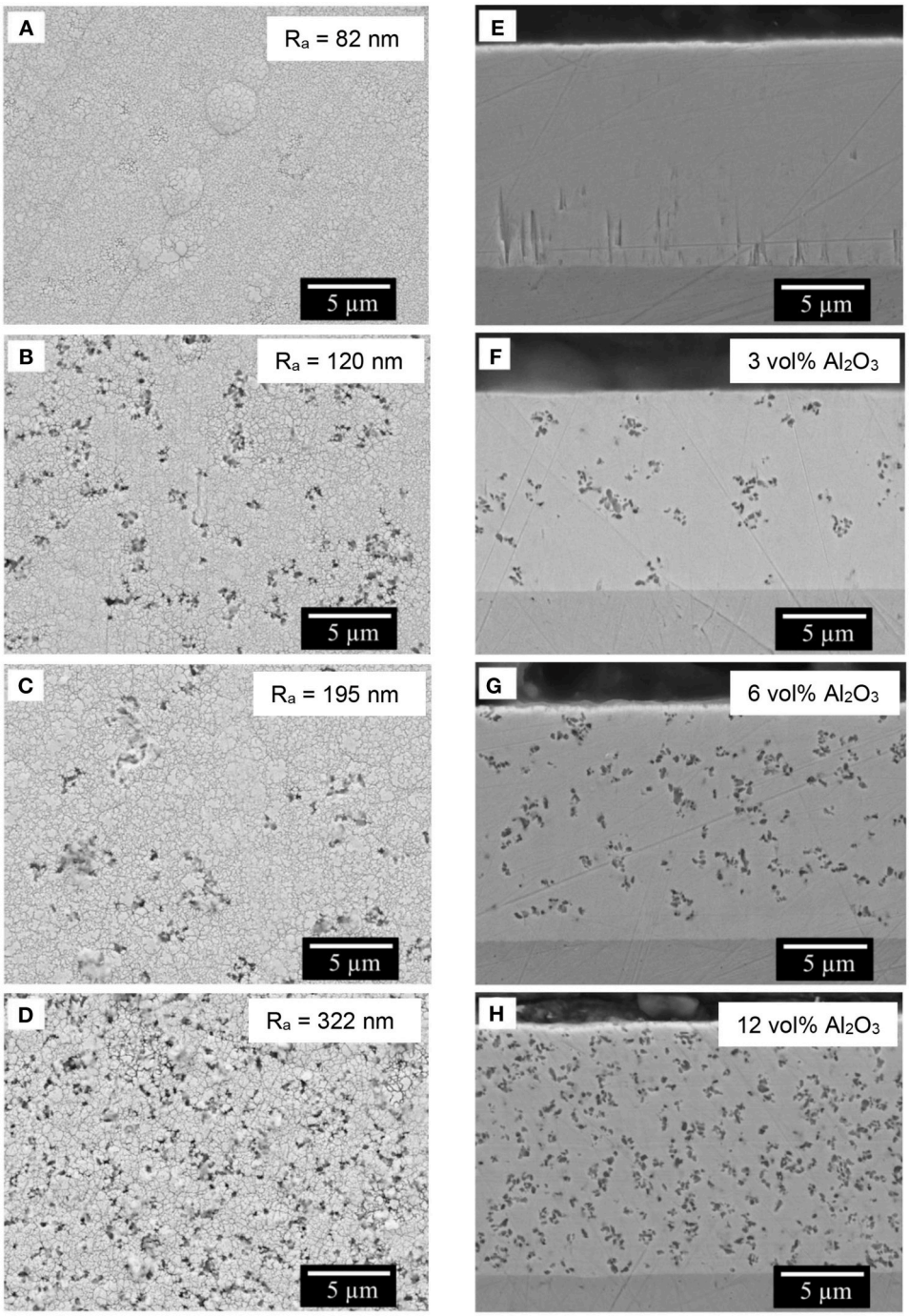

FIGURE 2 | SEM images of the top surface **(A–D)** and the cross-section polished with 1 µm finishing **(E–H)** of the composite coatings obtained with different concentration of alumina in electrolyte: 0 g L^{-1} **(A,E)**, 25 g L^{-1} **(B,F)**, 50 g L^{-1} **(C,G),** and 100 g L^{-1} **(D,H)**. The average roughness of the surface is indicated in the corresponding images **A–D**. In inserts **F–H** is the volume percentage of embedded alumina particles determined by corresponding image analysis. Electrodeposition was carried out at 40 mA cm^{-2}, 65°C, 200 rpm.

Haber capillary tip. The exposed area of the sample was 1 cm^2. The tests were performed in 0.1 M NaCl solution at room temperature. The open circuit potential was recorded for 15 min followed by a linear potentiodynamic sweep from −1 to 0 V with a scan rate of 1 mV s^{-1}. EIS measurements were conducted by applying sinusoidal voltage with 5 mV (vs. OCP) amplitude in the frequency range 10 kHz−0.01 Hz, and the fitting of data has been performed using Z-View software.

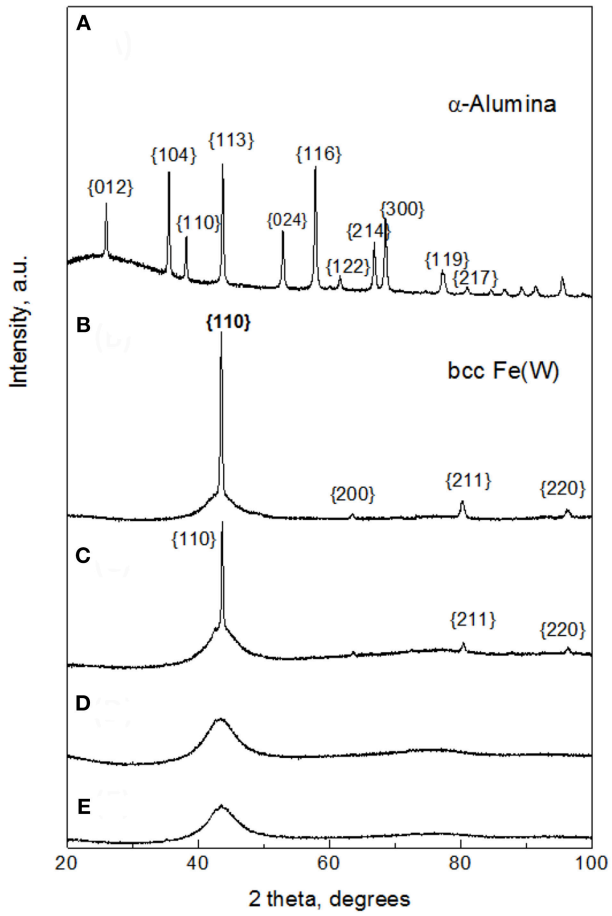

FIGURE 3 | XRD patterns of sub-microsized alumina powder **(A)**; Fe-W coating **(B)**, and Fe-W/Al_2O_3 composite coatings obtained with different concentration of alumina in electrolyte: 25 g L^{-1} **(C)**, 50 g L^{-1} **(D)**, and 100 g L^{-1} **(E)**.

RESULTS AND DISCUSSION

Effect of Alumina Particles on the Composition, Morphology, and Structure of the Fe-W Composite Coatings

Considerable attention in composite coatings electrodeposition was directed primarily toward determination of optimum conditions for their production, i.e., temperature, pH, current density, rotation speed, etc. (Low et al., 2006). However, it is often difficult to generalize the findings due to the large difference in experimental conditions. Therefore, in order to investigate the effect of sub-micron alumina particles on the composition, morphology and structure of Fe-W composite coatings, the same parameters as for electrodeposition of compact Fe-W alloys with high W content and high current efficiency were used, i.e., the deposition conditions applied were 65°C, pH 7, 40 mA cm^{-2}, and 200 rpm. The different content of alumina particles in the deposits was achieved by variation of the concentration of alumina particles in the bath.

The compositional analysis of the electrodeposited coatings was performed on the cross-section area where two different regions were selected for examination: a wider area embracing Al_2O_3 particles, and a particle-free region (Fe-W matrix). Both regions were inspected at four different locations of each sample. The average atomic fraction of incorporated Al, and the Fe and W % contents in the matrix are shown in **Figures 1A,B**, respectively. It is seen that the content of aluminum (alumina particles) increases sharply with the increase of the particles concentration in electrolyte up to 100 g L^{-1}. The maximum percentage of incorporated alumina is obtained at the maximum studied concentration of particles in solution, as predicted by Guglielmi's two-step adsorption model (Low et al., 2006; Wasekar et al., 2016).

In its simplest form, the mechanism of alumina particles co-deposition with Fe-W alloy can be described as follows: in a first step, suspended alumina particles are transported from the bulk of the solution to the cathode through the Nernst diffusion layer, where they become loosely adsorbed at the cathode's surface. It is supposed that the transportation of particles is not only due to convection force, but also due to the formation of ionic clouds (i.e., adsorption of charged metal complexes in the bulk electrolyte) on the particles surface, which move toward the cathode under electric field and thus drag the particles (Low et al., 2006; Wasekar et al., 2016). In a second step, the charge transfer reaction breaks the ionic shell surrounding the particles and thus they become irreversibly encapsulated into the growing metallic layer. Although the particles co-deposition mechanism has been studied by many authors and using different approaches, the Guglielmi's model still remains one of the most commonly adopted to describe the behavior of the particles during electrodeposition. It was actually validated for some binary alloys composites with inert particles, such as Ni-Fe/Al_2O_3 (Starosta and Zielinski, 2004; Torabinejad et al., 2016), Ni-W/SiC (Wasekar et al., 2016) and others (Low et al., 2006).

Taking into account the electrochemically inert nature of alumina particles one can expect that the composition of the metallic matrix should not be affected by the particles concentration in the solution unless their incorporation does not cause an apparent decrease of the active cathode surface area (Beltowska-Lehman et al., 2012). Indeed, as it is seen from **Figure 1B**, the incorporation of alumina particles does not influence on the W content in Fe-W matrix. However, slightly lower W content was achieved within the matrix when the concentration of particles in solution reached 100 g L^{-1}. This is probably due to the partial blocking of the cathode area by non-conductive alumina, which resulted in an increased cathodic current density of the alloy deposition and a shift of cathodic polarization curve toward more negative potentials (**Figure S2**). As a result, deposition of coatings from the bath containing 100 g L^{-1} of Al_2O_3 occurs at slightly higher overpotential, that is −1.32 V compared to −1.25 V recorded in the case of Fe-W alloy deposition at the same cathodic current density applied (**Figure S3**). Thus, the W content in Fe-W matrix attains 21 at.% when the concentration of particles does not exceed 50 g L^{-1}, and 17 at.% at higher alumina particles concentrations, respectively. Therefore, despite the non-conductive nature of Al_2O_3 particles,

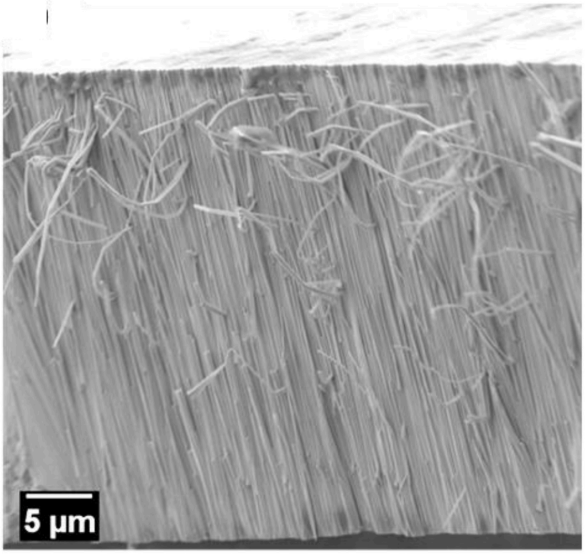

FIGURE 4 | SEM micrograph of a fracture surface of the Fe-W coating showing a fibrous structure.

the current efficiency and the deposition rate remained rather unchanged as compared to Fe-W alloy deposition. These findings are consistent with other studies emphasizing the effect of alumina particles on the composition of binary alloy metallic matrix (Yari and Dehghanian, 2013; Wasekar et al., 2016).

The morphology of Fe-W alloy and Fe-W/Al_2O_3 composite coatings electrodeposited at the same conditions was analyzed by SEM and the representative images of the coatings surface are shown in **Figures 2A–D** (left). SEM images of Fe-W alloy surface depict a smooth, cracks-free globular structure with the average roughness of ∼80 nm (**Figure 2A**). The addition of particles does not change the morphology of the coatings. However, the surface roughness increases gradually up to 300 nm due to protrusion of Al_2O_3 particles (**Figures 2B–D**). The panels e-g of **Figure 2** (right) illustrate the corresponding cross-sectional images of the studied samples. Remarkably, the distribution of Al_2O_3 across the whole thickness of the coatings is uniform; although, the particles tend to incorporate in form of the small agglomerates with ∼200 nm size. The volume percentage of embedded alumina particles was determined by the image analysis of the corresponding cross-sectional surface of the coatings. According to that, the volume fraction of the Al_2O_3 in deposit increases linearly from ∼3 vol% to a maximum 12 vol% with the increase in particles concentration in the bath up to 100 g L^{-1}. All the coatings have approximately the same thickness, about 14–15 μm, which confirms the minor effect of alumina particles on the deposition rate of the composites.

The microstructural changes caused by addition of Al_2O_3 particles to the Fe-W matrix were investigated by XRD and EBSD techniques. **Figure 3A** shows the XRD pattern of the sub-microsized alumina particles where the main peaks corresponding to rhombohedral Al_2O_3 were indexed. Remarkably, in the XRD patterns of Fe-W/ Al_2O_3 composites (**Figures 3C,D**) the peaks corresponding to the Al_2O_3 particles are not observed. It can be suggested that the amount of co-deposited alumina particles is insufficient to provide strong reflections. In fact, their amount ranges between 2 and 12 vol% (**Figure 2**) which roughly corresponds to <4 wt.%. This is, however, in the limit of X-Ray diffraction in a multi-component materials, where at least 2–3 wt.% is needed to have clear diffraction peaks (Newman et al., 2015).

The corresponding XRD pattern of the Fe-W alloy (**Figure 3B**) illustrates that the matrix of the composite coatings is composed of a crystalline body-centered cubic (bcc) single phase Fe(W) solid solution. In fact, the identified peaks are shifted to lower angles as compared to the characteristic peaks of bcc Fe due to the expansion of Fe lattice parameter with incorporation of bigger W atoms. However, the appearance of a broad shoulder at ∼43° indicates that the coating contains an amorphous-like fraction. It is worth noticing that appearance of crystalline peaks in Fe-W alloy having ∼ 20 at.% of W is rather unusual because at the W contents above ∼16 at.% the transformation to amorphous structure typically occurs (Nicolenco et al., 2018a). In fact, the deposition of Fe-W alloys previously reported by different authors (Bobanova et al., 2009; Wang et al., 2016) was performed under stagnant conditions, while the effect of the hydrodynamic conditions on the structure development during electrodeposition of this type of alloy has not been investigated yet. It was, however, observed that under stirring conditions the adsorption state of an intermediate electroactive complex and the pH of the near-electrode layer are modified as compared to stagnant conditions, thus leading to the growth of coatings with coarser grains (i.e., having stronger X-ray reflection) (Belevskii et al., 2010).

By increasing the content of alumina particles, a gradual variation in the microstructure is observed. The intensity of the Fe(W) crystalline peaks is reduced with the incorporation of a small amount of Al_2O_3 particles and only one broad peak is observed with further increase in concentration of alumina in solution and in the coating (**Figures 3C,D**). Typically, the broadening of XRD peaks indicates the decrease in grain size that is commonly observed with the incorporation of second phase particles. The particles can restrain grain growth in two ways: (i) disordering the regular structure providing more active sites for crystal nucleation and hence, by themselves, limiting the crystallites growth (Yilmaz et al., 2014; Bhogal et al., 2015); (ii) causing a shift of overpotential, thus leading to compositional variations in metallic matrix, which in turn causes a decrease (or increase) in the average grain size (Beltowska-Lehman et al., 2012; Yari and Dehghanian, 2013), that is the typical case of W alloys with iron group metals (Tsyntsaru et al., 2012). As has been discussed above, the incorporation of alumina particles does not change significantly the W content in Fe-W matrix. Therefore, it is possible to separate the direct contribution of reinforcement particles to the grain refinement of the composite from the amorphization of the electrodeposited matrix due to the W content variation.

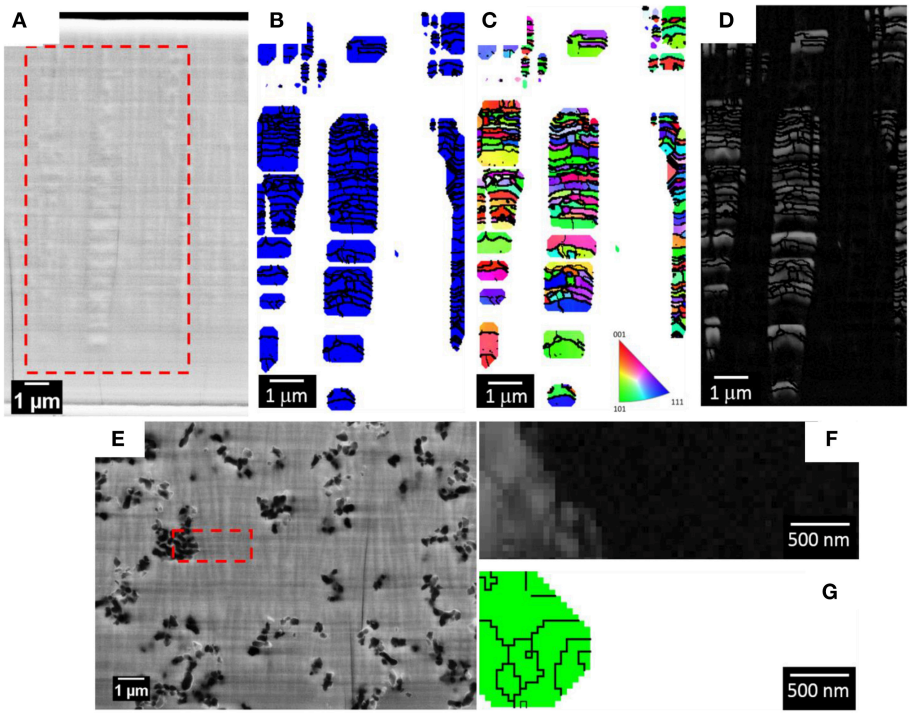

FIGURE 5 | SEM micrograph of the polished cross-section of the Fe-W coating for EBSD analysis **(A)**. The red dashed box is highlighting the area from where the EBSD maps were acquired: phase map **(B)**, orientation map in inverse pole figure coloring along growth direction with the corresponding code **(C),** and band contrast map **(D)**. In the phase map the blue grains belong to the Fe(W) phase. SEM micrograph of the polished cross-section of the sample deposited with 100 g L^{-1} of Al_2O_3 particles for EBSD analysis **(E)** with a band contrast map **(F)** and phase map **(G)**. In the phase map the green grains belong to the Al_2O_3 phase. The zero solutions are indicated as white pixel in both the orientation and phase maps, as dark pixel in the band contrast map.

To get further insight into the structure of the coatings, EBSD analyses were performed on selected areas of the coatings cross-sections. During metallographic preparation of the samples the formation of columns growing perpendicular to the substrate plane was noted in the fracture surface of the Fe-W alloys (**Figure 4**). A previous study suggested the formation of nanofibers in Ni-W and Co-W alloys rich in W electrodeposited onto copper substrate (Donten et al., 2003), while another study on Co-W alloys revealed a columnar structure only for the coatings with low W content, i.e., around 3 at.% (Tsyntsaru et al., 2013). This implies that the columnar structure is strictly determined by the electrochemical and hydrodynamic conditions, whose modification may greatly change the nucleation and growth processes. As a matter of fact, no columnar structure was revealed in Fe-W alloys electrodeposited under stagnant conditions (Nicolenco et al., 2018a).

Figure 5A shows a secondary electron image of the polished cross-sections of the sample deposited with 0 g L^{-1} of Al_2O_3 particles (Fe-W alloy) and the red dashed box defines the area where the EBSD phase map (**Figure 5B**), orientation map (**Figure 5C**), and band contrast map (**Figure 5D**) were acquired. A Fe(W) solid solution phase (i.e., bcc cubic cell with 2.9231 Å lattice constant), generated from the XRD results (**Figure 3B**) was used as the reference phase for the EBSD indexing. As shown in the SEM image in **Figure 5A**, the 50 nm polishing of the cross-section reveals the presence of pillars of various thicknesses. EBSD analysis performed at these areas shows that such pillars consist of several sub-micron/nano Fe(W) grains, presented in blue in the phase map of **Figure 5B**. The majority of Fe(W) grains have a diameter between 50 and 250 nm. The Fe(W) grains are characterized by random texture, as there is no predominant color in the orientation map shown in **Figure 5C**. A large fraction of zero solutions, that is 71%, is found in between the pillars. Zero solutions are shown in the phase and orientation maps as white pixels, while in the band contrast map as dark pixels. The band contrast map shown in **Figure 5D** is providing information about the quality of the EBSD patterns acquired from the analyzed area: crystalline regions appear bright, while areas providing poor quality patterns (e.g., grain boundaries, amorphous phase, or deformed grains) appear dark. Hence, the absence of EBSD pattern in between the Fe(W) pillars could be related to an amorphous phase, or to a nanocrystalline phase with sizes below the EBSD detection limits, that is 20 nm. Such high fraction of zero solutions would be expected considering the broad shoulder in XRD pattern of the sample, as can be seen in **Figure 3B**.

Figure 5E shows a secondary electron image of the polished cross-sections of the sample deposited with 100 g L^{-1} of Al_2O_3 particles and the red dashed box defines the area where the EBSD

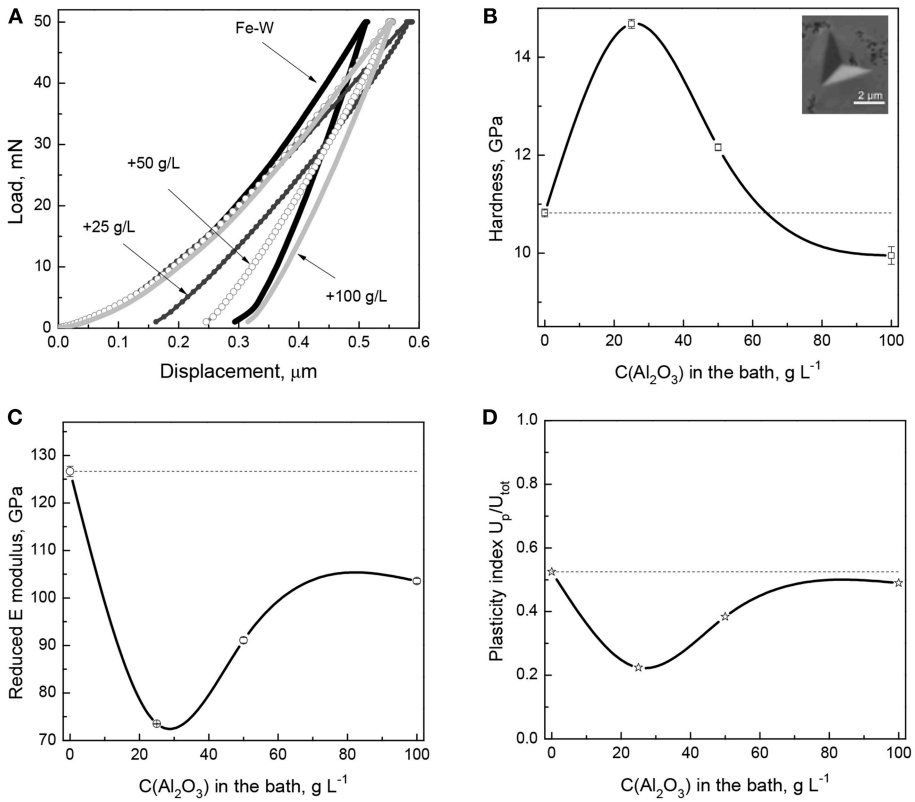

FIGURE 6 | Load-displacement curves **(A)** and extracted dependence of hardness **(B)**, elastic modulus **(C)**, and plasticity index **(D)** as a function of the particles concentration in the bath. In insert **(B)** is the representative SEM image of the indentation imprint on the cross-section area of Fe-W/Al_2O_3 composite with lowest particles concentration.

band contrast map (**Figure 5E**) and phase map (**Figure 5G**) were acquired. As revealed from the SEM image of the polished cross-section, a columnar structure is found also in the Fe-W/Al_2O_3 composite sample. The size of the columns, both in thickness and length, appears smaller as compared to the columns found for the sample deposited with 0 g L^{-1} of Al_2O_3 (see **Figures 5A,D**). Their extension along the cross-section appears to be limited by the presence of the alumina particles. However, as shown in the band contrast map (**Figure 5F**), it was not possible to acquire any EBSD pattern from the areas in the cross-section that were including the columnar structures. Only areas containing Al_2O_3 particles were correctly indexed (the grains of the Al_2O_3 particles are shown with a green color in the phase map in **Figure 5G**). These results are in agreement with the XRD findings (**Figure 3E**) regarding the presence of an amorphous phase, or of a nanocrystalline phase with smaller grain sizes compared to the Fe-W alloy. Hence, as observed from XRD and EBSD results, the incorporation of Al_2O_3 particles in the coatings leads to a reduction of the grain size but it does not prevent the development of columnar growth. Based on these observations one can infer the inherent porosity between the columnar Fe-W matrix and incorporated spherical shape Al_2O_3 particles, which is however challenging to confirm experimentally.

Effect of Alumina Particles on Mechanical Properties of Fe-W Composite Coatings

The mechanical properties (hardness, reduced elastic modulus, plasticity index, and elastic strain to failure) of the Fe-W and Fe-W/Al_2O_3 coatings were obtained by nanoindentation on cross-section and the representative load–displacement curves are shown in **Figure 6A**. It can be seen that compared to the Fe-W matrix, the composite coatings show rather complex behavior.

The hardness values extracted from the load-displacement curves show that with the incorporation of small amounts of particles into the Fe-W matrix the hardness increases sharply from ∼10 GPa to ∼15 GPa (**Figure 6B**). It is commonly observed that the addition of particles improves the hardness of the coatings due to the two synergistic effects: (i) dispersion-strengthening, related to the presence of mechanically hard fine particles retarding the plastic deformation of the matrix, and (ii) grain refinement, resulting in an increased number of grain boundaries able to stop the dislocation motions. The former mechanism is described by the Orowan's equation, which assumes that the dislocations bend out when passing the obstacles (particles), thus creating some resisting force which leads to improved hardness of the material. However, as the concentration of incorporated particles further increases, then a continuous decrease in hardness is observed (**Figure 6B**),

so the hardness of the composite coating with the highest particles concentration is even lower than that of pure Fe-W matrix. This can be attributed to the apparent grain size refinement/amorphization confirmed by XRD and EBSD analyses (**Figures 3**, **5**). The mechanical behavior of a composite is then governed by the inverse Hall-Petch relation, which describes the decrease of hardness as being due to grain boundary sliding and triple junctions (i.e., plastic deformation mechanisms different than dislocation motion), similar as it was observed elsewhere (Giallonardo et al., 2011; Wasekar et al., 2016).

Contrary to what is observed for the hardness, the trend in elastic modulus is more unexpected. **Figure 6C** reveals that E_r reduces with the incorporation of a small amount of particles (25 g L^{-1} Al_2O_3 particles in the bath). This is in contradiction with a large number of studies showing the increase in elastic modulus with the addition of particles (Beltowska-Lehman et al., 2012; García-Lecina et al., 2013; Mahidashti et al., 2018). Often, the so-called rule of mixtures is used to infer the strengthening of composite materials containing reinforcing fibers (i.e., with columnar microstructure), which can roughly predict the elasticity of the material if the load is applied parallel to the fibers direction (isostrain conditions). Taking into account the columnar structure of Fe-W revealed in **Figures 4**, **5** and the rather spherical (non-columnar) shape of the reinforcing particles, it can be expected that applying the load on cross-section, i.e., perpendicular to the Fe-W fibrous, the reinforcing effect of the particles would be less pronounced than in isostrain conditions. Nonetheless, even if the microstructure of Fe-W/Al_2O_3 composite does not correspond to the ideal "isostrain" conditions, an increase of the Young's modulus of the composite with respect to that of the matrix should be expected, since the Al_2O_3 particles possess a Young's modulus larger than the Fe-W matrix. However, other factors like loose Al_2O_3 particles-matrix interfaces (Zhou et al., 2016) and, more in particular, nanoporosity surrounding the embedded particles could explain the reduction of E_r. Actually, a strong dependence of the Young's modulus on porosity in nanoporous materials is well-known and it has been confirmed by nanoindentation and finite element simulations in a variety of works (Ramakrishnan and Arunachalam, 1993; Gibson and Ashby, 1999; Pellicer et al., 2012). Higher porosity causes a decrease of the reduced Young's modulus during nanoindentation (Esqué-de los Ojos et al., 2016). When the amount of incorporated particles increases, since alumina has a very high Young's modulus (300–400 GPa) the net effect is that E_r increases but remains always lower than for the pure Fe-W alloy.

The plasticity index was also derived from the nanoindentation data in order to provide further insight into mechanical properties of electrodeposited composite coatings. Thus, the U_p/U_{tot} reduces with the incorporation of small amount of particles (**Figure 6D**), indicating rather elastic nature of the composites and their improved resistance to permanent deformation in contrast to rather plastic nature of Fe-W matrix. An increase in plasticity observed in the composites with higher particles concentration is most likely due to the grain refinement which promotes branching of the shear bands in nanocrystalline/amorphous matrix (**Figure 6D**).

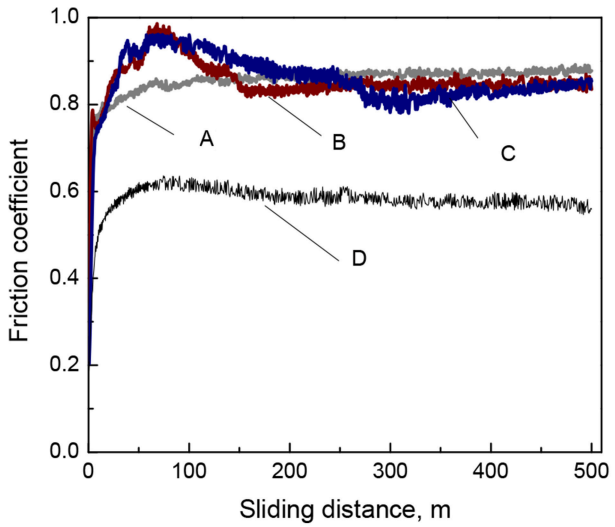

FIGURE 7 | Evolution of the coefficient of friction of Fe-W **(A)** and Fe-W/Al_2O_3 composite coatings obtained with different concentration of alumina in electrolyte: 25 g L^{-1} **(B)**, 50 g L^{-1} **(C)**, and 100 g L^{-1} **(D)** tested under dry friction conditions at 2 N load, 4 cm s^{-1}, 500 m.

Effect of Alumina Particles on Tribological Properties of Fe-W Composite Coatings

The investigation of tribological behavior of electrodeposited Fe-W and Fe-W/Al_2O_3 composite coatings was carried out using ball-on-disk configuration sliding tests where conditions were the same for all the tested tribo-pairs. The variation of the coefficient of friction (COF) recorded during the tests as a function of sliding distance is shown in **Figure 7**. The COF of the Fe-W alloys and composite coatings with low particles concentration is high, ∼0.8–0.9, while it decreases to ∼0.6 for the composite coating with the highest particles concentration. Typically, the high values of COF are ascribed to the presence of microscopic irregularities of materials surfaces. Taking into account that the initial surface roughness of both Fe-W coatings and alumina counter body was in order of hundred nanometers, such high values of the COF can be attributed to the presence of adhered debris which increase the asperity contact between two bodies in contact.

The nature of debris particles was investigated by SEM/EDS techniques on the resulted wear tracks (**Figure 8**). Indeed, the debris particles were found to be distributed within the whole length of the wear track accumulating mainly in piles. The oxygen content in these regions is increased up to 50 at.% which corresponds to the oxygen content in mixed iron oxide Fe_3O_4. This is consistent with the previous studies on the tribological behavior of electrodeposited Fe-W alloys which showed that these coatings undergo severe oxidation during fretting (tribo-oxidation) (Bobanova et al., 2009; Nicolenco et al., 2018b). The tribo-oxidation phenomenon can be explained as follows: when two surfaces slide together, the friction work is turned into thermal energy, which tends to maximize the potential energy at the interface. Since the maximized thermal energy is naturally an unstable state, the oxidation itself is a form of intrinsic

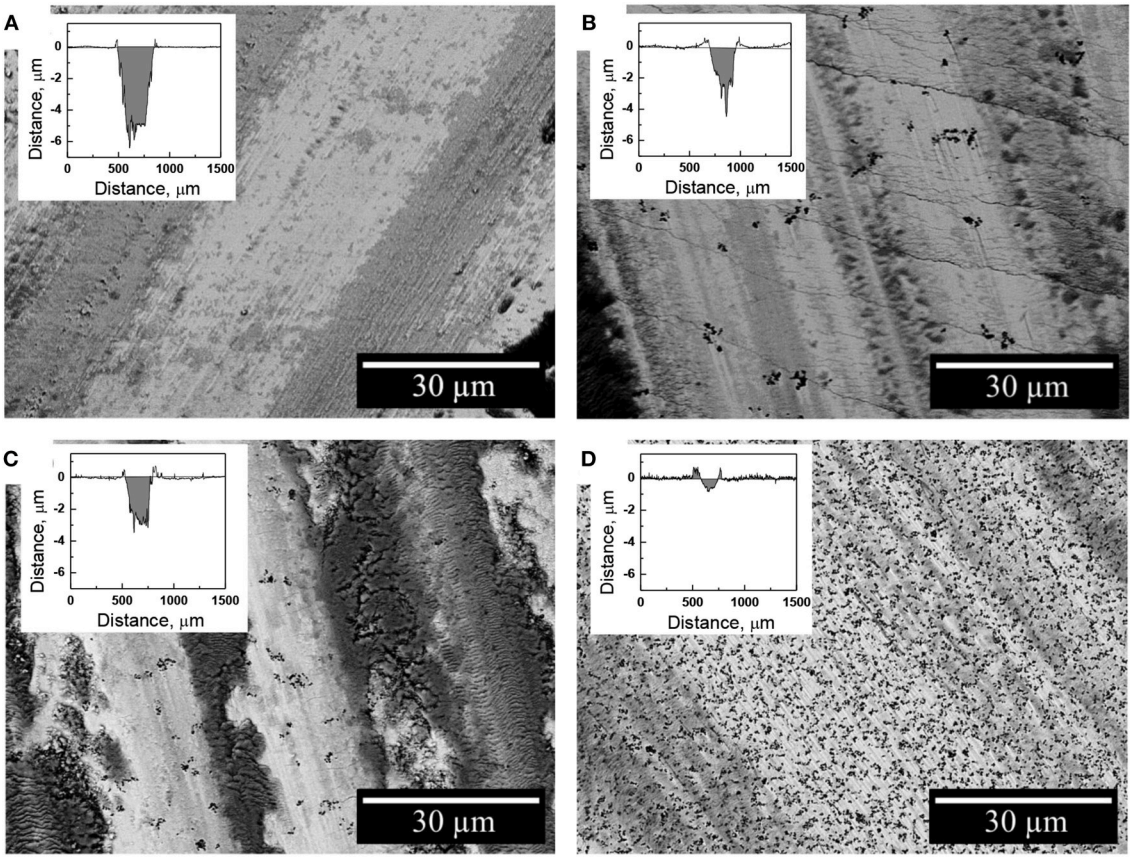

FIGURE 8 | SEM images of the worn surface of the Fe-W **(A)** and Fe-W/Al_2O_3 coatings obtained with different concentration of alumina in electrolyte: 25 g L^{-1} **(B)**, 50 g L^{-1} **(C)**, and 100 g L^{-1} **(D)** presented along with the corresponding wear track depth profiles.

response of the material to recover the system equilibrium under friction conditions (Abdel-Aal, 2003). Thus, the formation of iron oxides during dry friction can be considered a driving factor determining the resultant tribological behavior of the Fe-W coatings (COF, wear depth/volume, cracks initiation, plastic deformations, etc.). As it can be seen from **Figure 8C**, the presence of micro-sized Al_2O_3 particles significantly reduce the area of the exposed Fe-W matrix, thus reducing the asperity contact between two sliding surfaces what results in a lower COF and wear depths (**Figure 8**).

The wear rate of Fe-W alloy and Fe-W/Al_2O_3 composite coatings was calculated by integration the cross-section area of the wear tracks shown in inserts **Figure 8** and the obtained results are shown in **Figure 9**. The interpretation of the depth profiles was sometimes not straightforward due to the presence of debris which remained adhered in the wear track even after ultrasound cleaning that increased the error in calculation of the wear depth and wear rate. Nevertheless, it is clearly seen that the addition of Al_2O_3 particles reduces the specific wear rate, i.e., increases the wear resistance of the coatings under the tested conditions. The lowest wear rate ($1.8 \cdot 10^{-6}$ mm^3 N^{-1} m^{-1}) was obtained for the sample with the highest particles concentration, which is an order of magnitude lower than that of pure Fe-W alloy matrix. It is also comparable to the wear rate of annealed Fe-W alloy and even electrodeposited hard chromium coatings tested by using a similar set-up and dry friction conditions applied (Mulone et al., 2019). Thus, in annealed Fe-W alloys the reduction in the tribooxidation was achieved mainly due to the phase transformation, that is, the formation of Fe_2W and $FeWO_4$ hard phases which are not prone to oxidation. Hence, electrodeposited Fe-W/Al_2O_3 composite coatings are getting advantageous in terms of fabrication (one-step electrodeposition, no post-treatment required, environmentally-friendly bath composition) and sustainability (suitable for chromium replacement). Taking into account the outstanding thermal resistance of the amorphous-like Fe-W deposits (Mulone et al., 2018a) (up to 600°C) and remarkable hardness of these coatings (10–16 GPa), the novel Fe-W/Al_2O_3 composites can be considered as alternative appealing materials for a wide range of technically-demanding applications, such as components and mechanisms where lubrication is recognized as ineffective or inapplicable, e.g., in high-temperature vacuum systems.

Many researchers address the importance of the mechanical characteristics for the good wear resistance and show a linear relationship between the hardness (or H/E ratio) and wear for different polycrystalline materials like Ni-W (Sriraman et al.,

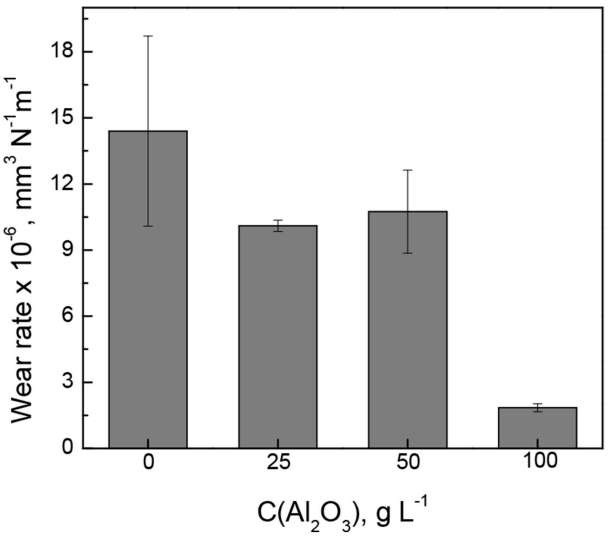

FIGURE 9 | The wear rate of Fe-W alloy and Fe-W/Al_2O_3 composite coatings at dry friction conditions at 2 N load, 4 cm s^{-1}, 500 m.

2006), Ni-P (Jeong et al., 2003), and different type of composites (Leyland and Matthews, 2000; Shi et al., 2006; García-Lecina et al., 2013; Man et al., 2014; Bajwa et al., 2016). It is assumed in these cases that the abrasive wear originates from plastic deformation. Therefore, materials with higher H (or H/E ratio) should better resist the plastic deformations and thus have lower wear. However, in the Fe-W system the tribological behavior is primarily governed by the tribo-oxidation (Mulone et al., 2019), i.e., the chemical reactivity of the material and the nature of the oxidation products formed are the determining factors. Nevertheless, the high hardness of Fe-W/Al_2O_3 composites may result in an excessive coating brittleness contributing to the cracks propagation inside the wear tracks as depicted in **Figures 8B,C**.

Effect of Alumina Particles on Corrosion Properties of Fe-W Composite Coatings

Corrosion of Fe-W alloys and composites was induced by using 0.1 M NaCl solution, which is commonly used to simulate marine environment. The obtained potentiodynamic polarization curves and Nyquist plots are presented in **Figures 10A,B**, respectively, and the extracted parameters are given in the **Table 1**. It can be seen from **Figure 10A** that the Fe-W based coatings exhibit a very similar behavior with an active anodic metal dissolution that do not transfer into passive state. With the increase in particles concentration the corrosion potential (E_{corr}) slightly shifts toward more negative potentials. Usually, the lowering of corrosion potential indicates a higher tendency of the electrode to be dissolved in an electrolyte. Nevertheless, different hydrogen overvoltage on Fe-W surface with different alumina contents may vary without a direct correlation with the corrosion rate. Moreover, accumulation of corrosion products on the surface could also cause the lower values of E_{corr}. The corrosion current density (j_{corr}) was calculated from the presented polarization curves. Usually, the corrosion current is determined by the extrapolation of the rectilinear dependences of log j vs. E to E_{corr} in the Tafel region. However, due to the peculiarities of cathodic hydrogen evolution and active anodic metal dissolution the cathodic and anodic branches of recorded voltammograms are asymmetric (**Figure 10A**), what makes the standard j_{corr} determination not reliably applicable. Therefore, the values of j_{corr} were obtained by using Allen-Hickling equation which enables to accurately estimate the corrosion current from the data obtained in a relatively narrow potential range close to E_{corr} (Kublanovsky et al., 2008; Vernickaite et al., 2016). The obtained results show that the corrosion current density for all the studied samples is the same order, independently of the content of co-deposited alumina particles (**Table 1**).

In the **Figure 10B**, each point in the plot corresponds to the measured impedance at a certain frequency, while the continuous line presents the best-fit data obtained by using an equivalent circuit shown in insert **Figure 10B**. The used equivalent circuit for fitting of EIS data supposes the complicated mechanism of alloy corrosion, which perhaps involves intermediate stages with the adsorption of corrosion products (Vernickaite et al., 2016). The equivalent circuit used to simulate the EIS consisted of R_s–solution resistance (uncompensated resistance); R_{ct}–charge transfer resistance; C_{dl}–a constant phase element having meaning of double layer capacitance of the electrolyte at alloy surface; and Cd which is adsorption-related capacitance of intermediates. Accordingly, circuit $R_{ct}C_{dl}$ describes the Faraday process, i.e., the resistance and capacities of the layer against electrochemical reaction, and Cad represents the process of blocking the coating's surface by adsorbed species. Generally, the higher the charge transfer resistance R_{ct}, the greater corrosion resistance of the system. Thus, according to **Table 1**, the lowest corrosion resistance was obtained for the Fe-W coating without particles. The highest values R_{ct} are obtained for the composite coatings produced from the bath with 50 and 100 g L^{-1} of particles (6 and 12 vol% Al_2O_3, respectively).

Noticeably, the R_{ct} obtained for Fe-W coatings electrodeposited from glycolate-citrate electrolyte and tested in chloride medium can be roughly comparable to other Fe-containing deposits described in literature: Fe-W alloy electrodeposited from citrate bath and tested in sulfate-chloride medium (380.7 Ω cm^2) (Vernickaite et al., 2015), Ni-Fe-W alloy tested in similar corrosion medium (207.0 Ω cm^2) (Sriraman et al., 2007) and with Ni-Fe/Al_2O_3 composite in sodium sulfate (∼250 Ω cm^2) (Starosta and Zielinski, 2004); whereas the corrosion resistance of Co-W and Ni-W alloys in neutral mediums is much higher, i.e., 1,200 and 6,770 Ω cm^2, respectively (Sriraman et al., 2007; Vernickaite et al., 2016). Taking this into account, and the small variations in corrosion currents obtained for investigated Fe-W composite coatings, one could suspect the detrimental and prevalent effect of Fe dissolution from the coating.

The surface of investigated Fe-W coatings after corrosion test is cracked and the cracks propagation is along the grain boundaries as it can be observed in **Figure 11A**. The corrosion medium can penetrate faster through these cracks, thus

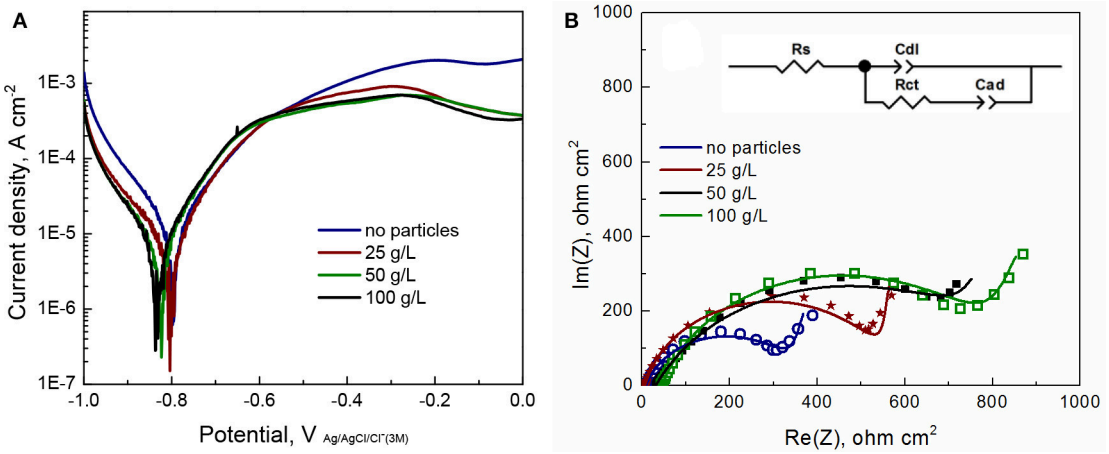

FIGURE 10 | Linear sweep voltammograms **(A)** and EIS Nyquist plots **(B)** for Fe-W and Fe-W/Al_2O_3 coatings electrodeposited under similar conditions and examined in 0.1 M NaCl solution at OCP. In insert **(B)** is the electrochemical circuit used for data fitting. R_s, solution resistance; R_{ct}, charge transfer resistance; C_{dl} is a constant phase element having meaning of the double layer capacitance of alloy surface and C_{ad} is adsorption-related capacitance of intermediates.

TABLE 1 | Extracted corrosion parameters from E vs. j plots shown in **Figure 10A** and corresponding equivalent circuit parameters determined by fitting the impedance spectra of electrodeposited Fe-W and Fe-W/Al_2O_3 coatings (**Figure 10B**) in 0.1 M NaCl medium at room temperature.

Coating	$-E_{corr}$, V	$-j_{corr}$, A/cm^2	R_{ct}, Ω cm^2	C_{dl}, F/ cm^2	n(C_{dl})	C_{ad}, F/ cm^2	n(C_d)	R_s, Ω cm^2
Fe-W	0.795	5×10^{-4}	355.2	1.54×10^{-3}	0.80	6.36×10^{-2}	0.89	8.8
Fe-W+25 g/L Al_2O_3	0.804	3×10^{-4}	569.1	8.61×10^{-4}	0.85	5.66×10^{-2}	0.95	6.9
Fe-W+50 g/L Al_2O_3	0.823	3×10^{-4}	843.8	1.55×10^{-3}	0.71	6.92×10^{-2}	0.98	31.2
Fe-W+100 g/L Al_2O_3	0.837	3×10^{-4}	795.1	8.18×10^{-4}	0.81	3.32×10^{-2}	0.85	45.6

"n"—is the exponent in the equation for the constant phase element that measures how far the interface is from an ideal capacitor ($0 < n < 1$).

accelerating the dissolution of Fe-W matrix. The EDS analysis of corroded surface of the studied coatings showed a significant increase in both oxygen content (up to 50 at.%) and the W content (up to 28 at.%), which is in accordance with other studies performed on W alloys with Fe group metals (Wang et al., 2014; He Y. et al., 2016; Vernickaite et al., 2016). This indicates that the corrosion process occurs through the preferential dissolution of Fe from the matrix, which leads to the formation of iron oxides and hydroxides at the electrode surface and to release of free Fe^{2+} ions into solution (Sriraman et al., 2007; He Y. et al., 2016). It is supposed that during corrosion process W preferentially form oxides, or can be also released into solution in form of WO_4^{2-} ion. Thus, $FeWO_4$ and $Fe_2(WO_4)_3$ compounds could be found in corrosion products, as shown in He et al. (2016). Slightly increased corrosion resistance shown by EIS can be attributed to the presence of alumina particles which partially block the surface and hinder the propagation of corrosion cracks, thus no cracks are evidenced on the surface and cross-section of the composite coatings after corrosion test (**Figure 11B**).

CONCLUSIONS

The electrodeposition of novel Fe-W/Al_2O_3 composite coatings with various alumina concentrations has been carried out from an Fe(III)-based electrolyte. The addition of alumina particles with concentrations ranging from 25 to 100 g L^{-1} to the Fe-W plating bath did not influence the W content in Fe-W matrix and the deposition rate remains also virtually unchanged. The content of co-deposited Al_2O_3 increased linearly from 2 to 12 vol% with the increase in particles concentration in the bath. The obtained Fe-W and Fe-W/Al_2O_3 composite coatings were characterized by a columnar growth structure. In the Fe-W coating such columns consisted of several sub-microns and nano Fe(W) grains. As observed from XRD and EBSD results, the incorporation of alumina particles in the Fe-W/Al_2O_3 composite coatings led to a reduction of the grain size and amorphization, but it did not prevent the development of columnar growth. These structural changes partially contributed to an increase in measured hardness up to 15 GPa obtained with the addition of small amount of particles (25 g L^{-1} in the bath, 2 vol% in deposit), followed by a decrease below 10 GPa for the coating with maximum volume fraction of alumina. The dependence of the elastic modulus on the Al_2O_3 particles concentration is not the typical one expected for composite coatings with reinforcing particles. For low particles concentration the Young's modulus decreases by around 40% and it increases with further increase of the particles concentration, but still remains lower than for the pure Fe-W alloy. The observed reduction in Young's modulus could be explained by the presence of nanopores surrounding the particles, among other possible reasons. A

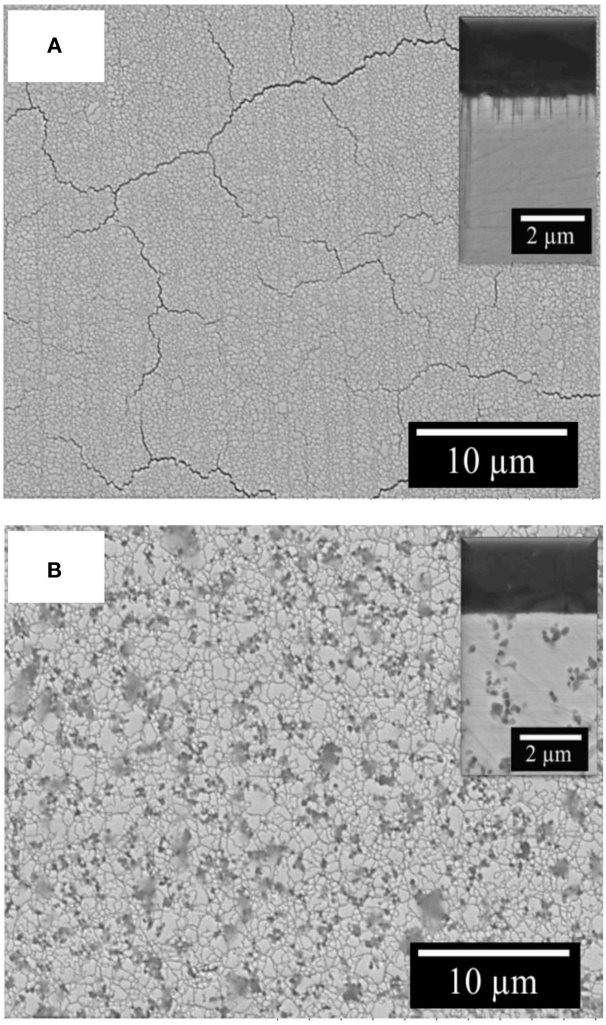

FIGURE 11 | SEM images of Fe-W **(A)** and Fe-W+100 g/L Al_2O_3 coatings **(B)** after corrosion test in 0.1 M NaCl at room temperature. In inserts are the corresponding cross-sectional images of the samples.

superior tribological behavior, the lowest wear rate of $1.8 \cdot 10^{-6}$ mm^3 N^{-1} m^{-1}, was obtained for the Fe-W/Al_2O_3 composite coating with the highest particles concentration (100 g L^{-1} in the bath, 12 vol% in deposit). The wear rate was reduced by an order of magnitude as compared to the pure Fe-W alloy matrix mainly due to the reduction of the exposed area of the Fe-W matrix and lowering the tribo-oxidation. Electrodeposited Fe-W and Fe-W/Al_2O_3 composite coating show similar corrosion behavior in 0.1 NaCl medium. The corrosion occurs via the formation of Fe and W oxygen compounds and preferential Fe dissolution from the matrix independently from alumina particles concentration. Nevertheless, the presence of Al_2O_3 in the deposits results in a slightly increase corrosion resistance (up to ~800 Ω cm^2) obtained by EIS due to the partial blocking of the surface and hindering the propagation of corrosion cracks.

The results presented in this work provide a possibility to integrate the nanocrystalline Fe-W/Al_2O_3 composite coatings into various mechanical systems working under dry friction, and in particular those working at elevated temperatures.

AUTHOR CONTRIBUTIONS

The electrodeposition of the coatings, wear, and corrosion measurements were performed by AN together with NI, under the supervision of NT, HC, and EG-L. The structural characterization was performed by AM under the supervision of UK. The mechanical characterization was performed by JS and EP. Writing-original draft preparation by AN and AM. All the authors contributed to the writing-review and editing.

FUNDING

This work has been funded by the European Union's Horizon 2020 research and innovation programme under the Marie Skłodowska-Curie grant agreement N° 642642 (SELECTA), H2020 SMARTELECTRODES project (No.778357) and Research Council of Lithuania No 09.3.3-LMT-K-712-08-0003. Partial financial support from the Generalitat de Catalunya (2017-SGR-292 project) and the Spanish Government (MAT2017-86357-C3-1-R and MAT2017-86357-C3-2-R) is also acknowledged. The authors also thank the Departamento de Desarrollo Económico y Competitividad of the Basque government (ELKARTEK, KK-2017/00096, KK-2018/00108) for partially supporting this research.

SUPPLEMENTARY MATERIAL

The Supplementary Material for this article can be found online at: https://www.frontiersin.org/articles/10.3389/fchem.2019.00241/full#supplementary-material

REFERENCES

Abdel-Aal, H. A. (2003). On the interdependence between kinetics of friction-released thermal energy and the transition in wear mechanisms during sliding of metallic pairs. *Wear* 254, 884–900. doi: 10.1016/S0043-1648(03)00243-6

Anwar, D. I., and Mulyadi, D. (2015). Synthesis of Fe-TiO2 composite as a photocatalyst for degradation of methylene blue. *Proce. Chem.* 17, 49–54. doi: 10.1016/j.proche.2015.12.131

Bajwa, R. S., Khan, Z., Bakolas, V., and Braun, W. (2016). Water-lubricated Ni-based composite (Ni-Al2O3, Ni-SiC and Ni-ZrO2) thin film coatings for industrial applications. *Acta Metallurg. Sinica* 29, 8–16. doi: 10.1007/s40195-015-0354-1

Belevskii, S. S., Cesiulis, H., Tsyntsaru, N., I., and Dikusar, A. I. (2010). The role of mass transfer in the formation of the composition and structure of CoW coatings electrodeposited from citrate solutions. *Surface Eng. Appl. Electrochem.* 46, 570–578. doi: 10.3103/S1068375510060050

Beltowska-Lehman, E., Indyka, P., Bigos, A., Kot, M., and Tarkowski, L. (2012). Electrodeposition of nanocrystalline Ni-W coatings strengthened by ultrafine alumina particles. *Surf. Coat. Technol.* 211, 62–66. doi: 10.1016/j.surfcoat.2011.10.021

Bhogal, S. S., Kumar, V., Dhami, S. S., and Pabla, B. S. (2015). Tribological properties and preparation of electrodeposited Ni-TiO2 composite coating. *J. Electrochem. Sci. Eng.* 5, 37–45. doi: 10.5599/jese.135

Bobanova, Z. I., Dikusar, A. I., Cesiulis, H., Celis, J.-P., Tsyntsaru, N. I., and Prosycevas, I. (2009). Micromechanical and tribological properties of nanocrystalline coatings of iron-tungsten alloys electrodeposited from citrate-ammonia solutions. *Russ. J. Electrochem.* 45, 895–901. doi: 10.1134/S1023193509080096

Cardinal, M. F., Castro, P. A., Baxi, J., Liang, H., and Williams, F. J. (2009). Characterization and frictional behavior of nanostructured Ni-W-MoS2 composite coatings. *Surf. Coat. Technol.* 204, 85–90. doi: 10.1016/j.surfcoat.2009.06.037

Donten, M., Stojek, Z., and Cesiulis, H. (2003). Formation of nanofibers in thin layers of amorphous W alloys with Ni, Co, and Fe obtained by electrodeposition. *J. Electrochem. Soc.* 150, C95– C98. doi: 10.1149/1.1536994

Esqué-de los Ojos, D., Zhang, J., Fornell, J., Pellicer, E., and Sort, J. (2016). Nanomechanical behaviour of open-cell nanoporous metals: homogeneous versus thickness-dependent porosity. *Mech. Mater.* 100, 167–174. doi: 10.1016/j.mechmat.2016.06.014

García-Lecina, E., García-Urrutia, I., Díez, J. A., Fornell, J., Pellicer, E., and Sort, J. (2013). Codeposition of inorganic fullerene-like WS2 nanoparticles in an electrodeposited nickel matrix under the influence of ultrasonic agitation. *Electrochim. Acta* 114, 859–867. doi: 10.1016/j.electacta.2013.04.088

Giallonardo, J. D., Erb, U., Aust, K. T., and Palumbo, G. (2011). The influence of grain size and texture on the Young's Modulus of nanocrystalline nickel and nickel-iron alloys. *Philos. Magaz.* 91, 4594–4605. doi: 10.1080/14786435.2011.615350

Gibson, L. J. and Ashby, M. F. (1999). *Cellular Solids: Structures and Properties*. Cambridge: Cambridge Solid State Science Series. doi: 10.1557/mrs2003.79

He, J., He, F.-L., Li, D.-W., Liu, Y.-L., and Yin, D.-C. (2016). A novel porous Fe/Fe-W alloy scaffold with a double-layer structured skeleton: preparation, *in vitro* degradability and biocompatibility. *Colloids Surf. B. Biointerfaces* 142, 325–333. doi: 10.1016/j.colsurfb.2016.03.002

He, Y., Wang, S. C., Walsh, F. C., Chiu, Y. L., and Reed, P. A. S. (2016). Self-lubricating Ni-P-MoS2 composite coatings. *Surf. Coat. Technol.* 307, 926–934. doi: 10.1016/j.surfcoat.2016.09.078

Hosseini, M. G., Abdolmaleki, M., and Ghahremani, J. (2014). Investigation of corrosion resistance of electrodeposited Ni–W/SiC composite coatings. *Corrosion Eng. Sci. Technol.* 49, 247–253. doi: 10.1179/1743278213Y.0000000120

Hu, X. G., Cai, W. J., Xu, Y. F., Wan, J. C., and Sun, X. J. (2009). Electroless Ni-P-(Nano-MoS_2) composite coatings and their corrosion properties. *Surf. Eng.* 25, 361–366. doi: 10.1179/174329408X282532

Jeong, D. H., Erb, U., Aust, K. T., and Palumbo, G. (2003). The relationship between hardness and abrasive wear resistance of electrodeposited nanocrystalline Ni-P coatings. *Scr. Mater.* 48, 1067–1072. doi: 10.1016/S1359-6462(02)00633-4

Kublanovsky, V., Dikusar, A I., Cesiulis, H., and Prosycevas, I. (2008). Electrodeposition and corrosion properties of nanocrystalline Fe-W alloys. *Physicochem. Mech. Mater.* 7, 308–314.

Leyland, A., and Matthews, A. (2000). On the significance of the H/E ratio in wear control: a nanocomposite coating approach to optimised tribological behaviour. *Wear* 246, 1–11. doi: 10.1016/S0043-1648(00)00488-9

Low, C. T.J., Wills, R. G. A., and Walsh, F.,C. (2006). Electrodeposition of composite coatings containing nanoparticles in a metal deposit. *Surf. Coat. Technol.* 201, 371–83. doi: 10.1016/j.surfcoat.2005.11.123

Mahidashti, Z., Aliofkhazraei, M., and Lotfi, N. (2018). Review of nickel-based electrodeposited tribo-coatings. *Trans. Indian Instit. Metals* 71, 257–295. doi: 10.1007/s12666-017-1175-x

Man, J, Zhang, S., Jianfeng, Li, Zhao, B., and Chen, Y. (2014). Effects of electrolyte pH on morphologies and mechanical properties of α-Al2O3/Ni composite coatings and role of zeta potentials in co-deposition process. *Surf. Coat. Technol.* 249, 118–124. doi: 10.1016/j.surfcoat.2014.03.054

Mulone, A., Nicolenco, A., Fornell, J., Pellicer, E., Tsyntsaru, N., Cesiulis, H., et al. (2018a). Enhanced mechanical properties and microstructural modifications in electrodeposited Fe-W alloys through controlled heat treatments. *Surf. Coat. Technol.* 350, 20–30. doi: 10.1016/j.surfcoat.2018.07.007

Mulone, A., Nicolenco, A., Hoffmann, V., Klement, U., Tsyntsaru, N., and Cesiulis, H. (2018b). In-depth characterization of as-deposited and annealed Fe-W coatings electrodeposited from glycolate-citrate plating bath. *Electrochim. Acta* 261, 167–177. doi: 10.1016/j.electacta.2017.12.051

Mulone, A., Nicolenco, A., Imaz, N., Martinez-Nogues, V., Tsyntsaru, N., Cesiulis, H., et al. (2019). Improvement in the wear resistance under dry friction of electrodeposited Fe-W coatings through heat treatments. *Coatings* 9:66. doi: 10.3390/coatings9020066

Newman, J.A., Schmitt, P. D., Toth, S. J., Deng, F., Zhang, S., and Simpson, G. J. (2015). Parts per million powder X-Ray diffraction justin. *Anal. Chem.* 87, 10950–10955. doi: 10.1021/acs.analchem.5b02758

Nicolenco, A., Tsyntsaru, N., and Cesiulis, H. (2017). Fe (III)-based ammonia-free bath for electrodeposition of Fe-W alloys. *J. Electrochem. Soc.* 164, D590–D596. doi: 10.1149/2.1001709jes

Nicolenco, A., Tsyntsaru, N., Fornell, J., Pellicer, E., Reklaitis, J., Baltrunas, D., et al. (2018a) Mapping of magnetic and mechanical properties of Fe-W alloys electrodeposited from Fe(III)-based glycolate-citrate bath. *Mater. Design* 139, 429–438. doi: 10.1016/j.matdes.2017.11.011

Nicolenco, A., Tsyntsaru, N., Matijošius, T., Asadauskas, S., and Cesiulis, H. (2018b). Wear resistance of electrodeposited Fe-W alloy coatings under dry conditions and in the presence of rapeseed oil. *Green Tribol.* 1, 16–23. doi: 10.15544/greentribo.2018.04

Oliver, W.C., and Pharr, G. M. (2004). Measurement of hardness and elastic modulus by instrumented indentation: advances in understanding and refinements to methodology. *J. Mater. Res.* 19, 3–20. doi: 10.1557/jmr.2004.19.1.3

Pellicer, E., Pané, S., Panagiotopoulou, V., Fusco, S., Sivaraman, K. M., Suriñach, S., et al. (2012). Localized electrochemical deposition of porous Cu-Ni microcolumns: insights into the growth mechanisms and the mechanical performance. *Int. J. Electrochem. Sci.* 7, 4014–4029.

Ramakrishnan, N., and Arunachalam, V. S. (1993). Effective elastic moduli of porous ceramic materials. *J. Am. Ceram. Soc.* 76, 2745–2752. doi: 10.1111/j.1151-2916.1993.tb04011.x

Rupert, T. J., and Schuh, C. A. (2010). Sliding wear of nanocrystalline Ni-W: structural and the apparent breakdown of archard scaling. *Acta Mater.* 58, 4137–4148. doi: 10.1016/j.actamat.2010.04.005

Shi, L., Sun, C., Gao, P., Zhou, F., and Liu, W. (2006). Mechanical properties and wear and corrosion resistance of electrodeposited Ni-Co/SiC nanocomposite coating. *Appl. Surf. Sci.* 252, 3591–3599. doi: 10.1016/j.apsusc.2005.05.035

Sriraman, K. R., Raman, S. G. S., and Seshadri, S. K. (2007). Corrosion behaviour of electrodeposited nanocrystalline Ni-W and Ni-Fe-W alloys. *Mater. Sci. Eng. A* 460–461, 39–45. doi: 10.1016/j.msea.2007.02.055

Sriraman, K. R., S., Raman, G. S., and Seshadri, S. K. (2006). Synthesis and evaluation of hardness and sliding wear resistance of electrodeposited nanocrystalline Ni-W alloys. *Mater. Sci. Eng. A* 418, 303–311. doi: 10.1016/j.msea.2005.11.046

Starosta, R., and Zielinski, A. (2004). Effect of chemical composition on corrosion and wear behaviour of the composite Ni-Fe-Al2O3 coatings. *J. Mater. Process. Technol.* 157–158, 434–441. doi: 10.1016/j.jmatprotec.2004.09.068

Torabinejad, V., Rouhaghdam, S. A., Aliofkhazraei, M., and Allahyarzadeh, M. H. (2016). Ni-Fe-Al2O3 electrodeposited nanocomposite coating with functionally graded microstructure. *Bull. Mater. Sci.* 39, 857–864. doi: 10.1007/s12034-016-1211-1

Tsyntsaru, N., Cesiulis, H., Donten, M., Sort, J., Pellicer, E., and Podlaha-Murphy, E. J. (2012). Modern trends in tungsten alloys electrodeposition with iron group metals. *Surf. Eng. Appl. Electrochem.* 48, 491–520. doi: 10.3103/S1068375512060038

Tsyntsaru, N., Cesiulis, H., Pellicer, E., Celis, J. P., and Sort, J. (2013). Structural, magnetic, and mechanical properties of electrodeposited cobalt-tungsten alloys: intrinsic and extrinsic interdependencies. *Electrochim. Acta* 104, 94–103. doi: 10.1016/j.electacta.2013.04.022

Vernickaite, E., Antar, Z. Z., Nicolenco, A., Kreivaitis, R., Tsyntsaru, N., and Cesiulis, H. (2015). "Tribological and corrosion properties of iron-based alloys," in *Proceedings of the 8th International Scientific Conference BALTTRIB 2015* (Kaunas). doi: 10.15544/balttrib.2015.29

Vernickaite, E., Tsyntsaru, N., and Cesiulis, H. (2016). Electrodeposition and corrosion behaviour of nanostructured Cobalt–tungsten alloys coatings. *Trans. Inst. Metal Finishing* 94, 313–321. doi: 10.1080/00202967.2016.1220071

Wang, M., Wang, Z., and Guo, Z. (2014). Electrodeposited free-crack NiW films under super gravity filed: structure and excellent corrosion property. *Mater. Chem. Phys.* 148, 245–252. doi: 10.1016/j.matchemphys.2014.07.041

Wang, S., Zeng, C., Ling, Y., Wang, J., and Xu, G. (2016). Phase transformations and electrochemical characterizations of electrodeposited amorphous Fe–W coatings. *Surf. Coat. Technol.* 286, 36–41. doi: 10.1016/j.surfcoat.2015.12.011

Wasekar, N. P., Latha, S. M., Ramakrishna, M., Rao, D. S., and Sundararajan, G. (2016). Pulsed electrodeposition and mechanical properties of Ni-W/SiC nano-composite coatings. *Mater. Design* 112, 140–150. doi: 10.1016/j.matdes.2016.09.070

Wu, G., Li, N., Wang, D. L., Zhou, D. R., Xu, B. Q., and Mitsuo, K. (2004). Effect of α-Al2O3particles on the electrochemical codeposition of Co-Ni alloys from sulfamate electrolytes. *Mater. Chem. Phys.* 87, 411–419. doi: 10.1016/j.matchemphys.2004.06.016

Yari, S., and Dehghanian, C. (2013). Deposition and characterization of nanocrystalline and amorphous Ni-W coatings with embedded alumina nanoparticles. *Ceram. Int.* 39, 7759–7766. doi: 10.1016/j.ceramint.2013.03.033

Yilmaz, G., Hapçi, G., and Orhan, G. (2014). Properties of Ni/Nano-TiO2 composite coatings prepared by direct and pulse current electroplating. *J. Mater. Eng. Perform.* 24, 709–720. doi: 10.1007/s11665-014-1346-4

Zhou, W., Yamamoto, G., Fan, Y., Kwon, H., Hashida, T., and Kawasaki, A. (2016). *In-situ* characterization of interfacial shear strength in multi-walled carbon nanotube reinforced aluminum matrix composites. *Carbon* 106, 37–47. doi: 10.1016/j.carbon.2016.05.015

Conflict of Interest Statement: The authors declare that the research was conducted in the absence of any commercial or financial relationships that could be construed as a potential conflict of interest.

frontiers in Chemistry

ORIGINAL RESEARCH
published: 14 May 2019
doi: 10.3389/fchem.2019.00340

Exploring the Kinetic and Thermodynamic Relationship of Charge Transfer Reactions Used in Localized Electrodeposition and Patterning in a Scanning Bipolar Cell

Trevor M. Braun[1,2]* *and Daniel T. Schwartz*[2]*

[1] Functional Nanostructured Materials Group, Materials Science and Engineering Division, National Institute of Standards and Technology, Gaithersburg, MD, United States, [2] Electrochemical Materials and Interfaces Laboratory, Chemical Engineering Department, University of Washington, Seattle, WA, United States

OPEN ACCESS

Edited by:
Elizabeth J. Podlaha, Clarkson University, United States

Reviewed by:
Mohammad Farkhondeh, Renault, France
Deyang Li, Hutchinson Technology Inc., United States

***Correspondence:**
Trevor M. Braun
trevor.braun@nist.gov
Daniel T. Schwartz
dts@uw.edu

Specialty section:
This article was submitted to Electrochemistry, a section of the journal Frontiers in Chemistry

Received: *27 February 2019*
Accepted: *25 April 2019*
Published: *14 May 2019*

Citation:
Braun TM and Schwartz DT (2019) Exploring the Kinetic and Thermodynamic Relationship of Charge Transfer Reactions Used in Localized Electrodeposition and Patterning in a Scanning Bipolar Cell. Front. Chem. 7:340. doi: 10.3389/fchem.2019.00340

Bipolar electrochemistry involves spatial separation of charge balanced reduction and oxidation reactions on an electrically floating electrode, a result of intricate coupling of the work piece with the ohmic drop in the electrochemical cell and to the thermodynamics and kinetics of the respective bipolar reactions. When paired with a rastering microjet electrode, in a scanning bipolar cell (SBC), local electrodeposition and patterning of metals beneath the microjet can be realized without direct electrical connections to the workpiece. Here, we expand on prior research detailing electrolyte design guidelines for electrodeposition and patterning with the SBC, focusing on the relationship between kinetics and thermodynamics of the respective bipolar reactions. The kinetic reversibility or irreversibility of the desired deposition reaction influences the range of possible effective bipolar counter reactions. For kinetically irreversible deposition systems (i.e., nickel), a wider thermodynamic window is available for selection of the counter reaction. For kinetically reversible systems (i.e., copper or silver) that can be easily etched, tight thermodynamic windows with a small downhill driving force for spontaneous reduction are required to prevent metal patterns from electrochemical dissolution. Furthermore, additives used for the bipolar counter reaction can influence not only the kinetics of deposition, but also the morphology and microstructure of the deposit. Cyclic voltammetry measurements help elucidate secondary parasitic reduction reactions occurring during bipolar nickel deposition and describe the thermodynamic relationship of both irreversible and reversible bipolar couples. Finally, finite element method simulations explore the influence of bipolar electrode area on current efficiency and connect experimental observations of pattern etching to thermodynamic and kinetic relationships.

Keywords: bipolar electrochemistry, electrodeposition, material fabrication, current distribution, electrolyte design

INTRODUCTION

Bipolar electrochemistry—a phenomenon involving spatially segregated, equal and opposite reduction and oxidation charge transfer reactions on an electrically floating electrode—has recently proven valuable for a range of applications where traditional electrochemical methods are inadequate. Bipolar electrochemical reduction and oxidation reactions are driven by the potential gradient in solution that polarizes an electrically floating electrode (aka bipolar electrode or BPE) positioned within the electric field. When the solution ohmic resistance responsible for generating potential gradients is substantial relative to the charge transfer resistance of these reactions, a portion of the total applied current can pass through the BPE, manifesting in spatially bifurcated reduction and oxidation reactions on a single conductor. Because charge must be conserved on the BPE, the reduction current equals that of oxidation. Complete understanding of the intricate coupling between the kinetics of the bipolar redox reactions, their thermodynamic relationship, and ionic/electronic transport through the cell is critical to designing effective bipolar electrochemical systems.

Precise control of both reduction and oxidation reactions on an electrode free of direct electrical contact has generated several new bipolar electrochemical applications, ranging from electroanalytical chemistry to material fabrication. A powerful development involves addressing large microfabricated electrode arrays with a single set of feeder electrodes, demonstrating high throughput screening of material properties (Munktell et al., 2015), measuring electrocatalytic activity coupled to electrochemiluminescence signatures (Chow et al., 2009; Lin et al., 2012; Xiao et al., 2017), and developing sensors based on metal dissolution (Chow et al., 2010; Fosdick et al., 2013). The potential gradient driving electrochemistry in bipolar systems has further been utilized to develop compositionally graded material systems (Ulrich et al., 2008; Ishiguro et al., 2011; Tisserant et al., 2015; Xu et al., 2018). Bipolar electrochemistry is also useful in device fabrication, including deposition of non-line-of-sight interconnects between electrically isolated posts (Bradley et al., 1997, 1999), production of anisotropic functionalized microparticles (Loget et al., 2012; Tiewcharoen et al., 2017), and growth of single metal nanowires (Wood and Zhang, 2015).

Previous work by our group demonstrated that a rastering microjet nozzle can be employed for localized bipolar electrodeposition and patterning on an electrically floating substrate, a system we called a scanning bipolar cell (SBC) (Braun and Schwartz, 2015, 2016a,b,c). Initial applications of the SBC on a copper bipolar electrode involved copper electrodeposition in the region beneath the nozzle (near-field) and copper dissolution of the substrate material in the region surrounding the nozzle (far-field) (Braun and Schwartz, 2015). The equal but opposite nature of bipolar electrochemistry resulted in a "sculpting" of the originally planar substrate; in a high faradaic efficiency system like copper, every copper ion reduced beneath the nozzle resulted in an atom of copper metal etched in the far-field. Reduction of other metal cations, such as Ni^{2+}, on a copper BPE resulted in a similar displacement of copper in the far-field while nickel electrodeposited beneath the nozzle (Braun and Schwartz, 2016b). In these experiments the far-field area for oxidation was about 1,000× greater than the near-field reduction region, resulting in only a nanometer of material etched for every micron of material deposited. Controlling the initial quantity of copper charge on the substrate available for oxidation translated to self-limited patterning with the SBC, where local nickel deposition (electron acceptor) terminated upon complete etching of the copper "fuel" (electron donor). Rather than rely on metal dissolution as the bipolar counter reaction, an electrolyte-born redox couple was used to generalize electrodeposition in the SBC for a diverse range of metals (Braun and Schwartz, 2016c). Computational methods validated analytical scaling relationships approximating current flow and coupling between thermodynamics, kinetics, and transport in the SBC (Braun and Schwartz, 2016a).

Electrochemical advanced manufacturing methods have experienced a recent growth similar to traditional additive manufacturing techniques (i.e., stereolithography, fused deposition modeling, selective laser sintering, etc.) as industry shifts to more sustainable fabrication options (Braun and Schwartz, 2016d; Hirt et al., 2017). In particular, advantages of electrodeposition in additive manufacturing include improved material flexibility (capabilities include metals, alloys, semiconductors, and polymers) while achieving superior voxel resolutions, far below that of state-of-the-art two-photon stereolithography (Kawata et al., 2001). Standard scanning ion conductance microscopy (SICM) pipettes have fabricated features <500 nm in size (Momotenko et al., 2016), while electrohydrodynamic printing has shown material deposition rates on the order of 1–10 μm/s (Hirt et al., 2017). Bipolar electrochemistry with the SBC offers the unique ability to do electrodeposition-based additive manufacturing without requiring electrical connections to the workpiece. This attribute is particularly useful when fabricating on complex substrates at sub-micron lengthscales, such as in electronics manufacturing, where electrically connecting to patterned conducting and non-conducting surfaces can be challenging.

The work presented here expands upon prior experimental and computational research with the SBC. Characteristics of kinetically irreversible and reversible electrodeposition chemistries are described in more detail, including electroanalytical measurements of mixed potential systems comprised of representative bipolar couples. Patterned arrays of nickel demonstrate the challenges with parasitic reduction chemistries and the impact of bipolar additives on deposit appearance. Finite element method simulations are used to assess the impact of the far-field couple's kinetics on current efficiency, a circuit element that becomes increasingly relevant as substrate geometry and aspect ratio are constrained. Finally, simulations describe the coupling between applied current and spatiotemporal deposit stability for reversible electrolyte systems, correlating theory to experimental observations.

METHODS

Scanning Bipolar Cell

Figure 1A shows a perspective view of the key features and configuration of the electrochemical cell used to perform localized bipolar electrodeposition on electrically floating conductive substrates. Electrolyte is pumped through an electrically insulating microcapillary nozzle with a syringe pump. A platinum wire "feeder" electrode (the anode when configured to drive local reduction electrochemistry) is inserted in the microcapillary upstream of the nozzle outlet, where electrolyte jets onto the conductive substrate (bipolar electrode, or BPE). The electrolytes forms a liquid pool on the BPE, contacting a platinum "feeder" ring electrode (i.e., cathode when performing local reduction electrochemistry) attached to the acrylic housing of the microjet nozzle. The microjet nozzle dimensions and flowrates are such that considerable mass-transport is achieved, with limiting current densities exceeding 10 A/cm^2 in some cases (Nelson and Schwartz, 2005).

Figure 1B depicts the axisymmetric geometry and key features of the SBC used in finite element simulations for the case where $H = 2r_i$. The inner ($r_i = 100\,\mu m$) and outer ($r_o = 335\,\mu m$) radii and the fly-height of the nozzle above the substrate (H) tailor the ohmic drop in the annular gap between the nozzle and substrate, controlling the breakdown of ionic and electronic current pathways in the electrochemical cell. Current sourced from the upstream platinum feeder electrode (I_{app}) has two pathway options upon exiting the nozzle: (1) it can travel entirely through the electrolyte to the downstream ring feeder electrode entirely as ionic current (I_i), or, (2) it can undergo charge transfer at the substrate in the region beneath the nozzle, pass as electronic current (I_e) through the BPE, undergo a second (equal and opposite) charge transfer reaction in the far-field area, and then travel as ionic current to the feeder ring electrode. The fraction of applied current that passes through the electronic pathway (I_e) defines the bipolar current efficiency (BCE)

$$BCE = \frac{I_e}{I_{app}} \tag{1}$$

and is coupled to the ohmic drop through solution, charge transfer kinetics of the bipolar reactions, and thermodynamic relationship of the bipolar pair.

The current pathways depicted in **Figure 1B** are approximated by the equivalent circuit in **Figure 1C**. The resistance for current flow through the ionic pathway is dominated by the ohmic resistance beneath the microjet nozzle (R_{ionic}). The total resistance to current flow through the conductive substrate is the sum of the charge transfer resistances related to the kinetics of the bipolar reactions beneath the nozzle ($R_{CT,near}$) and in the far-field ($R_{CT,far}$), assuming the electrical resistance of the conductor is negligible. When the bipolar reaction pair is thermodynamically uphill (i.e., non-spontaneous), current cannot flow through the conductor until the potential drop through solution exceeds the thermodynamic potential difference of the bipolar couple (ΔE_{BC})

$$\Delta E_{BC} = E^{eq}_{red} - E^{eq}_{ox} \tag{2}$$

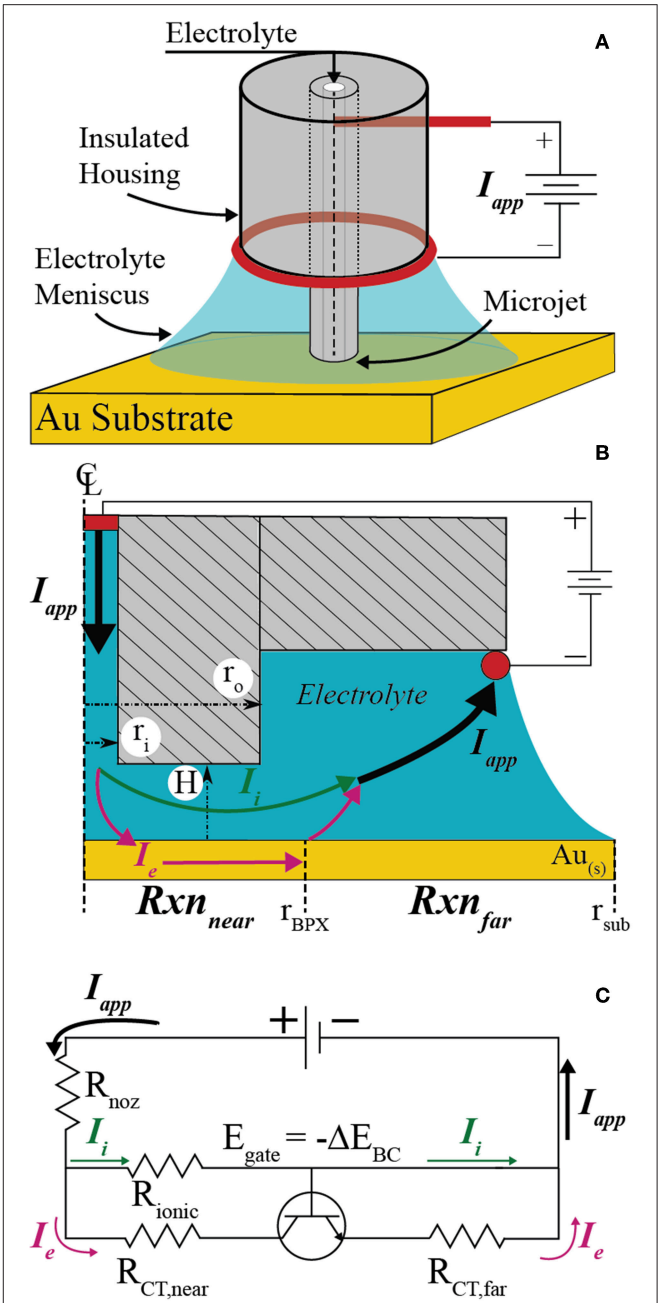

FIGURE 1 | (A) Schematic of the scanning bipolar cell (SBC) and components. **(B)** To-scale axisymmetric geometry used in finite element method simulations when $H = 2r_i$ with key features and current pathways emphasized. **(C)** Equivalent circuit approximating current flow pathways through the SBC.

where the subscripts *red* and *ox* refer to the bipolar reduction and oxidation reactions occurring on the substrate. Equation 2 effectively acts as a threshold voltage. The equivalent circuit models this as an ideal transistor having infinite resistance until the gate voltage ($E_{gate} = -\Delta E_{BC}$) is exceeded, after which the transistor has zero resistance and current flows at a rate regulated by other circuit elements. The transition between *off* and *on*

states is considered to be instantaneous. Thus, current flows entirely through the ionic pathway (*off*) until the potential drop through the annular gap ($E = I_{app}R_{ionic}$) is $> -\Delta E_{BC}$. When the potential drop exceeds E_{gate} (*on*), current may flow through the electronic branch of the parallel circuit at a rate regulated by the relationship between ohmic and kinetic resistances. Previous studies described R_{ionic-} using primary current simulations and explored the relationship between ohmic and kinetic resistance ($R_{CT,near}$) for a reversible bipolar couple (i.e., $\Delta E_{BC} = 0$) and for a thermodynamically uphill bipolar couple ($\Delta E_{BC} < 0$) (Braun and Schwartz, 2016a). In those simulations the kinetic resistances of the far-field reactions were negligible, arising from the experimental far-field region having a much larger surface area than the near-field region and thus lower current densities.

Chemicals

Unless noted otherwise, the following chemicals were used as received: $NiSO_4 \cdot 5H_2O$ (Sigma Aldrich, 99–102.0%), L-ascorbic acid (Sigma Aldrich, 99%), $CuSO_4 \cdot 5H_2O$ (Fisher Scientific, technical grade), $AgNO_3$ (Sigma Aldrich, 99.0%), $FeSO_4 \cdot 7H_2O$ (Sigma Aldrich, 98%), $Fe_2(SO_4)_3 \cdot 5H_2O$ (Sigma Aldrich, 97%), K_2SO_4 (Alfa Aesar, 98.0%), concentrated HNO_3 (Fisher Scientific, certified ACS plus), and concentrated $H\text{-}_2SO_4$ (Mallinckrodt Chemicals, 95–98%). All aqueous electrolytes were prepared with high purity deionized (DI) water.

Bipolar Plating Electrolyte

Local bipolar electrodeposition in the SBC is experimentally demonstrated for two characteristic systems: kinetically irreversible (Ni) and kinetically reversible (Cu or Ag) electrodeposition chemistries. Prior work outlined the electrolyte design guidelines necessary to achieve both spatially and temporally stable deposits using the SBC for these bipolar systems (Braun and Schwartz, 2016c). Specifically, kinetically irreversible electrodeposition chemistries can be paired with any bipolar oxidation chemistry resulting in $\Delta E_{BC} < 0$, whereas kinetically reversible electrodeposition chemistries must be paired with a bipolar oxidation reaction that produces a marginally downhill thermodynamic relationship (i.e., $\Delta E_{BC} > 0$). These metastable formulations for reversible bipolar systems are similar to electroless deposition systems, except with only a 10–50 mV of downhill driving force. This results in a thermodynamic buffer for the desired oxidation chemistry to occur at lower overpotentials than metal etching, as the rastering of the SBC nozzle exposes previously deposited metal to electrochemically oxidizing conditions. Because irreversible deposition systems are kinetically passivated against dissolution, a wider range of bipolar oxidation couples can be utilized.

For kinetically irreversible nickel electrodeposition, ascorbic acid (AA) oxidation forming dehydroascorbic acid (DHAA) and protons is the bipolar counter reaction

$$\begin{aligned} Near: &\quad Ni^{2+} + 2e^- \rightarrow Ni_{(s)}, \quad E^{eq}_{near} = -0.29V \\ Far: &\quad AA \rightarrow DHAA + 2H^+ + 2e^-, \; E^{eq}_{far} = 0.30\ V \quad \text{[Scheme 1]} \\ Net: &\quad Ni^{2+} + AA \rightarrow Ni_{(s)} + DHAA + 2H^+, \; \Delta E_{BC} = -0.59V \end{aligned}$$

producing a stable electrolyte with a negative ΔE_{BC} in 0.1 mol/L $NiSO_4$ + 0.01 mol/L ascorbic acid (pH = 2.9). Equilibrium potentials are calculated by the Nernst equation using the above reactant concentrations. All potentials reported are referenced to the standard hydrogen electrode (SHE) unless otherwise noted. Formation of a passivating oxide layer protects nickel from bulk electrooxidation during SBC operation, allowing design of thermodynamically uphill electrolytes that require applied current to drive the bipolar reaction sequence in Scheme 1.

For kinetically reversible copper electrodeposition, ascorbic acid (AA) oxidation is also selected as the bipolar counter reaction:

$$\begin{aligned} Near: &\quad Cu^{2+} + 2e^- \rightarrow Cu_{(s)}, \quad E^{eq}_{near} = 0.30\ V \\ Far: &\quad AA \rightarrow DHAA + 2H^+ + 2e^-, \; E^{eq}_{far} = 0.29\ V \quad \text{[Scheme 2]} \\ Net: &\quad Cu^{2+} + AA \rightarrow Cu_{(s)} + DHAA + 2H^+, \; \Delta E_{BC} = +0.01V \end{aligned}$$

The above estimated equilibrium reduction potentials for 0.05 mol/L $CuSO_4$ + 0.005 mol/L ascorbic acid (pH = 2.6) produce a metastable electrolyte with a marginally positive ΔE_{BC}. This downhill thermodynamic driving force provides protection for previously deposited copper but is not sufficient to drive heterogeneous deposition, let alone overcome the nucleation barrier for homogenous reduction of cupric ions in solution.

For kinetically reversible silver electrodeposition, ferrous (Fe^{2+}) ion oxidation to ferric (Fe^{3+}) ion acts as the bipolar counter reaction:

$$\begin{aligned} Near: &\quad Ag^+ + e^- \rightarrow Ag_{(s)}, \quad E^{eq}_{near} = 0.67V \\ Far: &\quad Fe^{2+} \rightarrow Fe^{3+} + e^-, \quad E^{eq}_{far} = 0.63\ V \quad \text{[Scheme 3]} \\ Net: &\quad Ag^+ + Fe^{2+} \rightarrow Ag_{(s)} + Fe^{3+}, \quad \Delta E_{BC} = +0.04V \end{aligned}$$

The equilibrium potentials above are estimated from open circuit potential measurements in a solution containing 0.01 mol/L $AgNO_3$ + 0.1 mol/L K_2SO_4 and a solution containing 0.01 mol/L $FeSO_4$ + 0.005 mol/L $Fe_2(SO_4)_3$ + 0.1 mol/L K_2SO_4. Measured open circuit potentials varied slightly, falling between 0.67 and 0.68 V for $Ag(I)/Ag_{(s)}$ and between 0.63 and 0.66 V for Fe(III)/Fe(II). Similar to Scheme 2, this $\approx +40$ mV downhill driving force is less than the nucleation overpotential for homogeneous reduction of silver, providing a thermodynamic window for Fe^{2+} oxidation to occur before electrochemical silver dissolution in bipolar experiments. However, long-term stability (>1 day) of this electrolyte has not been evaluated. As noted previously (Braun and Schwartz, 2016c), inclusion of both ferrous sulfate and ferric sulfate in the electrolyte is required to tailor the equilibrium potential. As a result, Fe^{3+} reduction to Fe^{2+} competes with the desired silver electrodeposition beneath the nozzle, reducing the overall faradaic efficiency of the bipolar system.

Bipolar Electrode Substrate Preparation

All electrodeposition experiments were performed on gold substrates. Silicon wafers with 50 nm gold on a 5 nm titanium

adhesion layer were prepared using an E-beam evaporator at the University of Washington Nanofabrication Facility. Prior to bipolar experiments, the gold substrates were cleaned via 20 cyclic voltammetry sweeps at 50 mV s^{-1} from −0.25 to 1.5 V vs. SCE in a 1 mol/L H_2SO_4 solution with a Pine Model AFRDE5 Bipotentiostat. Clean gold substrates were then rinsed with deionized (DI) water and dried with N_2 gas. Substrates were masked to make a circular exposed area of 0.45 cm^2. For the electrolytes flow rates and small number of printed features used here, the meniscus was pinned on the SBC feeder cathode/outer nozzle housing. As the droplet of pooled electrolyte grew during liquid injection, it drained over the much larger masked substrate. All electrodeposition steps were carried out at room temperature.

Electroanalytical Measurements

Cyclic voltammetry (CV) was performed on a Biologic model VSP potentiostat with a platinum wire counter electrode and saturated mercury sulfate (SSE) reference electrode. All potentials have been referenced to the SHE unless otherwise noted. A gold Pine rotating disk electrode (RDE) with a 0.5 cm diameter was used for all RDE experiments. Between experiments involving nickel, the Au RDE was polished with 4000 grit SiC and rinsed in deionized water. Between experiments involving silver or copper, the Au RDE was rinsed in 1 mol/L HNO_3 and subsequently rinsed in deionized water.

Cyclic voltammetry exploring nickel deposition in Scheme 1 used 0.1 mol/L $NiSO_4$ while varying ascorbic acid concentration from 0 to 0.2 mol/L. Potential sweeps were done at 20 mV/s beginning at −0.4 V vs. SSE, sweeping to −1.6 V vs. SSE, and then to 0.5 V vs. SSE for 5 cycles without rotation. The 1st cycle for each concentration was selected for comparison. Cyclic voltammetry exploring silver deposition in Scheme 3 compared three solutions: (1) 0.01 mol/L $FeSO_4$ + 0.005 mol/L $Fe_2(SO_4)_3$ + 0.1 mol/L K_2SO_4, (2) 0.01 mol/L $AgNO_3$ + 0.1 mol/L K_2SO_4, and (3) 0.01 mol/L $AgNO_3$ + 0.01 mol/L $FeSO_4$ + 0.005 mol/L $Fe_2(SO_4)_3$ + 0.1 mol/L K_2SO_4. Potential sweeps were done at 20 mV/s beginning at 0.1 V vs. SSE, sweeping to −0.2 V vs. SSE, and then to 0.4 V vs. SSE for 10 cycles while rotating at 0 RPM or 100 RPM (1 RPM = 0.105 rad/s). The potential limits for CV of solution (1) containing only iron components varied slightly, by beginning at 0 V vs. SSE and sweeping negative to −0.3 V. Cycles 2–10 were selected for comparison of electrolyte components from Scheme 3.

Linear sweep voltammetry (LSV) on 25 μm diameter Au microlectrodes (UMEs) was also used to evaluate the nickel deposition system. Prior to voltammetric measurements, the Au UMEs were polished on 4000 grit SiC, rinsed in deionized water, rinsed in 1 mol/L HNO_3, and rinsed again in deionized water. The same nickel electrolyte used in RDE measurements was also used on UMEs. Voltammetry in electrolytes without nickel in solution used 0.1 mol/L K_2SO_4 as supporting salt. Potential sweeps were done at 20 mV/s beginning at −0.4 V vs. SSE and sweeping to −1.9 V vs. SSE. Voltammetry on microelectrodes exploring the impact of pH in the absence of ascorbic acid used electrolytes with 0.1 mol/L $NiSO_4$ and dosed in H_2SO_4 to vary pH.

Characterization Tools

An Olympus BX51 optical microscope with an Olympus QColor3 digital camera using 5.0x objectives was used to take optical micrographs of each sample. Coarse and grainy silver deposits were visibly metallic, however, appeared dark in coloration when imaged with bright-field on the optical microscope. Therefore, silver optical micrographs were acquired using dark-field imaging. An Oakton model no. 510 pH/conductivity meter was used to measure pH.

Computational Methods

Finite element method computations were performed in the axisymmetric 2D computational domain shown in **Figure 1B** to assess the current flow pathways in the SBC. All simulations use a microjet nozzle with dimensions of $r_i = 100\,\mu m$ and $r_o = 335\,\mu m$, consistent with experiments, unless otherwise noted. Details on the computational methods, including relevant equations and boundary conditions, may be found in the **Appendix**.

Simulations for near-field copper reduction on a gold substrate with ascorbic acid as the far-field bipolar counter reaction in Scheme 2 were used to explore electrochemical behavior for a kinetically reversible bipolar electrodeposition reaction. The $Cu^{2+}/Cu_{(s)}$ redox couple is kinetically reversible, using kinetic parameters taken from literature (Mattsson and Bockris, 1959): $i_{o,Cu} = 33.5$ A/m^2, $\alpha_{a,Cu} = 0.73$, and $n = 2$. The ascorbic acid redox couple is also kinetically reversible, however, only trace amounts of dehydroascorbic acid are present in solution. We deal with this uncontrolled, trace dehydroascorbic acid in a manner that is easy to implement, produces results that are consistent with experimental measurables (such as open-circuit potential, threshold voltages/currents, etc.), and whose magnitude (within reasonable bounds) has negligible influence on the computational results we report. Specifically, for the electrode boundary conditions (**Appendix**), we use the Butler-Volmer form with $f_{AA} = 1$ for the oxidation branch and set a small limiting current for dehydroascorbic acid reduction ($i_L = i_{o,AA}$) with $g_{AA} = (1\text{-}i/i_{o,AA-})$. Kinetic parameters for ascorbic acid are taken from literature (Tanaka and Tamamushi, 1964): $i_{o,AA} = 10.2$ A/m^2, $\alpha_{a,AA} = 0.20$, and $n = 2$.

Simulations exploring the impact of substrate area on BCE assume irreversible deposition beneath the nozzle, employing Tafel kinetics for reduction and using a $\Delta E_{BC} = -0.1$ V. The generic far-field oxidation chemistry is assumed to have kinetics similar to that of ascorbic acid. Kinetic parameters for the irreversible reduction chemistry are: $i_{o,near} = 10$ A/m^2, $\alpha_{near} = 0.50$, and $n = 2$. Kinetic parameters for the oxidation bipolar couple are: $i_{o,far} = 1$ A/m^2 or 10 A/m^2, $\alpha_{far} = 0.50$, and $n = 2$. Parameters are varied to explore how factors such as nozzle dimensions, electrochemical cell configuration, and oxidation kinetics impact the BCE as substrate area (A_{subs}) is constrained. **Table 1** presents the parameter combinations used in simulations. The distance of the feeder cathode from nozzle center is $r_{cathode}$.

Mesh refinement in the regions of high potential gradient was used so that the overall charge balance and the substrate integral on the bipolar electrode both converged to <0.01%

TABLE 1 | Parameters varied in simulations exploring the impact of substrate area on current flow in the SBC and bipolar current efficiency (BCE) values at select ratios of substrate area to nozzle area.

	$i_{-0,far}$ (A m^{-2})	r_i (μm)	r_o (μm)	$r_{cathode}$ (mm)	*BCE* at maximum	*BCE at* $A_{Subs}/A_{noz} = 4$	*BCE at* $A_{Subs}/A_{noz} = 1.44$
Parameter set 1	10	100	335	2	0.921	0.686	0.200
Parameter set 2	1	100	335	2	0.901	0.641	0.142
Parameter set 3	10	200	670	2	0.957	0.756	0.243
Parameter set 4	10	100	335	8	0.951	0.686	0.200
Parameter set 5	10	100	670	2	0.975	0.686	0.200
Parameter set 6	10	50	335	2	0.946	0.611	0.161

TABLE 2 | Parameters used in computational models exploring bipolar copper deposition (Scheme 2) and a generic irreversible reduction chemistry used to assess the impact of substrate area on current flow in the SBC.

PARAMETERS FOR BIPOLAR CU REDUCTION AND AA OXIDATION SIMULATIONS		
$i_{o,Cu}$	33.5 A/m^2	Exchange current density for copper redox couple
$i_{o,AA}$	10.2 A/m^2	Exchange current density for ascorbic acid redox couple
$\alpha_{a,Cu}$	0.73	Transfer coefficient for copper redox couple
$\alpha_{a,AA}$	0.2	Transfer coefficient for ascorbic acid redox couple
E_{Cu}^{eq}	0.30 V	Equilibrium potential for copper redox couple
E_{Cu}^{eq}	0.29 V	Equilibrium potential for ascorbic acid redox couple
H	15 μm	Fly-height of nozzle
I_{app}	20 or 200 μA	Applied current to cell
κ	1 S/m	Conductivity of electrolyte
PARAMETERS FOR SIMULATIONS ON IMPACT OF SUBSTRATE AREA		
$i_{o,near}$	10 A/m^2	Exchange current density for local redox couple
$i_{o,far}$	1 or 10 A/m^2	Exchange current density for far-field redox couple
$\alpha_{a,near}$	0.5	Transfer coefficient for local redox couple
$\alpha_{a,far}$	0.5	Transfer coefficient for far-field redox couple
ΔE_{BC}	−0.1 V	Equilibrium potential difference of bipolar redox pairs
H	10 μm	Fly-height of nozzle
I_{app}	100 μA	Applied current to cell
κ	1 S/m	Conductivity of electrolyte

error. This resulted in about 200,000 to 500,000 mesh elements and computation times ranging from 1 to 10 min for a typical converged solution. All simulations were performed on a Dell Optiplex 980 desktop computer with an Intel Core i5 CPU@ 3.20 GHz and 8 GB RAM using Windows 7 Enterprise 64-bit operating system. FEM simulations employed the secondary current distribution module in COMSOL version 5.3.

RESULTS AND DISCUSSION

Bipolar electrochemical systems require careful mating of the thermodynamics and kinetics of the bipolar reaction couple, a result of the potential-induced bifurcation of the substrate into separated reduction and oxidation regions. In the case of a rastering electrode (i.e., SBC microjet nozzle), the local reduction and oxidation regions move with the nozzle, exposing previously deposited material (in cathodic regions) to anodic environments capable of etching the material. How the deposited material responds to the oxidizing environment depends on whether it is passive or active at the potentials of the oxidizing region.

Figure 2a shows an optical micrograph of an array of nickel material electrodeposited with the SBC in a 0.1 mol/L $NiSO_4$ + 0.2 mol/L ascorbic acid electrolyte ($\Delta E_{BC} = -0.59$ V). Each deposit in the 7×7 array is grown at $I_{app} = 900$ μA, $Q = 4{,}500$ μC, and $H = 18$ μm. Deposit spacing is 400 μm and electrolyte flowrate is 400 μL/min. The same spacing and flowrate are used for all experiments unless otherwise noted. Individual deposits in the array appear optically identical, as they were deposited at the same conditions. Despite nickel oxidation being thermodynamically preferential to ascorbic acid oxidation ($E_{Ni}^{eq} = -0.29$ V and $E_{AA}^{eq} = 0.30$ V), formation of a thin passivating oxide layer after deposition kinetically prevents electrochemical etching of the material as the SBC moves across the substrate and the deposits experience an oxidizing potential.

Several metal deposition systems do not have the irreversibility characteristic of nickel passivation, and can dissolve in anodic environments. For example, **Figure 2b** shows an optical micrograph of an array of silver deposits, a kinetically reversible deposition chemistry, where most of the deposited material has etched from the substrate. The electrolyte contains only 0.05 mol/L $AgNO_3$ with the bipolar counter reaction being water oxidation

$$Far: \quad 2H_2O \rightarrow O_{2(g)} + 4H^+ 4e^-, \quad E_{far}^{eq} \approx 1.02\ V \qquad (3)$$

resulting in a bipolar couple with a $\Delta E_{BC} = -0.30$ V. Each deposit in this 7×7 array was grown at $I_{app} = 50$ μA, $Q = 250$ μC and $H = 30$ μm. Like nickel in **Figure 2a**, silver oxidation is thermodynamically preferential to water oxidation ($E_{Ag}^{eq} = 0.72$ V and $E_{H2O}^{eq} = 1.02$ V). In contrast to nickel, oxidation of silver is kinetically active and will electrochemically etch when exposed to anodic potentials in the far-field during SBC operation. The result is an array where the material deposited earliest, and exposed to

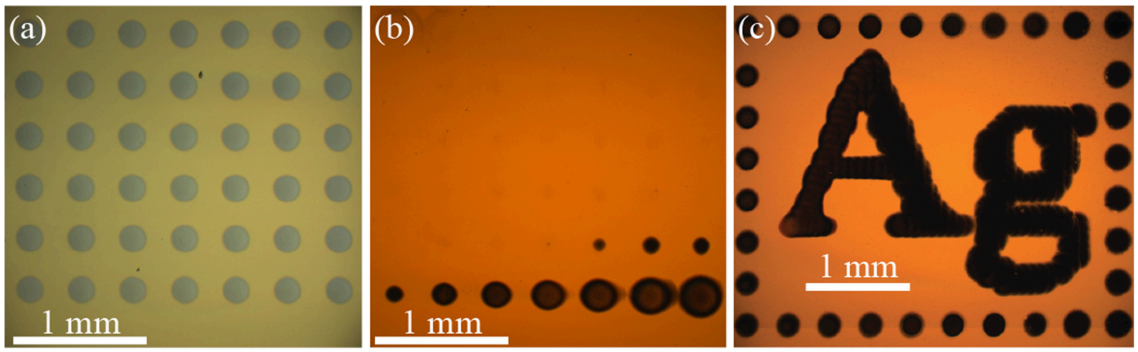

FIGURE 2 | Optical micrographs of metal patterns deposited from a SBC with a 200 μm ID nozzle at 400 μL/min flowrate. **(a)** A 7 × 7 array of nickel grown in 0.1 mol/L $NiSO_4$ + 0.2 mol/L ascorbic acid at 900 μA with 4,500 μC per deposit, a nozzle fly-height of 18 μm, and 400 μm deposit spacing. **(b)** A 7×7 array of silver grown in 0.05 mol/L AgNO-$_3$ at 50 μA with 250 μC per deposit, a nozzle fly-height of 30 μm, and 400 μm deposit spacing. **(c)** Pattern consisting of 282 individual silver deposits grown in 0.01 mol/L $AgNO_3$ + 0.01 mol/L $FeSO_4$ + 0.005 mol/L $Fe_2(SO_4)_3$ at 15 μA with 30 μC per deposit, a nozzle fly-height of 30 μm, and 75 μm deposit spacing.

oxidation longest, has been fully removed from the substrate (the SBC scanned from left to right, top to bottom in the **Figure 2** experiments). History of silver etching is evident in the systematic decrease of deposit size over the final 10 deposits. In stationary bipolar electrochemical systems separation of the cathodic and anodic regions remain fixed, providing inherent stability for electrodeposited metals. With the SBC, moving anodic and cathodic regions during patterning requires temporal deposit stability to be linked to the thermodynamics of the bipolar pair.

As described in the experimental methods section, temporal deposit stability of kinetically reversible materials systems can be achieved by selecting a bipolar counter reaction producing a marginally positive ΔE_{BC}. **Figure 2c** shows an optical micrograph of a silver pattern containing 282 individual silver deposits on a gold substrate that is stable over 20 min during fabrication [adapted from (Braun and Schwartz, 2016c)]. The bipolar counter reaction is oxidation of ferrous ion (Fe^{2+}) to ferric ion (Fe^{3+}) by Scheme 3 in an electrolyte containing 0.01 mol/L $AgNO_3$ + 0.01 mol/L $FeSO_4$ + 0.005 mol/L $Fe_2(SO_4)_3$. Each deposit is grown at $I_{app} = 15$ μA, $Q = 30$ μC and $H = 30$ μm. Deposit spacing is 75 μm. In contrast to **Figure 2b**, Fe^{2+} oxidation is thermodynamically preferential to Ag^+ oxidation ($E^{eq}_{Ag} = 0.67$ V and $E^{eq}_{Fe(II)} = 0.63$ V). The downhill thermodynamics ($\Delta E_{BC} = +40$ mV) of this bipolar couple protects silver from electrochemical dissolution, but is modest enough to prevent spontaneous reduction of silver in solution. In both types of kinetic systems applied current drives local deposition on the substrate. For silver, only a small amount of current (15 μA in **Figure 2c**) is needed to drive heterogeneous nucleation on the substrate. Nickel requires a much larger applied current (900 μA in **Figure 2a**) to overcome the thermodynamic barrier and drive the bipolar reactions. The applied current for driving nickel deposition could be reduced by selecting a bipolar counter reaction producing a less negative ΔE_{BC}. In the following sections, electrolyte design attributes for characteristic irreversible and reversible bipolar electrodeposition systems will be discussed in more detail.

Irreversible Materials Systems

A wide range of redox couples for the bipolar counter reaction are available for local electrodeposition of kinetically irreversible material systems in the SBC. Essentially, any redox couple with an equilibrium potential more positive than that of the metal ion reduction chemistry can be utilized, with the consequence that bipolar couples with more negative values of ΔE_{BC} require more applied current to drive both reactions. Selecting an appropriate bipolar counter reactant also requires consideration of that constituent's impact on the characteristics of the electrodeposited metal and the reaction itself. Solution additives can affect electrodeposition in several ways, including: significantly altering deposit morphology; metal ion chelation, which changes the reversible potential of metal deposition; and controlling the pH, which can impact the stability of the metal phase in solution and influence secondary parasitic reactions (Schlesinger, 2010). Thus, it is important to consider how the ascorbic acid additive serving as the bipolar counter reactant affects electrodeposition of nickel beyond bipolar behavior. **Figure 3** shows a series of optical micrographs depicting 10×10 nickel arrays in 0.1 mol/L $NiSO_4$ at varying ascorbic acid concentrations. In each array, the applied current (I_{app}) is varied from 100 to 800 μA (the lowest 3 columns not shown have no nickel deposited) and nozzle fly-height (H) is varied from 9 μm to 36 μm. Each deposit was grown using a 5 s dwell time. The ohmic resistance beneath the nozzle (R_{ionic}) and near-field charge transfer resistance ($R_{CT,near}$) depicted in **Figure 1C** dictate current flow in the SBC. Prior simulations (Braun and Schwartz, 2016a) of the primary current distribution in the SBC show that $R\text{-}_{ionic}$ is related to the electrolyte conductivity (κ) and nozzle geometry by

$$R_{ionic} = \frac{1}{4\kappa r_i}\left(1 - \frac{2}{\pi\sqrt{1 + 0.16\left(\frac{H}{r_i}\right)^2}}\right) + \frac{Ln\left(\frac{r_o}{r_i}\right)}{2\pi\kappa H}. \quad (4)$$

As fly-height is increased, the ionic resistance defined by Equation 4 decreases, and less of the applied current follows

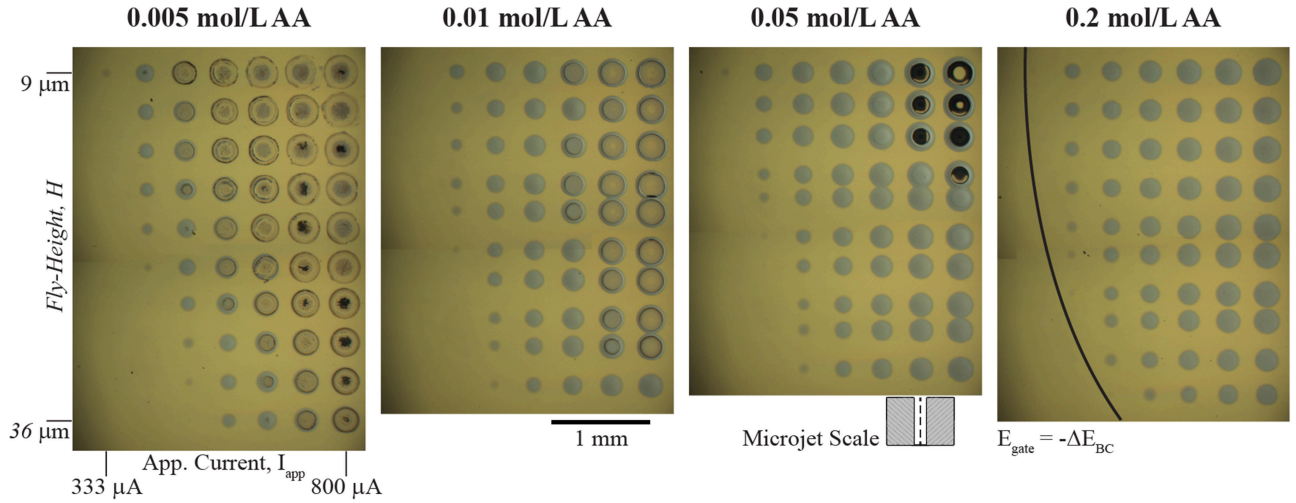

FIGURE 3 | Optical micrographs of arrays of nickel deposits in 0.1 mol/L $NiSO_4$ at the indicated ascorbic acid concentrations. 10×10 arrays of nickel deposits vary applied current (I_{app}) from 100 to 800 μA (lowest 3 columns not shown) and nozzle fly-height (H) from 9 to 36 μm. Each deposit has a 5 s dwell time. A 200 μm ID nozzle at 400 μL/min electrolyte flowrate and deposit spacing of 400 μm was used for each experiment. Certain rows in the 0.01, 0.05, and 0.2 mol/L ascorbic acid arrays are more closely spaced than others due to a misstep in the y-axis motor during movement. The schematic of the microjet nozzle is provided for scale. The black line in the 0.2 mol/L array indicates the threshold potential (ΔE_{BC}) to drive bipolar nickel deposition and ascorbic acid oxidation.

the bipolar pathway resulting in smaller nickel deposits in the **Figure 3** arrays. Secondary current distribution simulations (Braun and Schwartz, 2016a) for nickel indicated that the kinetic resistance of the local reaction at high overpotentials beneath the nozzle scales by

$$R_{CT,near} = \frac{RT}{\left(I_{app} - I_{\min}\right)\alpha_j n_j F} \tag{5}$$

I_{min} is the minimum current required to polarize the substrate sufficiently (i.e., exceed $-\Delta E_{BC}$) that drives both nickel reduction beneath the nozzle and ascorbic acid across the far-field. The portion of the arrays without nickel deposits have yet to exceed the threshold substrate polarization. Once the minimum current for $-\Delta E_{BC}$ has been exceeded, additional applied current beyond I_{min} can participate in bipolar nickel deposition. Increasing applied current reduces the kinetic resistance by Equation 5, driving more current through the bipolar pathway resulting in larger nickel deposits. Of course, larger deposits at higher currents are also partially due to an increase in total charge passed during the 5 s dwell time of each deposit.

Before the kinetic pathway is activated (i.e., substrate polarization exceeds $-\Delta E_{BC}$) all of the applied current passes through the ionic pathway and the potential drop through the gap (E) follows

$$E = I_{app} R_{ionic.} \tag{6}$$

Once E exceeds $-\Delta E_{BC}$, current can flow through the bipolar electrode via charge transfer reactions and nickel deposits appear on the substrate. The deposits appearing at the lowest current for each fly-height (where $E \approx -E_{BC}$) can be used to estimate R_{ionic}. For example, in the 333 μA column of the 0.05 mol/L AA solution the faintest trace of nickel material is visible at a fly-height of 15 μm. With a ΔE_{BC} of −0.56 V, Equation 6 gives an estimation for R_{ionic} as 1,680 Ω. Similarly, the faintest deposit in the I_{app} column of 411 μA appears at $H = 27$ μm, giving a value for R_{ionic} of 1,360 Ω. However, estimations for R_{ionic} using the analytical expression in Equation 4 for these fly-heights are 14,000 Ω and 8,200 Ω, respectively. This large deviation from theoretical expectation likely reflects the non-idealized geometry in the experimental microjet nozzles, which have rounded edges and asymmetries as a result of hand-polishing of the glass capillaries. However, the expected qualitative trends are reproduced in the **Figure 3** arrays.

A section of the nickel arrays in **Figure 3** show crater-like deposits at the conditions of highest applied current and lowest fly-height. The quantity of these features decreases with increasing ascorbic acid concentration, suggesting they are related to the ascorbic acid reactant. Since the craters appear at conditions of greatest substrate polarization (high I_{app} and low H), they are most likely caused by a secondary reduction reaction occurring at potentials more negative than nickel deposition. Deposition of iron group metals (Ni, Co, Fe) from aqueous electrolytes is often accompanied by proton and water reduction reactions

$$2H^+ + 2e^- \rightarrow H_2 \tag{7}$$

$$2H_2O + 2e^- \rightarrow H_2 + OH^-. \tag{8}$$

Ascorbic acid is a weak acid with two protons (pK_a values of 4.2 and 11.6) and concentration changes affect the solution pH. The measured pH values of the solutions used in **Figure 3** are 3.4, 3.3, 2.9, and 2.6 by increasing ascorbic acid concentration. Thus, onset potentials for both proton reduction and water

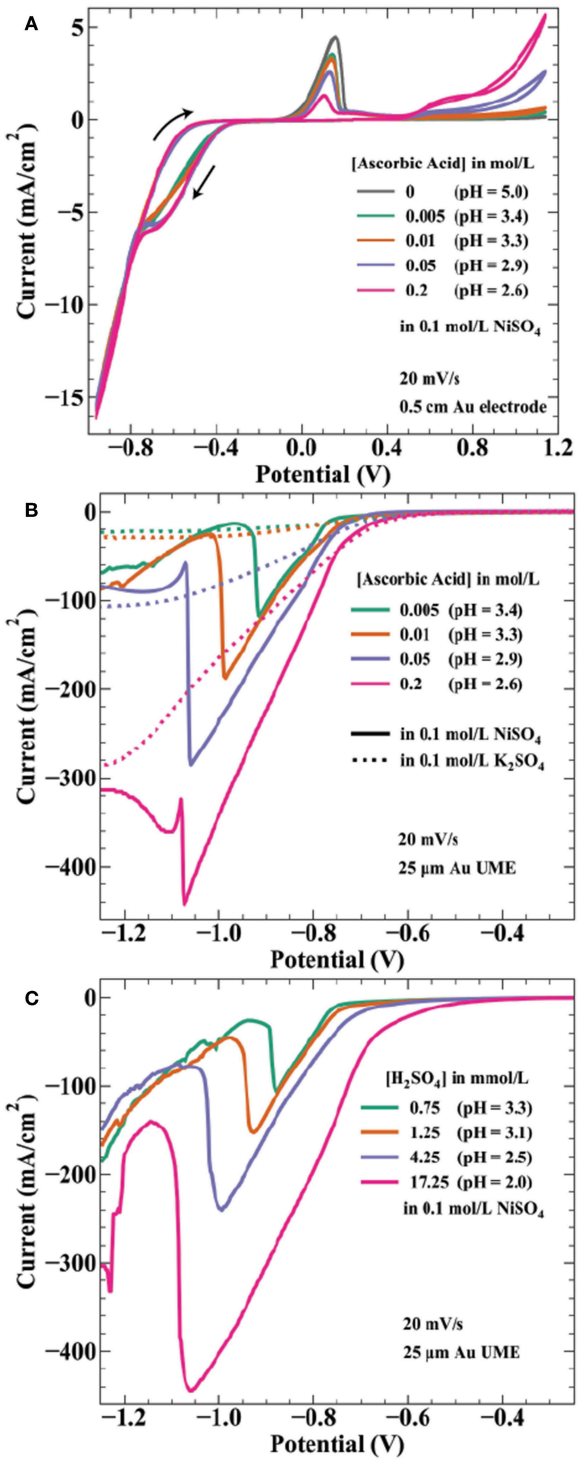

FIGURE 4 | Voltammetric measurements of nickel deposition in ascorbic acid and sulfuric acid containing electrolytes. **(A)** Cyclic voltammetry at 20 mV/s on a 0.5 cm diameter Au electrode in 0.1 mol/L $NiSO_4$ and the indicated ascorbic acid concentrations. Voltammograms initiated at 0.24 V, swept negative to −0.96 V, positive to 1.14 V, ending at 0.24 V. Linear sweep voltammetry at 20 mV/s from 0.24 to −1.26 V on a 25 µm diameter Au microelectrode for **(B)** the indicated ascorbic acid concentrations in 0.1 mol/L $NiSO_4$ (——) or 0.1 mol/L K_2SO_4 (....) and for **(C)** the indicated H_2SO_4 concentrations in 0.1 mol/L $NiSO_4$. pH values are indicated for each solution.

reduction will vary between each array. **Figure 4A** shows cyclic voltammetry of the electrolytes used in **Figure 3** experiments. As potential is swept negative, current is first observed around −0.26 V. The onset potential for this wave (taken at a current density of −0.1 mA/cm^2) shifts from −0.25 to −0.28 V as ascorbic acid increases from 0.005 to 0.2 mol/L. This potential range is in agreement with estimations by the Nernst equation for proton reduction of −0.15 to −0.20 V for pH = 3.3–2.6 solutions, with additional overpotential likely due to sluggish kinetics of proton reduction on gold (Norskov et al., 2005).

The estimated Nernst potential for Ni^{2+} reduction of −0.28 V suggests that nickel deposits concurrently with proton reduction at potentials negative of this value. Near −0.75 V, the individual curves from each concentration merge to the same path, possibly indicating a shift to current dominated by nickel deposition. The CV shows hysteresis on the return sweep between −0.8 and −0.4 V, likely a result of the 20 mV/s scan rate. As the potential sweeps positive the characteristic nickel passivation behavior is observed: increasing anodic current due to nickel dissolution followed by a sharp decrease in current resulting from formation of a passive hydroxide layer and subsequent thin oxide (Smith et al., 1987; Scherer et al., 2003). The onset of nickel dissolution (taken at a current density of 0.1 mA/cm^2) shifts more positive with increasing ascorbic acid concentration (and proton reduction), occurring at −0.054 V for 0.005 mol/L AA and −0.006 V for 0.2 mol/L AA. This positive 48 mV shift correlates well with the 59 mV/pH unit (47 mV from pH = 3.4 to pH = 2.6) expected for electrochemical formation of NiO (Sato and Okamoto, 1963). Interestingly, the presence of additional ascorbic acid results in decreased peak current prior to metal passivation. This effect is counter to the expectation of a decrease in pH, which should make formation of a passivating hydroxide layer more difficult. At still higher potentials, ascorbic acid oxidation to dehydroascorbic acid and protons initiates around 0.4 V with higher current densities achieved for more concentrated AA solutions. This onset potential is consistent with literature values of the reversible potential of ascorbic acid in this pH range (Borsook and Keighley, 1933).

Due to the high convective transport of the jetted electrolyte, current densities achieved in the SBC can often exceed 100 mA/cm^2. For example, at a fly-height of 15 µm with an I_{min} of 333 µA, the total current available for nickel reduction at I_{app} = 566 µA is 233 µA. In reality, a portion of this current passes through the ionic pathway (**Figure 1C**) as shunt current. Even assuming a BCE of 50%, the current density at this condition (scaled by the deposit area with a diameter = 250 µm) is 237 mA/cm^2. As a result, voltammetry using microelectrodes was utilized to better connect electroanalytical measurements to transport conditions and lengthscales relevant to SBC operation. Linear sweep voltammetry (LSV) on a 25 µm gold microelectrode (UME) seen in **Figure 4B** was further used to probe the potential regime where proton and water reduction compete with nickel deposition. Potential is swept from −0.4 to −1.9 V at 20 mV/s. Ascorbic acid variation in 0.1 mol/L K_2SO_4 (dashed lines) shows proton reduction followed by water reduction in the absence of nickel deposition. Similar to CVs in **Figure 4A**, current from proton reduction initiates prior to nickel

deposition. For example, in 0.2 mol/L ascorbic acid + 0.1 mol/L $NiSO_4$ current in the voltammogram begins to deviate from the nickel free electrolyte at about −0.75 V, indicating the onset of nickel reduction at a more negative potential. This ≈ 450 mV overpotential ($E_{Ni}^{eq} = -0.28$ V) before nickel reduction current is observed is due to a combination of nucleation overpotential and nickel reduction having very slow kinetics (Tanaka and Tamamushi, 1964). A decrease in the faradaic efficiency for nickel deposition is observed with additional proton in solution; estimations at −0.86 V being 76, 74, 55, and 46% with increasing ascorbic acid concentration.

A previous hypothesis for the craters depicted in **Figure 3** was coevolution of hydrogen gas bubbles disrupting nickel nucleation on the gold bipolar electrode (Braun and Schwartz, 2016c). This now seems unlikely, as the voltammetry shows proton reduction occurs at potentials more positive than that of nickel deposition. At potentials more negative than nickel reduction, significant hydroxide generation from water reduction can cause metal-hydroxide phases to form in the deposit. To counter this, buffered electrolytes are often employed to combat local pH changes near the electrode interface (Ji et al., 1995; Zech and Landolt, 2000). As potential is swept further negative in **Figure 4B**, a sharp decrease in current is observed for the nickel-containing electrolytes. A previous study on deposition of Ni, Co, and Fe from an aqueous solution demonstrated quenching of metal film growth concurrently with the onset of OH^- generation by water reduction, producing a hydroxylated surface (i.e., $Ni(OH)_x^{2-x}$) that blocks subsequent metal deposition (Wang et al., 2016). The sharp decrease in current observed in **Figure 4B** is similarly attributed to formation of a nickel hydroxide surface phase at the onset of water reduction, terminating nickel deposition. This voltammetric feature shifts to more negative potentials as ascorbic acid (and proton) concentration increases, by ≈ 200 mV/pH unit over the range explored. The Nernst potential shift by pH is greater than expected for water reduction, 59 mV/pH unit, suggesting ascorbic acid also has buffering qualities similar to boric acid. Indeed, voltammetry in ascorbic acid free electrolyte when pH is controlled by additions of sulfuric acid (**Figure 4C**) shows a potential shift of the spike by only 122 mV/pH. This value is comparable to a similar study observing a voltammetric spike attributed to OH^- generation by Equation 8, reporting a 110 mV/pH unit shift of the voltammetric feature (Ritzert and Moffat, 2016). Both potential shifts of the spike exceed that expected by thermodynamics for the 2 electron water reduction reaction, possibly indicating a more complicated mechanism for formation of the nickel hydroxide surface species than simply

$$Ni^{2+} + xOH^- \rightarrow Ni(OH)_x^{2-x} \tag{9}$$

where hydroxide is primarily produced by water reduction.

The electroanalytical measurements in **Figure 4** help clarify the formation of crater-like deposits observed in **Figure 3**. At sufficiently negative cathodic overpotentials (i.e., high I_{app} and low H), water reduction occurs subsequently with nickel deposition, producing OH^- and causing nickel deposition to terminate due to formation of a nickel hydroxide surface phase. The local solution potential is at a minimum (most reducing) directly beneath the nozzle, increasing in potential (less reducing) radially from the nozzle center in a gaussian-like profile. As a result, the craters are composed of a thin nickel hydroxide surface phase in the high overpotential region beneath the center of the nozzle, with subsequent passed charge only manifesting in water reduction. Further from the nozzle center, reduction of Ni^{2+} at more positive potentials forms a ring of thicker nickel metal. The black material in a few of the crater-like deposits is likely residue from bulk $Ni(OH)_2$ precipitation after sustained OH^- generation during water reduction. **Figure 4B** indicated that the overpotential necessary to drive OH^- generation is greater for higher ascorbic acid concentration due to its buffering qualities as well as a decrease in pH. Thus, fewer crater-like deposits appear in **Figure 3** for higher ascorbic acid concentrations.

All prior experimental systems using the SBC have been designed such that the total charge transfer resistance of the far-field oxidation chemistry is negligible relative to that of the near-field reduction reaction, a result of the much larger area of the far-field region. Factors influencing the kinetic resistances in the equivalent circuit in **Figure 1C** are the exchange current densities ($i_{o,i}$) and transfer coefficients ($\alpha_{a,i}$) for the bipolar reactions, as well as the total area each reaction is taking place in. Typical SBC experiments use a 200 μm inner diameter nozzle (the approximate dimension of a metal deposit) on a masked substrate with 0.45 cm^2 circular area, resulting in an oxidation area roughly 1000× larger than the reduction area. Here, finite element method computations are used to explore how reducing the substrate area available for oxidation impacts the *BCE* of the SBC. Six different kinetic and geometric parameter combinations are tested (see **Table 1**), varying either the exchange current density of the far-field reaction ($i_{o,far}$), the geometry of the microjet nozzle through r_i or r_o, or the distance of the feeder cathode from the nozzle center ($r_{cathode}$). **Figure 5** shows the *BCE* plotted vs. the ratio of the total circular substrate area (A_{subs}) to the nozzle area (A_{noz}) calculated by r_i. The applied current is 100 μA and fly-height is 10 μm in all simulations. Generally, the effect of reducing the substrate area results in a decay of *BCE* from a plateau to zero as substrate area becomes increasingly constrained. When the area of the substrate is large relative to the SBC nozzle, the *BCE* is at a high value, varying little as A_{subs}/A_{noz} decreases from 10,000 to 100. A substantial decrease in *BCE* occurs below a ratio of 10, quickly decaying to 0 as the substrate area approaches the same size as the nozzle area. The parameter sets tested in **Table 1** show greater variation at values of large A_{subs}/A_{noz}, where changing nozzle geometry is expected to impact R_{ionic} more than the $R_{CT,far}$. Changing the cathode location has a minimal impact on *BCE*, with an average of 0.65% difference between parameter sets 1 and 4.

The simulated *BCE* for all 6 parameter sets was fit to a decay equation of the form

$$BCE = A\left(1 - e^{\left(-B^*\left(\frac{A_{subs}}{A_{noz}} - 1\right)\right)}\right) + (D - A)^*\left(e^{\left(-\frac{C}{\left(\frac{A_{subs}}{A_{noz}}\right)}\right)}\right) \tag{10}$$

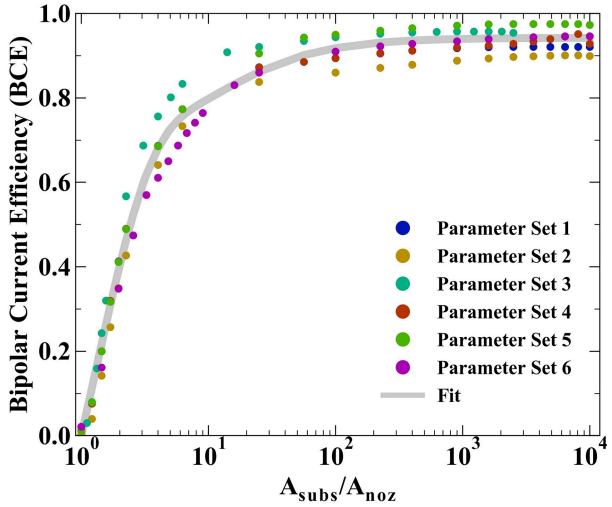

FIGURE 5 | Bipolar current efficiencies (BCE) plotted vs. the ratio of total substrate area (A_{subs}) to nozzle area (A_{noz}) defined by r_j. The varied parameters are highlighted in **Table 1** and the fit is modeled by Equation 10.

where A, B, and C are constants fit by non-linear least squares regression (equaling 0.744, 0.778, and 15.1, respectively) and D is the average of the maximum values for *BCE* in **Table 1**. The first term in Equation 10 captures the sharp decay below $A_{subs}/A_{noz} \approx 10$ while the second term captures the more gradual decay in *BCE* at higher ratios of A_{subs}/A_{noz}. Despite the variation in *BCE* across the parameters explored in **Table 1**, particularly at higher values of A_{subs}/A_{noz}, Equation 10 qualitatively describes how restricting the substrate area affects current flow in the SBC. Simulations suggest that the substrate area should be at least 2.45× that of the microjet nozzle area to achieve 50% BCE by Equation 10 for a fly-height of 10 μm.

Reversible Materials Systems

As outlined above, kinetically reversible electrodeposition chemistries such as Cu and Ag require a more thermodynamically favorable bipolar oxidation redox couple (i.e., $\Delta E_{BC} > 0$) to prevent metal etching as the SBC rasters across the substrate. If the bipolar counter reaction is too reducing (i.e., $\Delta E_{BC} >> 0$) metal cations will homogenously reduce in solution. Prior studies with the SBC demonstrated temporally stable patterning of kinetically reversible metals by designing electrolytes where ΔE_{BC} is only marginally positive by a few 10s of millivolts (Braun and Schwartz, 2016c). This provides enough of a thermodynamic cushion that the desired bipolar counter reaction is driven before metal etching during SBC patterning, but not enough driving force to overcome the nucleation barrier to cause spontaneous, homogeneous reduction in solution.

Electroanalytical methods such as cyclic voltammetry help describe the thermodynamic and kinetic relationship between reversible electrodeposition systems and their bipolar oxidation couple. **Figure 6** shows cyclic voltammetry relating the $Ag^+/Ag_{(s)}$ redox couple to the Fe^{3+}/Fe^{2+} bipolar counter reaction described by Scheme 3. Specifically, CVs in **Figure 6** are done for the following solutions: (1) 0.01 mol/L $FeSO_4$ + 0.005 mol/L $Fe_2(SO_4)_3$, (2) 0.01 mol/L $AgNO_3$, and (3) 0.01 mol/L $AgNO_3$ + 0.01 mol/L $FeSO_4$ + 0.005 mol/L $Fe_2(SO_4)_3$, with all three containing 0.1 mol/L K_2SO_4. At a rotation rate of 0 RPM (**Figure 6A**), solution (1) shows reduction of Fe^{3+} to Fe^{2+} with a peak current at 0.56 V and half peak potential of 0.635 V; oxidation of the reverse having a peak at 0.74 V and half peak potential of 0.645 V. The reversible Nernst potential estimated by CV of 0.64 V is in agreement with the measured open circuit potential of 0.63 V. For the silver only solution (2), deposition initiates after a small nucleation overpotential near 0.66 V reaching peak current at 0.63 V. On the return sweep, current crosses zero at 30 mV more positive than the iron solution, before exhibiting a characteristic metal stripping peak at 0.7 V.

Cyclic voltammetry in solution (3) with Ag(I), Fe(III), and Fe(II) ions results in a combination of features from voltammetry of the individual constituents. As potential is swept negative, peak current from combined ferric ion and silver ion reduction is at 0.57 V, with an estimated faradaic efficiency for silver reduction of 65% at this potential. Anodic stripping of silver in the return sweep appears more efficient than the Ag(I) solution. In solution (2), the total charge from the stripping wave is only 15% of the charge from the deposition wave, whereas solution (3) shows 86% of the total silver deposition charge in the stripping wave (estimated by assuming silver deposition efficiency is 65% throughout the combined Ag(I) and Fe(III) reduction wave). After silver is fully stripped, the i-V profile merges with that of solution (1) containing only ferric and ferrous ion components. Solution (3) voltammetry remains stable over 10 cycles despite the thermodynamic driving force for homogeneous silver reduction in solution.

Figure 6B shows the same solutions under forced hydrodynamics with a rotation rate of 100 RPM. The Fe(II)/Fe(III) redox couple exhibits strong stability over 10 cycles. The limiting currents for Fe(III) reduction and Fe(II) oxidation are −0.85 and 1.27 mA/cm^2, respectively. Using the Levich equation and an assumed solution viscosity of 0.01 cm^2/s, the calculated diffusivities for Fe(III) and Fe(II) are 2.9 × 10^{-6} cm^2/s and 5.3 × 10^{-6} cm^2/s, respectively. These values are comparable to previously reported diffusivities of 3–5.5 × 10^{-6} cm^2/s for Fe(III) (Gil et al., 1996) and 1.1–5.7 × 10^{-6} cm^2/s for Fe(II) (Andricacos et al., 1998; Hawthorne et al., 2014). Silver deposition in solution (2) shows variation in the transport limited current across 10 cycles, increasing in magnitude from 2.4 to −3.3 mA/cm^2. The calculated diffusivity using the Levich equation for Ag(I) is 1.4–2.2 × 10^{-5} cm^2/s, comparable to the literature value of 1.27 × 10^{-5} cm^2/s (Okeefe et al., 1987). Peak anodic current in the stripping wave also decreases from 3.8 to 2.5 mA/cm^2 from the first to last cycle, resulting in a stripping efficiency decrease from 34 to 20%. The combined Ag(I), Fe(II), and Fe(II) solution shows similar variation in the reduction and stripping waves as seen in the Ag(I) solution. A possible explanation for the low silver stripping efficiency in **Figure 6** voltammetry is detachment of dendritic silver from the electrode surface prior to full oxidation of the deposited charge. The inset

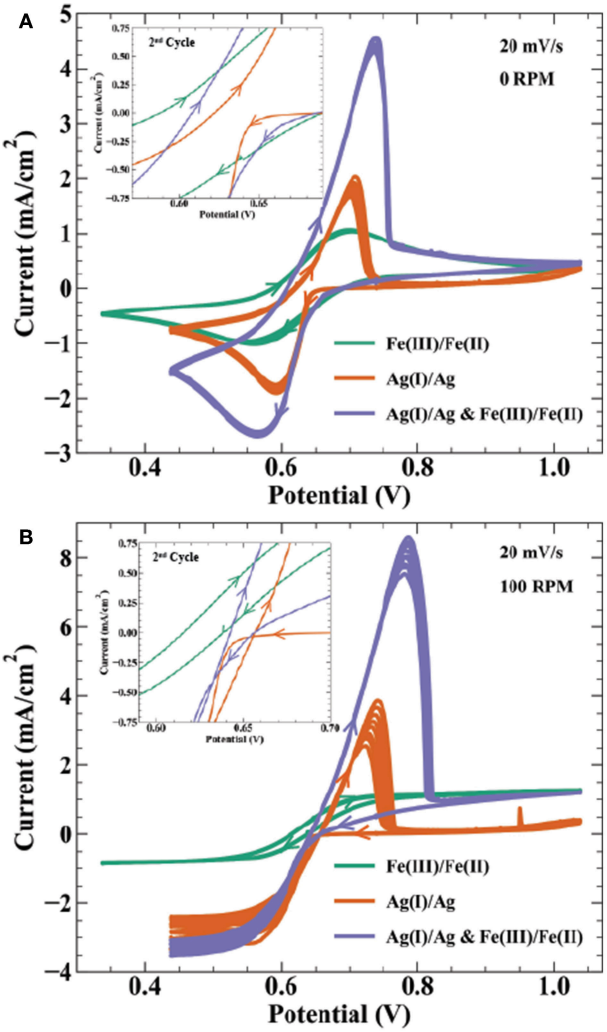

FIGURE 6 | Cyclic voltammetry at 20 mV/s on a 0.5 cm Au electrode for 9 cycles at **(A)** 0 RPM and **(B)** 100 RPM in electrolyte containing 0.01 mol/L $FeSO_4$ + 0.005 mol/L $Fe_2(SO_4)_3$ (—), 0.01 mol/L $AgNO_3$ (—), and 0.01 mol/L $AgNO_3$ + 0.01 mol/L $FeSO_4$ + 0.005 mol/L $Fe_2(SO_4)_3$ (—). All solutions contain 0.1 mol/L K_2SO_4 as supporting salt. Inset figures highlight the voltammetric curves near zero current, showing the 2nd cycle for each CV.

highlighting the region near zero current shows the Fe(III)/Fe(II) voltammetry crossing zero current between 0.62 and 0.64 V, consistent with the measured open circuit potential of 0.63 V. In the Ag(I) solution, the intersection of the return sweep with the forward sweep, often considered the reversible potential in deposition systems, occurs at 0.66 V. Cyclic voltammetry in **Figure 6** and open-circuit voltage measurements indicate that the reversible potentials for the Fe(III)/Fe(II) and Ag(I)/Ag redox couples produce a bipolar electrolyte with $\Delta E_{BC} \approx$ 30–40 mV. This thermodynamic cushion is sufficient for the temporally stable silver deposition observed in **Figure 2c**.

Despite these efforts to design the thermodynamics of the bipolar redox couples for stable metal patterning, metal dissolution can still be kinetically activated if the substrate is polarized sufficiently. **Figure 7** shows a series of experiments for bipolar copper electrodeposition (**Figure 7A**) and bipolar silver deposition (**Figure 7B**) performed at the indicated applied currents. Each pattern was deposited with a 200 μm ID nozzle at 400 μL/min flowrate, 30 μm fly-height, 75 μm deposit spacing, and 2 second dwell time per deposit. The copper electrolyte was 0.05 mol/L $CuSO_4$ + 0.005 mol/L ascorbic acid and the silver electrolyte was 0.01 mol/L $AgNO_3$ + 0.01 mol/L $FeSO_4$ + 0.005 mol/L $Fe_2(SO_4)_3$. Copper images were acquired in bright field imaging. Silver images, however, were acquired with dark field imaging because the coarse, large grained silver deposits scatter light and appeared dark in bright field (as in **Figure 2c**). For each metal, the pattern at the lowest current is fully retained on the gold substrate. However, as applied current increases more of the metal pattern is electrochemically etched from the surface; the SBC, beginning in the top left corner, rasters top-to-bottom and then left-to-right. Additional applied current creates a larger voltage drop beneath the nozzle, manifesting in increased substrate polarization and larger surface overpotentials for the bipolar reaction couple. The increase in surface overpotential exceeds the thermodynamic cushion designed into the metastable electrolytes, activating metal oxidation and resulting in pattern removal from the bipolar electrode.

Finite element method simulations relate qualitative observations of **Figure 7** to theoretical predictions regarding potential distribution on the bipolar electrode. **Figure 8** shows simulated surface overpotentials for the copper (—) and ascorbic acid (—) redox couples radially on the conductive substrate (zero is nozzle center) at the indicated applied currents. The surface overpotential is

$$\eta_{s,j} = V_m - \phi\,(r) - E_j^{eq} \tag{11}$$

where the solution potential (ϕ) evaluated at the substrate surface is a function of radial position. Equilibrium potentials (E_j^{eq}) are listed in Scheme 2, producing a $\Delta E_{BC} = +10$ mV, and the open-circuit mixed potential of the conductive substrate (V_m) reflects the thermodynamics and kinetics of the reactions when net current and potential are equal to zero. Simulations use a fly-height of 15 μm and nozzle ID of 200 μm. The inset emphasizes overpotential in the far-field oxidation region, with solid lines indicating oxidizing overpotentials and dotted lines reducing overpotentials. At 20 μA, the peak cathodic overpotentials beneath the nozzle for copper and ascorbic acid are −105 and −95 mV, respectively. The most positive overpotentials appear in the far-field region of the substrate, equal to −2 mV for copper and 8 mV for ascorbic acid. The surface overpotentials of the bipolar redox couples maintain a separation of 10 mV (equal to the value for ΔE_{BC}) across the substrate. The local copper overpotential ($\eta_{s,Cu}$) is negative everywhere on the substrate, therefore, the only thermodynamically possible anodic chemistry is ascorbic acid oxidation. Despite the large cathodic overpotential for dehydroascorbic acid reduction, only moderate amounts of current are produced due to the trace amounts of DHAA present in solution, with a computed faradaic efficiency for copper reduction equal to 99.9%.

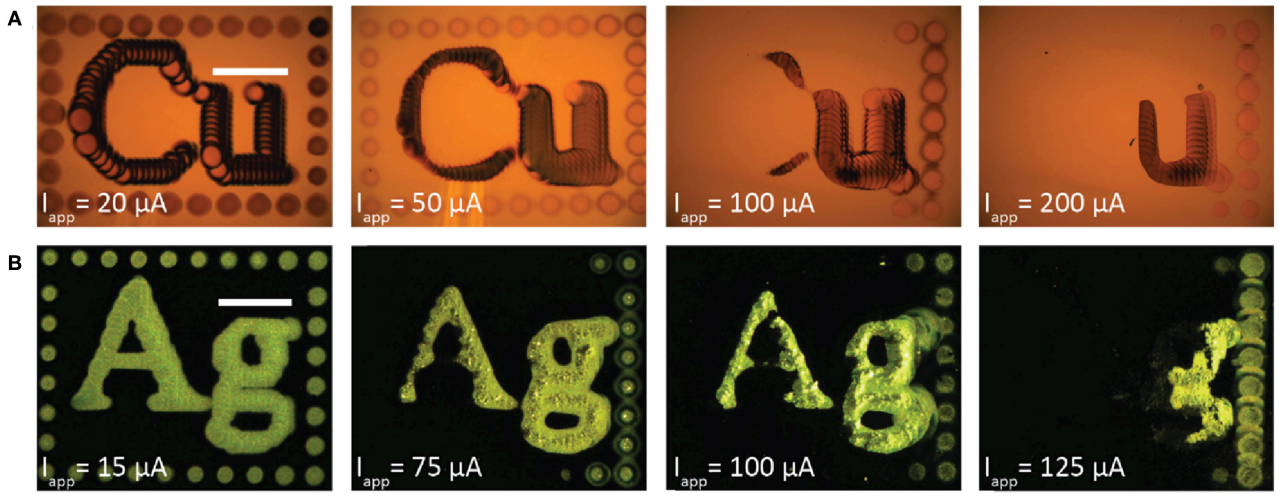

FIGURE 7 | Optical micrographs of patterned metal deposited from the SBC with a 200 μm ID nozzle at 400 μL/min electrolyte flowrate, fly-height of 30 μm, 75 μm deposit spacing, 2 second dwell time per deposit, and the indicated applied currents for **(A)** copper from a 0.05 mol/L $CuSO_4$ + 0.005 mol/L ascorbic acid electrolyte and **(B)** silver from a 0.01 mol/L $AgNO_3$ + 0.01 mol/L $FeSO_4$ + 0.005 mol/L $Fe_2(SO_4)_3$ electrolyte. Copper patterns were imaged in bright field mode and silver images imaged in dark field mode.

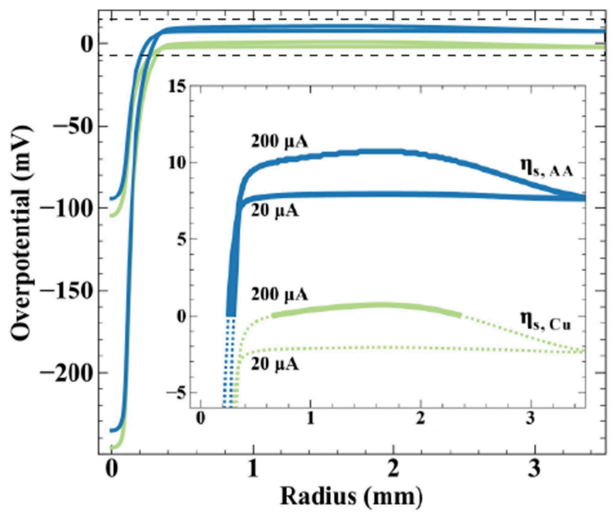

FIGURE 8 | Simulated surface overpotentials for copper (——) and ascorbic acid (——) on the substrate for a 200 μm ID nozzle at a fly-height of 15 μm and the indicated applied currents. Inset emphasizes far-field oxidation region (denoted by the dashed box), with solid lines indicating oxidizing overpotentials and dashed lines indicating reducing overpotentials.

Increasing applied current to 200 μA generates greater substrate polarization, shifting peak cathodic overpotentials to −245 and −235 mV for copper and ascorbic acid, respectively. The magnitude of overpotential change in the far-field region is less substantial, a result of its much larger surface area, producing maximum overpotentials of 1 mV for copper and 11 mV for ascorbic acid. The substrate now exhibits a region with a positive value for $\eta_{s,Cu}$ capable of driving copper oxidation. Simulations estimate a modest decrease in faradaic efficiency for ascorbic acid oxidation, from 100 to 92%. Increased substrate polarization as a result of higher applied currents kinetically activates metal oxidation, leading to the removal of material observed in **Figure 7**. Due to the uncertainty in measurements of the reversible potentials for the copper and ascorbic acid redox couples, the treatment of dilute DHAA in the electrolyte, and assumption of an ideal SBC nozzle geometry, these simulations are not intended to be quantitative predictors of experimental observations, but instead used as theoretical assessments of the underlying phenomena.

CONCLUSIONS

The SBC provides a unique platform for electrochemical materials patterning on conducting substrates without direct electrical connections. Efficient bipolar patterning begins with effective electrolyte design, where understanding the kinetics of the desired bipolar reduction chemistry are critical for stable patterning. Metals with a large kinetic barrier to electrochemical oxidation are inherently stable on the bipolar electrode, permitting a wider range of redox couples suitable for the bipolar counter reaction as well as greater latitude in SBC operating conditions. Metals that are kinetically capable of dissolving must instead have stability built into the thermodynamic relationship between the desired reduction reaction and the bipolar counter reaction, limiting the redox couples available as bipolar counter reactions as well as the applied currents permitting spatiotemporal patterning. In addition to these bipolar design criteria, traditional electrolyte considerations such as pH balance and secondary parasitic reactions may impact deposit morphology and microstructure. Cyclic voltammetry measurements clarify experimental observations of secondary reactions during bipolar nickel deposition and

support hypotheses for design guidelines of kinetically reversible electrodeposition systems. Finally, finite element method simulations indicate reduced bipolar electrode surface areas will dramatically impact BCE.

DATA AVAILABILITY

The datasets generated for this study are available on request to the corresponding author.

AUTHOR CONTRIBUTIONS

TB conducted experiments and simulations. DS provided funding support. TB and DS provided input to the manuscript.

ACKNOWLEDGMENTS

Identification of commercial products in this paper is done to specify the experimental procedure. In no case does this imply endorsement or recommendation by the National Institute of Standards and Technology. The authors gratefully acknowledge partial support of this research provided by the U.S. Department of Education grant P200A120023 and the Boeing Endowment for Excellence. TB acknowledges the National Institute of Standards and Technology-National Research Council research associateship program for a postdoctoral fellowship. Use of the Washington Nanofabrication Facility, a NSF national Nanotechnology Coordinated Infrastructure Site (grant ECCS-1542101), is appreciated.

REFERENCES

Andricacos, P. C., Uzoh, C., Dukovic, J. O., Horkans, J., and Delgianni, H. (1998). Damascene copper electroplating for chip interconnections. *IBM J. Res. Dev.* 42, 567–574. doi: 10.1147/rd.425.0567

Borsook, H., and Keighley, G. (1933). Oxidation reduction potential of ascorbic acid (Vitamin C). *Proc. Natl. Acad. Sci. U.S.A.* 19, 875–878. doi: 10.1073/pnas.19.9.875

Bradley, J. C., Chen, H. M., Crawford, J., Eckert, J., Ernazarova, K., Kurzeja, T., et al. (1997). Creating electrical contacts between metal particles using directed electrochemical growth. *Nature*. 389, 268–271. doi: 10.1038/38464

Bradley, J. C., Ma, Z. M., Clark, E., Crawford, J., and Stephens, S. G. (1999). Programmable ward-wiring of circuitry using spatially coupled bipolar electrochemistry. *J. Electrochem. Soc.* 146, 194–198. doi: 10.1149/1.1391586

Braun, T. M., and Schwartz, D. T. (2015). Localized electrodeposition and patterning using bipolar electrochemistry. *J. Electrochem. Soc.* 162, D180–D185. doi: 10.1149/2.1031504jes

Braun, T. M., and Schwartz, D. T. (2016a). Analytical and computational scaling relationships for the coupled phenomena that control local bipolar electrochemical behavior. *J. Electrochem. Soc.* 163, E354–E362. doi: 10.1149/2.0041614jes

Braun, T. M., and Schwartz, D. T. (2016b). Bipolar electrochemical displacement: a new phenomenon with implication for self-limiting materials patterning. *ChemElectroChem*. 3, 441–449. doi: 10.1002/celc.201500356

Braun, T. M., and Schwartz, D. T. (2016c). Remote control electrodeposition: principles for bipolar patterning of substrates without an electrical connection. *J. Electroche. Soc.* 163, D3014–D3019. doi: 10.1149/2.0031612jes

Braun, T. M., and Schwartz, D. T. (2016d). The emergin role of electrodeposition in additive manufacturing. *Electrochem. Soc. Int.* 25, 69–73. doi: 10.1149/2.F07161if

Chow, K. F., Chang, B. Y., Zaccheo, B. A., Mavré, F., and Crooks, R. M. (2010). A sensing platform based on electrodissolution of a Ag bipolar electrode. *J. Am. Chem. Soc.* 132, 9228–9229. doi: 10.1021/ja103715u

Chow, K. F., Mavré, F., Crooks, J. A., Chang, B. Y., and Crooks, R. M. (2009). A large-scale, wireless electrochemical bipolar electrode microarray. *J. Am. Chem. Soc.* 131, 8364–8365. doi: 10.1021/ja902683f

Fosdick, S. E., Berglund, S. P., Mullins, C. B., and Crooks, R. M. (2013). Parallel screening of electrocatalyst candidates using bipolar electrochemistry. *Anal. Chem.* 85, 2493–2499. doi: 10.1021/ac303581b

Gil, A. F., Galicia, L., and Gonzalez, I. (1996). Diffusion coefficients and electrode kinetic parameters of different Fe(III)-sulfate complexes. *J. Electroanal. Chem.* 417, 129–134. doi: 10.1016/S0022-0728(96)04735-3

Hawthorne, K. L., Wainright, J. S., and Savinell, R. F. (2014). Studies of iron-ligand complexes for an all-iron flow battery application. *J. Electrochem. Soc.* 161, A1662–A1671. doi: 10.1149/2.0761410jes

Hirt, L., Reiser, A., Spolenak, R., and Zambelli, T. (2017). Additive manufacturing of metal structures at the micrometer scale. *Adv. Mater.* 29:1604211. doi: 10.1002/adma.201604211

Ishiguro, Y., Inagi, S., and Fuchigami, T. (2011). Gradient doping of conducting polymer films by means of bipolar electrochemistry. *Langmuir*. 27, 7158–7162. doi: 10.1021/la200464t

Ji, J., Cooper, W. C., Dreisinger, D. B., and Peters, E. (1995). Surface pH measurements during nickel electrodeposition. *J. Appl. Electrochem.* 25, 642–650. doi: 10.1007/BF00241925

Kawata, S., Sun, H. B., Tanaka, T., and Takada, K. (2001). Finer features for functional microdevices - Micromachines can be created with higher resolution using two-photon absorption. *Nature* 412, 697–698. doi: 10.1038/35089130

Lin, X., Zheng, L., Gao, G., Chi, Y., and Chen, G. (2012). Electrochemiluminescence imaging-based high-throughput screening platform for electrocatalysts used in fuel cells. *Anal. Chem. A* 84, 7700–7707. doi: 10.1021/ac300875x

Loget, G., Roche, J., and Kuhn, A. (2012). True bulk synthesis of janus objects by bipolar electrochemistry. *Adv. Mater.* 24, 5111–5116. doi: 10.1002/adma.201201623

Mattsson, E., and Bockris, J. (1959). Galvanostatic studies of the kinetics of depostion and dissolution in the copper + copper sulphate system. *T. Farday. Soc.* 55, 1586–1601. doi: 10.1039/tf9595501586

Momotenko, D., Page, A., Adobes-Vidal, M., and Unwin, P. R. (2016). Write-read 3D patterning with a dual-channel nanopipette. *ACS Nano*. 10, 8871–8878. doi: 10.1021/acsnano.6b04761

Munktell, S., Nyholm, L., and Bjorefors, F. (2015). Towards high throughput corrosion screening using arrays of bipolar electrodes. *J. Electroanal. Chem.* 747, 77–82. doi: 10.1016/j.jelechem.2015.04.008

Nelson, J. B., and Schwartz, D. T. (2005). Electrochemical printing: in situ characterization using an electrochemical quartz crystal microbalance. *J. Micromech. Microeng.* 15, 2479–2484. doi: 10.1088/0960-1317/15/12/033

Norskov, J. K., Bligaard, T., Logadottir, A., Kitchin, J. R., Chen, J. G., and Pandelov, S. (2005). Trends in the exchange current for hydrogen evolution. *J. Electrochem. Soc.* 152, J23–J26. doi: 10.1149/1.1856988

Okeefe, T. J., Cuzmar, J. S., and Chen, S. F. (1987). Calculation of mass-transfer coefficients in metal-deposition using electrochemical tracer techniques. *J. Electrochem. Soc.* 134, 547–551. doi: 10.1149/1.2100507

Ritzert, N. L., and Moffat, T. P. (2016). Ultramicroelectrode studies of self-terminated nickel electrodeposition and nickel hydroxide formation upon water reduction. *J. Phys. Chem. C* 120, 27478–27489. doi: 10.1021/acs.jpcc.6b10006

Sato, N., and Okamoto, J. (1963). Anodic passivation of nickel in sulfuric acid solutions. *J. Electrochem. Soc.* 110, 605–614. doi: 10.1149/1.2425838

Scherer, J., Ocko, B. M., and Magnussen, O. M. (2003). Structure, dissolution, and passivation of Ni(111) electrodes in sulfuric acid solution: an in situ STM, X-ray scattering, and electrochemical study. *Electrochim. Acta.* 48, 1169–1191. doi: 10.1016/S0013-4686(02)00827-7

Schlesinger, M. (2010). *Modern Electroplating*. Hoboken, NJ: Wiley.

Smith, R. J., Hummel, R. E., and Ambrose, J. R. (1987). The passivation of nickel in aqueous-solutions. 2. An in-situ investigation of the passivation of

nickel using optical and electrochemical techniques. *Corros. Sci.* 27, 815–826. doi: 10.1016/0010-938X(87)90039-4

Tanaka, N., and Tamamushi, R. (1964). Kinetic parameters of electrode reactions. *Electrochim. Acta* 45, 3461–3471. doi: 10.1016/0013-4686(64)85045-3

Tiewcharoen, S., Warakulwit, C., Lapeyre, V., Garrigue, P., Fourier, L., Elissalde, C., et al. (2017). Anisotropic metal deposition on TiO2 particles by electric-field-induced charge separation. *Angew. Chem. Int. Edit* 56, 11431–11435. doi: 10.1002/anie.201704393

Tisserant, G., Fattah, Z., Ayela, C., Roche, J., Plano, B., Ziga, D., et al. (2015). Generation of metal composition gradients by means of bipolar electrodeposition. *Electrochim. Acta* 179, 276–281. doi: 10.1016/j.electacta.2015.03.102

Ulrich, C., Andersson, O., Nyholm, L., and Björefors, F. (2008). Formation of molecular gradients on bipolar electrodes. *Angew. Chem. Int. Ed.* 47, 3034–3036. doi: 10.1002/anie.200705824

Wang, R. Y., Bertocci, U., Tan, H. Y., Bendersky, L. A., and Moffat, T. P. (2016). Self-terminated electrodeposition of Ni, Co, and Fe ultrathin films. *J. Phys. Chem. C* 120, 16228–16237. doi: 10.1021/acs.jpcc.6b01901

Wood, M., and Zhang, B. (2015). Bipolar electrochemical method for dynamic *in situ* control of single metal nanowire growth. *ACS Nano* 9, 2454–2464. doi: 10.1021/acsnano.5b00139

Xiao, Y., Xu, L., and Qi, L. W. (2017). Electrochemiluminescence bipolar electrode array for the multiplexed detection of glucose, lactate and choline based on a versatile enzymatic approach. *Talanta* 165, 577–583. doi: 10.1016/j.talanta.2017.01.019

Xu, F., Wang, H., He, X. D., Deng, N., Li, F., Li, B., et al. (2018). One-step deposition of NixCu1-x alloys with both composition gradient and morphology evolution by bipolar electrochemistry. *J. Electroanal. Chem.* 823, 213–220. doi: 10.1016/j.jelechem.2018.06.003

Zech, N., and Landolt, D. (2000). The influence of boric acid and sulfate ions on the hydrogen formation in Ni-Fe plating electrolytes. *Electrochim. Acta* 45, 3461–3471. doi: 10.1016/S0013-4686(00)00415-1

Conflict of Interest Statement: The authors declare that the research was conducted in the absence of any commercial or financial relationships that could be construed as a potential conflict of interest.

APPENDIX: COMPUTATIONAL MODEL DETAILS

A secondary current distribution is appropriate here because the concentration is substantially uniform, a result of high transport rates from the jetted electrolyte (limiting current densities can exceed 10 A/cm^2), and thus concentration gradients can be neglected (Nelson and Schwartz, 2005). Potential distribution (ϕ) in the electrolyte is defined by Laplace's equation.

$$\nabla^2\phi = 0 \tag{A1}$$

The nozzle, housing walls, and electrolyte meniscus are treated as insulating boundary conditions,

$$\boldsymbol{n}\cdot\nabla\phi = 0 \tag{A2}$$

where $\boldsymbol{n}$ is the unit normal vector pointing out of the computational domain. The feeder anode boundary condition at the microjet inlet is

$$-\kappa\boldsymbol{n}\cdot\nabla\phi = \frac{I_{app}}{A_{nozzle}} \tag{A3}$$

where κ is the electrolyte conductivity, A_{nozzle} is the area of the nozzle where current is applied and I_{app} is the total applied current to the system. The feeder cathode boundary condition is

$$-\kappa\mathbf{n}\cdot\nabla\phi = \frac{-I_{app}}{A_{nozzle}} \tag{A4}$$

with the area, $A_{cathode}$, equal to the area of the platinum outer ring cathode.

The most general form for the bipolar reaction rates at the conductive substrate is given by a modified Butler-Volmer kinetic approximation

$$i_j = i_{o,j}\left[f_j e^{\left(\frac{\alpha_{a,j}n_jF}{RT}\eta_{s,j}\right)} - g_j e^{\left(\frac{-(1-\alpha_{a,j})n_jF}{RT}\eta_{s,j}\right)}\right] \tag{A5}$$

where $i_{o,j}$ is the exchange current density for reaction j, n_j is the number of electrons transferred for reaction j and $\alpha_{a,j}$ is the transfer coefficient for the anodic branch of reaction j. The parameter T is the temperature of the system (298 K), F is Faraday's constant, and R is the ideal gas constant. The surface overpotential in Equation A.5 is defined by Equation 11. The functions f_j and g_j modify the Butler-Volmer equation to account for the reversibility of the respective branches. For example, the general Butler-Volmer equation with reversible kinetics, such as for copper, has functions f_j and g_j both equal to 1. In the case of an irreversible chemistry such as nickel, a Tafel approximation for reduction is produced when $f_j = 0$ and $g_j = 1$. The total current at the substrate is the sum of the individual partial currents:

$$i = \sum i_j. \tag{A6}$$

To remain charge neutral, the conductive substrate requires equal magnitudes of reduction and oxidation reactions, which is expressed by the integral constraint over the substrate area

$$I_{e,net} = 2\pi\int_o^{r_{sub}} irdr = \sum I_{e,red} + \sum I_{e,ox} = 0 \tag{A7}$$

where i is defined by Equations A.5-A.6 and $I_{e,net}$ is the net electronic current passing through the conductive substrate, equaling zero when integrated over the entire substrate. The currents $I_{e,red}$ and $I_{e,ox}$ are contributions from any bipolar reactions occurring on the substrate. The location along the radial axis where the partial current density for each reaction equals zero is defined as a bipolar cross-over point (*BPX*), with each bipolar couple yielding a *BPX*. Integrating the current density on the substrate from the nozzle center ($r = o$) to the BPX yields $I_{e,red}$ to calculate *BCE* in Equation 1.

For simulations of near-field copper reduction in Scheme 2, the treatment of the small amounts of dehydroascorbic acid reduction by setting $g_{AA} = (1\text{-}i/i_{o,AA})$ with f_{AA}, g_{Cu}, and $f_{Cu} = 1$ results in a boundary condition for total current density on the bipolar substrate as

$$\begin{aligned}-\kappa\boldsymbol{n}\cdot\nabla\phi = i \;\; &= i_{o,AA}e^{\left(\frac{\alpha_{a,AA}n}{RT}\eta_{s,AA}\right)} \\ &\quad -i_{o,AA}\left[1-\frac{i}{i_{o,AA}}\right]e^{\left(-\frac{(1-\alpha_{a,AA})n}{RT}\eta_{s,AA}\right)} \\ &\quad -i_{o,Cu}\left[e^{\left(\frac{\alpha_{a,Cu}n}{RT}\eta_{s,Cu}\right)} - e^{\left(-\frac{(1-\alpha_{a,Cu})n}{RT}\eta_{s,Cu}\right)}\right]\end{aligned} \tag{A8}$$

where $n = 2$ since both electrons transfer two reactions and other model parameters are listed in **Table 2**.

frontiers in Chemistry

ORIGINAL RESEARCH
published: 28 May 2019
doi: 10.3389/fchem.2019.00361

High Lithium Ion Transport Through rGO-Wrapped $LiNi_{0.6}Co_{0.2}Mn_{0.2}O_2$ Cathode Material for High-Rate Capable Lithium Ion Batteries

Wook Ahn[1], Min-Ho Seo[2], Tuan Kiet Pham[1], Quoc Hung Nguyen[1], Van Tung Luu[1], Younghyun Cho[1], Young-Woo Lee[1], Namchul Cho[1] and Soon-Ki Jeong[1]*

[1] Department of Energy Systems Engineering, Soonchunhyang University, Asan-si, South Korea, [2] New and Renewable Energy Research Division, Hydrogen and Fuel Cell Center, Korea Institute of Energy Research, Daejeon, South Korea

In this work, we show an effective ultrasonication-assisted self-assembly method under surfactant solution for a high-rate capable rGO-wrapped $LiNi_{0.6}Co_{0.2}Mn_{0.2}O_2$ (Ni-rich cathode material) composite. Ultrasonication indicates the pulverization of the aggregated bulk material into primary nanoparticles, which is effectively beneficial for synthesizing a homogeneous wrapped composite with rGO. The cathode composite demonstrates a high initial capacity of 196.5 mAh/g and a stable capacity retention of 83% after 100 cycles at a current density of 20 mA/g. The high-rate capability shows 195 and 140 mAh/g at a current density of 50 and 500 mA/g, respectively. The high-rate capable performance is attributed to the rapid lithium ion diffusivity, which is confirmed by calculating the transformation kinetics of the lithium ion by galvanostatic intermittent titration technique (GITT) measurement. The lithium ion diffusion rate (D_{Li}) of the rGO-wrapped $LiNi_{0.6}Co_{0.2}Mn_{0.2}O_2$ composite is *ca.* 20 times higher than that of lithium metal plating on anode during the charge procedure, and this is demonstrated by the high interconnection of $LiNi_{0.6}Co_{0.2}Mn_{0.2}O_2$ and conductive rGO sheets in the composite. The unique transformation kinetics of the cathode composite presented in this study is an unprecedented verification example of a high-rate capable Ni-rich cathode material wrapped by highly conductive rGO sheets.

Keywords: lithium ion battery, graphene-based cathode composite, nickel-rich, $LiNi_{0.6}Co_{0.2}Mn_{0.2}O_2$, galvanostatic intermittent titration technique

OPEN ACCESS

Edited by:
Syed Mubeen Jawahar Hussaini, The University of Iowa, United States

Reviewed by:
Fouran Singh, Inter-University Accelerator Centre, India
Sung Mook Choi, Korea Institute of Materials Science, South Korea

****Correspondence:***
Wook Ahn
wahn21@sch.ac.kr

Specialty section:
This article was submitted to Electrochemistry, a section of the journal Frontiers in Chemistry

Received: *25 January 2019*
Accepted: *01 May 2019*
Published: *28 May 2019*

Citation:
Ahn W, Seo M-H, Pham TK, Nguyen QH, Luu VT, Cho Y, Lee Y-W, Cho N and Jeong S-K (2019) High Lithium Ion Transport Through rGO-Wrapped $LiNi_{0.6}Co_{0.2}Mn_{0.2}O_2$ Cathode Material for High-Rate Capable Lithium Ion Batteries. Front. Chem. 7:361. doi: 10.3389/fchem.2019.00361

INTRODUCTION

With the increasing environmental concerns such as energy depletion and gas emission problems, interest in novel energy storage systems (ESSs) and renewable energy such as photovoltaic and wind power is at an all-time high (Li et al., 2015; Zhao et al., 2015). As the world population continues to grow, we could not fulfill the energy consumption requirement without developing a clean energy system (Majeau-Bettez et al., 2011; Catenacci et al., 2013). To address this, many research groups have recently been contributing to the development of electrochemical energy conversion and storage devices such as hybrid capacitors, metal–air batteries, and high-power lithium ion batteries (Lim et al., 2015; Ahn et al., 2016a,b, 2018; Seo et al., 2018). Among them, technology advancement in high-power lithium ion batteries that can be applied to electric

vehicles (EVs) has been investigated (Lin et al., 2017; Cano et al., 2018; Fu et al., 2018). $LiCoO_2$ and $LiNi_{1/3}Co_{1/3}Mn_{1/3}O_2$ have been used as conventional cathode materials for mobile devices because of their stable cyclability with ease of manufacture (Venkateswara Rao et al., 2011; Byeon et al., 2018). However, there are still issues on whether conventional cathode materials can improve energy and power density for ESSs and EVs. A strong candidate for a high-energy and high-power-density material is the Ni-rich $LiNi_{0.6}Co_{0.2}Mn_{0.2}O_2$ layered material, which has a practical capacity of *ca.* ∼190 mAh/g (Kim et al., 2015; Shim et al., 2017; Fu et al., 2018; Liao et al., 2018). Also, this Ni-rich material has the advantages of being relatively cheap and environmental friendly. However, this material still has the critical problem of having low electrical conductivity with poor cycle life, which is difficult to apply to ESSs and EVs for high power density with long cycle stability. To overcome such challenges, numerous research have been focusing on the development of element-doped materials and carbon-based (carbon coating, mixing, etc.) composites (Ju et al., 2014, 2018; Lim et al., 2014a, 2015).

Particularly, a graphene (rGO)-based cathode composite is prepared by various chemical reaction routes to demonstrate high-rate capability for lithium ion batteries. Most reported studies on high-power composites have been limited to aggregated mixture of cathode either dispersed in the graphene matrix or wrapped by graphene sheets (Yang et al., 2012; Kucinskis et al., 2013; Lim et al., 2014b; Shim et al., 2017). Furthermore, an in-depth study with emphasis on confirming the transformation kinetics of lithium ion during charge–discharge to further investigate the rate capability tendency of cathode material has never been reported.

Here, we introduce an ultrasonication-assisted self-assembly route under a surfactant solution environment, where the final morphology of rGO-wrapped $LiNi_{0.6}Co_{0.2}Mn_{0.2}O_2$ (NCM622) forms a homogeneous nanoparticle interconnected with a thin layer of rGO nanosheets. Furthermore, practical transformation kinetics of $LiNi_{0.6}Co_{0.2}Mn_{0.2}O_2$ during lithium ion intercalation–deintercalation advances will be verified by galvanostatic intermittent titration technique (GITT) measurement.

EXPERIMENTAL

Synthesis of the rGO-Wrapped $LiNi_{0.6}Co_{0.2}Mn_{0.2}O_2$ Composite

The detailed synthesis procedure for $LiNi_{0.6}Co_{0.2}Mn_{0.2}O_2$ preparation was followed by our previous research paper using a combustion synthesis method (Ahn et al., 2014a). The appropriate NH_2CONH_2 (urea):nitrate ratio (3:2 mol/mol) dissolved in deionized (DI) water is effective for preparing nanostructured material, and it confirmed that high crystalline $LiNi_{0.6}Co_{0.2}Mn_{0.2}O_2$ was synthesized at the sintering temperature of 800°C on that study. The rGO was also synthesized based on the previous methodology—called the modified improved hummers' method—where the rGO consists of under 4.2 layers of graphene sheets, resulting in high electrical conductivity and surface area (Ahn et al., 2014b, 2016a). For the preparation of rGO-wrapped $LiNi_{0.6}Co_{0.2}Mn_{0.2}O_2$, 0.1 g of rGO powder was firstly dispersed into 150 ml of DI water and then 2 ml of 1% Triton X-100 surfactant was added into the solution with vigorous stirring for 30 min to functionalize the hydrophilic nature of the rGO surface. In another beaker, 0.9 g of pristine NCM622 ($LiNi_{0.6}Co_{0.2}Mn_{0.2}O_2$) active material was dispersed into 150 ml of DI water, and ultrasonication was carried out to pulverize the aggregated bulk powder for the preparation of primary nanoparticles at an energy of 100 kJ. Then, the NCM622 solution was added into the activated rGO dispersed solution and sonicated for 1 h to prepare a homogenously self-assembled composite.

CHARACTERIZATIONS

To confirm the structure and crystallinity of each material, X-ray diffraction (AXS D8 Advance, Bruker) of the phases was carried out with Cu Kα radiation ($\lambda = 1.5405$ Å) in the 2θ range of 5–80° with 0.02° intervals, at a 2° min^{-1} scanning rate. The morphologies and microstructures were analyzed using a scanning electron microscope (SEM; S400, Hitachi), and high-resolution transmission electron microscopy (HR-TEM; JEOL 2010F, JEOL Ltd.) was carried out to confirm the microscopic images of synthesized materials. To ascertain the binding energy and verify the oxidation states of each transition metal element, X-ray photoelectron spectroscopy (XPS) was conducted (K-Alpha XPS spectrometer, Thermal Scientific). For electrochemical testing, the cathode electrodes were prepared by mixing 10 wt.% of poly(vinylidene fluoride-co-hexafluoropropylene) (PVDF-co-HFP, KYNAR® 2801) binder, 5 wt.% of Super-P (C65 super-P, Timcal co. LTD) conductive carbon, and 85 wt.% of the rGO-wrapped NCM622 composite in *N*-methyl-2-pyrrolidone (NMP); then, this slurry was mixed and coated on Al foil (20 μm) to a 60-μm thickness of mixed slurry using a doctor blade to coat a uniform cathode electrode. The electrode was dried in oven at 60°C for 24 h and then pressed using a twin roller. The final thickness of the cathode material on the Al foil was 45 μm. CR2032 coin-type cells were assembled using 1.0 M solution of $LiPF_6$ dissolved in a mixture of ethylene carbonate and diethyl carbonate (EC/DEC, 50:50 vol.%) as an electrolyte and Celgard 2400 as a separator. A lithium chip was used as the counter electrode for the half-cell evaluation. The electrode size is 14Ø (electrode loading mass: 2.20 mg/cm^2, loaded mass based on active material: 1.76 mg/cm^2) and 50 μl/mg of the electrolyte was injected into the coin cell. The coin cell assembly procedure was completely performed in an argon (Ar)-filled glove box. The electrochemical evaluation was carried out (CT2001C, LANHE, China) at a current density of 20 to 1,000 mA/g with a voltage range between 3.0 and 4.3 V at room temperature. GITT of the coin cell with NCM/rGO material was also carried out to investigate the evolution of lithium diffusivity as a function of induced potential at the state of charge and discharge with a battery tester at room temperature.

RESULTS AND DISCUSSION

The schematic illustration of a facile synthesis procedure for the NCM/rGO composite is presented in **Figure 1**. The rGO nanosheet of approximately under 4.2 layers is functionalized with Triton X-100 surfactant to create hydrophilic surface on the rGO, after which, agglomerated rGO powder is homogeneously dispersed into DI water. Triton X-100 is a well-known surfactant that has hydrophilic and hydrophobic parts at both ends of the chain, respectively, resulting in an increase in hydrophilicity of rGO sheets, and this surfactant could help obtain the rGO-wrapped composite (Patey et al., 2009). For the preparation of NCM622, we could effectively synthesize the secondary bulk material which consists of primary nanoparticles from the combustion synthesis method. In order to materialize a high mass loading electrode, a relatively bulk micron-sized particle is better than a nanosized particle; however, the aggregated powder is unfavorable for preparing surface modification such as an rGO-wrapped or a carbon-based material coated composite. Therefore, ultrasonication is used to pulverize the bulk secondary particle of NCM622. On the other hand, ultrasonication treatment affects the morphological change of a wrinkled rGO sheet, resulting in a flattened rGO sheet, which has more surface exposure to the NCM-rich environment in the solution (Ahn et al., 2014b). Finally, the ultrasonication-assisted self-assembly methodology successfully obtains a homogeneously rGO-wrapped NCM composite.

The XRD patterns obtained with the NCM/rGO composite, pristine NCM, and pristine rGO are presented in **Figure 2A**, and the result of the NCM/rGO composite is consistent with results from the mixed XRD patterns of pristine NCM and pristine rGO. All the characteristic peaks of the NCM/rGO composite show a hexagonal structure with an R-3m space group (Ahn et al., 2014a; Salitra et al., 2018). From the inset image (**Figure 2B**) of XRD patterns in the range of 5–35°, the characteristic broad diffraction peak of rGO indicates that rGO is homogeneously mixed with the NCM material, resulting in strong ultrasonication treatment that did not generate the phase transformation or decomposition of the NCM material during the self-assembly procedure. The lattice constant (*a*, *c*) of NCM/rGO was calculated following Bragg's law, with values of 2.895 and 14.287 Å, respectively. The high *c/a* (4.939) ratio is related to the well-defined hexagonal layered structure, and *c* represents the distance of a metal–metal interslab, which is directly associated with crystallinity, verifying that the NCM/rGO nanocomposite obtains a high crystalline structure (Ahn et al., 2014a). In order to estimate the cation mixing of the sample, the $I_{(003)}/I_{(104)}$ peak ratio was calculated, and NCM/rGO from this study shows 1.35, which supports the well-crystalline structure without cation mixing.

Morphological analyses with SEM and TEM images are presented in **Figure 3**. **Figure 3a** shows the bulk secondary particle by forming the aggregated morphology of the primary particle for the NCM material with a dense structure, facilitating a high mass loading electrode. The bulk secondary particle, however, has a disadvantage in surface modification, and the rGO nanosheet could not virtually cover the entire bulk particle. Therefore, ultrasonication is essentially required to pulverize the bulk secondary particle into a nanosized primary particle to be modified further. **Figure 3b** shows pristine rGO nanosheets with numerous wrinkles; the crumpled structure is derived from the high surface energy, indicating an agglomerated structure throughout the rGO sheets. The NCM/rGO composites without and with ultrasonication assistance are presented in **Figures 3c,d** respectively. From the result, aggregated bulk NCM/rGO cannot be homogeneously dispersed into the solution, and then the final product exists mostly in a separated phase. It is verified that the ultrasonication-assisted procedure effectively contributes to the preparation of the homogeneous rGO-wrapped NCM composite, and TEM images support this result. TEM analysis of the NCM/rGO composite under ultrasonication-assisted self-assembly has been conducted (**Figures 3d–h**), where the average particle size of the NCM/rGO composite is observed to be ∼100–150 nm, as shown in **Figures 3e,f**. The wrapped rGO sheet observed in a high-resolution TEM image (**Figure 3g**) shows a clear indication that the rGO sheet has been successfully covered throughout the NCM particle with ∼7 nm of rGO thickness. Further diffraction analysis (**Figure 3h**) confirms that the SAED pattern of NCM has no phase transition after the strong ultrasonication-assisted self-assembly process, whose SAED pattern of NCM is obviously in accordance with our previous result (Ahn et al., 2014a). Finally, the resultant NCM/rGO composite with ultrasonication process effectively obtains a homogeneous rGO-wrapped NCM cathode material without damaging NCM primary nanoparticles.

Figure 4 shows typical Raman spectra of the rGO sheet and the NCM-rGO composite corresponding to D and G for rGO and E_g and A_{1g} for the TM-O bond in the NCM material, respectively. The high intensity of the D-band peak is ascribed to the defects of the graphene layer ($I_D/I_G = 1.7$ for the NCM/rGO composite and 1.5 for the rGO sheet), resulting in the NCM/rGO composite being stably synthesized with the decrease in rGO defect. The relative decrease of rGO defect after composite synthesis probably happened due to the bonding effect between edge defect of the rGO sheet and the Triton X-100 surfactant. The two peaks of the NCM/rGO composite near 495 cm^{-1} (E_g) and 535 cm^{-1} (A_{1g}) correspond to specific bands of TM-O arrangements in the layered structure with the R-3m space group (Shim et al., 2017), and the Raman study provides strong evidence that the ultrasonication-assisted self-assembly method could effectively synthesize the NCM/rGO composite without any side reaction.

The XPS spectra of each transition metal ion presented in **Figure 5** very closely match our previously reported work, which confirms no phase transformation and decomposition during the ultrasonication procedure. The XPS survey profile of NCM/rGO presented in **Figure 5A** also verifies that the high content of the NCM material is homogeneously mixed with the rGO sheet. **Figure 5B** displays the XPS results of Ni 2p, and the area ratio of the Ni transition metal is decoupled in characteristic oxidation peaks (around 854 and 856 eV), resulting in Ni nearly consisting of 33% Ni^{2+} and 67% Ni^{3+} in the layered structure. The binding energy for each spectrum of Co 2p and Mn 2p (**Figures 5C,D**) indicates that the Co ion and Mn ion in the sample correspond to the 3+ and 4+ oxidation state, respectively, and this result

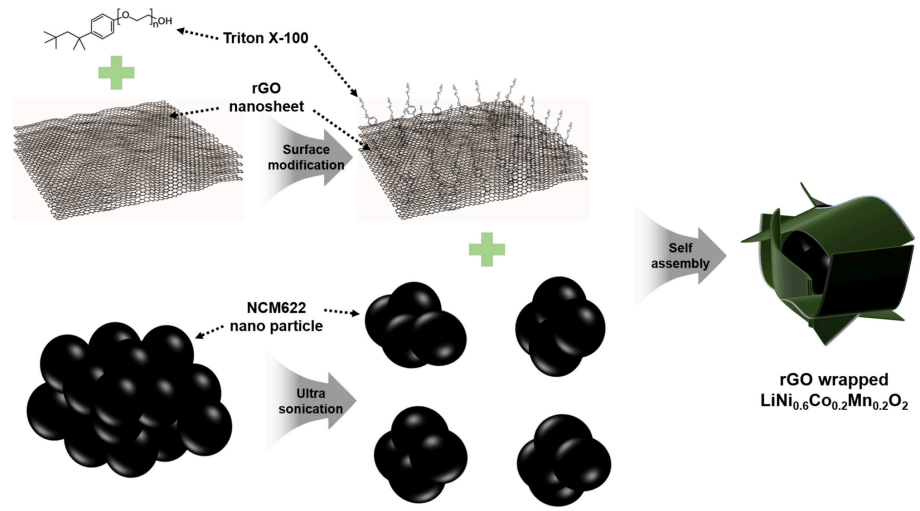

FIGURE 1 | The schematic synthesis procedure of the rGO-wrapped NCM622 composite. The unique NCM622/rGO composite is prepared by a facile self-assembly method using a Triton X-100 surfactant. The hydrophilic part of the rGO sheet easily connects to the NCM622 nanoparticle, effectively decreasing overall contact resistance.

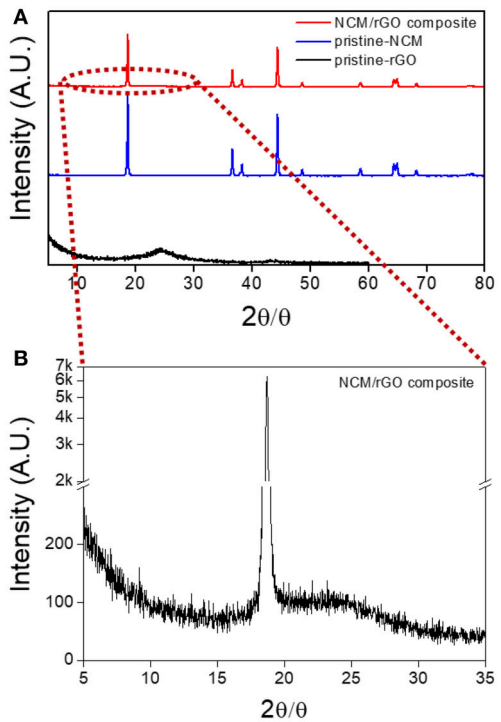

FIGURE 2 | XRD patterns of **(A)** NCM/rGO composite, pristine NCM, and pristine rGO materials; **(B)** the inset image of the NCM/rGO composite in the range of 5–35° to confirm the specific rGO peak. The XRD patterns of the NCM/rGO composite show peaks that closely match those of pristine NCM and pristine rGO without any impurity peaks.

is perfectly consistent with the theoretical electron valence of the $LiNi_{0.6}Co_{0.2}Mn_{0.2}O_2$ material (Tran et al., 2006; Ahn et al., 2014a). From the result of the XRD, it is verified that the cation mixing was not determined, and the low content of Ni^{2+} from XPS analysis also supports the low possibility of Ni/Li cation mixing under raw material preparation by combustion synthesis.

Based on the above physical characterization results, the ultrasonication-assisted self-assembly mechanism of NCM/rGO formation is hypothesized as follows. The surface-activated rGO constructed from rGO with Triton X-100 water suspension suppresses agglomeration of graphene sheets in rGO, resulting in a homogeneously distributed solution. It is noted that the ultrasonication to the rGO sheet is reported to be effective for creating flattened planes of rGO sheets, and this helps to maintain the structure. The highly dispersed flattened rGO sheets then effectively expose a much larger area of graphene surfaces compared to conventional wrinkled rGO sheets that agglomerate much readily, significantly losing their active surface area. This means that the exposure degree of the rGO surface is much larger as well, allowing a higher rate of electrostatic interaction with the NCM material. This prolific interaction between the rGO sheet and the NCM material leads to the generation of a properly distributed composite. In contrast, no ultrasonication under the self-assembly reaction would lead to the formation of separated and aggregated bulk particles either dispersed in the rGO matrix or wrapped by rGO sheets due to the lack of interaction with the exposed surface.

Having created a unique morphology of NCM nanoparticle-distributed rGO and having elucidated its high impact, the electrochemical performance of the cathode composite for lithium ion battery is demonstrated. **Figures 6A,B** shows the charge–discharge profile of the NCM/rGO composite obtained by electrochemical evaluations of the half-cell manufacture at a current density of 20 mA/g. It is noted that the NCM622 material has irreversible capacity during the first cycle, with *ca.* 27.7 mAh/g in our study. The first discharge and second

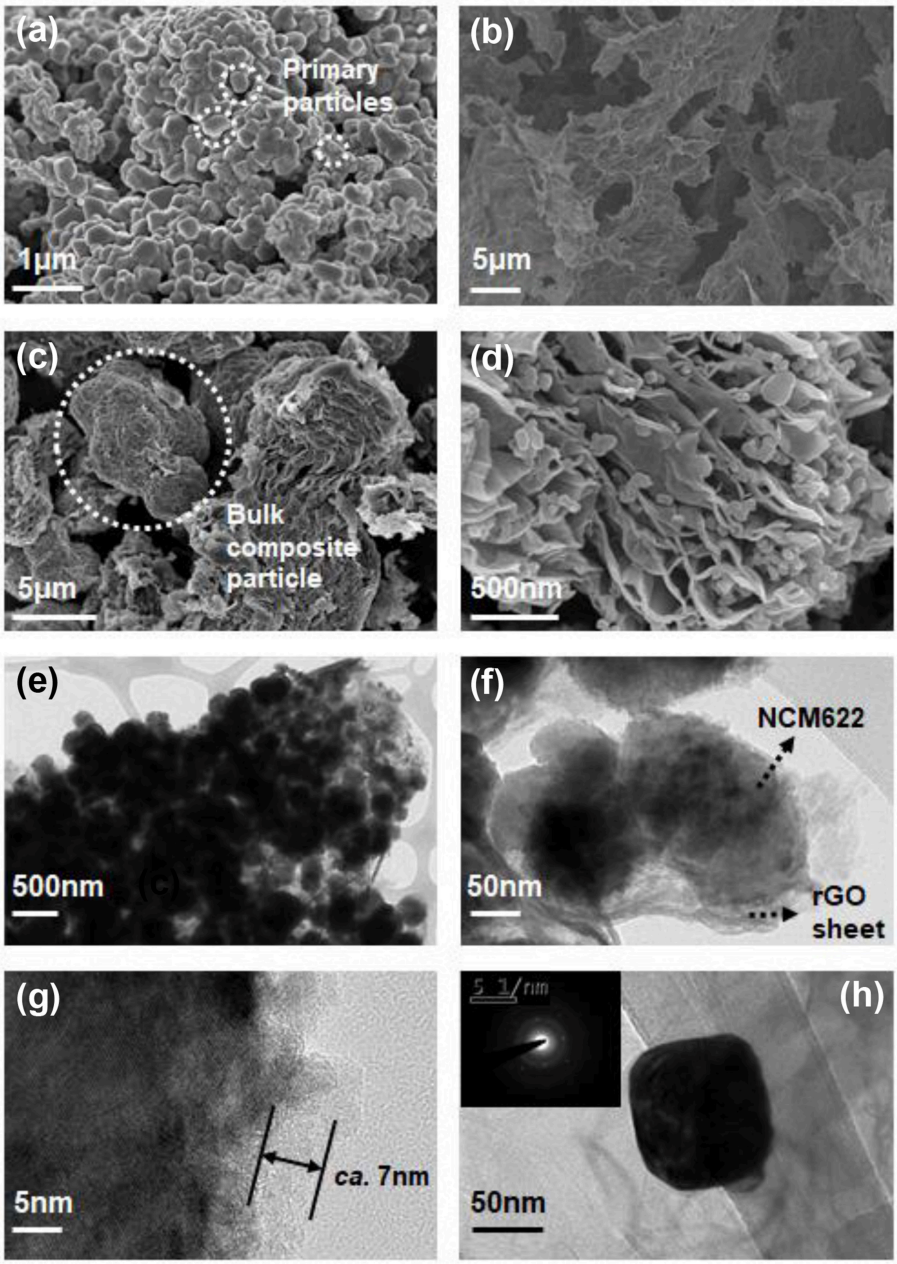

FIGURE 3 | SEM images of various morphologies of **(a)** pristine NCM, **(b)** rGO, and **(c)** NCM/rGO without ultrasonication procedure, and **(d)** NCM/rGO composite ultrasonication-assisted self-assembly. The microscopic morphologies of the NCM/rGO composite **(e–h)**; the NCM/rGO composite without ultrasonication forms aggregated bulk particles after the self-assembly procedure.

charge capacity showed a similar gravimetric capacity of 196.5 mAh/g (see the blue dotted line of the figure), which means only one cycle contributes to the activation and formation of a passive layer on the surface of the cathode material. The average potential during cycle advances is *ca.* 3.75 V until it goes to the 100th cycle, which means that the structure of NCM/rGO is stably maintained. On the other hand, the comparable charge–discharge capacity of the pristine NCM material is shown in **Figure 6C**. The initial capacity of pristine NCM is ∼170 mAh/g, which is lower than that of the NCM/rGO composite. A cycle life and plot of differential capacity (dQ/dV) vs. potential (V) reproduced from the 1st to the 100th discharge–charge profile is presented in **Figures 6D,E**. Two pairs of peaks are observed on the dQ/dV vs. V plot at 3.67 and 3.77 V (vs. Li/Li^+) during charge, and 3.63 and 3.71 V (vs. Li/Li^+) during discharge, respectively. These peaks correspond to the typical characteristic two-step oxidation and reduction reaction of the NCM622 material. As expected,

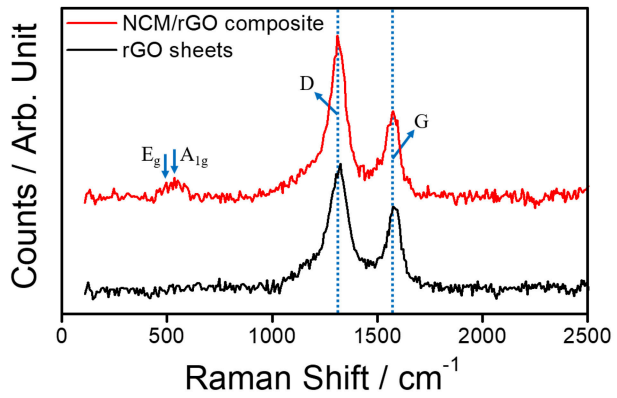

FIGURE 4 | Raman spectra of the pristine rGO sheet and the NCM/rGO composite, which correspond to the specific peak of rGO (D and G) and TM-O (E_g and A_{1g}), respectively.

an outstanding initial discharge capacity of 196.5 mAh/g is observed at a current density of 20 mA/g, and the capacity of 163.4 mAh/g with 83.1% capacity retention even after 100 cycles has been achieved. Due to the formation of a passive layer and activation, the coulombic efficiencies of the initial capacity is only 87.7%; however, 98.1% of the average coulombic efficiency obtained during 100 cycles advanced, and the capacity diminution is 0.33 mAh/g per cycle. Furthermore, the capacity retention of the NCM/rGO composite is 163 mAh/g even after 100 cycles, and this result verifies that the superior capacity retention of the NCM/rGO composite is attributed to the direct connectivity between homogenous rGO sheets and the NCM material. In order to compare overall electrical conductivity, EIS measurement was carried out, and typical Nyquist plots obtained from pristine NCM and the NCM/rGO composite are illustrated in **Figure 6F**. The observed ac-impedance spectra showed relatively low charge transfer resistance for the NCM/rGO composite, which supports an increase in overall electrical conductivity of rGO, and this result is in accordance with the superior initial capacity of the NCM/rGO composite compared with the pristine NCM material. It is noted that the each EIS plot showed two independent semicircles, and the first and second semicircle correspond to the R_f (surface film resistance) and R_{ct} (charge-transfer resistance), which are 48 and 154 Ω for pristine NCM and 41 and 62 Ω for the NCM/rGO composite, respectively. The result in the first semicircle determined that rGO does not affect the formation of a passivation layer, and it only acts as an electric conducting path site for fast charge transfer during advanced electrochemical reaction.

The rate capability and the dQ/dV vs. V plot presented in **Figure 7** show initial capacities of 195 and 140 mAh/g obtained at a current density of 50 and 500 mA/g, respectively. The rate capability performance at those current densities demonstrates reliable capacity even at the high-rate cell test, and this is one of the benefits of EV application. In contrast, the capacity at a current density of 1 A/g showed a relatively low capacity of 65 mAh/g, which is caused by the polarization-concentration resistance and IR drop and the low lithium ion diffusivity of the cathode material.

To further understand the transformation kinetics of lithium ion by calculating practical lithium ion diffusivity during oxidation and reduction reaction under cell operation, GITT measurement was carried out as a function of cell potential. The area and mass loading of the cell are similar with the half-cell test, and the result is presented in **Figure 8**. It is noticed that the lithium ion diffusivity was calculated by the Weppner–Huggins-derived expression (Hess et al., 2015; Ahn et al., 2016a):

$$D_{Li} = \frac{4L^2}{\pi\tau}\left[\frac{\Delta E_s}{\Delta E_t}\right]^2$$

where L and τ refer to the electrode thickness and relaxation time of the current pulse (600 s), respectively, ΔE_s is the steady-state potential change derived from the current pulse, and ΔE_t is the potential difference during the constant current pulse, eliminating the iR drop. The resultant lithium ion diffusivity as a function of charge and discharge in **Figures 8B,D** respectively, shows several inflection points, as pointed out by the red arrows. Each inflection point is a determined step of lithium ion diffusion, which is attributed to the dominant region of lithium deintercalation, lithium ion migration as solvated ion in the electrolyte, aggregation on the surface of Li metal, lithium ion plating on the Li metal anode, and the complete lithium reduction on anode during charging step advances. The reversible determined reaction was obtained during discharge with dominant state of lithium stripping from the Li metal anode, lithium ion migration in electrolyte, aggregation on the surface of NCM, and lithium ion diffusion into the bulk particle of NCM. All the GITT results exhibit a similar tendency toward a conventional plot shape for the lithium ion diffusion state. The lithium ion diffusivities of NCM/rGO have been measured at five distinct points as the aforementioned determining steps during charge and discharge procedures, specifying five dominant split reactions as summarized in **Table 1** and plotted in **Figure 8**. First, at the starting point of the charging reaction, the lithium ion begins to diffuse from the bulk NCM particle; then, it starts to migrate toward the organic electrolyte as a solvated ion until reaching 2.20 V. From this step, most of the lithium ions exist inside the bulk particle; thus, the dominant determining step is the migration of the Li ion toward the electrolyte, which is maintained until the concentration of the solvated ion in the electrolyte has increased (2.56 V), resulting in the decrease in lithium ion diffusivity as presented in **Figure 8B**. Then, lithium ion diffusivity is slightly increased up to 2.78 V, which is attributed to the starting point of aggregation on the surface of the Li anode from the lithium ion migration dominant step, resulting in increased lithium ion diffusivity. The lithium ion starts to plate onto the Li anode from the aggregated solvated ion, and this step is also associated with the decrease in the amount of lithium ion in the electrolyte, which is maintained until 3.65 V. From this step, the lithium ion starts to show low kinetics, which is accompanied by a charge transfer reaction of the lithium ion from a solvated electrolyte molecule to the Li metal anode. Finally, lithium

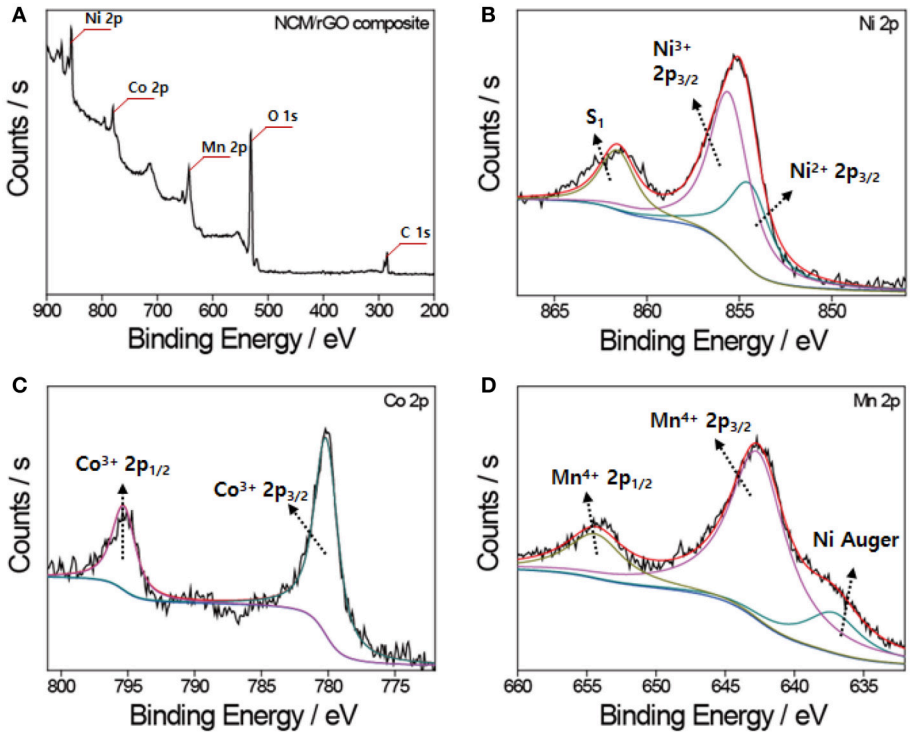

FIGURE 5 | XPS analysis of the NCM/rGO composite. **(A)** The survey XPS spectra of the NCM-rGO composite confirming the existence of expected elements. XPS results of **(B)** Ni 2p spectra, **(C)** Co 2p spectra, and **(D)** Mn 2P spectra. The characteristic peaks of each transition metal element are identified in accordance with our previous research.

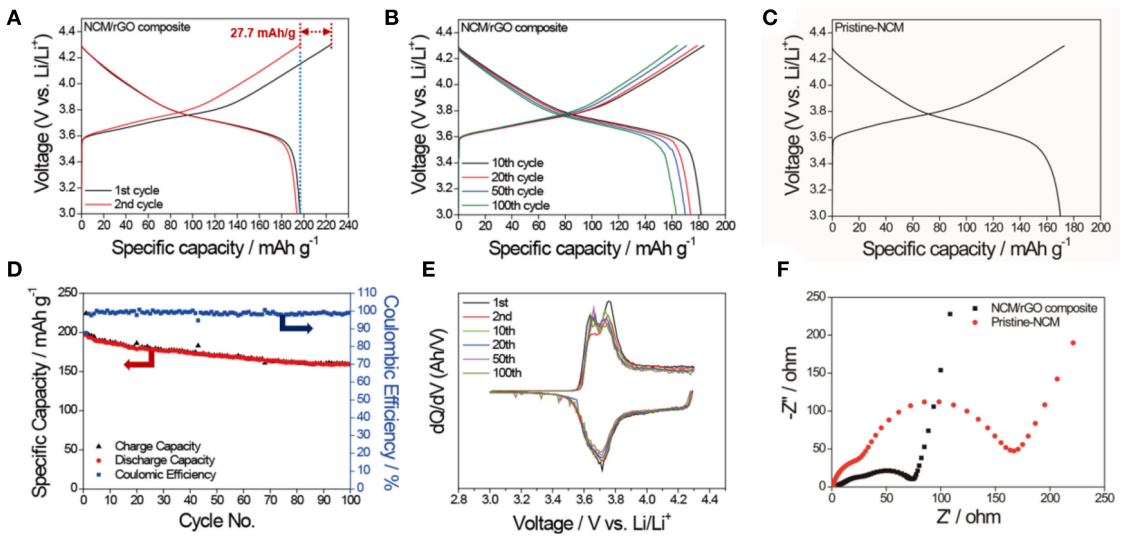

FIGURE 6 | (A) The initial charge–discharge profile of the NCM/rGO composite at a current density of 20 mA/g, and **(B)** the stable charge–discharge profiles from the 10th to the 100th cycle. **(C)** The comparison charge–discharge profile of the pristine NCM material, which shows a lower initial capacity than the NCM/rGO composite. **(D)** Cycle durability test and corresponding coulombic efficiency obtained at a current density of 20 mA/g. **(E)** d*Q*/d*V* curves based on the charge–discharge profile from the 1st to the 100th cycle. **(F)** Comparison Nyquist plots obtained from pristine NCM and the NCM/rGO composite.

ion diffusivity is stabilized from 3.65 V to the end point of 4.50 V with lowest kinetic reaction in this potential range. The transformation kinetics of the lithium ion during the charge procedure can be divided into four steps, and these individual reaction steps show a similar lithium ion diffusion rate at the discharge procedure. These four distinct steps of transformation

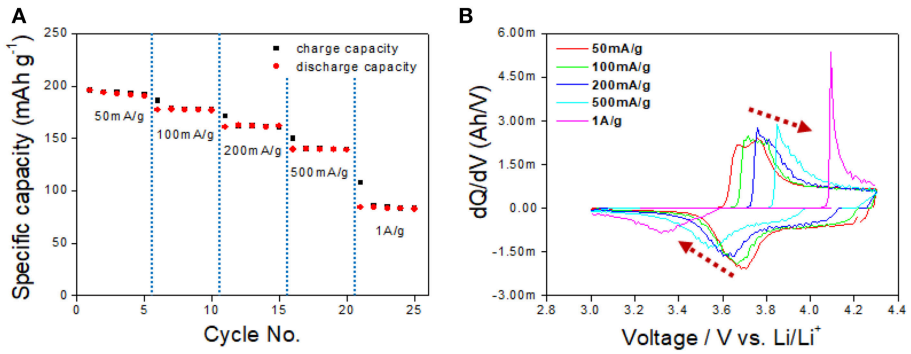

FIGURE 7 | (A) The rate capability test at a current density of 50 mA/g to 1 A/g. **(B)** dQ/d*V* curve based on the rate capability performance result.

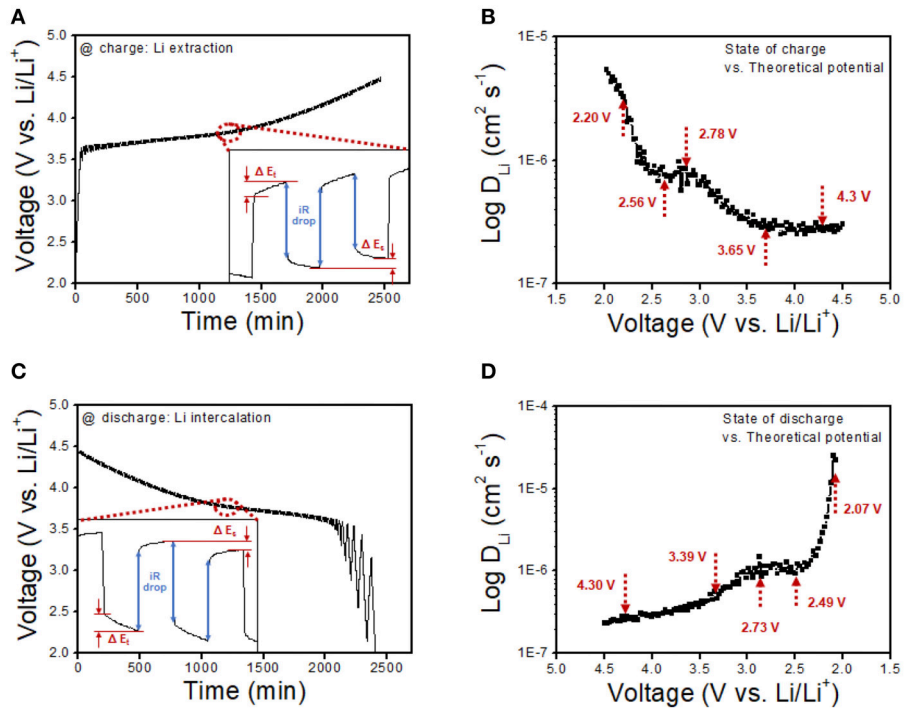

FIGURE 8 | Galvanostatic intermittent titration technique (GITT) curves vs. time at **(A)** the charge procedure and **(C)** the discharge procedure. The duration of the charge and discharge pulses was calculated based on a current density of 20 mA/g. **(B,D)** Lithium diffusivities of the NCM/rGO composite during the charge and discharge procedure as a function of the cell potential. Each inflection point refers to the transformational kinetics in depth of lithium diffusion followed by GITT measurement results.

kinetic reactions show a similar tendency at the discharge procedure. From the resultant transformation kinetics of the lithium ion during charge–discharge advances, the high lithium ion diffusion could be verified at the cathode electrode part where the lithium ion intercalation–deintercalation procedure was carried out on the surface of the material. It should be noted that lithium ion intercalation–deintercalation is accompanied by charge transfer at the solid–electrolyte interface; hence, the highly electrically conductive material determines the relatively rapid charge transfer of the lithium ion. Even the dominant part of this reaction is lithium ion diffusion in the interlayer of the cathode slab, the charge transfer barrier is the key role in the rate determining step of lithium ion mobility. Therefore, the highly electrically conductive rGO-wrapped NCM composite shows relatively high lithium ion diffusivity (D_{Li}: 5.34×10^{-6}) compared with the plating process on the Li metal anode (D_{Li}: 2.67×10^{-7}) in this work and our previous study on pristine NCM622 material (24) (D_{Li}: 4.03×10^{-14}). As a result, it is explained that the dominant kinetic reaction in each step denotes lithium ion diffusivity, resulting in a correlation with the high electric conductivity of the active material.

TABLE 1 | Lithium ion diffusivity of the NCM/rGO composite obtained at five distinct potentials during charge–discharge advances.

State	Electrochemical state at charge					Electrochemical state at discharge				
Potential	2.02 V	2.56 V	2.78 V	3.65 V	4.30 V	4.30 V	3.39 V	3.03 V	2.49 V	2.07 V
D_{Li} (cm^2/s)	5.34×10^{-6}	6.77×10^{-7}	9.74×10^{-7}	2.86×10^{-7}	2.67×10^{-7}	2.81×10^{-7}	5.2×10^{-7}	9.79×10^{-7}	9.22×10^{-7}	2.2×10^{-6}

CONCLUSIONS

In summary, a homogeneous and uniformly self-assembled rGO-wrapped NCM622 composite for lithium ion batteries has been successfully synthesized by using an ultrasonication-assisted self-assembly method under a Triton X-100 surfactant environment, and the electrochemical properties of cell performance with lithium ion transformation kinetics on the cathode and anode side has been verified. Based on XRD results, ultrasonication indicates a homogeneous mixture of the composite, and the high electrical conductivity of the composite supports this result. The morphology and microstructure of the composite indicated that ultrasonication could effectively pulverize the composite into uniform primary nanoparticles. The rGO-wrapped NCM622 composite exhibits excellent performance with a high specific capacity of 196.5 mAh/g at the initial discharge capacity and 163 mAh/g after 100 cycles with 83% capacity retention at 20 mA/g current density. Furthermore, the discharge capacity with rate capability test showed 140 and 65 mAh/g at 500 mA/g and 1 A/g current density, respectively. The high-rate capability is attributed to the transformation kinetics of lithium ion accompanied by a charge-transfer reaction, which, as confirmed by GITT measurement, likely to have originated from the highly conductive electron paths formed by the perfectly connected NCM622 material on rGO sheets. Based on the enhanced cycle and high-rate performance, it can be concluded that the NCM/rGO composite is a promising cathode material for rechargeable lithium ion batteries, which is highly applicable to the EV field.

AUTHOR CONTRIBUTIONS

All authors listed have made substantial, direct and intellectual contribution to the work, and approved it for publication.

FUNDING

This research was supported by the Korea Institute of Energy Technology Evaluation and Planning (KETEP) and the Ministry of Trade, Industry & Energy (MOTIE) of the Republic of Korea (No. 20184030202130), as well as by the Soonchunhyang University Research Fund (No. 20170811).

REFERENCES

Ahn, W., Lee, D. U., Li, G., Feng, K., Wang, X., Yu, A., et al. (2016a). Highly oriented graphene sponge electrode for ultra-high energy density lithium ion hybrid capacitors. *ACS Appl. Mater. Interfaces* 8, 25297–25305. doi: 10.1021/acsami.6b08298

Ahn, W., Lim, S. N., Jung, K. N., Yeon, S. H., Kim, K. B., Song, H. S., et al. (2014a). Combustion-synthesized $LiNi_{0.6}Mn_{0.2}Co_{0.2}O_2$ as cathode material for lithium ion batteries. *J. Alloys Compd.* 609, 143–149. doi: 10.1016/j.jallcom.2014.03.123

Ahn, W., Park, M. G., Lee, D. U., Seo, M. H., Jiang, G., Cano, Z. P., et al. (2018). Hollow multivoid nanocuboids derived from ternary Ni–Co–Fe prussian blue analog for dual-electrocatalysis of oxygen and hydrogen evolution reactions. *Adv. Funct. Mater.* 28:1802129. doi: 10.1002/adfm.201802129

Ahn, W., Seo, M. H., Jun, Y. S., Lee, D. U., Hassan, F. M., Wang, X., et al. (2016b). Sulfur nanogranular film-coated three-dimensional graphene sponge-based high power lithium sulfur battery. *ACS Appl. Mater. Interfaces* 8, 1984–1991. doi: 10.1021/acsami.5b10267

Ahn, W., Song, H. S., Park, S. H., Kim, K. B., Shin, K. H., Lim, S. N., et al. (2014b). Morphology-controlled graphene nanosheets as anode material for lithium-ion batteries. *Electrochim. Acta* 132, 172–179. doi: 10.1016/j.electacta.2014.03.078

Byeon, P., Bae, H. B., Chung, H. S., Lee, S. G., Kim, J. G., Suh, I. H., et al. (2018). Atomic-scale observation of $LiFePO_4$ and $LiCoO_2$ dissolution behavior in aqueous solutions. *Adv. Funct. Mater.* 28:1804564. doi: 10.1002/adfm.201804564

Cano, Z. P., Banham, D., Ye, S., Hintennach, A., Lu, J., Fowler, M., et al. (2018). Batteries and fuel cells for emerging electric vehicle markets. *Nat. Energy* 3, 279–289. doi: 10.1038/s41560-018-0108-1

Catenacci, M., Banham, D., Ye, S., Hintennach, A., Lu, J., Fowler, M., et al. (2013). Going electric: expert survey on the future of battery technologies for electric vehicles. *Energy Policy* 61, 403–413. doi: 10.1016/j.enpol.2013.06.078

Fu, J., Mu, D., Wu, B., Bi, J., Cui, H.0, Yang, H., et al. (2018). Electrochemical properties of the $LiNi_{0.6}Co_{0.2}Mn_{0.2}O_2$ cathode material modified by lithium tungstate under high voltage. *ACS Appl. Mater. Interfaces* 10, 19704–19711. doi: 10.1021/acsami.8b04167

Hess, A., Roode-Gutzmer, Q., Heubner, C., Schneider, M., Michaelis, A., Bobeth, M., et al. (2015). Determination of state of charge-dependent asymmetric Butler–Volmer kinetics for $LixCoO_2$ electrode using GITT measurements. *J. Power Sources* 299, 156–161. doi: 10.1016/j.jpowsour.2015.07.080

Ju, S. H., Kang, I. S., Lee, Y. S., Shin, W. K., Kim, S., Shin, K., et al. (2014). Improvement of the cycling performance of LiNi(0.6)Co(0.2)Mn(0.2)O(2) cathode active materials by a dual-conductive polymer coating. *ACS Appl. Mater. Interfaces* 6, 2546–2552. doi: 10.1021/am404965p

Ju, X., Huang, H., He, W., Zheng, H., Deng, P., Li, S., et al. (2018). Surfactant-assisted synthesis of high energy {010} facets beneficial to Li-ion transport kinetics with layered $LiNi_{0.6}Co_{0.2}Mn_{0.2}O_2$. *ACS Sust. Chem. Eng.* 6, 6312–6320. doi: 10.1021/acssuschemeng.8b00126

Kim, H., Kim, M. G., Jeong, H. Y., Nam, H., and Cho, J. (2015). A new coating method for alleviating surface degradation of $LiNi_{0.6}Mn_{0.2}O_2$ cathode material: nanoscale surface treatment of primary particles. *Nano Lett.* 15, 2111–2119. doi: 10.1021/acs.nanolett.5b00045

Kucinskis, G., Bajars, G., and Kleperis, J. (2013). Graphene in lithium ion battery cathode materials: a review. *J. Power Sources* 240, 66–79. doi: 10.1016/j.jpowsour.2013.03.160

Li, N., Wang, Y., Tang, D., and Zhou, H. (2015). Integrating a photocatalyst into a hybrid lithium-sulfur battery for direct storage of solar energy. *Angew. Chem. Int. Ed. Engl.* 54, 9271–9274. doi: 10.1002/anie.201503425

Liao, B., Hu, X., Xu, M., Li, H., Yu, L., Fan, W., et al. (2018). Constructing unique cathode interface by manipulating functional groups of electrolyte additive for graphite/$LiNi_{0.6}Co_{0.2}Mn_{0.2}O_2$ cells at high voltage. *J. Phys. Chem. Lett.* 9, 3434–3445. doi: 10.1021/acs.jpclett.8b01099

Lim, S. N., Ahn, W., Yeon, S. H., and Park, S. B. (2014a). Preparation of a reduced graphene oxide wrapped lithium-rich cathode material by self-assembly. *Chem. Asian J.* 9 , 2946–2952. doi: 10.1002/asia.201402517

Lim, S. N., Ahn, W., Yeon, S. W., and Park, S. B. (2014b). Enhanced elevated-temperature performance of $Li(Ni_{0.8}Co_{0.15}Al_{0.05})O_2$ electrodes coated with Li_2O-$2B_2O_3$ glass. *Electrochim. Acta* 136, 1–9. doi: 10.1016/j.electacta.2014.05.056

Lim, S. N., Seo, J. Y., Jung, D. S., Ahn, W., Song, H. S., Yeon, S. H., et al. (2015). Rate capability for Na-doped $Li_{1.167}Ni_{0.18}Mn_{0.548}Co_{0.105}O_2$ cathode material and characterization of Li-ion diffusion using galvanostatic intermittent titration technique. *J. Alloys Compd.* 623, 55–61. doi: 10.1016/j.jallcom.2014.09.203

Lin, D., Liu, Y., and Cui, Y. (2017). Reviving the lithium metal anode for high-energy batteries. *Nat. Nanotechnol.* 12, 194–206. doi: 10.1038/nnano.2017.16

Majeau-Bettez, G., Hawkins, T. R., and Strømman, A. H. (2011). Life cycle environmental assessment of lithium-ion and nickel metal hydride batteries for plug-in hybrid and battery electric vehicles. *Environ. Sci. Technol.* 45, 4548–4554. doi: 10.1021/es103607c

Patey, T. J., Hintennach, A., Mantia, F. L., and Novák, P. (2009). Electrode engineering of nanoparticles for lithium-ion batteries—Role of dispersion technique. *J. Power Sourc.* 189, 590–593. doi: 10.1016/j.jpowsour.2008.09.091

Salitra, G., Markevich, E., Afri, M., Talyosef, Y., Hartmann, P., Kulisch, J., et al. (2018). High-performance cells containing lithium metal anodes, $LiNi_{0.6}Co_{0.2}Mn_{0.2}O_2$. (NCM 622) cathodes, and fluoroethylene carbonate-based electrolyte solution with practical loading. *ACS Appl. Mater. Interfaces* 10, 19773–82. doi: 10.1021/acsami.8b07004

Seo, M. H., Park, M. G., Lee, D. U., Wang, X., Ahn, W., Noh, S., H., et al. (2018). Bifunctionally active and durable hierarchically porous transition metal-based hybrid electrocatalyst for rechargeable metal–air batteries. *Appl. Catal. B* 239, 677–687. doi: 10.1016/j.apcatb.2018.06.006

Shim, J. H., Kim, Y. M., Park, M., Kim, J., and Lee, S. (2017). Reduced graphene oxide-wrapped nickel-rich cathode materials for lithium ion batteries. *ACS Appl. Mater. Interfaces* 9, 18720–18729. doi: 10.1021/acsami.7b02654

Tran, N., Croguennec, L., Labrugère, C., Jordy, C., Biensan, P. H., and Delmas, C. (2006). Layered $Li_{1+x}(Ni_{0.425}Mn_{0.425}Co_{0.15})_{1--x}O_2$ positive electrode materials for lithium-ion batteries. *J. Electrochem. Soc.* 153:A261. doi: 10.1149/1.2138573

Venkateswara Rao, C., Leela Mohana Reddy, A., Ishikawa, Y., and Ajayan, P. M. (2011). LiNi(1)/(3)Co(1)/(3)Mn(1)/(3)O(2)-graphene composite as a promising cathode for lithium-ion batteries. *ACS Appl. Mater. Interfaces* 3, 2966–2972. doi: 10.1021/am200421h

Yang, J., Wang, J., Wang, D., Li, X., Geng, D., Liang, G., et al. (2012). 3D porous $LiFePO_4$/graphene hybrid cathodes with enhanced performance for Li-ion batteries. *J. Power Sources* 208, 340–344. doi: 10.1016/j.jpowsour.2012.02.032

Zhao, H., Wu, Q., Hu, S., Xu, H., and Rasmussen, C. N. (2015). Review of energy storage system for wind power integration support. *Appl. Energy* 137, 545–553. doi: 10.1016/j.apenergy.2014.04.103

Conflict of Interest Statement: The authors declare that the research was conducted in the absence of any commercial or financial relationships that could be construed as a potential conflict of interest.

frontiers in Chemistry

ORIGINAL RESEARCH
published: 06 June 2019
doi: 10.3389/fchem.2019.00415

Template-Free Electrochemical Growth of Ni-Decorated ZnO Nanorod Array: Application to an Anode of Lithium Ion Battery

Han Nah Park[1,2‡], *Sun Hwa Park*[1‡], *Jeong Ho Shin*[1†], *Soo-Hwan Jeong*[2*] and *Jae Yong Song*[1*]

[1] Center for Convergence Property Measurement, Korea Research Institute of Standards and Science, Daejeon, South Korea, [2] Department of Chemical Engineering, Kyungpook National University, Daegu, South Korea

OPEN ACCESS

Edited by:
Syed Mubeen Jawahar Hussaini,
The University of Iowa, United States

Reviewed by:
Lili Xing,
University of Electronic Science and Technology of China, China
Piercarlo Mustarelli,
University of Milano-Bicocca, Italy

***Correspondence:**
Soo-Hwan Jeong
shjeong@knu.ac.kr
Jae Yong Song
jysong@kriss.re.kr

†Present Address:
Jeong Ho Shin,
Office of Information and Smart Factory for Firms, Korea Technology and Information Promotion Agency for SMEs, Daejeon, South Korea

‡These authors have contributed equally to this work

Specialty section:
This article was submitted to Electrochemistry, a section of the journal Frontiers in Chemistry

Received: 18 January 2019
Accepted: 20 May 2019
Published: 06 June 2019

Citation:
Park HN, Park SH, Shin JH, Jeong S-H and Song JY (2019) Template-Free Electrochemical Growth of Ni-Decorated ZnO Nanorod Array: Application to an Anode of Lithium Ion Battery. Front. Chem. 7:415. doi: 10.3389/fchem.2019.00415

ZnO nanorods (NRs) decorated with Ni nanoparticles were synthesized using a template-free electrochemical deposition in an ultra-dilute aqueous electrolyte and a subsequent galvanic reaction. The electrochemical properties of the ZnO NRs as an anode material for rechargeable Li-ion batteries were evaluated for different binder morphologies (film and close-packed spherical particles) of polyvinylidene fluoride (PVDF). Results showed that the close-packed spherical PVDF simultaneously improved electrochemical capacity and cyclability because the free-volume between the spherical PVDF helped to accommodate the volume change in the anode caused by the Li ions discharge and charge processes. Furthermore, the Ni nanoparticles decorated on the surface of ZnO NRs enhanced the electrical conductivity of the ZnO NR anode, which enabled faster electronic and ionic transport at the interface between the electrolyte and the electrode, resulting in improved electrochemical capacity. The free-volume formed by the close-packed spherical PVDF, and the decoration of metal nanoparticles are expected to provide insight on the simultaneous improvement of electrochemical capacity and cyclability in other metal oxide anode nanostructures.

Keywords: ZnO, nanorod, electrochemical property, spherical PVDF, Ni nanoparticle

INTRODUCTION

Rechargeable Li-ion batteries (LIBs) have been widely used for energy storage in portable devices such as cellular phones, cameras, and lap-top computers (Tarascon and Armand, 2001; Li et al., 2009; Scrosati and Garche, 2010). However, there are still several challenging issues that need to be resolved to improve LiB performance. For example, to meet the increasing demand for LiBs with higher energy density, the capacity of the anode must be improved, because the Li storage capacity of commercialized graphite anode is limited to the theoretical maximum capacity of 372 mAh/g (Tokumitsu et al., 1999; Li et al., 2009; Liu and Cao, 2010). For this reason, extensive studies have focused on developing new anode materials to replace graphite. Transition metal oxides (MO, M = Fe, Co, Ni, Cu, and Zn) in particular have attracted much attention because the electrochemical capacities of these materials are two times higher than that of graphite (Park et al., 2009; Huang et al., 2012; Caballero et al., 2013; He et al., 2013; Yanga et al., 2013). Among them, ZnO has several advantages, including high theoretical capacity (978 mAh/g), low cost and chemical stability (Zhang et al., 2007, 2016; Pan et al., 2010; Huang et al., 2011). Unfortunately, ZnO has a critical

drawback. The anode is mechanically disintegrated by the large volume expansion and shrinkage that occurs with the reaction of ZnO and Li, and this degrades structural stability and electrical conductivity, affecting electrochemical performance (Belliard and Irvine, 2001; Laurenti et al., 2015; Song et al., 2017). To avoid this degradation, several nanostructures have been investigated in anodes, including nanorods, nanosheets, nanoparticles, and porous nanostructures (Belliard and Irvine, 2001; Zhang et al., 2007; Huang et al., 2011, 2014a; Laurenti et al., 2015). Vertically aligned nanorods are expected to accommodate the huge volume changes, while providing faster transport of charge carriers, due to the free volume between the nanorods, high specific surface area and short diffusion path (Liu et al., 2009; Wang et al., 2009).

In the present study, we were motivated to synthesize a vertically aligned ZnO NR array using a low-cost template-free electrochemical deposition method, which was developed to grow a nanorod array of pure metals (Au, Ag, and Cu) and metal oxide (Cu_2O) (Park et al., 2013a,b; Shin et al., 2014). And, instead of using a polyvinylidene fluoride (PVDF) film structure, close-packed spherical nanoparticles of PVDF (sPVDF) were used to reduce the large volume expansion caused by Li intercalation. For faster transport of charge carriers, Ni nanoparticles were decorated on the surface of ZnO NRs using electroless deposition. The improved electrochemical performance of the sPVDF-embedded ZnO NRs decorated with Ni nanoparticles was then investigated.

EXPERIMENTAL

Preparation of ZnO Nanostructures

ZnO NRs were synthesized using a potentiodynamic electrodeposition process. The electrodeposition was carried out with a three-electrode system (Solartron 1280z). The working electrode was Cu foil (99.8 at%, Nippon Foil Mfg, Co.) with an exposed area of 1.5 × 1.5 cm^2. Pt wire (Aldrich) and KCl–saturated Ag/AgCl were used as the counter and reference electrodes, respectively. The electrolyte was composed of 100 μM $ZnCl_2$ (Aldrich) in deionized water and set at 40°C. The pH and conductivity of the electrolyte were 5.5 and 24 μS/cm, respectively. In the potentiodynamic mode, the reduction potential (V_R) and oxidation potential (V_O) were set to be −8 V and +0.5 V. The duty and frequency of the potentiodynamic mode were 50% and 1 Hz, respectively. For the deposition of Ni nanoparticles on the surface of ZnO NRs, we conducted electroless Ni plating in an aqueous solution of 95 mM $NiSO_4{\cdot}6H_2O$ and 284 mM $NaPH_2O_2$. The pH value of the solution was set to be 6.0 by adding 21.9 mM NaOH. Commercial sPVDF (Kynar HSV 900) nanoparticles were used. The sPVDF nanoparticles were dispersed in 15 wt% acetone and several spin-coatings were conducted until they were completely infiltrated between the NRs.

Structural Characterization

A field emission scanning electron microscope (FE–SEM, Hitachi S−4800) was employed for the morphological characterization of the samples. The crystal structures and components of the ZnO nanostructures were analyzed using x-ray diffraction (XRD, Cu–K, Rigaku D/max–B), field emission transmission electron microscope (FE–TEM, FEI Tecnai F30), and energy dispersive x-ray spectrometry (EDS, EDAX Genesis XM4).

Measurement of Electrochemical Properties

The electrochemical properties of the ZnO nanostructures as an LIB anode were investigated using a CR2032 coin cell. Li metal foil was used as a counter electrode and the separator was microporous polyethylene (Celgard 2400). The electrolyte was a 1 mol/L $LiPF_6$ in a 1:1 (v/v ratio) mixture of ethylene carbonate and diethyl carbonate (Techno Semichem Co.). Galvanostatic charge-discharge tests were carried out using an automatic battery test system (Wonatech Co., WBCS3000S) in the voltage window of 0.05–2.4 V (vs. Li/Li^+) with a rate of 0.5 C. The cyclic voltammetry (CV) measurement was conducted at a rate of 1 mV/s. The electrochemical impedance spectrometry (EIS) measurement was carried out with a range of 0.1 Hz to 100 kHz.

RESULTS AND DISCUSSIONS

Figure 1 shows the morphological and crystal structure characterization of the ZnO NRs and the Ni nanoparticle-decorated ZnO NRs. Short ZnO NRs (less than 500 nm in length and 200 nm in diameter) were densely grown on Cu substrates, and then long ZnO NRs (more than 10 μm in length and 800 nm in diameter) were sparsely grown, as shown in **Figure 1A**. Sharp ZnO NRs were grown, with an apex on top (Qiu et al., 2011; Spitsina and Kahrizi, 2012). This might suggest that the growth of the ZnO NRs was caused by electric field enhancement in the dilute electrolyte (Elias et al., 2008). The possible reactions during the electrodeposition of ZnO NRs in the acidic electrolyte can be described, as follows (Qiu et al., 2011; Spitsina and Kahrizi, 2012):

$$O_2 + 2H_2O + 4e^- \rightarrow 4OH^- \quad (1)$$

$$Zn^{2+} + 2OH^- \rightarrow Zn(OH)_2 \quad (2)$$

$$Zn(OH)_2 \rightarrow ZnO + H_2O \quad (3)$$

According to Equation (1), water decomposition generates hydroxyl ions (OH^-) near the cathode, where an alkaline state is locally formed (Manzano et al., 2013). Zn cations in the electrolyte react with hydroxyl ions, and zinc hydroxide is formed following Equation (2). Subsequently, the zinc hydroxide undergoes a dehydration process, as shown in Equation (3). This might be ascribed to the high electric field in the dilute electrolyte, which is similar to the previous result, which found that Cu_2O nanorods grew in a dilute acidic electrolyte of copper sulfate (Shin et al., 2014).

The ZnO NRs had a hexagonal crystal structure (JCPDS # 36-1451) and grew in the longitudinal <002> direction, as indexed in the TEM analyses shown in **Figure 1B**. The preferred growth of the ZnO NRs was confirmed by XRD analyses, which indicated that the (002) peak was the strongest (see supporting information, **Figure S1**). **Figure 1C** shows that Ni nanoparticles (20–50 nm in size) marked by red arrows have formed on the

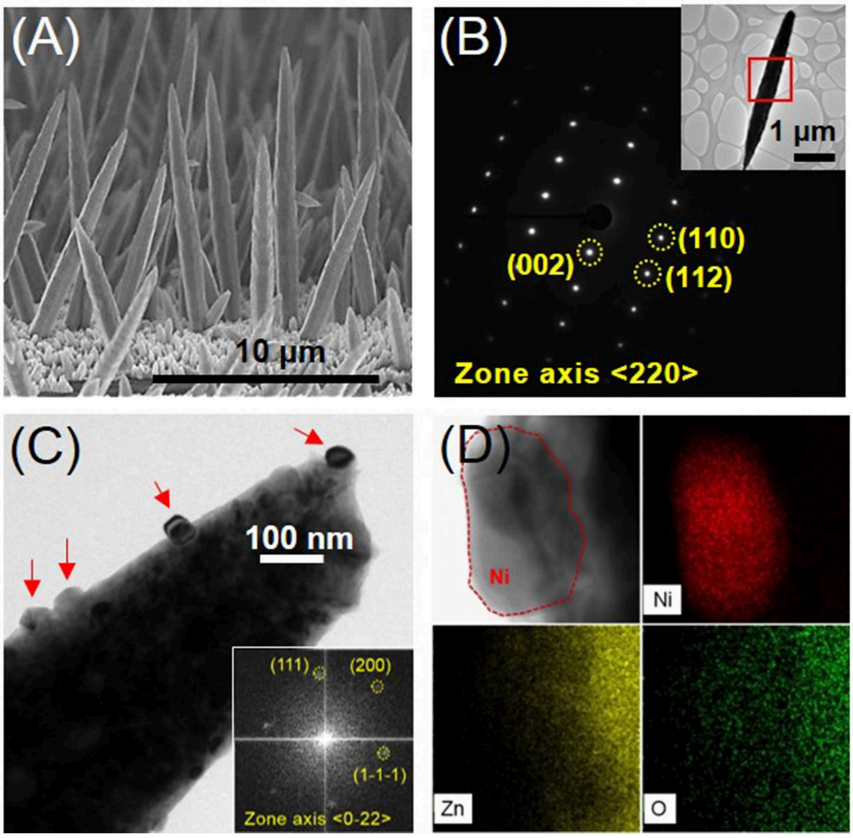

FIGURE 1 | (A) Cross-sectional SEM image of the ZnO NRs grown on Cu foil, **(B)** SAED (Selected Area Electron Diffraction) pattern of the position marked in the inset of a single ZnO nanorod, **(C)** BF (bright field) TEM image of Ni-decorated ZnO NR (The right inset indicates the FFT (Fast Fourier Transform) pattern of a Ni nanoparticle, corresponding to the red-dashed position in the left inset TEM image, on the surface of a ZnO NR.) **(D)** BFTEM image and EDS mappings according to the compositional elements Ni, Zn, and O on the surface of Ni-coated ZnO NRs.

surface of the ZnO NRs, obtained from the EDS mapping analyses in **Figure 1D**. XRD peaks were not observed for the Ni phase due to the small amount of Ni nanoparticles (**Figure S1**). However, the TEM analyses of the Ni nanoparticle shown in the inset of **Figure 1C** was indexed to have a face-centered cubic crystal structure (JCPDS # 04-0850) and the Ni-decorated ZnO NRs had identical crystal structures. The electroless deposition of Ni nanoparticles by hypophosphite reduction in nickel sulfate is represented as follows (Iniewski, 2011).

$$Ni^{2+} + H_2PO_{2^-} + H_2O \rightarrow Ni + 2H^+ + H(HPO_3)^- \quad (4)$$

The ZnO NRs directly grown on Cu foil were then electrochemically evaluated as an anode in an LIB. Four kinds of anodes were prepared, for comparison, i.e., as-prepared ZnO NRs, ZnO NRs embedded in PVDF film, sPVDF-infiltrated ZnO NRs, and sPVDF-infiltrated ZnO NRs decorated with Ni nanoparticles, respectively, as shown in **Figures 2A–D**. The typical top-view SEM images of ZnO NRs in PVDF film and ZnO NRs in sPVDF particles are shown in **Figures 2E,F**, respectively. The ZnO NRs were fully embedded in the PVDF film, as shown in **Figure 2E**, while the sPVDF particles were densely packed between ZnO NRs by several spin-coatings, as shown in **Figure 2F**. As shown in the inset of **Figure 2F**, the ZnO NRs were surrounded by the sPVDF particles with an average size of 150 nm.

Figure 3 shows the discharge-charge voltage profiles of the four ZnO NRs samples obtained between 0.05 and 2.4 V (vs. Li/Li^+) at the rate of 0.5 C. According to previous studies (Zhang et al., 2007; Huang et al., 2011; Laurenti et al., 2015), the electrochemical Li-storage mechanism of ZnO is composed of two reversible reactions, as noted below.

$$ZnO + 2Li^+ + 2e^- \leftrightarrow Zn + Li_2O \quad (5)$$

$$Zn + xLi^+ + xe^- \leftrightarrow Li_xZn\ (x \leq 1) \quad (6)$$

The behavior of the voltage profiles of the four ZnO NRs anodes was similar. The 1st discharge curves of the four anodes exhibited long voltage plateaus at 0.5 V, but the 1st charge curves showed shorter plateaus at 1.4 V. It can be seen that the 1st voltage profiles are somewhat irreversible due to the typical characteristics of transition-metal oxides (Huang et al., 2014b). In particular, the sPVDF-infiltrated ZnO NRs and the sPVDF-infiltrated ZnO NRs decorated with Ni nanoparticles exhibited 1st discharge capacities of 1,459 and 1,902 mAh/g, which are higher than the theoretical value of ZnO (978 mAh/g). The excess

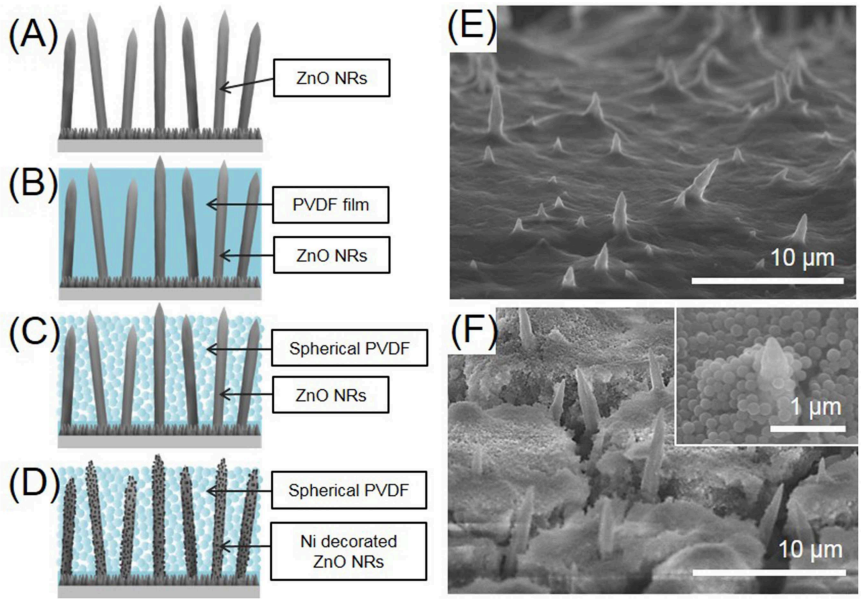

FIGURE 2 | Schematic diagrams of **(A)** as-prepared ZnO NRs, **(B)** ZnO NRs embedded in PVDF film, **(C)** sPVDF-infiltrated ZnO NRs, and **(D)** sPVDF-infiltrated ZnO NRs decorated with Ni nanoparticles. The top-view SEM image of **(E)** ZnO NRs in PVDF film and **(F)** sPVDF-infiltrated ZnO NRs.

capacities are caused by the formation of irreversible Li_2O and a solution electrolyte interface (SEI) layer, as well as electrolyte decomposition in the low potential window (Zhang et al., 2007; Huang et al., 2014b; Shen and Wang, 2015). After the 2nd voltage profiles, the reactions of the four anodes became more reversible. And the plateaus on the voltage profiles coincided with the peaks in the CV curves.

Figure S2A shows the CV curves of sPVDF-infiltrated ZnO NRs between 0.05 and 2.4 V (vs. Li/Li^+) at a scan rate of 1 mV/s. In the 1st cathodic reaction, there is only one peak below 0.3 V due to the irreversible reaction. For the 2nd and 5th cycles, the CV curves indicate a more reversible electrode reaction since the curves almost coincide in shape. The CV curves also exhibit typical reduction and oxidation peaks, indicating the Li-storage mechanism of ZnO. In the cathodic curve, the reduction peaks in the potential range of 0–0.7 V correspond to the formation of Li-Zn alloy and a solid electrolyte interphase (SEI) layer as well as the reduction of ZnO to Zn, yielding Li_2O. In the anodic curve, the oxidation peaks in the potential range below 0.8 V are related to the multi-step dealloying of the Li-Zn alloy. And the strong broad oxidation peak located near 1.5 V is associated with the decomposition of Li_2O (Zhang et al., 2007; Ahmad et al., 2011; Huang et al., 2014a; Xie et al., 2015). The CV curve of the sPVDF-infiltrated ZnO NRs is quite similar to those of the as-prepared ZnO NRs and ZnO NRs embedded in PVDF film as shown in **Figure S2B**. And the CV curve for the sPVDF-infiltrated ZnO NRs decorated with Ni nanoparticles showed a higher current intensity near 0.5 V of the cathodic peak and 1.5 V of the anodic peak. It may be possible to improve the oxidation-reduction reaction of the Li-Zn alloy as well as the reduction of Li_2O, by using Ni as a catalyst, affecting the capacity (Zhang et al., 2007; Ahmad et al., 2011; Huang et al., 2014a; Xie et al., 2015).

The long-term cycling performance of the four ZnO NRs samples was measured at the rate of 0.5 C for 100 cycles, as shown in **Figure 4A**i. For the as-prepared ZnO NRs, the specific capacity drastically decreased after 40 cycles, and the poor discharge capacity retention of 36 mAh/g was observed after 100 cycles.

Since the reactions are accompanied by the huge theoretical volume change of ∼228%, the volume change-driven mechanical stress tends to deteriorate the anode (**Figure S3A**) (Xie et al., 2015). To suppress the disintegration of the ZnO NRs, the PVDF film was used to fill the gap between the ZnO NRs as a binder. In **Figure 4A**ii, the ZnO NRs embedded in the PVDF film show more stable cycling behavior as a result. However, the maximum discharge capacity value of the ZnO NRs embedded in the PVDF film was about 44% lower than that of the as-prepared ZnO NRs. It is noted that the PVDF, which completely surrounds the ZnO NRs, suppresses the volume expansion of the ZnO NRs caused by lithiation process, and interferes with the diffusion of Li ions between the ZnO NRs and electrolyte during the charge/discharge processes. **Figure S3B** and **Figure 2E** show that the PVDF film with embedded ZnO NRs retained its initial shape, even after 100 cycles.

As shown in **Figure 4A**iii, spherical nanoparticles of PVDF (sPVDF) were infiltrated between the ZnO NRs to facilitate the diffusion of Li ions and to allow greater volume expansion, i.e., more electrochemical capacity caused by the lithiation process. **Figure 4A**iii shows that the sPVDF-infiltrated ZnO NRs had an average specific capacity of around 406 mAh/g, which is two times higher than that of the ZnO NRs embedded in the PVDF film.

In addition, the 2nd discharge capacity of the sPVDF-infiltrated ZnO NRs was 143 mAh/g higher than that (about 589 mAh/g) of the as-prepared ZnO NRs. This result might be explained if the free-volume formed by the sPVDF contributed

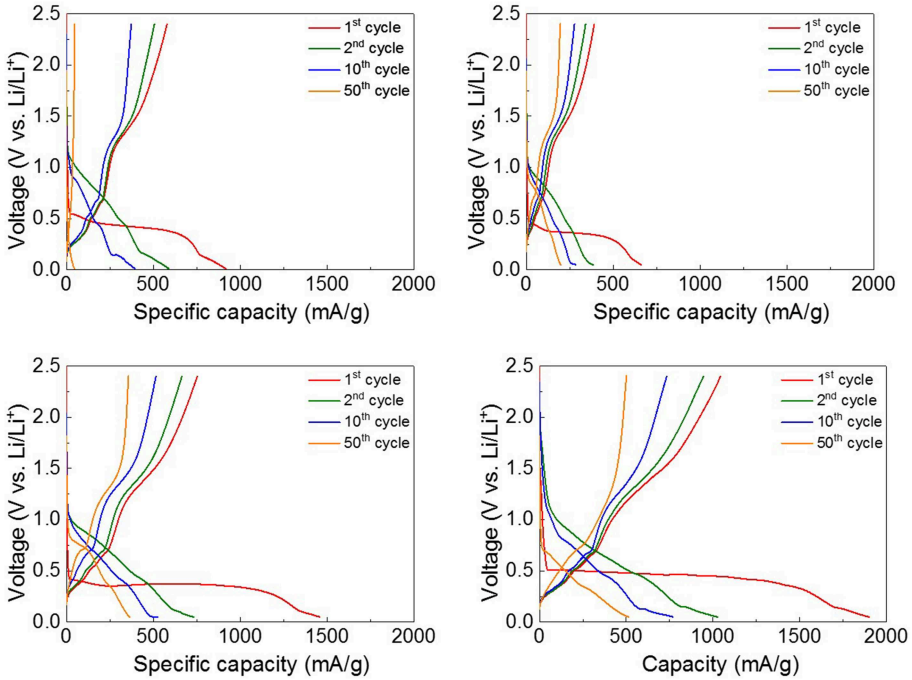

FIGURE 3 | The discharge-charge voltage profiles between 0.05 and 2.4 V of **(A)** as-prepared ZnO NRs, **(B)** ZnO NRs embedded in PVDF film, **(C)** sPVDF-infiltrated ZnO NRs, and **(D)** sPVDF-infiltrated ZnO NRs decorated with Ni nanoparticles.

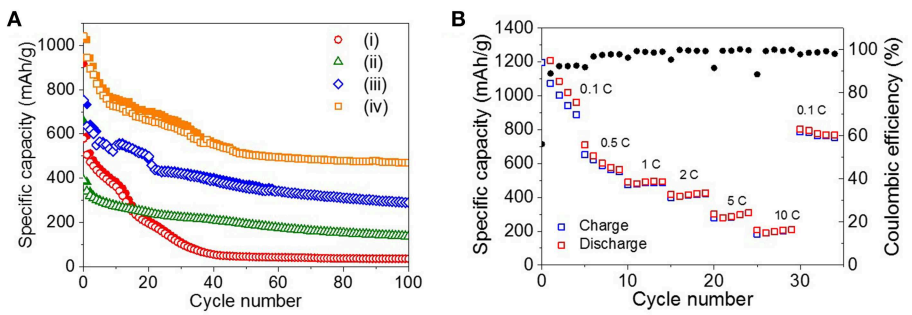

FIGURE 4 | (A) Cycling performance of (i) as-prepared ZnO NRs, (ii) ZnO NRs embedded in PVDF film, (iii) sPVDF-infiltrated ZnO NRs, and (iv) sPVDF-infiltrated ZnO NRs decorated with Ni nanoparticles over 100 cycles at 0.5 C. (The solid and open symbols indicate charge and discharge capacities, respectively). **(B)** Rate capability of (iv) sPVDF-infiltrated ZnO NRs decorated with Ni nanoparticles.

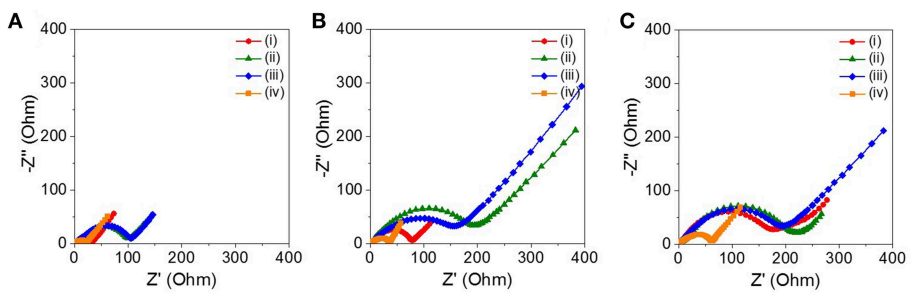

FIGURE 5 | Nyquist plots of the cell with the (i) as-prepared ZnO NRs, (ii) ZnO NRs embedded in PVDF film, (iii) sPVDF-infiltrated ZnO NRs, and (iv) sPVDF-infiltrated ZnO NRs decorated with Ni nanoparticles at the end of the **(A)** 10th, **(B)** 30th, and **(C)** 50th charge cycles.

to the fast intercalation and de-intercalation of Li^+ ions between the electrolyte and the ZnO NRs (Gowda et al., 2011). After 100 cycles, the specific capacity of the sPVDF-infiltrated ZnO NRs was two times higher than that of the ZnO NRs embedded in the PVDF film and eight times higher than that of the as-prepared ZnO NRs. It is supposed that the close-packed sPVDF acted as a binder and effectively prevented the delamination of the ZnO NRs from the Cu foil as shown in **Figure S3C**. **Figures S3D,E** show SEM images of the interface between the ZnO NRs and Cu foil before and after the 100 cycles of the sPVDF-infiltrated ZnO NRs. This indicates that the ZnO NRs were well-preserved in the initial structure without delamination after the 100 cycling charge-discharge process. This confirms that the close-packed sPVDF-infiltrated ZnO NRs are an effective structure for accommodating the strains caused by the electrochemical processes, and simultaneously allow enhanced electrochemical performances.

Figure 4Aiv shows the specific capacity of the sPVDF-infiltrated ZnO NRs decorated with Ni nanoparticles. The average specific capacity for 100 cycles was about 595 mAh/g, 1.5 times higher than that of the sPVDF-infiltrated ZnO NRs. And the discharge capacity at the 2nd cycle increased more than 20 %, compared to that of the sPVDF-infiltrated ZnO NRs. This indicates that the decoration of Ni nanoparticles improved the electrochemical performance of the ZnO NRs (Zhang et al., 2007; Xie et al., 2015).

Figure 4B shows the rate capability of the sPVDF-infiltrated ZnO NRs decorated with Ni nanoparticles. The average discharge capacities at the rates of 0.1, 0.5, 1, 2, 5, and 10 C are 1,280, 619, 490, 417, 295, and 202 mAh/g, respectively. The capacity gradually decreases at 0.1 and 0.5 C. However, when the c-rate returns back to 0.1 C from 10 C, this anode showed a recovered capacity up to 782 mAh/g and the high coulomb efficiency of 98%, indicating the good stability. At high rates of 1, 2, 5, and 10 C, this anode has high capacity compared to the previous studies, and good cycle characteristics for the fast discharge-charge feature (Pan et al., 2010; Ahmad et al., 2011; Gowda et al., 2011; Laurenti et al., 2015).

Figure 5 shows the Nyquist plots of the four ZnO NRs at the end of the 10, 30, and 50th charge cycles, respectively. The solution resistance (R_s) and the charge transfer resistance (R_{ct}) were estimated by a semicircle in the high-to-medium region and by a simple equivalent circuit model. The four ZnO NRs samples had similar R_s values, in the range of 2–4 Ω, regardless of the charge cycles. The sPVDF-infiltrated ZnO NRs decorated with Ni nanoparticles and the as-prepared ZnO NRs exhibited an R_{ct} value (22 and 33 Ω) at the 10th charge cycle, which was much smaller than that those (105 and 100 Ω) of the sPVDF-infiltrated ZnO NRs, and the ZnO NRs embedded in PVDF film. With the increase of the charge cycles, the R_{ct} values of the sPVDF-infiltrated ZnO NRs and the ZnO NRs embedded in PVDF film increased to 178 and 205 Ω in the 30th cycle, reaching 221 and 234 Ω in the 50th cycle, respectively. And the R_{ct} value of the as-prepared ZnO NRs slightly increased to 79 Ω in the 30th cycle and reached 200 Ω in the 50th cycle, similar to the R_{ct} values of the sPVDF-infiltrated ZnO NRs and the ZnO NRs embedded in PVDF film. Even though the R_{ct} values of the sPVDF-infiltrated ZnO NRs decorated with Ni nanoparticles slightly increased with the charge cycling, it had a much lower R_{ct} than the others. This suggests that the presence of Ni nanoparticles increased the electrical conductivity of the ZnO NRs as an active material, and facilitated a faster kinetics process toward the formation/decomposition of Li_2O, thus leading to high specific capacity (Zhang et al., 2007; Liu et al., 2009; Huang et al., 2014b).

CONCLUSIONS

In summary, we successfully synthesized ZnO NRs decorated with Ni nanoparticles using a template-free electrochemical deposition and subsequent galvanic reaction. The specific electrochemical capacities of the four specimens, i.e., as-prepared ZnO NRs, ZnO NRs embedded in PVDF film, sPVDF-infiltrated ZnO NRs, and sPVDF-infiltrated ZnO NRs decorated with Ni nanoparticles, were evaluated as anodes for LIB, respectively. The close-packed sPVDF infiltrated between the ZnO NRs, as well as the Ni nanoparticles decorated on the ZnO NR surface, led to the simultaneous enhancement of electrochemical capacity and cyclability as an anode material. The free-volume formed by the sPVDF contributed to accommodation of the strain induced by the fast intercalation/de-intercalation of Li^+ ions. And the Ni nanoparticles deposited on the surface of the ZnO NRs both increased electrical conductivity, and facilitated a faster kinetics in the process of the formation/decomposition of Li_2O. The present results are expected to contribute to the enhancement of the electrochemical performance of other metal oxide nanostructures.

AUTHOR CONTRIBUTIONS

HP and SP conducted the experiments and TEM analysis and drafted the manuscript. JHS analyzed the electrochemical properties. S-HJ and JS initiated and organized the work and finalized the manuscript. All authors read and approved the final manuscript.

ACKNOWLEDGMENTS

This research was supported by Low-dimensional Materials Genome Development by Korea Research Institute of Standards and Science (KRISS-2018-18011084) and by Creative Materials Discovery Program through the National Research Foundation of Korea (NRF) funded by the Ministry of Science, ICT and Future Planning (NRF-2017M3D1A1039561).

SUPPLEMENTARY MATERIAL

The Supplementary Material for this article can be found online at: https://www.frontiersin.org/articles/10.3389/fchem.2019.00415/full#supplementary-material

REFERENCES

Ahmad, M., Yingying, S., Nisar, A., Sun, H., Shen, W., Wei, M., et al. (2011). Synthesis of hierarchical flower-like ZnO nanostructures and their functionalization by Au nanoparticles for improved photocatalytic and high performance Li-ion battery anodes. *J. Mater. Chem.* 21, 7723–7729. doi: 10.1039/c1jm10720h

Belliard, F., and Irvine, J. T. S. (2001). Electrochemical performance of ball-milled ZnO-SnO_2 systems as anodes in lithium-ion battery. *J. Power. Sources* 97, 219–222. doi: 10.1016/S0378-7753(01)00544-4

Caballero, A., Hernán, L., and Morales, J. (2013). High-capacity anode for lithium batteries consisting of mesoporous NiO nanoplatelets. *Energy Fuels* 27, 5545–5551. doi: 10.1021/ef400797r

Elias, J., Tena-Zaera, R., and Lévy-Clément, C. (2008). Electrochemical deposition of ZnO nanowire arrays with tailored dimensions. *J. Electroanal. Chem.* 621, 171–177. doi: 10.1016/j.jelechem.2007.09.015

Gowda, S. R., Reddy, A. L., Shaijumon, M. M., Zhan, X., Ci, L., and Ajayan, P. M. (2011). Conformal coating of thin polymer electrolyte layer on nanostructured electrode materials for three-dimensional battery applications. *Nano Lett.* 11, 101–106. doi: 10.1021/nl102919m

He, C., Wu, S., Zhao, N., Shi, C., Liu, E., and Li, J. (2013). Carbon-encapsulated Fe_3O_4 nanoparticles as a high-rate lithium ion battery anode material. *ACS Nano* 7, 4459–4469. doi: 10.1021/nn401059h

Huang, H., Zhu, W., Tao, X., Xia, Y., Yu, Z., Fang, J., et al. (2012). Nanocrystal-constructed mesoporous single-crystalline Co_3O_4 nanobelts with superior rate capability for advanced lithium-ion batteries. *ACS Appl. Mater. Interfaces* 4, 5974–5980. doi: 10.1021/am301641y

Huang, X. H., Guo, R. Q., Wu, J. B., and Zhang, P. (2014a). Mesoporous ZnO nanosheets for lithium ion batteries. *Mater. Lett.* 122, 82–85. doi: 10.1016/j.matlet.2014.02.012

Huang, X. H., Wu, J. B., Lin, Y., Guo, R. Q., and Zhong, W. W. (2014b). Ag decorated hierarchical structured ZnO Microspheres and their enhanced electrochemical performance for lithium ion batterise. *J. Electrochem. Sci.* 9, 6707–6716.

Huang, X. H., Xia, X. H., Yuan, Y. F., and Zhou, F. (2011). Porous ZnO nanosheets grown on copper substrates as anodes for lithium ion Batteries. *Electrochim. Acta* 56, 4960–4965. doi: 10.1016/j.electacta.2011.03.129

Iniewski, K. (2011). *Nano-Semiconductor: Devices and Technology*. Boca Raton, FL: CRC Press.

Laurenti, M., Garino, N., Porro, S., Fontana, M., and Gerbaldi, C. (2015). Zinc oxide nanostructures by chemical vapour deposition as anodes for Li-ion batteries. *J. Alloys Comp.* 640, 321–326. doi: 10.1016/j.jallcom.2015.03.222

Li, H., Wang, Z., Chen, L., and Huang, X. (2009). Research on advanced materials for li-ion batteries. *Adv. Mater.* 21, 4593–4607. doi: 10.1002/adma.200901710

Liu, D., and Cao, G. (2010). Engineering nanostructured electrodes and fabrication of film electrodes for efficient lithium ion intercalation. *Energy Environ. Sci.* 3, 1218–1237. doi: 10.1039/b922656g

Liu, J., Li, Y., Ding, R., Jiang, J., Hu, Y., Ji, X., et al. (2009). Carbon/ZnO Nanorod array electrode with significantly improved lithium storage capability. *J. Phys. Chem. C* 113, 5536–5339. doi: 10.1021/jp900427c

Manzano, C. V., Calero, O. C., Hormeno, S., Penedo, M., Luna, M., and Gonzalez, M. S. M. (2013). ZnO morphology control by pulsed electrodeposition. *J. Phys. Chem. C* 117, 1502–1508. doi: 10.1021/jp3107099

Pan, Q., Qin, L., Liu, J., and Wang, H. (2010). Flower-like ZnO–NiO–C films with high reversible capacity and rate capability for lithium-ion batteries. *Electrochim. Acta* 55, 5780–5785. doi: 10.1016/j.electacta.2010.05.017

Park, J. C., Kim, J., Kwon, H., and Song, H. (2009). Gram-Scale Synthesis of Cu_2O Nanocubes and subsequent oxidation to CuO hollow nanostructures for lithium-ion battery anode materials. *Adv. Mater.* 21, 803–807. doi: 10.1002/adma.200800596

Park, S. H., Shin, H. S., Kim, Y. H., Park, H. M., and Song, J. Y. (2013a). Filamentary one-dimensionalnanocrystal growth of Cu, AgCu, and Au in ultra-dilute electrolytes. *J. Alloys Comp.* 580, 152–156. doi: 10.1016/j.jallcom.2013.05.130

Park, S. H., Shin, H. S., Kim, Y. H., Park, H. M., and Song, J. Y. (2013b). Template-free and filamentary growth of silver nanowires: application to anisotropic conductive transparent flexible electrodes. *Nanoscale* 5, 1864–1869. doi: 10.1039/c2nr33056c

Qiu, J., Guo, M., Feng, Y., and Wang, X. (2011). Electrochemical deposition of branched hierarchical ZnO nanowire arrays and its photoelectrochemical properties. *Electrochim. Acta* 56, 5776–5782. doi: 10.1016/j.electacta.2011.04.059

Scrosati, B., and Garche, J. (2010). Lithium batteries: Status, prospects and future. *J. Power Sources* 195, 2419–2430. doi: 10.1016/j.jpowsour.2009.11.048

Shen, L., and Wang, C. (2015). *RSC Adv.* 5, 88989–88995. doi: 10.1039/c5ra18254a

Shin, J. H., Park, S. H., Hyun, S. M., Kim, J. W., Park, H. M., and Song, J. Y. (2014). Electrochemical flow-based solution–solid growth of the Cu_2O nanorod array: potential application to lithium ion batteries. *Phys. Chem. Chem. Phys.* 16, 18226. doi: 10.1039/c4cp02049a

Song, Y., Chen, Y., Wu, J., Fu, Y., Zhou, R., Chen, S., et al. (2017). Hollow metal organic frameworks-derived porous ZnO/C nanocages as anode materials for lithium-ion batteries. *J. Alloy. Compd.* 694, 1246–1253. doi: 10.1016/j.jallcom.2016.10.110

Spitsina, S., and Kahrizi, M. (2012). "Design of the shape, size, and distribution of the array of crystalline ZnO nanowires," in *IEEE Canadian Conference on Electrical and Computer Engineering* (Montreal, QC)

Tarascon, J. M., and Armand, M. (2001). Issues and challenges facing rechargeable lithium batteries. *Nature* 414, 359–367. doi: 10.1038/35104644

Tokumitsu, K., Fujimoto, H., Mabuchi, A., and Kasuh, T. (1999). High capacity carbon anode for Li-ion battery a theoretical explanation. *Carbon* 37, 1599–1605. doi: 10.1016/S0008-6223(99)00031-7

Wang, H., Pan, Q., Cheng, Y., Zhao, J., and Yin, G. (2009). Evaluation of ZnO nanorod arrays with dandelion-like morphology as negative electrodes for lithium-ion batteries. *Electrochim. Acta* 54, 2851–2855. doi: 10.1016/j.electacta.2008.11.019

Xie, Q., Ma, Y., Zeng, D., Wang, L., Yue, G., and Peng, D. L. (2015). Facile fabrication of various zinc-nickel citrate microspheres and their transformation to ZnO-NiO hybrid microspheres with excellent lithium storage properties. *Sci. Rep.* 5:8351. doi: 10.1038/srep08351

Yanga, G. Z., Song, H. W., Cui, H., Liu, Y. C., and Wang, C. X. (2013). Ultra fast Li-ion battery anode with super long life and excellent cycling stability from strongly coupled ZnO nanoparticle/conductive nanocarbon skeleton hybrid materials. *Nano Energy* 2, 579–585. doi: 10.1016/j.nanoen.2013.06.013

Zhang, C. Q., Tu, J. P., Yuan, Y. F., Huang, X. H., Chen, X. T., and Mao, F. (2007). Electrochemical performances of Ni-coated ZnO as an anode material for lithium-ion batteries. *J. Electrochem. Soc.* 154, A65–A69. doi: 10.1149/1.2400609

Zhang, J., Gu, P., Xu, J., Xue, H., and Pang, H. (2016). High performance of electrochemical lithium storage batteries: ZnO-based nanomaterials for lithium-ion and lithium-sulfur batteries. *Nanoscale* 8, 18578–18595. doi: 10.1039/c6nr07207k

Conflict of Interest Statement: The authors declare that the research was conducted in the absence of any commercial or financial relationships that could be construed as a potential conflict of interest.

frontiers in Chemistry

ORIGINAL RESEARCH
published: 02 August 2019
doi: 10.3389/fchem.2019.00542

Coupled Electrodeposition of Fe–Co–W Alloys: Thin Films and Nanowires

Tatjana Maliar[1,2], *Henrikas Cesiulis*[2] *and Elizabeth J. Podlaha*[1,3]*

[1] Department of Chemical Engineering, Northeastern University, Boston, MA, United States, [2] Department of Physical Chemistry, Vilnius University, Vilnius, Lithuania, [3] Department of Chemical and Biomolecular Engineering, Clarkson University, Potsdam, NY, United States

The electrodeposition of Fe–Co–W alloys was examined using a rotating cylinder Hull (RCH) cell and conditions were determined to create nanowires. The metal ion reduction mechanism was a combination of induced and anomalous codeposition, with water reduction as a gas evolving side reaction, rending deposition into recesses a challenge. In thin film deposition, under kinetic control, the addition of Fe ions into the electrolyte, greatly reduced the Co partial current density, and thus it's content in the deposit. The change of Co partial current density was attributed to an anomalous codeposition behavior, but it had a minimal effect in changing the W wt% in the deposit, despite the expected inducing characteristic of Fe when codeposited with tungsten. Deposition conditions were determined to electrodeposit Fe–Co–W nanowires having similar concentration as the thin films. Nanowires were electrodeposited into polycarbonate membranes under pulsed current at room temperature.

Keywords: tungsten alloy, nanowires, electrodeposition, induced codeposition, Fe-Co-W

OPEN ACCESS

Edited by:
Nosang Vincent Myung, University of California, Riverside, United States

Reviewed by:
Laszlo Peter, Wigner Research Centre for Physics, Hungarian Academy of Sciences, Hungary
Zheng Chen, University of California, San Diego, United States

***Correspondence:**
Elizabeth J. Podlaha
epodlaha@clarkson.edu

Specialty section:
This article was submitted to Electrochemistry, a section of the journal Frontiers in Chemistry

Received: *25 February 2019*
Accepted: *16 July 2019*
Published: *02 August 2019*

Citation:
Maliar T, Cesiulis H and Podlaha EJ (2019) Coupled Electrodeposition of Fe–Co–W Alloys: Thin Films and Nanowires. Front. Chem. 7:542. doi: 10.3389/fchem.2019.00542

INTRODUCTION

The reduction of tungsten ions is of fundamental interest due to its unique reduction behavior in aqueous electrolytes. Without an inducing element, such as Ni, Co, and Fe, the reduction of tungsten ions to W metal does not occur. This behavior has been referred to as induced codeposition by Brenner (Brenner, 1963), and has been characterized for Ni-W, Co-W, Fe-W electrodeposition as reviewed by Fukushima et al. (1979), Eliaz and Gileadi (2008), and Tsyntsaru et al. (2012). The inducing elements, Ni, Co, and Fe, when codeposited together from aqueous electrolytes exhibit another type of reduction behavior described as anomalous codeposition. As similarly mentioned by Brenner and others (Dahms and Croll, 1955; Hessami and Tobias, 1989; Gangasingh and Talbot, 1991; Grande and Talbot, 1993; Matlosz, 1993; Sasaki and Talbot, 1995; Zech et al., 1999a) the less noble alloy component in the electrolyte (e.g., Fe, in NiFe) can inhibit the more noble alloy component rate (e.g., Ni, in NiFe). Both of these electrodeposition behaviors, induced and anomalous codeposition, make it difficult to predict the deposit concentration of the alloy *a prior*, and a mixture of the two systems adds another level of complexity. This paper examines such a mixed behavior case, Fe-Co-W, having features of both induced and anomalous codeposition.

The first electrodeposited Fe–Co–W alloys from citrate electrolytes was presented by Brenner et al. (1947). Their parametric study showed that the tungsten content of the deposit slightly increased with an increase of iron in the electrolyte, at a given current density. When the electrolyte

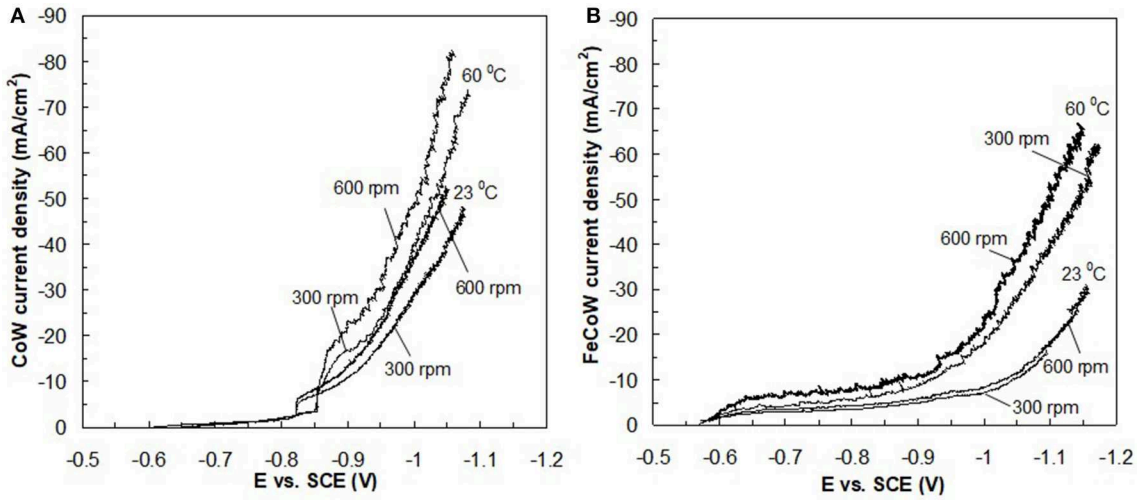

FIGURE 1 | RCE polarization curves of **(A)** Co–W and **(B)** Fe–Co–W alloys at two temperatures 23 and 60°C, and two rotation rates 300 and 600 rpm. The surface of the electrode was a pretreated deposit of **(A)** Co–W and **(B)** Fe–Co–W, respectively, at the start of polarization.

TABLE 1 | Estimated Wagner numbers.

Electrolyte	*T*, °C	κ, S/cm	Slopes from Figure 1 ($V \bullet cm^2/A$)		W_a	
			300 rpm	600 rpm	300 rpm	600 rpm
CoW	23	0.0564	4.1	4.7	0.029	0.033
	60	0.0665	3.7	3.9	0.030	0.032
FeCoW	23	0.063	3.2	3.0	0.025	0.023
	60	0.0846	3.3	4.8	0.035	0.050

contained a high concentration of iron ions (0.45 M) there was a change in the Co and Fe deposit concentration with applied cathodic current density but the W content remained constant at 17 wt%. However, with a lower concentration of iron ions in the electrolyte (0.09 M) the Co, Fe, and W deposit concentration was insensitive to changes in applied current density. Although the induced codeposition behavior was recognized over 50 years ago (Brenner, 1963), the mechanism is still not well-understood. Molybdenum ion reduction falls under the same category as tungsten and similarly, cannot be reduced to an appreciable extent without the iron-group elements. Podlaha and Landolt (1996) and Podlaha and Landolt (1997) have noted that if the metal ions that induce molybdate reduction is in excess, the Mo metal reaction rate is insensitive to the rate of the codepositing inducing elements, such as nickel ions or complexed nickel species, In other words, the Mo reduction rate would appear decoupled. In the opposite case, if the reluctant metal ions, such as molybdate ions, in the electrolyte are in excess compared to the ions needed to induce them, then the rate follows that of the inducing element. They showed that when the nickel concentration is under a mass transport control the molybdenum reduction rate also can show behavior associated with mass transfer even though its concentration is in great excess, thus, mimicking the nickel rate. The coupled reaction rate was attributed to a mixed-metal intermediate that adsorbs at the electrode surface. The coupled nature of the tungstate ion with nickel ion reduction has also been observed by Eliaz and Gileadi (2007) and Eliaz and Gileadi (2008). They however suggest that the mixed-metal intermediate is a soluble species in the electrolyte, rather than an adsorbed one. Either approach can predict a coupled kinetic and coupled kinetic-transport behavior. Belevskii et al. (2010) examined Co-W codeposition with electrochemical impedance spectroscopy and the results were consistent with the occurrence of slow adsorption processes. Sun et al. (2013) examined the ternary electrodeposition of Ni-Mo-W, and found that the reaction orders of the nickel and tungsten reduction with molybdate electrolyte concentration have a negative reaction order, thus their rates decrease, as molybdate is added to the electrolyte. The reaction order was found to be consistent with a model that includes an adsorbed intermediate and where the inducing species is not the nickel ion, but rather an adsorbed nickel intermediate.

Models of anomalous codeposition of iron-group metals, without W or Mo, are grounded on a reaction mechanism that includes chemical equilibria of monohydroxide species and their adsorbed intermediates that can block co-reducing elements (Hessami and Tobias, 1989; Gangasingh and Talbot, 1991; Grande and Talbot, 1993; Sasaki and Talbot, 1995). Adsorption models were first developed with the Ni–Fe system, where Fe inhibits the Ni reaction rate (Matlosz, 1993; Zech et al., 1999a,b), including a consistency with EIS behavior (Baker and West, 1997). In a similar manner, the inhibition of Co by Fe, during Co–Fe co-deposition has been reported (Zech et al., 1998, 1999a,b).

The goal of this work is to examine the effect of Fe on Co–W reduction from a neutral citrate-borate electrolyte in order to better understanding the different reduction mechanisms and to apply the results to develop alloy nanowires of these elements. This work is motivated in part by the known enhancement of

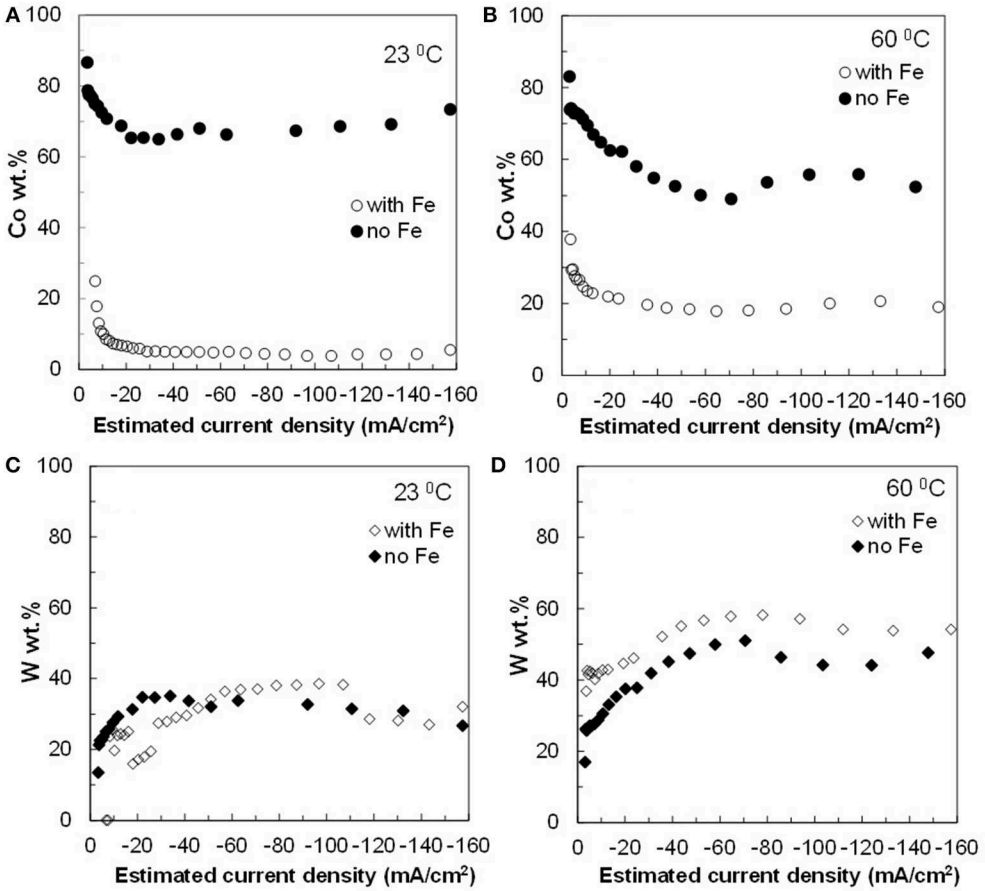

FIGURE 2 | Concentration of **(A,B)** Co and **(C,D)** W in Co–W and Fe–Co–W alloy films at two different temperatures 23 and 60°C, and at an electrode rotation rate of 300 rpm.

hardness and corrosion resistance by adding W to Co, as Co–W alloys (Hamid, 2003; Tsyntsaru et al., 2008, 2009; Weston et al., 2009), and with Co-W-Fe alloys (Capel et al., 2003). Recently, Fe–Co–W cathodes have been shown to be promising candidates as electrocatalyst for the hydrogen evolution reaction (HER) for alkaline electrolyzers (Ramesh et al., 1998). To address and determine the metal deposition reaction rates a rotating cylinder Hull (RCH) was employed that has a current distribution along its length to electrodeposit thin films over a large current density range under controlled hydrodynamic conditions. The local current density-potential relations were inferred from linear sweep polarization data using rotating cylinder electrodes with uniform current distribution. Results developed for thin film alloy deposition are then used to electrodeposit Co-W and Fe–Co–W nanowires. This work is the first demonstration of Fe–Co–W nanowires, and that adding Fe to Co-W deposits by electrodeposition is dominated by the anomalous codeposition behavior with Co serving to induce tungsten ions to reduce to W metal.

MATERIALS AND METHODS

Co–W and Fe–Co–W thin films and nanowires were electrodeposited from an ammonia free electrolyte, based on the electrolyte presented by Tsyntsaru et al. (2008) including citrate and boric acid. Since citrate species can complex both Co and Fe, the quantity of citrate was increased in proportion to the addition of Fe ions in the electrolyte. The Fe-Co-W and Co-W electrolyte concentrations were (1) $FeSO_4$−0.2 M; $CoSO_4$−0.2 M; Na_2WO_4−0.2 M; $C_6H_8O_7$−0.08 M; $Na_3C_6H_5O_7$−0.5 M; H_3BO_3−1.3 M and (2) $CoSO_4$−0.2 M; Na_2WO_4−0.2 M; $C_6H_8O_7$−0.04 M; $Na_3C_6H_5O_7$−0.25 M; H_3BO_3−0.65 M. The pH was adjusted to 6.7 by the addition of NaOH or H_2SO_4. The electrolyte temperature was 23 and 60°C controlled by a water bath. The conductivity was measured with an Oakton conductivity meter and probe and calibrated with conductivity standards. Two values of the cathode rotation rate, 300 and 600 rpm, were used and the deposition time was 25 min. The average cathodic current density was 32 mA/cm^2. The tungsten alloy films were deposited using a rotating cylinder Hull Cell (RCHC), (Autolab HT Rota-Hull®, Eco–Chemie B.V., Utrecht, Netherlands) with a varying current distribution along the electrode length. In this configuration, the cathode is surrounded by a plastic insulator open at the bottom edge where the anode is located. Mechanically polished, chemically cleaned brass cylindrical rods were used as a working electrode with 0.6 cm diameter, and 12 cm total length, with 8.1 cm length exposed to the

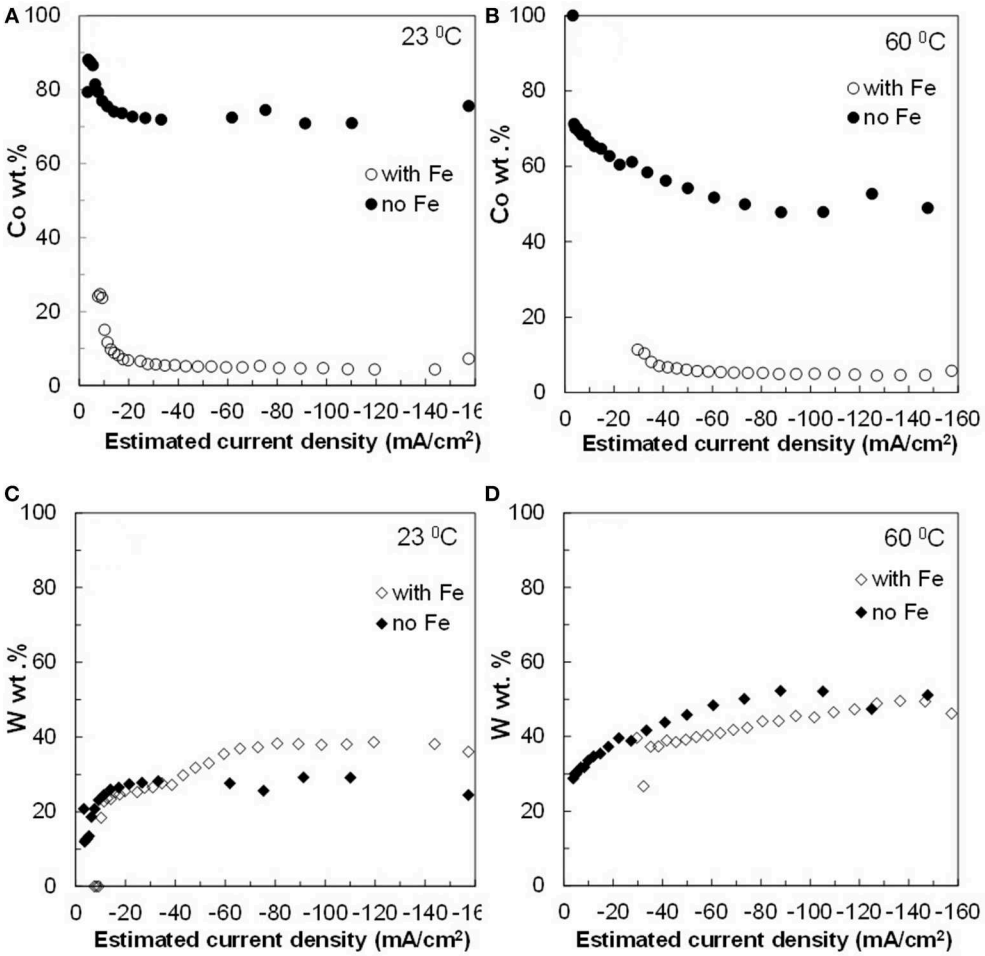

FIGURE 3 | Concentration of **(A,B)** Co and **(C,D)** W in Co–W and Fe–Co–W alloy films at two different temperatures 23 and 60°C, and at an electrode rotation rate of 600 rpm.

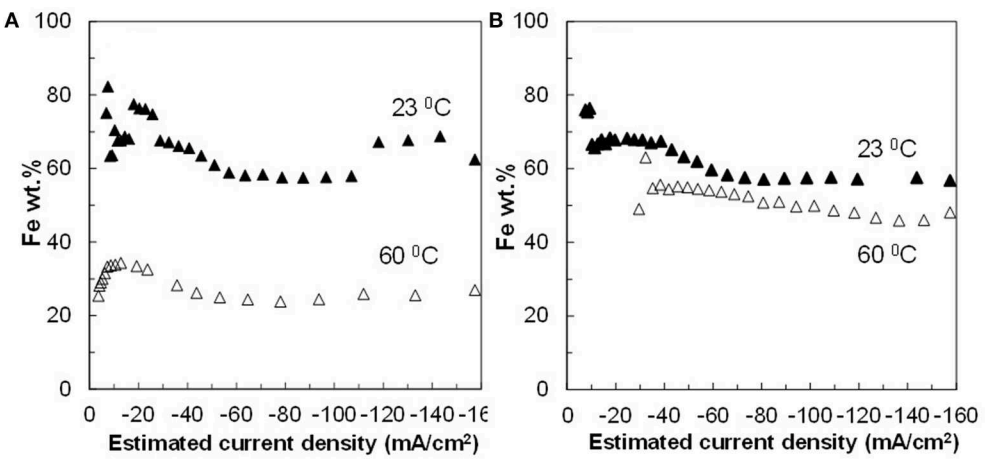

FIGURE 4 | Fe concentration in Fe–Co–W alloy films at two different temperatures 23 and 60°C, and at an electrode rotation rate of **(A)** 300 and **(B)** 600 rpm.

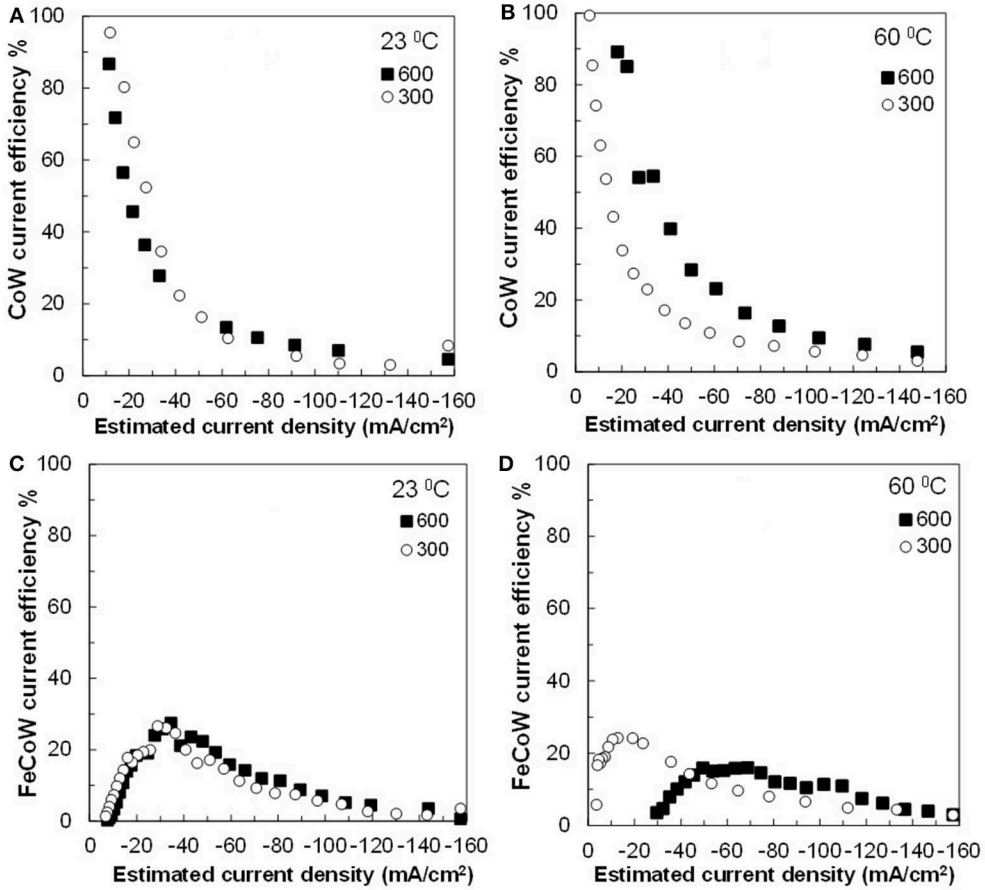

FIGURE 5 | Current efficiency for **(A,B)** Co–W and **(C,D)** Fe–Co–W deposits at two temperatures 23 and 60°C, and at an electrode rotation rates of 300 and 600 rpm.

electrolyte. The surface area of the cylinder electrode was 15.3 cm^2. The anode was an electrodeposited gold film onto a titanium mesh.

Polarization curves of electrodeposited Co–W and Fe–Co–W were recorded using a Solartron 1287 Electrochemical Interface and a Solartron 1255 Frequency Response Analyzer in a three–electrode cell, with a gold covered titanium mesh anode, a saturated calomel electrode (SCE) reference, and a brass rod working cylindrical electrode. The working electrode was rotated using a controller (Pine Instrument Company, model AFMSRCE); the rotation rates were the same as that used by Autolab HT Rota-Hull equipment. The potential scan rate was 2 mV/s.

Before polarization, the working electrode surface was pre-treated with a corresponding alloy deposit. The pre-treatment included deposition of either Co–W and Fe–Co–W alloys at temperature of 23 and 60°C for the respective polarization curves, and an electrode rotation rate of 600 rpm, with a current density of 30 mA/cm^2 for 30 min. All potential values are presented vs. a SCE electrode and corrected for ohmic drop by impedance spectroscopy.

Co–W and Fe–Co–W nanowires were electrodeposited into polycarbonate templates from Osmonics Inc. (100 nm stated pore diameter, 6 μm thickness). In order to provide an electrical contact to the membrane a layer of gold was sputtered for 10 min (Anatech Inc., model #Hummer^{TM} 6.2) on the one side of the template. The template with the sputtered Au layer was fixed in a stationary holder.

Fabrication parameters were taken from the results obtained for Co–W and Fe–Co–W thin films in order to achieve nanowires. Co–W nanowires were deposited under −18 mA (exposed area of 2.24 cm^2) pulse cathodic current, with an applied pulse on– and off–time of 0.1 s. Fe–Co–W nanowires were similarly deposited with an applied current of −20.3 mA (exposed area of 2.54 cm^2). Deposition in both cases was carried out at 23°C. The bulk electrolyte was agitated using a stir bar. After deposition of Co–W and Fe–Co–W nanowires, the polycarbonate membranes with deposited alloys were dissolved in dichloromethane, thus releasing Co–W and Fe–Co–W nanowires into solution.

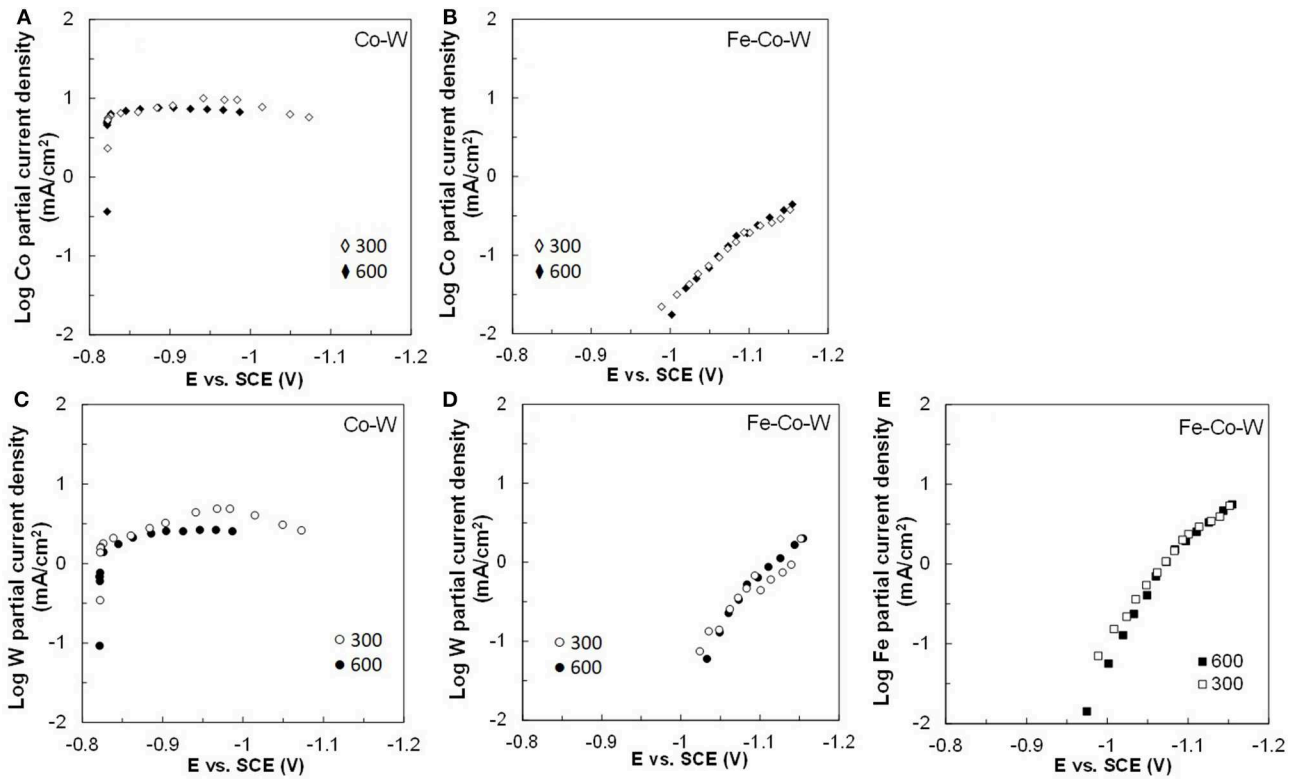

FIGURE 6 | Partial current densities of **(A,B)** Co, **(C,D)** W, and **(E)** Fe in Co–W and Fe–Co–W electrolytes at 23°C and at an electrode rotation rates of 300 and 600 rpm.

An energy dispersive X-ray fluorescence analyzer (XRF, Omicron, Kevex) was used to analyze the deposit thickness and concentration. Twenty eight equidistant points were measured with a constant 0.28 cm increment along the electrode length. The shape of Co–W and Fe–Co–W nanowires was examined by transition electron microscopy (TEM) JEM-100CX operated at 80 keV.

RESULTS AND DISCUSSION

Electrodeposition of Thin Films

Figure 1 presents the polarization curves for (a) Co–W and (b) Fe–Co–W alloys obtained at 23 and 60°C, and a rotation rate of 300 and 600 rpm onto the RCE with a uniform current distribution. The effect of temperature on the polarization curves for both Co–W and Fe–Co–W codeposition increases the total current density at a given potential. The Co–W and Fe–Co–W polarization curves are slightly affected by rotation rates. Increasing rotation rate leads to higher current density for any temperature during Co–W codeposition. The addition of Fe to the electrolyte increases the total current densities at more positives potentials, but decreases at more negative potentials (E < -1 V) in the region where there is a large rate of hydrogen evolution. In Fe–Co–W tertiary deposition at 23°C there is little change in the total current density with rotation rate suggesting a kinetic control. However, at 60°C, there is a significant change in the total current density with rotation rate. In order to determine which reaction contributes to the changes in the total current density, the partial current densities were examined.

To determine the electrodeposition characteristics and partial current densities occurring during the deposition of the Co–W and Fe–Co–W alloys, knowledge of the current distribution along the RCHC is required. A primary current distribution adequately describes the current change along the electrode length, if the Wagner number $W_a = \frac{\kappa \partial E / \partial i}{L}$ is considerably less than one in the absence of mass transport. At small Wagner numbers the primary current distribution can be used to closely estimate the local current density along the rotating cylinder electrode length. **Table 1** summarizes the parameters of the Wagner number, W_a. The solution conductivity, κ, was measured for electrolytes at different temperatures and the derivative of the potential with applied current density was obtained from the slopes of the polarizations curves (**Figure 1**) at the applied average current density (-32 mA/cm^2). All of the W_a numbers are an order of magnitude below one, thus a primary current distribution is a valid approximation of the local current density along the electrode length. The non-linear current distribution along the electrode length for the RCHC geometry is described by the expression by Madore and Landolt (1993). The measured deposit concentrations at different positions is then correlated to the corresponding current densities. Additionally, with a measure of the total

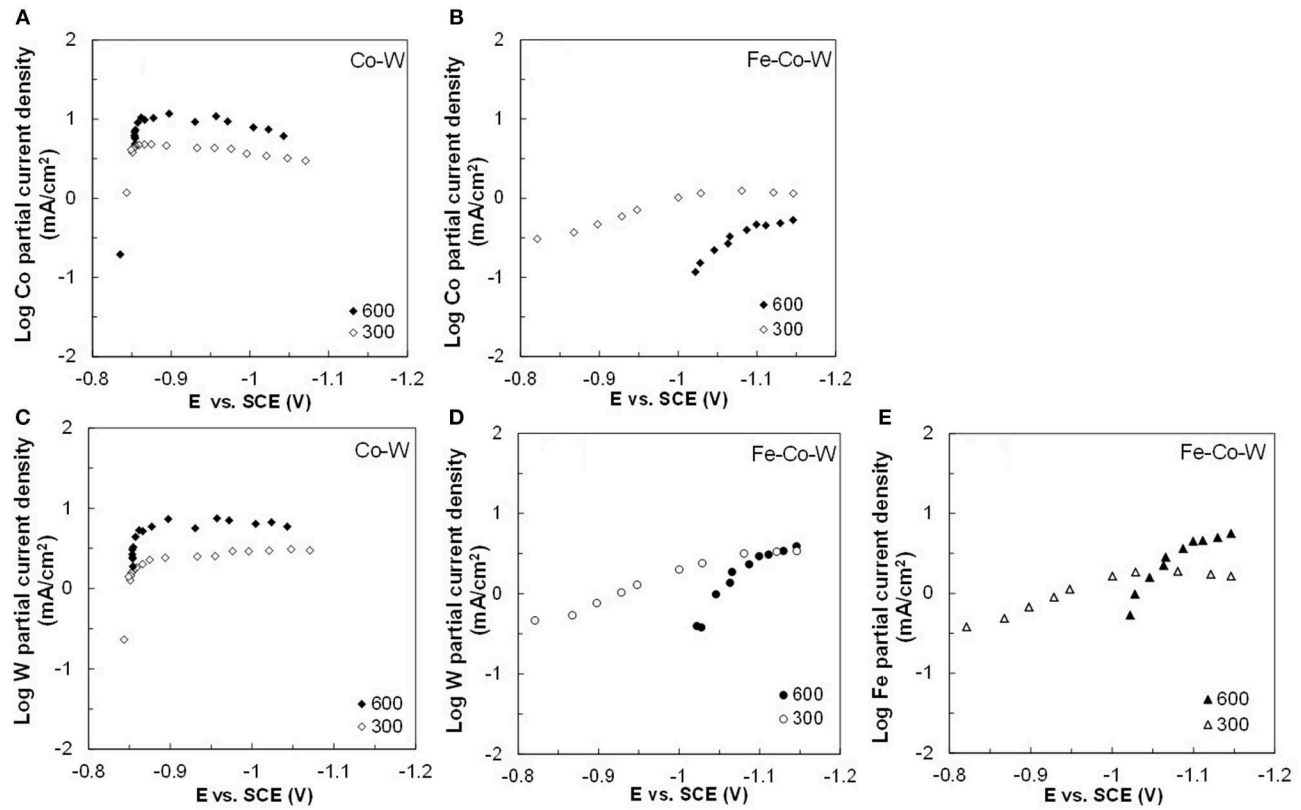

FIGURE 7 | Partial current densities **(A,B)** Co, **(C,D)** W, and **(E)** Fe in Co–W and Fe–Co–W electrolytes at 60°C and at an electrode rotation rates of 300 and 600 rpm.

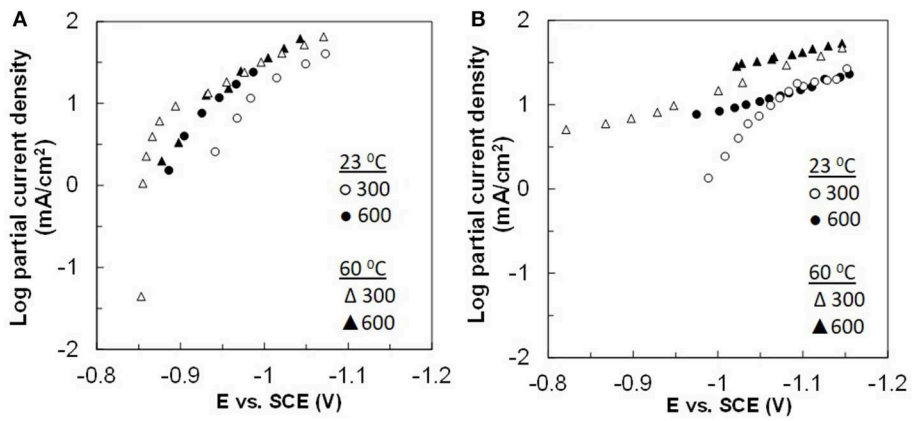

FIGURE 8 | Partial current densities of the side reaction for **(A)** Co–W and **(B)** Fe–Co–W deposition at two different temperatures of 23 and 60°C, and at electrode rotation rates of 300 and 600 rpm.

polarization with potential, the local current density at each point along the electrode corresponds to a working electrode potential.

The resulting deposit concentrations (**Figures 2–4**) for both Co–W and Fe–Co–W electrolytes on the RCHC were galvanostatically deposited at two temperatures, 23 and 60°C, and two rotation rates of 300 and 600 rpm. The deposit Co concentration when the electrode rotation rate was 300 rpm are shown in **Figures 2A,B** and at 600 rpm in **Figures 3A,B** with and without the addition of Fe to the electrolyte. In all cases, there is a dramatic decrease in the Co deposit content with the addition of Fe to the electrolyte and in the alloy. The largest change of Co wt% in the deposit occurs at the low temperature. For example, at 23°C and at cathodic current densities >40 mA/cm^2 the Co

TABLE 2 | Tafel constants (mV/decade) at 23°C.

Potential range, V	Thin film	Co	W	Fe
−0.8 to −0.85 V	Co–W	75	45	–
−1.0 to −1.1 V	Fe–Co–W	109	74	70

wt% is ∼65 wt% when no Fe is present, but when the Fe is added, the Co wt% in this range plummets to 5 wt%. In contrast, there is very little change of the W deposit concentration with Fe addition. **Figures 2C,D** and **Figures 3C,D** present the W wt% in the deposit with and without Fe, at 300 and 600 rpm, respectively. The W wt% in the Co–W and Fe–Co–W alloy films slightly rises with an increase of current density and then remains relatively constant, similar to Co. Comparing **Figures 2**, **3**, the effect of rotation rate does not significantly change the W wt%, however there is a change in the Co wt% with rotation rate only at the higher temperature when Fe is codeposited. The content of Co at 60°C in Fe–Co–W thin films strongly decreases with an increase in rotation rate. The Fe wt% in the Fe–Co–W alloy is presented in **Figure 4** at (a) 300 rpm and (b) 600 rpm for both temperatures. The Fe wt% is strongly affected by temperature at 300 rpm, but less so at 600 rpm, with a decreasing Fe wt% in the deposit with an increase in temperature. The highest Fe wt% in the ternary alloys is observed at 23°C at both 300 and 600 rpm. At 60°C, more Fe is found in the deposit with higher rotation rate, indicating a transport effect.

The current efficiency is shown in **Figure 5**. The current efficiency sharply decreases with an increase of current density for Co–W. There is a slight improvement of current efficiency for Co–W deposition at the higher temperature (60°C) and higher rotation rate (600 rpm). The current efficiency for Fe–Co–W ternary deposition is significantly lower and increases as the current density is increased, reaches a maximum, and then decreases as expected from the onset of the water reduction side reaction. In all cases with the addition of Fe, the current efficiency for Fe–Co–W deposition does not exceed more than 30%.

Figures 2–5 show that the deposit concentration and current efficiency is not sensitive to the change in rotation rate at low temperature (23°C) and in this region kinetic information can be obtained. However, at the high temperature, there is a mass transport contribution. In an effort to better understand the coupled reaction behavior the partial current densities were determined and expressed as a function of potential. **Figures 6–8** show the calculated partial current densities of cobalt, tungsten, iron (**Figures 6**, **7**) and the side reaction (**Figure 8**) from Co–W and Fe–Co–W electrolytes estimated from the measured concentration and thickness data. The potential scale was interpolated from the polarization curves (**Figure 1**) assuming a primary current distribution at different temperatures and rotation rates. The codepositing Fe considerably inhibits the partial current densities of Co, as evident by comparing **Figures 6A,B**, at 23°C, and **Figures 7A,B** at 60°C. Moreover, the tungsten partial current density is also slightly decreased in the presence of Fe. Thus, the observed decrease in the Co wt% in the ternary alloy, when iron is codeposited, is due to the much larger decrease of the Co partial current density compared

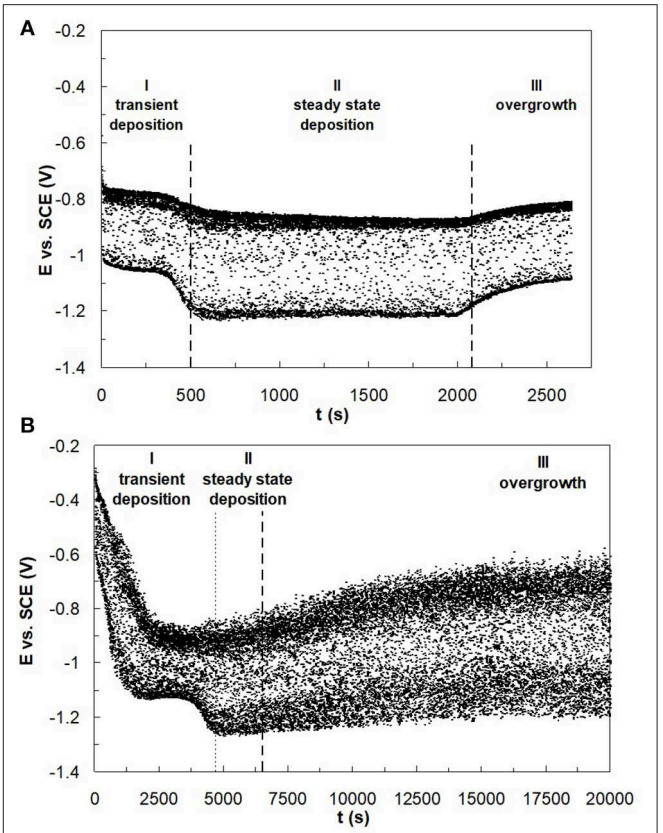

FIGURE 9 | Typical E-t dependence for **(A)** Co–W and **(B)** Fe–Co–W nanowire deposition reflecting nanowire growth into the pores of polycarbonate membrane at 23°C.

to the W partial current density. Inhibiting reduction rates by Fe have been observed in other binary systems, including Co–Fe (Zech et al., 1998, 1999a,b), and has been described by a preferential adsorption of Fe intermediate species that reduces the electrode surface area for Co adsorbed intermediates (Zech et al., 1999b). Interestingly, despite the increase of another inducing species, Fe(II), there is no increase in the tungsten rate, indicating a limiting inducing behavior. The equimolar Co:W ions in the electrolyte before the addition of Fe creates a limiting condition for the tungsten ion reduction. Thus, there is no further increase in the tungsten metal rate with the additional Fe(II) inducing species. The partial current densities of both Co and W, irrespective of temperature, follow a similar potential behavior and are parallel, further reflecting a coupled effect. This mirrored partial current density of W by Co is similar to what has been observed with Ni-Mo, another induced codeposition system by Podlaha and Landolt (1996) and Podlaha and Landolt (1997), when there is an excess of molybdate in the electrolyte.

At room temperature, the partial current densities in the Co–W electrolyte (**Figures 6A,C**) are not largely affected by rotation rate, until the potential is more negative than −0.95 V. In the Co-W-Fe electrolyte (**Figures 6B,D**), all three metal reduction partial current densities, Co, W, and Fe are not at all affected by

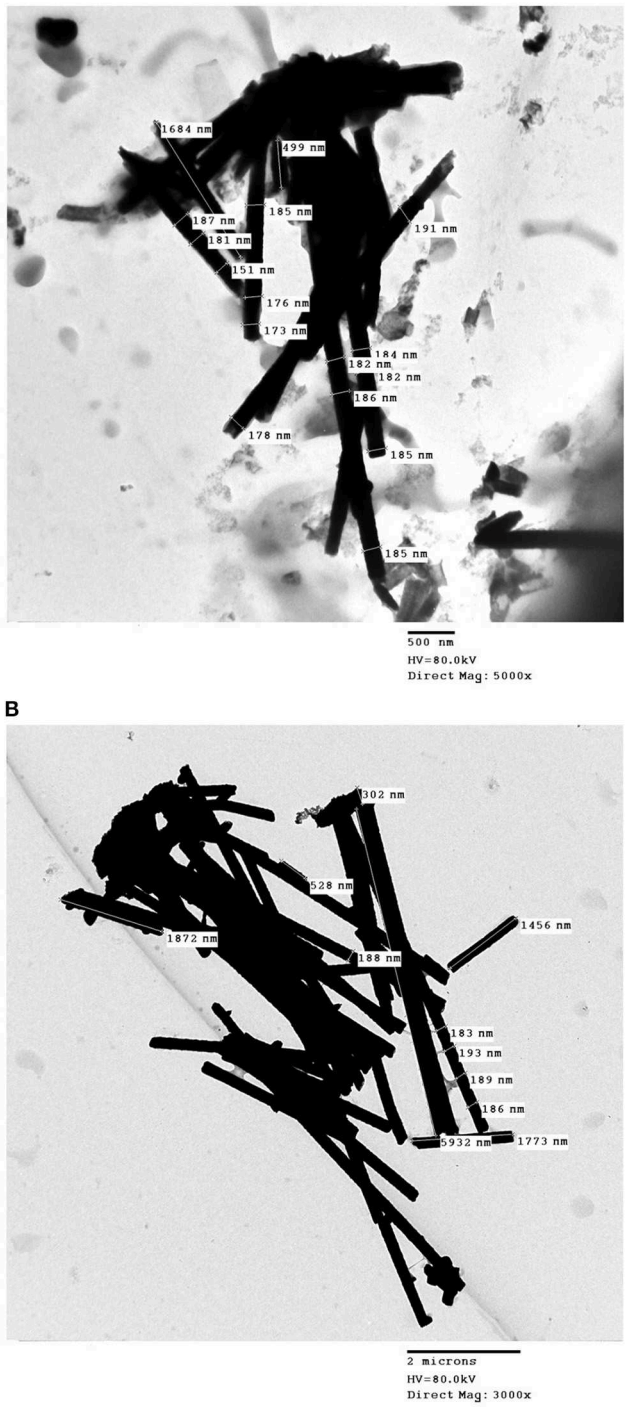

FIGURE 10 | TEM images of **(A)** Fe–Co–W and **(B)** Co–W nanowires. Fe–Co–W and Co–W nanowires were deposited under −20.32 mA (S = 2.54 cm2) and −18 mA (S = 2.25 cm2) pulse cathodic current density, respectively, with on– and off–time ton = toff = 0.1 s.

rotation rate and are in the kinetic region. The Tafel constants are listed in **Table 2**. There is a reduction of both the Co and W inverse Tafel slopes with Fe(II) addition to the electrolyte, or in other words, an increase of these Tafel slopes, ∼35%. At high electrolyte temperature, 60°C, there is a significant mass transport component (**Figure 7**) in both electrolyte systems and thus kinetic parameters cannot be assessed. The transport effect in Co-W is apparent with the partial current densities of both Co and W increasing with a higher rotation rate, and a limiting current density is observed. However, with the addition of Fe(II), the Co, and W partial current densities decrease at a higher rotation rate, and do not exhibit a unique transport controlled limiting current density. This behavior may be due to the larger inhibiting effect imparted by iron on the Co and W reduction rates.

The side reaction partial current densities for Co–W and Fe–Co–W alloy depositions are shown in **Figure 8** for the two different temperatures and rotation rates. During Co–W deposition the partial current densities of side reaction (**Figure 8A**) are nearly the same under all deposition conditions. For Fe–Co–W deposition (**Figure 8B**) there is a more significant change in the current density with temperature, but the magnitude of the side reaction is similar to Co-W. Thus, the large decrease in the current efficiency shown in **Figure 5** is due to the reduced metal rates, and not an enhanced side reaction. In both cases the side reaction is dominated by water reduction and changes observed in its reaction rate may be reflective of the deposit concentration and local pH changes that occur at the electrode surface.

Electrodeposition of Nanowires

In the electrodeposition of nanowires of non-noble elements when using a template approach, there are two challenges to consider: i. gas bubbles that are generated from the side reaction blocking the nanopore and ii. mass transport influences of the metal reaction rates that can lead to deposit concentration gradients due to the changing boundary layer on account of the pore depth changing as the wires grow. Despite a higher, favorable current efficiency at higher electrolyte temperature, there is a noted transport influence. Therefore, to avoid compositional gradients, Co–W and Fe–Co–W nanowires were electrodeposited at the lower electrolyte temperature, 23°C, to promote deposition in the kinetic regime. Pulse deposition was chosen over dc deposition in order to avoid a significant change in the local pH due to the recessed geometry of the nanopore, and to avoid hydrogen gas bubbles from blocking the pores. The "on" current was −20.3 mA for the Co–W with an "off" current of zero, over an exposed area of 2.54 cm^2, with the same "on" and "off" times of 0.1 s. The same current normalized to the planar area was used for the Fe–Co–W deposition with the same pulse duration and duty cycle. The actual current density has an uncertainty associated with it, as the porosity value is not precisely known and is reported by the manufacturer to vary from 4 to 20%. The deposition was halted after the potential response indicated that deposition reached the top of the membrane. For example, **Figure 9** shows the potential transient behavior during Co–W and Fe–Co–W nanowire deposition into the nanoporous membrane. Three distinct regions were observed. In the first region, I, nucleation of the initial layer onto the gold substrate occurs. In the second region deposition follows a kinetic control,

and the nanowires grow in the membrane. Stage III corresponds to the formation of a film that grows on top of the membrane, as the wires reach the top of the pores and grow together. In the case of Co–W deposition of nanowires (**Figure 9A**), three distinct regions are clearly defined, for Fe–Co–W, with significantly lower current efficiency, regions I and II (**Figure 9B**), are not as distinct and the transient region is extended.

Released Co–W and Fe–Co–W nanowires are presented in **Figure 10** by inspection by TEM. The wire diameter varied in the range approximately from 150 to 214 nm along the length of nanowires. It was also observed that both the Co–W and Fe–Co–W nanowires had variable lengths indicative of wires that possibly broke when released from the membrane.

The average deposit concentration of Co, W and Fe in the nanowires was measured. In the case of the Co–W nanowires, the obtained content of Co and W was 78 and 22 wt%, respectively. This deposit concentration is similar to that obtained in **Figure 2**. The content of the Fe–Co–W alloy nanowires was 7, 32, and 61 wt% for Co, W, and Fe, respectively, also similar to the concentration of the thin films at low current density.

CONCLUSIONS

Regardless of the electrolyte temperature or rotation rate, the addition of Fe ions into the electrolyte inhibited the Co partial current density, and thus the Co content into the deposit. In contrast, there was a weak effect of Fe ions on the W wt% in the deposit, however, the W partial current density considerably decreased at low current densities, despite the well-documented inducing behavior of Fe on W co-reduction. Thus, the addition of Fe ions to the electrolyte when the ratio of Co:W ions were 1:1 exhibited an anomalous codeposition behavior, inhibiting both the Co and W metal deposition rates. The addition of Fe had no effect in enhancing the W partial current densities. Guided by the thin film results, conditions were selected to replicate the thin film deposit concentration as nanowires, by applying a pulse current at 23°C.

DATA AVAILABILITY

All datasets generated for this study are included in the manuscript and/or the supplementary files.

AUTHOR CONTRIBUTIONS

The experiments were conducted by TM and were guided by HC and EP. All authors have read and approved the manuscript.

FUNDING

This study was supported by the European Research Council under European Union's Sevenths Framework Program TEMADEP (IRSES #05-104-7540), EU COMM # H2020-MSCA-RISE-2017 Research and Innovation Staff Exchange (RISE), the US National Science Foundation #CHE-0957448, and the Lithuanian ESF agency grant (code VP1-3.1-ŠMM-08-K-01-014).

ACKNOWLEDGMENTS

The authors thankfully acknowledge W. Fowle and T. Bairachna for help with TEM imaging.

REFERENCES

Baker, B. C., and West, A. C. (1997). Electrochemical impedance spectroscopy study of nickel-iron deposition I. Experimental results. *J. Electrochem. Soc.* 144, 164–169. doi: 10.1149/1.1837379

Belevskii, S. S., Cesiulis, H., Tsyntsaru, N. I., and Dikusar, A. I. (2010). The role of mass transfer in the formation of the composition and structure of CoW coatings electrodeposited from citrate solutions. *Surf. Eng. Appl. Electrochem.* 46, 570–578. doi: 10.3103/S1068375510060050

Brenner, A. (1963). *Electrodeposition of Alloys,* Vol. I. *New York, NY: Academic Press.*

Brenner, A., Burkhead, P., and Seegmiller, E. (1947). Electrodeposition of tungsten alloys containing iron, nickel and cobalt. *J. Res. Natl. Bur. Stand.* 39, 351–383. doi: 10.6028/jres.039.023

Capel, H., Shipway, P. H., and Harris, S. J. (2003). Sliding wear behaviour of electrodeposited cobalt–tungsten and cobalt–tungsten–iron alloys. *Wear* 255, 917–923. doi: 10.1016/S0043-1648(03)00241-2

Dahms, H., and Croll, I. M. (1955). The anomalous codeposition of iron-nickel alloys. *J. Electrochem. Soc.* 112, 771–775. doi: 10.1149/1.2423692

Eliaz, N., and Gileadi, E. (2007). The mechanism of induced codeposition of Ni-W alloys. *ECS Trans.* 2, 337–349. doi: 10.1149/1.2408887

Eliaz, N., and Gileadi, E. (2008). "Induced codeposition of alloys of tungsten, molybdenum and rhenium with transition metals," in *Modern Aspects of Electrochemistry,* Vol 42, eds *C. G. Vayenas, R. E. White, and M. E. Gamboa-Aldecop (New York, NY: Springer),* 191–301.

Fukushima, H., Akiyama, T., Akagi, S., and Higashi, K. (1979). Role of iron-group metals in the induced codeposition of molybdenum from aqueous solution. *T. Jpn. I. Met.* 20, 358–364. doi: 10.2320/matertrans1960.20.358

Gangasingh, D., and Talbot, J. B. (1991). Anomalous electrodeposition of nickel-iron. *J. Electrochem. Soc.* 138, 3605–3611. doi: 10.1149/1.2085466

Grande, W., and Talbot, J. B. (1993). Electrodeposition of thin films of nickel-iron II. Modeling. *J. Electrochem. Soc.* 140, 675–681. doi: 10.1149/1.2056141

Hamid, Z. A. (2003). Electrodeposition of cobalt–tungsten alloys from acidic bath containing cationic surfactants. *Mater. Lett.* 57, 2558–2564. doi: 10.1016/S0167-577X(02)01311-3

Hessami, S., and Tobias, C. W. (1989). A mathematical model for anomalous codeposition of nickel-iron on a rotating disk electrode. *J. Electrochem. Soc.* 136, 3611–3616. doi: 10.1149/1.2096519

Madore, C., and Landolt, D. (1993). The rotating cylinder Hull cell: design and application. *Plat. Surf. Finish.* 80, 73–78.

Matlosz, M. (1993). Competitive adsorption effects in the electrodeposition of iron-nickel alloys. *J. Electrochem. Soc.* 140, 2272–2279. doi: 10.1149/1.2220807

Podlaha, E. J., and Landolt, D. (1996). Induced codeposition: II. Mathematical modeling of Ni-Mo alloys. *J. Electrochem. Soc.* 143, 893–899. doi: 10.1149/1.1836554

Podlaha, E. J., and Landolt, D. (1997). Induced codeposition: III. Molybdenum alloys with nickel, cobalt and iron. *J. Electrochem. Soc.* 144, 1672–1680. doi: 10.1149/1.1837658

Ramesh, L., Sheshadri, B. S., and Mayanna, S. M. (1998). Development of Fe-Co-W alloys as cathode materials for fuel cell application. *Trans. Inst. Metal Finish.* 76, 101–104. doi: 10.1080/00202967.1998.11871204

Sasaki, K., and Talbot, J. B. (1995). Electrodeposition of binary iron-group alloys. *J. Electrochem. Soc.* 142, 775–782. doi: 10.1149/1.2048534

Sun, S., Bairchanya, T., and Podlaha, E. J. (2013). Induced codeposition behavior of electrodeposited NiMoW alloys. *J. Electrochem. Soc.* 160, D434–D440. doi: 10.1149/2.014310jes

Tsyntsaru, N., Belevsky, S., Dikusar, A., and Celis, J.-P. (2008). Tribological behavior of electrodeposited cobalt-tungsten coatings: dependence on current parameters. *Trans. Inst. Met. Finish.* 86, 301–307. doi: 10.1179/174591908X371131

Tsyntsaru, N., Cesiulis, H., Donten, M., Sorte, J., Pellicer, E., and Podlaha-Murphy, E. J. (2012). Modern trends in tungsten alloys electrodeposition with iron group metals. *Surf. Eng. Appl. Electrochem.* 48, 491–520. doi: 10.3103/S1068375512060038

Tsyntsaru, N., Dikusar, A., Cesiulis, H., Celis, J.-P., Bobanova, Z., Sidel'nikova, S., et al. (2009). Tribological an corrosive characteristics of electrochemical coatings based on cobalt and iron superalloys. *Powder Metal. Met. C+.* 48, 419–428. doi: 10.1007/s11106-009-9150-7

Weston, D. P., Shipway, P. H., Harris, S. H., and Cheng, M. K. (2009). Friction and sliding wear behaviour of electrodeposited cobalt and cobalt-tungsten alloy coatings for replacement of electrodeposited chromium. *Wear* 267, 934–943. doi: 10.1016/j.wear.2009.01.006

Zech, N., Podlaha, E. J., and Landolt, D. (1998). Rotating cylinder hull cell study of anomalous codeposition of binary iron-group alloys. *J. Appl. Electrochem.* 28, 1251–1260. doi: 10.1023/A:1003416328942

Zech, N., Podlaha, E. J., and Landolt, D. (1999a). Anomalous codeposition of iron-group alloys, I. *Experimental results. J. Electrochem. Soc.* 146, 2886–2891. doi: 10.1149/1.1392024

Zech, N., Podlaha, E. J., and Landolt, D. (1999b). Anomalous codeposition of iron-group alloys, II. Mathematical model. *J. Electrochem. Soc.* 146, 2892–2900. doi: 10.1149/1.1392025

Conflict of Interest Statement: The authors declare that the research was conducted in the absence of any commercial or financial relationships that could be construed as a potential conflict of interest.

frontiers in Chemistry

REVIEW
published: 06 August 2019
doi: 10.3389/fchem.2019.00516

Electrodeposition of V-VI Nanowires and Their Thermoelectric Properties

Cristina V. Manzano[†] *and Marisol Martin-Gonzalez*[*†]

Instituto de Micro y Nanotecnología, IMN-CNM, CSIC (CEI UAM+CSIC), Madrid, Spain

Nanostructuration is an intensive field of research due to the appearance of interesting properties at the nanoscale. For instance, in thermoelectricity the most outstanding improvements obtained lately are related to phenomena that appear as a result of nano-engineering different materials. The thermoelectric effect is the direct conversion from temperature gradients into electricity and *vice versa*. When going to low dimensions, for example in the particular case of thermoelectric nanowires, the transport properties of phonons are modified with respect to those found in bulk leading to a higher thermoelectric figure of merit *z*. In more detail, this review tries to compile some of the landmarks in the electrodeposition of Bi_2Te_3-based nanowires. We will focus on the achievements using different templates, electrolytes and deposition modes. We will also summarize the measurements performed in those nanowires and the main conclusions that can be extracted from the published works. Finally, an update of nanowire-based thermoelectric generators is also included.

Keywords: electrodeposition, Bi_2Te_3, nanowires, thermoelectric properties, Seebeck coefficient, electrical conductivity, thermal conductivity, anodic aluminum oxide

OPEN ACCESS

Edited by:
Jae-Hong Lim,
Gachon University, South Korea

Reviewed by:
Yuan Yang,
Columbia University, United States
Kimoon Lee,
Kunsan National University, South Korea

***Correspondence:**
Marisol Martin-Gonzalez
marisol@imm.cnm.csic.es
orcid.org/0000-0002-5687-3674

[†]*These authors have contributed equally to this work*

Specialty section:
This article was submitted to Electrochemistry, a section of the journal Frontiers in Chemistry

Received: *26 February 2019*
Accepted: *04 July 2019*
Published: *06 August 2019*

Citation:
Manzano CV and Martin-Gonzalez M (2019) Electrodeposition of V-VI Nanowires and Their Thermoelectric Properties. Front. Chem. 7:516. doi: 10.3389/fchem.2019.00516

INTRODUCTION

Thermoelectric materials have received significant attention in the last decades given that these materials are able to transform a temperature gradient into electricity, and thus they provide a sustainable source of electrical energy wherever a heat source can be found. The efficiency of these materials depends on the figure of merit (z), which is given by the following equation:

$$z \cdot T = \frac{\sigma \cdot S^2}{\kappa} \cdot T, \tag{1}$$

where T is the absolute temperature, σ is the electrical conductivity, S is the Seebeck coefficient and κ is the thermal conductivity. The thermoelectric efficiency (η) is defined as:

$$\eta\,(\%) = 100\left(\frac{T_H - T_C}{T_H}\right)\frac{\sqrt{1+z\cdot\overline{T}}-1}{\sqrt{1+z\cdot\overline{T}}+\left(\frac{T_H}{T_C}\right)}, \tag{2}$$

where T_H is the temperature at the hot side and T_C is the temperature on the cold side. Nowadays, the main drawback that these materials present is a lower efficiency when compared with other ways of obtaining electrical energy. In order to improve the efficiency of these materials, its figure of merit has to be increased.

Nanostructuration is one of the approaches to increase the figure of merit in thermoelectric materials (Dresselhaus et al., 2007; Martín-González et al., 2013; Ali et al., 2017; Chen et al., 2018; Goktas et al., 2018; Swinkels and Zardo, 2018; Selvan et al., 2019). In this sense, nanowires are

a great field of study to underline the physics behind the influence of the nanostructuration on the improvement of the figure of merit (Domínguez-Adame et al., 2019). One of the parameters that is more influenced by nanostructuration is the lattice thermal conductivity. This is due to the higher surface to volume ratio that these structures present (Domínguez-Adame et al., 2019). At the surface of the nanowires phonons are scattered, and this produces a reduction of the lattice thermal conductivity. Taking into account that the figure of merit is inversely proportional to the thermal conductivity, a reduction of this parameter produces an increase in the thermoelectric efficiency. Moreover, the smaller the nanowire diameter, the larger the phonon dispersion and, thus, the higher the thermoelectric figure of merit (Borca-Tasciuc et al., 2004).

Some of the most studied thermoelectric materials are Bismuth Telluride-based. Its best efficiency is around room temperature. And, its ternary compounds are the ones most used in commercially available devices. Bi_2Te_3-based materials, apart from being the best thermoelectric for room temperature applications, belong also to a class of quantum materials called three-dimensional topological insulators (3D-TIs) (Hasan and Kane, 2010; Qi and Zhang, 2011). This quantum form of matter presents unique and topologically protected surface states (Zhang H. et al., 2009; Zhang T. et al., 2009; Chen et al., 2012; Muñoz Rojo et al., 2016); Apart from that, Bi_2Te_3 has a band gap of 0.15 eV (Greenaway and Harbeke, 1965); and a rhombohedral structure with space group D^5_{3d} ($R\bar{3}m$), although it can also be described in hexagonal coordinates. The crystal structure has a layered disposition with five atomic layers with covalent bonding as the basic unit (cell), named as the quintuple layer (QL). The bonding between the QLs is much weaker than the inter-layer bonding since it is a van de Waals-type interaction. Due to this crystallographic structure (see **Figure 1**), this material presents high anisotropy in the electrical (Delves et al., 1961) and thermal conductivities (Goldsmid, 1961; Tritt and Subramanian, 2006), while the Seebeck coefficient is nearly isotropic (Rowe, 2012).

In more detail, the figure of merit of bulk single-crystalline bismuth telluride in the direction parallel to the *c-axis* of the structure was determined by Antonova et al. (Antonova and Looman, 2005). Its $zT_{//c}$ is of 0.31, with Seebeck coefficient, electrical conductivity, and thermal conductivity values of −240 μV/K, 0.02 $(\mu\Omega\cdot m)^{-1}$, and 1 W/m·K, respectively (Antonova and Looman, 2005). Conversely, when the crystal structure was oriented perpendicular to the *c-axis,* the values of the Seebeck coefficient, electrical conductivity, and thermal conductivity were −240 μV/K, 0.1 $(\mu\Omega\cdot m)^{-1}$, and 2.2 W/m·K, respectively, which corresponds to a higher figure of merit of $zT_{\perp c} = 0.78$ (Antonova and Looman, 2005).

In the case of electrodeposited Bi_2Te_3 films, Martin-Gonzalez's group (Manzano et al., 2016a) reported the effect of anisotropy in highly oriented [110] Bi_2Te_3 electrodeposited films. The electrical conductivity perpendicular to the *c-axis* is nearly five (4.8) times higher than the electrical conductivity parallel the *c-axis*. The Seebeck coefficient perpendicular to the c-*axis* is within the experimental uncertainty of the Seebeck coefficient along the c-*axis*, indicating the electrodeposited film is isotropic for this property. A two-fold increase from the in-plane to out-of-plane thermal conductivity was observed. From the measured in-plane and out-of-plane values at 300 K, figure of merits of $zT_{//c} = (5.6 \pm 1.2)\cdot10^{-2}$ and $zT_{\perp c} = (10.4 \pm 2.6)\cdot10^{-2}$ are respectively rendered, which yields an increase by a factor of 1.8 between the in-plane and out-of-plane thermoelectric performances (Manzano et al., 2016a). Because of this anisotropy, it is very important to achieve stoichiometric nanowire arrays oriented along [110] direction to obtain the best thermoelectric performance.

This review is focused on the efforts to obtain stoichiometric nanowires with the proper orientation by electrodeposition and their thermoelectric properties for the V-VI thermoelectric compounds (Bi_2Te_3, Se-doped Bi-Te, Sb-doped Bi-Te, and SbTe). We will analyze the influence of the electrodeposition conditions on morphology, composition and thermoelectric properties.

ELECTRODEPOSITION OF Bi_2Te_3 NANOWIRES

To obtain one-dimensional nanostructures, electrodeposition has some advantages over other growth methods as this technique enables obtaining high aspect-ratio structures, along with a good control over the crystallographic structure and the morphological properties. Moreover, it is cost effective and scalable to industrial requirements. In general, previously to the electrodeposition of nanowires, the electrodeposition of films was optimized, in order to find the most appropriate experimental parameters to obtain the desired composition, orientation, morphology, etc. In the literature, different reviews of electrodeposition thermoelectric films can be found (Xiao et al., 2008; Boulanger, 2010; Rostek et al., 2015). Therefore, in this work we will focus mainly on the electrodeposition of nanowires.

The most studied solution to obtain bismuth telluride films and nanowires is an aqueous solution of Bi^{3+}, TeO^{2+}, and HNO_3. The mechanism of electrodeposition using this solution was investigated by Stacy group (Martín-González et al., 2002) in detail. Based on the Pourbaix diagram developed in that work, it can be seen the necessity for a strong acidic media to stabilize the ionic species in solution.

In the specific case of electrochemically grown nanowires, different templates can be used, which allow the production of high-density nanowire arrays and, at the same time, give them certain mechanical stability (Caballero-Calero and Martín-González, 2016). The two most common templates to obtain nanowires by electrodeposition are polycarbonate (PC) and anodic aluminum oxide (AAO) membranes, being both templates electrically insulating and robust.

Anodic aluminum oxide membranes (Masuda and Fukuda, 1995; Lee et al., 2006; Martín et al., 2012, 2013; Lee and Park, 2014; Manzano et al., 2014, 2016b; Sousa et al., 2014) exhibit a higher density of pores (up to 10^{10} pores/cm^2) (Sander et al., 2003) and can achieve template thicknesses of more than 100 μm. These membranes display hexagonal ordering perpendicular to the surface and thermal conductivities of 1.07–1.32 W/m·K (Abad et al., 2016a). In the case of polycarbonate membranes, they

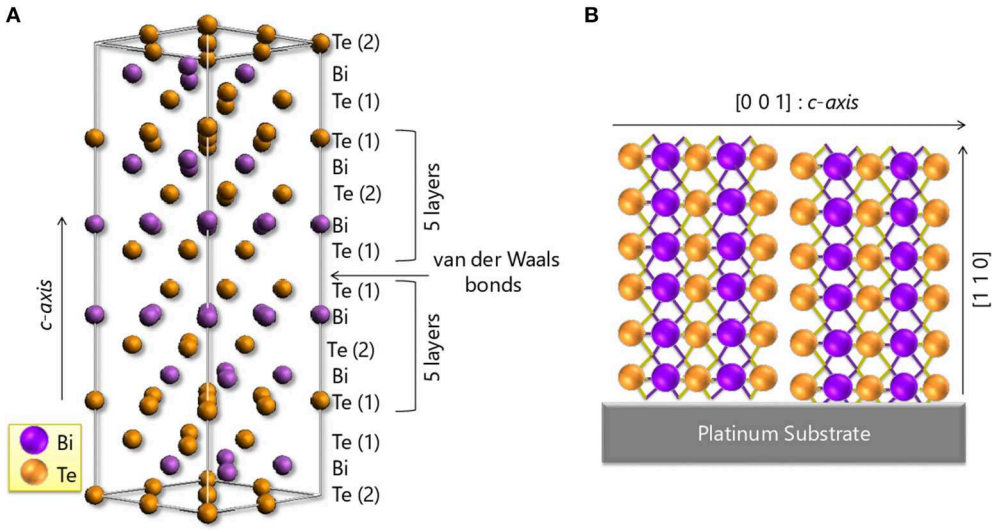

FIGURE 1 | (A) Crystal structure of bismuth telluride. The structure shows the five atomic layers stacked along the c-axis (quintuplet) separated by van der Waals bonds. **(B)** The orientation of a Bi_2Te_3 electrodeposited film, which main diffraction peaks will be [110] related. As can be observed in this configuration the quintuplets are perpendicular to the substrate and so the van der Walls bonds. Reproduced with permission from Manzano et al. (2016a). Copyright 2016 Scientific Reports-Nature.

have lower pore density ($\sim 10^8$ pores/cm^2) (Koukharenko et al., 2008), so fewer nanowires can be fabricated at the same time. These templates present lower thermal conductivity than AAO ($\sim$0.2 W/m·K) (Picht et al., 2012). It is important to stay at this point that there is also the possibility of growing nanowires without the necessity of a template, with techniques such as decorating the step edge of a substrate, see for instance (Menke et al., 2004). However, from now on we will only review the state of the art in nanowires obtained by electrodeposition inside a template.

There are different electrodeposition modes: constant potential or current density, and pulsed electrodeposition line pulsing between two potentials, or two current densities, or by pulsing by a combination between potential and current density. The principal achievements in the fabrication of bismuth telluride nanowires grown by electrodeposition are collected in **Table 1**.

The first work in electrodeposition of Bi_2Te_3 nanowires was reported in 1999 by Martin's group (Sapp et al., 1999) inside commercial anodic aluminum oxide. These nanowires were grown using constant current density in 280 $\pm$ 30 nm AAO templates. The resulting nanowires were polycrystalline. This landmark is the starting point of the temporal line for Bi_2Te_3 nanowire fabrication by electrodeposition that is presented in **Figure 2**.

From 2001 to 2003, Stacy's group spent many efforts in optimizing bismuth telluride nanowires. The obtained nanowires were oriented along [110] direction (which is the best direction to obtain the highest figure of merit for out-of-plane applications, with the *c-axis* perpendicular to the length of the nanowires, as explained before), a high filling ratio ($\sim$80%) and a high aspect ratio ($\sim$1,000) for diameters of 200, 75, 50, and 25 nm (Prieto et al., 2001; Sander et al., 2002, 2003). The electrochemistry was performed at 2°C.

Later on, Li's group worked on the growth of bismuth telluride nanowires also oriented along [110] direction, with a high filling ratio, uniform growth and 50 nm in diameter, by applying constant current density (Jin et al., 2004). In 2006 and 2007, different studies were reported changing the different parameters involved in the electrochemical process: using different reduction potentials to change the composition and crystallographic orientation (Wang et al., 2006), different Te and Bi concentrations in the electrolyte (Jun et al., 2006) and thermal annealings performed after the growth of the nanowires (Kim et al., 2007).

In order to further improve the filling factor of the nanowires, pulsed electrodeposition has been proved to be the best solution. The most commonly used method, so far, is pulsing between two different potentials at room temperature. The deposition consists on applying the reduction potential during a certain time, t_{on}, and then introduce a "rest" potential during a certain time, t_{off}. In 2006, Zhang's group (Liang et al., 2006) published the first study based on Bi_2Te_3 nanowires grown by pulsed-potential deposition. In this work, the effect of the reduction potential and the duration of the pulses in the crystallographic structure of the nanowires was analyzed. The produced nanowires were all oriented along the [015] direction. One year later, Stacy's group (Trahey et al., 2007) reported a study based on Bi_2Te_3 nanowires grown by pulsed-potential deposition in order to improve the filling ratio by enhancing the nucleation of the nanowires, which showed also the [110] direction. The nucleation rate obtained was found to be 95%. Furthermore, it was concluded that reducing the bath temperature to temperatures lower than 4°C (as they were doing in the previous works) improved

TABLE 1 | Principal achievements in the fabrication of bismuth telluride nanowires grown by electrodeposition.

Electrodeposition mode	Composition and orientation	Template	Nanowire diameter (nm)	References
Constant current density	Bi_2Te_3 Polycrystalline	AAO	280 ± 30	Sapp et al., 1999
Constant potential	Bi_2Te_3 [110]	AAO	200, 75, 50, and 25	Prieto et al., 2001; Sander et al., 2002, 2003
Constant current density	Bi_2Te_3 [110]	AAO	50	Jin et al., 2004
Pulsed electrodeposition between two potentials	Bi_2Te_3 [015]	AAO	40-60	Liang et al., 2006
Pulsed electrodeposition between two potentials	Bi_2Te_3 [110]	AAO	40	Trahey et al., 2007
Constant potential, constant current density and pulsed electrodeposition between two potentials	Bi_2Te_3 [110]	AAO	50-80	Jongmin et al., 2008; Lee et al., 2010a,b; Peranio et al., 2012
Constant potential in DMSO	Bi_2Te_3 [015]	PC	60	Frantz et al., 2010, 2012
Pulsed electrodeposition in DMSO	$Bi_{1.55}Te_{3.45}$ [110]	AAO	70	Li W.-J et al., 2011
Constant potential	Bi_2Te_3 [110]	PC	15-25	Picht et al., 2012
Pulsed electrodeposition	Bi_2Te_3 [015]	AAO	15	Martín et al., 2013
Pulsed electrodeposition in P0CCOV	Bi_2Te_3 [110]	AAO	25,45,52, and 300	Muñoz Rojo et al., 2016, 2017; Rodríguez-Fernández et al., 2016
Pulsed electrodeposition in P0CCOV	3D-Bi_2Te_3 [110]	AAO	52	Martín et al., 2014; Ruiz-Clavijo et al., 2018

the alumina filling factor and the nanowires crystallinity. In contrast, nanowires that were grown at temperatures between 7 and 10°C or around room temperature (22 to 23°C) presented more crystallographic orientations. In 2008, Nielsch's group (Jongmin et al., 2008) published a study where bismuth telluride nanowires grown at different deposition modes (constant potential, constant current density, and pulsing between two potentials) were compared. Pulsed-potential deposition showed nanowires preferably oriented along [110] direction. This mode was the procedure used by Nielsch's group from 2010 to 2012 (Lee et al., 2010a,b; Peranio et al., 2012). The nanowires reported in these papers followed Lee's et al. (Jongmin et al., 2008) recipe. Those nanowires presented a uniform filling ratio with 50–80 nm in diameter and 25–60 μm in length and were preferentially oriented along [110] direction.

Between 2010 and 2012, Boulanger's group (Frantz et al., 2010) reported for the first time the electrodeposition of Bi_2Te_3 nanowires in DMSO using PC membranes. They used a mixture of dimethyl sulfoxide (DMSO) and water. In the presence of DMSO, the current density decreases by a factor four in comparison with an aqueous solution. Because of this reduction in the diffusion coefficient, the growth rate of the nanowires is lower. This improves the filling ratio of the templates. Also a reduction in their crystallite size was observed when compared to those grown in aqueous solution (Frantz et al., 2010). The nanowires obtained in these studies were 60 nm in diameter, polycrystalline, and 25–30 μm in length, with a preferential orientation along [015] direction (Frantz et al., 2010, 2012) and homogeneous in composition (reaching the stoichiometric Bi_2Te_3) along the length of the nanowires (Frantz et al., 2012). In 2011, pulsed-potential electrodeposition was studied by Yen's group using a DMSO solution, and those nanowires exhibited a uniform filling ratio with 70 nm in diameter and 41 μm in length (Li W.-J et al., 2011). The nanowires were preferentially oriented along [110] direction and they had a composition of $Bi_{1.55}Te_{3.45}$, a little bit far from the stoichiometry.

In 2012, Toimil-Molares's group (Picht et al., 2012) observed a change in the crystallographic orientation by adjusting the reduction potentials, bath temperature (from 20 to 4°C), and electrolyte concentration for nanowires grown in ion-track PC membranes. Also, in 2012, Outzourhit's group (Elyaagoubi et al., 2017) reported the electrodeposition of Bi_2Te_3 nanowires inside 52 nm pore AAO templates grown with the DMSO:H_2O solution (Frantz et al., 2010). The nanowires obtained were polycrystalline and with a small crystallite size of 30 nm.

In 2013, Martin-Gonzalez's group reported 15 nm in diameter Bi_2Te_3 nanowires in AAO membranes with [015] as the main diffraction maxima (Martín et al., 2013). In order to do that, the group developed porous alumina templates with 15–12 nm in diameter by the addition of ethylene glycol during aluminum anodization (Martín et al., 2013; Manzano et al., 2014). And, more recently, the group has extended the process to obtain sub-10 nm templates (Resende and Martín-González, 2019) in concentrated sulphuric acid and 25% $_{V/V}$ of ethanol anodized under low current densities. **Figures 3A,B** show SEM images of 14 nm pore diameter AAO templates and 15 nm in diameter Bi_2Te_3 nanowires embedded into the AAO templates, respectively.

In 2014, Song's group generated 55 nm nanowires in AAO templates oriented in the [110] direction using constant potential in standard aqueous solution. They concluded that changing the reduction potential, the number of twins inside the nanowires

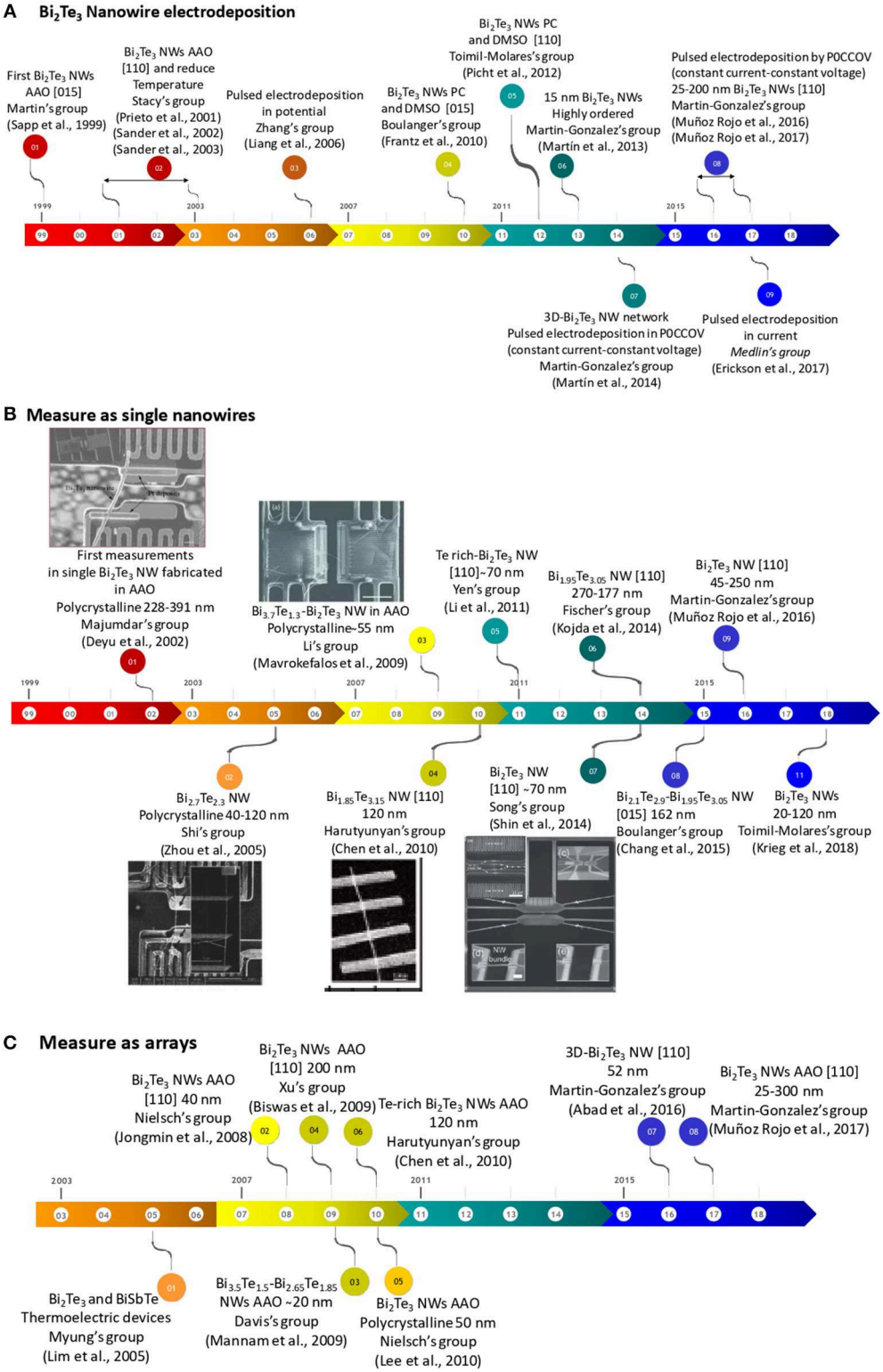

FIGURE 2 | (A) Temporal line of the principal achievements in the fabrication of bismuth telluride nanowires grown by electrodeposition. **(B)** The temporal line of the thermoelectric measurements in single bismuth telluride nanowires grown by electrodeposition. **(C)** The temporal line of the thermoelectric measurements of bismuth telluride nanowires embedded inside templates grown by electrodeposition. Reproduced with permission from Deyu et al. (2002), Zhou et al. (2005), Mavrokefalos et al. (2009), Chen et al. (2010), and Shin et al. (2014). Copyright 2002 IEEE, 2005 Applied Physics Letters, 2009 Journal of Applied Physics, 2010 American Chemical Society and 2014 Royal Society of Chemistry.

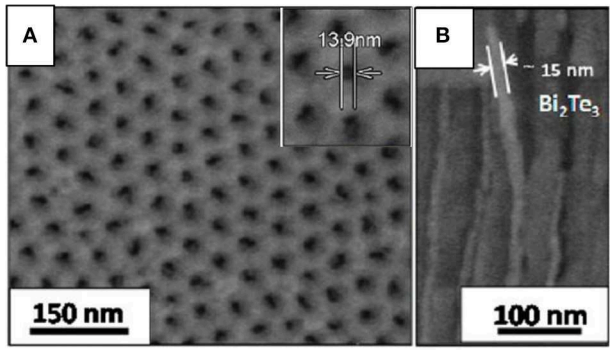

FIGURE 3 | (A) SEM images of highly ordered 14 nm pore diameter AAO templates and **(B)** a cross-section by SEM of 15 nm Bi_2Te_3 nanowires inside the AAO nanopores. Adapted with permission from Martín et al. (2013). Copyright 2013 ACS Publications.

(and so the crystallite size) could be controlled (Shin et al., 2014). In the same year, Fischer's group reported a similar deposition method, pulsed-potential, to obtain nanowires with 190–320 nm in diameter and oriented preferentially along [110] direction (Kojda et al., 2014). From 2014 to 2016, Bi_2Te_3 nanowires with different compositions were obtained applying different reduction potentials (Ng et al., 2014, 2016; Kok et al., 2016; Proenca et al., 2017). In 2015, Nandhakumar's group reported nanowires with 80 nm in diameter, obtained using aqueous solution into PC membranes with [110] as preferential direction (Koukharenko et al., 2015). In 2016, Cantarero's group reported Raman measurements performed in Bi_2Te_3 nanowires grown in AAO templates by Martin–Gonzalez's group (Rodríguez-Fernández et al., 2016). In this study, nanowires with different compositions were fabricated changing the reduction potential on purpose. The conclusion of the study is that the Raman spectra of Te-rich bismuth telluride nanowires exhibited an additional peak compared to stoichiometric Bi_2Te_3 nanowires. This peak corresponded to Te nanocrystals that cannot be observed by XRD because they are very small. Therefore, Raman spectroscopy seems to be a perfect tool to detect Te clusters inside the nanowires.

In 2016, Martin-Gonzalez's group published the first nanowires produced by pulsing between a certain potential and zero current. This procedure was tested in films before, see for example (Manzano et al., 2013). This methodology was used for the first time to obtain stoichiometric bismuth telluride films highly oriented along [110] direction (Manzano et al., 2013). This procedure has been called Pulsed ZERO Current COnstant Voltage (P0CCOV). It consists in alternating between potentiostatic and galvanostatic modes during each pulse, instead of pulsing between two potentials—only potentiostatic—(as done until that moment for Bi_2Te_3) or pulsing between two currents—only galvanostatic-, which is the other conventional way of pulsing. The reason to choose that different option of pulsing is that during the *on* time, the ions are deposited on the electrode surface and their concentration decreases at the interface between the substrate and the electrolyte. By using zero current periods during the *off* time, the system is allowed to be in a truly resting state, which helps to redistribute the remaining ions at the interface. In other words, at current = 0 A, there is no current going through the interface electrode/solution, so no driving force is applied during that time and the system can truly rest. This is slightly different than pulsing between one potential and the open circuit potential (OCP). The OCP was calculated at the beginning of the process, however the electrode surface is not the same as deposition takes place. The surface of the electrode changes in each pulse. Therefore, the initial OCP is not a real OCP after each pulse and at the initial OCP value, a residual current is still going through the system. While in the P0CCOV procedure the current is always 0 during the off time. So, no current is passing, allowing a real resting time for the electrodeposit material.

By this P0CCOV procedure bismuth telluride nanowires with different pore diameters (300, 52, 45, and 25 nm), high filling ratio, oriented along the [110] direction and with the desired stoichiometry (Bi_2Te_3) were obtained at 0°C (Muñoz Rojo et al., 2016, 2017). The length of these nanowires were 32, 50, 42, and 25 μm for different diameters 300, 52, 45, and 25 nm, respectively. **Figure 4** shows SEM images of the top view of Bi_2Te_3 nanowires for the different diameters.

In 2017, Medlin's group (Erickson et al., 2017) reported the electrodeposition at pulsed galvanostatic mode between two different current densities, followed by thermal annealing between 150 and 350°C to improve the crystallinity of stoichiometric Bi_2Te_3 nanowires with 75 nm in diameter. Those nanowires were oriented preferentially along [110] direction. The same year, bismuth-rich bismuth telluride nanowires with different diameters (10–275 nm) were electrodeposited using different current densities in order to change the composition of the wires by Hill's group. In order to reduce the pore diameter of the AAO templates, silica was deposited by dip-coating before the electrodeposition (Ryan et al., 2017).

It is known that the use of additives reduces the roughness of electrodeposited films. Normally, additives such as ethylenediaminetetraacetic acid (EDTA) are used because it forms a complex with bismuth and thus reduces its diffusion coefficient, or sodium lignosulfonate (SLS) (Kuleshova et al., 2010; Naylor et al., 2012; Caballero-Calero et al., 2014; Abad et al., 2015) which is used in the electrodeposition of tellurium and selenium because it reduces the crystallite size; this additive allows the formation of films with less roughness and favors the [110] orientation. Furthermore, White's and Martin-Gonzalez's groups observed an improvement in the Seebeck coefficient of Bi_2Te_3 films (Kuleshova et al., 2010; Caballero-Calero et al., 2014) and Se doped-BiTe films (Caballero-Calero et al., 2018) with the use of lignosulfonates like sodium lignosulfonate (SLS) in the solution. Nevertheless, the effect of additives is still to be studied in nanowires.

In conclusion, the most relevant results over the last two decades are that the smallest stoichiometric Bi_2Te_3 nanowires achieved are 15 nm in diameter. There are available stoichiometric nanowires oriented along the [110] direction in different diameters to perform different measurements. Pulsed electrodeposition (in its different forms) and bath temperatures

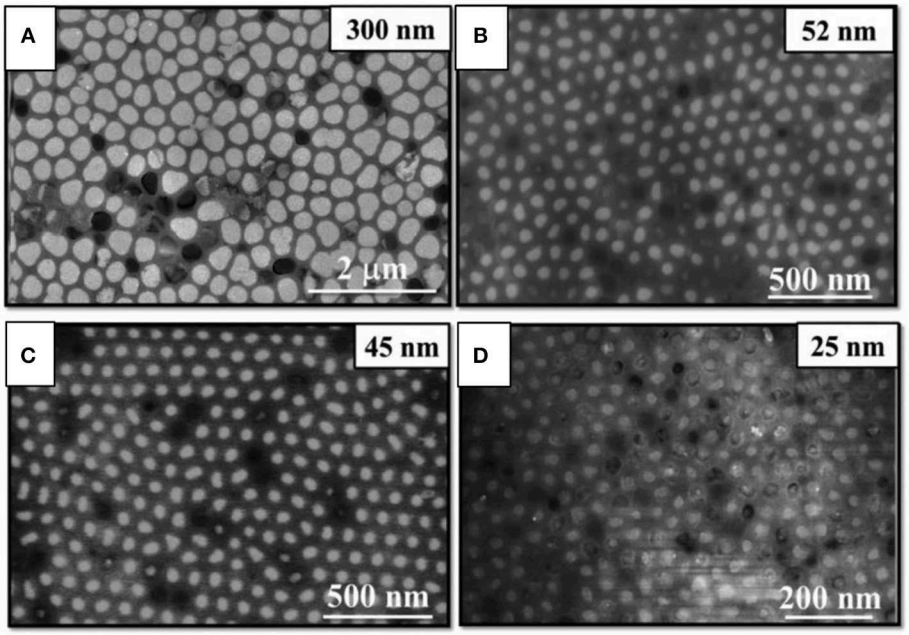

FIGURE 4 | SEM images of bismuth telluride nanowires with average different diameters: **(A)** 300 nm, **(B)** 52 nm, **(C)** 45 nm, and **(D)** 25 nm. Reproduced with permission from Muñoz Rojo et al. (2017). Copyright 2017 Nanoscale.

close to 0°C seem to be the best solution to improve the filling factor of the templates and to have high aspect-ratio (≈1,000).

THERMOELECTRIC PROPERTIES

As we have seen in the previous section, extensive work has been done in order to obtain stoichiometric nanowires, highly oriented along [110], and with different diameters. Now in this section, we are going to discuss the different measurements that have been performed to study the influence of the diameter in the different properties that affect their thermoelectric performance, such as Seebeck coefficient, thermal conductivity, and electrical conductivity.

In general, we can say that there are two approaches to measure the thermoelectric properties of bismuth telluride nanowires. One starts by selectively dissolving the template, dispersing or placing the nanowires in a microchip, and measuring the performance of a single nanowire. The second approach consists of carrying out the measurements on the nanowires embedded inside the templates for both polycarbonate membranes and anodic aluminum oxide matrices.

Thermoelectric Measurements on Single Nanowires

After selectively dissolving the template, the nanowires are obtained free-standing normally in solution. This procedure sometimes generates an oxide layer on the surface of the nanowire. Then, they must be placed in the right position on top of a lab fabricated microchip and contacts must be done to assure good electrical and thermal conductivity. Once all of that is done, different measurements can be performed, depending on the microchips configuration. For a review of the different type of microchips, please take a look to Rojo et al. (2013). Some of those kinds of microchips can be found in **Figure 5**.

In 2002, Majumdar's group (Deyu et al., 2002) reported for the first time the thermal conductivity (2.2–0.13 W/m·K for 228 and 391 nm, respectively) and Seebeck coefficient (-50 μV/K for 391 nm) of bismuth telluride nanowires grown in AAO by Stacy's group. The chip used for these measurements was a suspended two probes microfabricated chip with heaters. In that work, different contacts were tested.

In 2005, Shi's group (Zhou et al., 2005) reported thermoelectric measurements (σ, S, and κ) in single bismuth telluride nanowires grown in AAO. The nanowires were oriented along [110] direction with different compositions of bismuth and tellurium. Depending on the composition, different σ, S, and κ were obtained. The electrical conductivity, Seebeck coefficient and thermal conductivity at 300 K were found to be $0.8{\cdot}10^3$-$2{\cdot}10^3$ S/cm, −10 – −35 μV/K and 0.8–1.6 W/m·K. In this case, the composition of the nanowires were not stoichiometric. They were Bi-rich or Te-rich. The measurements were performed using four probes microchips.

In 2009, Li's group (Mavrokefalos et al., 2009) reported the thermoelectric properties (σ, S, and κ) of single bismuth telluride nanowires in AAO membranes measured using a four probes microchip. Here, the novelty was the use of thermal annealing in forming gas to make contact between the nanowires and the pre-patterned electrode to perform the measurements in order to reduce the superficial oxide layer. Polycrystalline

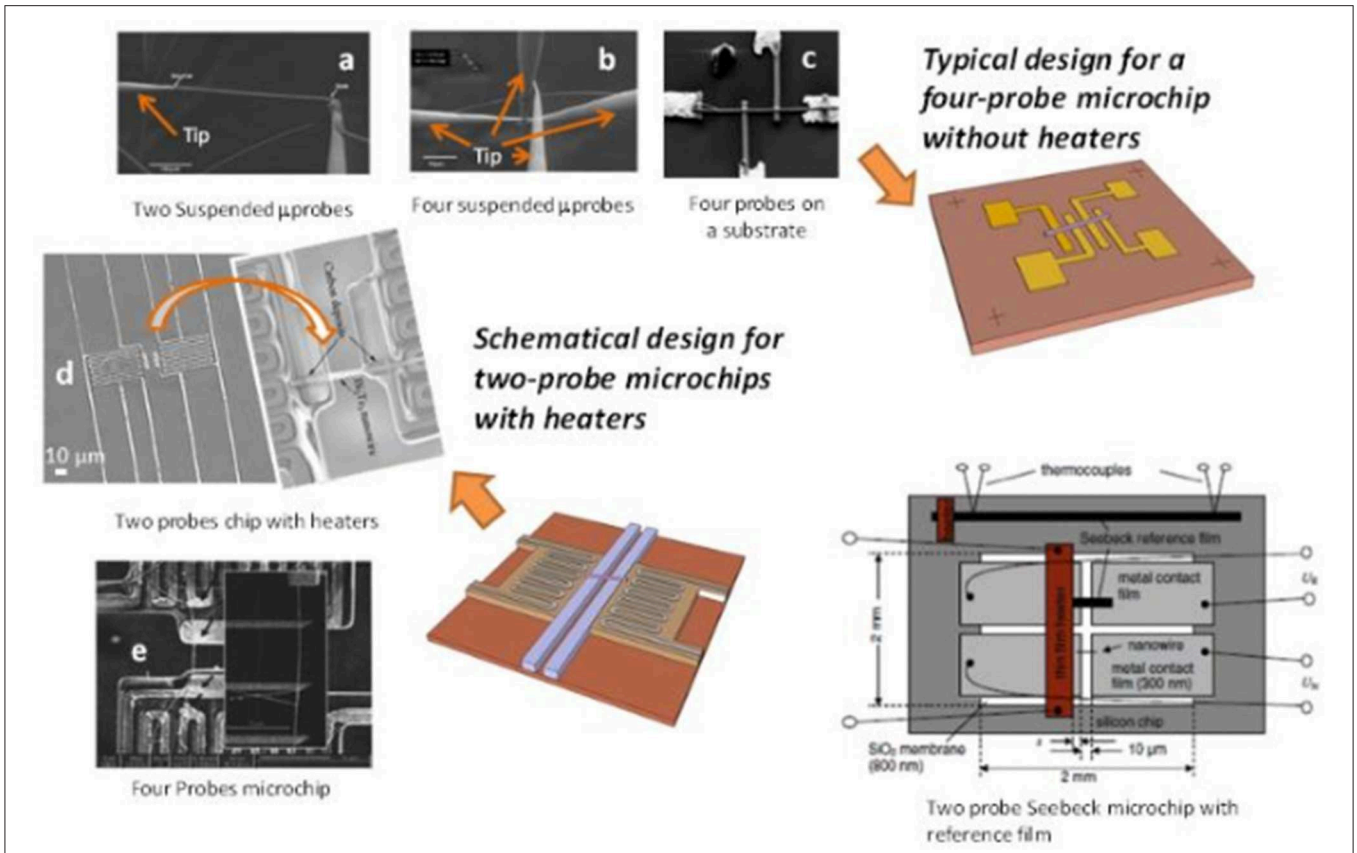

FIGURE 5 | Some types of microchips used for transport properties measurements in the literature. Reproduced with permission from Rojo et al. (2013). Copyright 2013 Nanoscale. **(a)** Two suspended μprobes, **(b)** four suspended μprobes, **(c)** four probes on a substrate, **(d)** two probes chip with heaters and **(e)** two probes microchip.

nanowires with different compositions ($Bi_{2.15}Te_{2.85}$, $Bi_{3.7}Te_{1.3}$, and Bi_2Te_3) were measured. Seebeck coefficients of −65 and −45 μV/K were obtained for Bi-rich $Bi_{3.7}Te_{1.3}$ and Bi_2Te_3, respectively at 300 K. The electrical conductivities range between 500 and 2200 S/cm at 300 K for Bi-rich $Bi_{3.7}Te_{1.3}$ and Bi_2Te_3, respectively. In addition, the thermal conductivities varied from 1.4 to 2.8 W/m·K for Bi-rich $Bi_{3.7}Te_{1.3}$ and Bi_2Te_3, respectively. In conclusion, the maximum figure of merit zT was found to be 0.06 for stoichiometric Bi_2Te_3 nanowires at RT and that value increases to $zT = 0.22$ at ∼450 K. The main conclusion is that better control over chemical composition is necessary to improve the zT of the electrodeposited NWs. In particular, they propose to maximize the care to minimize impurities present in the electrochemical deposition setup to avoid unintentional doping of the NWs.

One year after, Harutyunyan's group (Chen et al., 2010) reported the electrical resistivity of a single Te-rich $Bi_{1,85}Te_{3,15}$ nanowire grown at constant potential in aqueous solution using commercial AAO template. The nanowires were preferentially oriented along [110] direction with 120 nm in diameter. The electrical resistivity was found to be 12–4.3 μΩ·m for 1 to 350 K. The electrical resistivity decreased exponentially when the temperature increased. This value is smaller than the value expected for bulk Bi_2Te_3, 19 μΩ·m (Fleurial et al., 1988), probably due to the excess of tellurium of the nanowires. In general, when an excess of tellurium is observed, the electrical conductivity is much lower and the Seebeck coefficient is slightly higher than in stoichiometric Bi_2Te_3, which explains the results obtained. In this case, the measurements were performed using four probes microchips.

In 2011, Yen's group (Li W.-J et al., 2011) measured a value of 105 μΩ·m for Te-rich Bi_2Te_3 nanowires oriented along [110] direction, with 60–70 nm in diameter and grown in a DMSO solution by potential pulsed deposition inside AAO templates. According to the authors, this value is one order of magnitude higher than the value reported for single crystal Te-rich Bismuth Telluride (2.6 μΩ·m) (Rowe, 1995). The chip used in this case was a four-probes microchip.

In 2014, Song's group (Shin et al., 2014) reported the electrical conductivity of twin-free and twin-containing Bi_2Te_3 nanowires oriented preferentially along [110] direction and with 60–70 nm in diameter grown in AAO. The electrical conductivity value was similar for both cases, with a value of $2.3{\cdot}10^5$ S/m. However, the Seebeck coefficient was slightly smaller in the case of twin-containing (∼57 μV/K) than in the case of twin-free (∼70 μV/K). The thermal conductivity was smaller in the case of twin-containing (1.9 W/m·K) than in twin-free (2.3 W/m·K) due to the reduction of the carrier concentration and phonon scattering

(Shin et al., 2014). The chip used in this case was a four suspended microprobe chip. At the same time, Fischer's group published a study of $Bi_{1.95}Te_{3.05}$ nanowires grown in AAO using a two probes chip with heaters. The nanowires were oriented preferentially along [110] direction grown by pulsed electrodeposition with an electrical conductivity of 1.3–2.3·10^5 S/m, a Seebeck coefficient of −41 – −45 μV/K and thermal conductivity of 0.9–2 W/m·K for 270 and 177 nm in diameter, respectively (Kojda et al., 2014). This variation was explained by the difference in diameter along the nanowire.

In 2015, Boulanger's group reported the electrical conductivity and Seebeck coefficient of nanowires grown in PC membranes using DMSO solution. The nanowires were oriented along [015] direction with 162 nm in diameter, the value of the electrical conductivity and Seebeck coefficient was found to be 0.1–4·10^4 S/m and −10 – −80 μV/K for different concentrations of bismuth and tellurium, 0.42 and 0.39, respectively (Chang et al., 2015). In this case, the measurements were performed using four probes microchips.

In 2016, Martin-Gonzalez's group published a paper of stoichiometric Bi_2Te_3 nanowires grown in AAO templates. The nanowires were oriented preferentially along [110] direction grown by pulsed electrodeposition where the electrical conductivity was found to be 1·10^4, 1.6·10^4 and 2.9·10^4 S/m for different nanowire diameters, 250, 70, and 45 nm, respectively. The measurements were done using a four suspended microprobes chip. Furthermore, in this paper, the topological character of bismuth telluride nanowires was shown and the significance of the topological insulator surface states in room temperature nanowire working devices was demonstrated (Muñoz Rojo et al., 2016), since the ripples did not disappear when an electric current was passing through the nanowire.

More recently, 2018, Toimil-Molares's group reported an increment in the electrical resistivity from 0.2 to 2.4 mΩ·cm for diameters from 120 to 20 nm in Bi_2Te_3 nanowires oriented preferentially along [110] and [205] direction using polycarbonate membranes (Krieg et al., 2018). Furthermore, magneto-transport properties of these single nanowires were reported in this study. A metallic behavior was observed due to the highly-degenerate nature of the nanowires. The reduction in the electrical resistivity as diameter increases confirmed the quasi-ballistic nature of charge carriers, with the reduction of the number of surface conductance channels in disordered quantum wires with stronger quantum confinement. The chips used in this case were four probes microchips. The summary of the thermoelectric measurements of individual bismuth telluride nanowires is collected in **Table 2** in white.

Thermoelectric Measurements of Nanowires Embedded Inside the Template

For these measurements, the nanowires are not extracted from the template. So the oxide layer that appears upon template selective etching is avoided. Nanowire arrays embedded in matrices have a big advantage, given that it is possible to integrate the material directly into real thermoelectric devices (Biswas et al., 2009). Another interest of measuring the thermoelectric properties in nanowires embedded inside the templates is that the output current is enhanced (more nanowires are being measured at the same time, not only one) and the template adds mechanical stability to the system. There are different techniques to measure the nanowires embedded inside the templates (Rojo et al., 2013; Abad et al., 2017). For example, to measure the electrical conductivity one can use an AFM with a conductive tip (Muñoz Rojo et al., 2016). To measure the Seebeck coefficient, a development that uses two blocks of Cu has been used in several works, as it can be seen in **Figure 6**. For thermal conductivity, the most commonly used techniques are laser flash, 3*w*-scanning thermal microscopy (Muñoz Rojo et al., 2013), and Photoacoustic method (Muñoz Rojo et al., 2017). In **Figure 6A**, a diagram of the thermoelectric properties of nanowires embedded inside the templates is shown, with two examples of actual measurements (AFM conductive tip and two copper blocks).

Historically, the first measurements of this kind appeared in 2004, when Chen's group (Borca-Tasciuc et al., 2004) reported the thermal diffusivity (6.9·10^{-7} m^2/s at 300K) of bismuth telluride nanowires embedded into an AAO template grown by Stacy's group. Later, in 2008, Nielsch's group (Jongmin et al., 2008) published the electrical resistance (10^{-5} Ω·m) and Seebeck coefficient (−30 μV/K) of bismuth telluride nanowires grown via pulsed-potential deposition, being these nanowires highly preferred oriented along [110] direction with 40 nm in diameter. One year later, the electrical resistivity (30 and 0.4 mΩ·m) and Seebeck coefficient (−318.7 and 117 μV/K) for n and p-type non-stoichiometric bismuth telluride nanowires ($Bi_{3.5}Te_{1.5}$ and $Bi_{2.65}Te_{1.85}$), were presented by Mannam et al. (Mannam et al., 2009).

In 2009, the thermal conductivity of stoichiometric Bi_2Te_3 nanowires embedded in 200 nm AAO templates was published by Xu's group (Biswas et al., 2009). To perform the measurements, the AAO membrane (κ = 1.31 W/m·K) was replaced by an epoxy (SU-8) with lower thermal conductivity (0.2 W/m·K). The thermal conductivity of the nanowires measured was 1.44 W/m·K. It is worth noting that this value is smaller than the value found for single crystal bulk stoichiometric bismuth telluride (2.2 W/m·K) when the crystal structure was oriented perpendicular to the *c-axis* (Jacquot et al., 2010).

In 2010, Nielsch's group (Lee et al., 2010b) reported the electrical conductivity and Seebeck coefficient of stoichiometric Bi_2Te_3 nanowires inside AAO templates grown by pulsed-potential deposition. The nanowires were oriented preferentially along [110] direction with 50 nm in diameter. The electrical conductivity was measured using a conductive AFM tip and Seebeck coefficient was obtained placing the sample in an experimental system that consist of two Cu blocks (shown in **Figure 6C**). The electrical conductivity and Seebeck coefficient were found to be 5.3–16.9·10^4 $\Omega^{-1}\cdot m^{-1}$ and 46.6–55 μV/K, respectively, for polycrystalline Bi_2Te_3 nanowires oriented preferentially along [110] direction (Lee et al., 2010b). The Seebeck coefficient measured by Harutyunyan's group (Chen et al., 2010) using the same method in Te-rich bismuth telluride nanowires with 120 nm in diameter grown by constant potential was −70 μV/K. The thermal conductivity for these nanowires

TABLE 2 | Thermoelectric measurements of individual $Bi_{1-x}Te_x$ nanowires found in the literature.

Composition and orientation	Nanowire diameter (nm)	Template	σ (S/cm)	S (μV/K)	PF ($\mu W/K^2 \cdot m$)	k (W/m·K)	References
NON-STOICHIOMETRIC NANOWIRES							
Bi-rich Bi_7Te_5-Bi_4Te_5	10–40	AAO	–	2–79	–	2.4–0.1#	Ryan et al., 2017
$Bi_{2.7}Te_{2.3}$ [110]*	40–120	AAO	$0.8{\cdot}10^3$–$2{\cdot}10^3$	−10– (−35)	8–2.5 10^2	0.8–1.6	Zhou et al., 2005
Bi-rich and Te-rich $Bi_{3.5}Te_{1.5}$-$Bi_{2.65}Te_{1.85}$	∼20	AAO	0.33–25+	−318.7–117	3.4–3.4 10^1	–	Mannam et al., 2009
Bi_2Te_3 $Bi_{2.15}Te_{2.85}$ $Bi_{3.7}Te^*_{1.3}$ Polycrystalline	∼55	AAO	$5{\cdot}10^2$–$2.2{\cdot}10^3$	−45– (−65)	$1.0{\cdot}10^2$–$9.3{\cdot}10^2$	1.4–2.8	Mavrokefalos et al., 2009
Bi-rich $Bi_{2.1}Te_{2.9}$ Te-rich $Bi_{1.95}Te_{3.05}$ [015]	162	PC	$0.1{\cdot}10^2$–$4{\cdot}10^2$	−10–(−80)	$1.96{\cdot}10^2$	–	Chang et al., 2015
Bi_2Te_3 Polycrystalline*	228–391	AAO	–	−50 (391 nm)	–	2.2–0.13	Deyu et al., 2002
Te-rich Bi_2Te_3 Polycrystalline	60–70	AAO	$9.5{\cdot}10^1$	–	–	–	Li W.-J et al., 2011
NEAR TO STOICHIOMETRIC NANOWIRES							
$Bi_{1.9}Te_{3.1}$ Preferential [110]	120	AAO	$8.3{\cdot}10^2$–$2.3{\cdot}10^3$	–	–	–	Chen et al., 2010
$Bi_{1.9}Te_{3.1}$ Preferential [110]	120	AAO	–	−70	–	0.75+	Chen et al., 2010
$Bi_{1.95}Te_{3.05}$[110]	177–270	AAO	$2.3{\cdot}10^3$–$1.3{\cdot}10^3$	−45– (−41)	$4.7{\cdot}10^2$–$2.2{\cdot}10^2$	2–0.9	Kojda et al., 2014
STOICHIOMETRIC NANOWIRES							
Bi_2Te_3 [110]	25–300	AAO	–	–	–	0.52–1.78#	Muñoz Rojo et al., 2017
Bi_2Te_3 [110] preferential orientation	40	AAO	10^3+,?	−30	$9{\cdot}10^2$		Jongmin et al., 2008
Bi_2Te_3[110]	45–250	AAO	$2.9{\cdot}10^2$ – -10^2	–	–	–	Muñoz Rojo et al., 2016
Bi_2Te_3[110] Twins and without twins	60–70	AAO	$2.3{\cdot}10^3$	∼ −57– ∼(−70)	$5{\cdot}10^2$–$7.5{\cdot}10^2$	1.9–2.3	Shin et al., 2014
Bi_2Te_3 [110]	200	SU-8	–	–	–	1.44+	Biswas et al., 2009
Bi_2Te_3 [110]	200–400	AAO	–	–	–	1.37#	Muñoz Rojo et al., 2013
Bi_2Te_3	50	AAO	$16.9{\cdot}10^2$ +	−55	$4.7{\cdot}10^2$	–	Lee et al., 2010b
Bi_2Te_3[110] and [205]	20–120	PC	$5{\cdot}10^3$–$4.2{\cdot}10^2$	–	–	–	Krieg et al., 2018

In white are the measurements performed in single nanowires using microchips. In light green are the measurements performed in the nanowires embedded in a template. "" Stands for manuscripts were several NWs compositions were measured in microchips. "+" Stands for direct measurements within templates, "#" corresponds to calculated values using the effective medium theory, The symbol "?" corresponds to values that the authors are not sure about.*

was 0.75 W/m·K, being this parameter measured using a laser flash system.

In 2013, Martin-Gonzalez's group (Muñoz Rojo et al., 2013) reported the thermal conductivity, measured by 3*w*-scanning thermal microscopy, for Bi_2Te_3 nanowires preferentially oriented [110] and with 200–400 nm in diameter grown at a constant potential, obtaining a value of 1.37 W/m·K.

In 2017, the conductivity ratio of electrical-to-thermal and the Seebeck coefficient were measured using a modified Harman technique (Ryan et al., 2017) in Bi-rich bismuth telluride nanowires. A decrease in the electrical-thermal conductivity ratio by the Lorenz number, L_oT at 400 K, (0.24–0.08) was measured as nanowire diameter increased (10–40 nm) and the Seebeck coefficient was found to be two orders of magnitude lower than that found in the literature (Jongmin et al., 2008; Mannam et al., 2009) and it did not correlate with the diameter. This variation in the results can be due to the difficulty of using Harman methods to measure nanowires. For example, a theoretical study using COMSOL simulations for thermoelectric measurements employing Harman technique in films and nanowires, concluded that there is a strong dependence of f_{HF} on nanowire diameter, resulting in very high frequencies needed for the measurments ($f_{HF} > 106$ Hz for diameters below 250 nm). Therefore, this method cannot be applied for nanowires with diameter below 25 nm (Munoz Rojo et al., 2015).

In the same year, Martin-Gonzalez's group (Muñoz Rojo et al., 2017) reported a decrease of 70% in the thermal conductivity (from 1.78 to 0.52 W/m·K) when the nanowire diameter decreases (300 to 25 nm) using the photoacoustic and the SThM methods (Rojo et al., 2013; Wilson et al., 2015; Abad et al., 2017), and it was validated by theoretical calculations using the Kinetic-Collective model. The reduction in the thermal

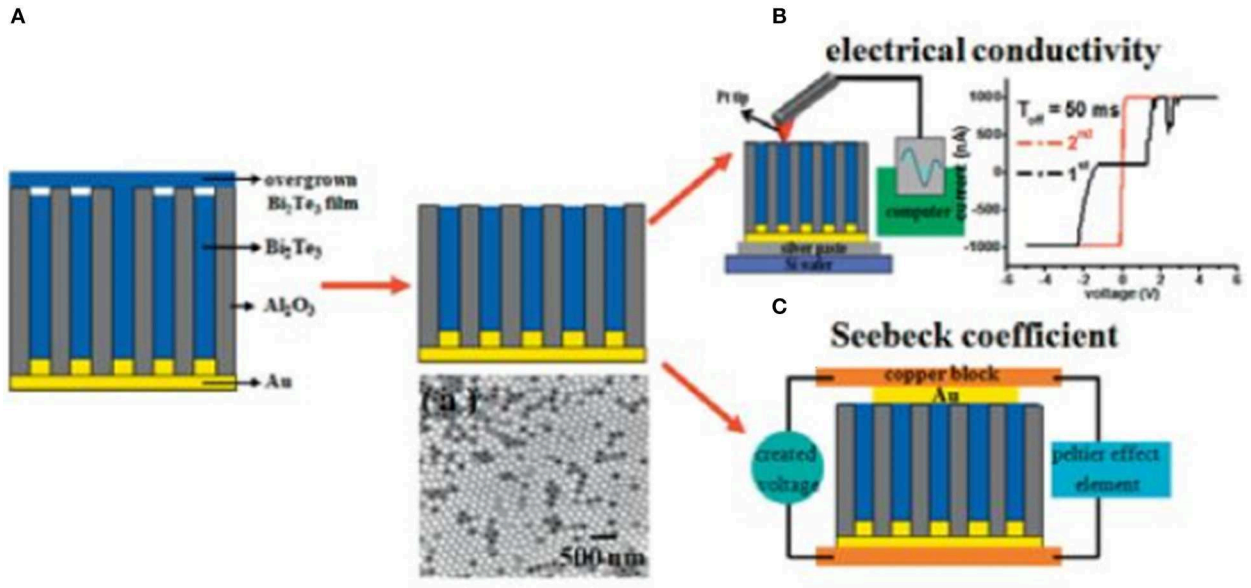

FIGURE 6 | (A) Scheme diagram of the process to prepare the nanowires for thermoelectric measurements. The initial overgrown at the top of the template is polished as shown in this figure. A SEM top view of the nanowires is shown. **(B)** The electrical conductivity setup for individual nanowire and **(C)** Seebeck coefficient of nanowire arrays. Reproduced with permission from Lee et al. (2010b). Copyright 2010 Physica Status Solidi (RRL).

conductivity of the nanowires can be explained in terms of an increment of phonon scattering. The main conclusion of that work is that the smaller the diameter of the nanowires, the larger the modification in the mean free path of the low-frequency phonons. These Bi_2Te_3 nanowires were grown by pulsed electrodeposition and were oriented preferentially along [110] direction. The summary of the thermoelectric measurements of bismuth telluride nanowires embedded into the template is collected in **Table 1** in light green/gray.

Discussion of the Different Results Obtained in Thermoelectric Nanowires

In general, from the results of **Table 2**, it can be concluded that as nanowire diameter decreases, electrical conductivity seems to increase slightly when compared with similar electrodeposited films. This conclusion can be reached when taking into account only the studies performed in stoichiometric Bi_2Te_3 nanowires oriented along [110] direction using PC and AAO templates. Those publications where, either the stoichiometry of the nanowires is not 2:3, or the orientation is not [110] have not been taken into account because the results obtained in such studies are not comparable, given that the different thermoelectric properties also depend on the stoichiometry and on the orientation of the nanowires.

Figure 7 shows the electrical conductivity as a function of nanowire diameter from different publications, where stoichiometric Bi_2Te_3 nanowires oriented along [110] direction have been measured at room temperature. In this graph, only the studies where the authors show in a reliable way that the nanowires are stoichiometric and oriented along [110] direction are collected. In more detail, the electrical conductivity increases

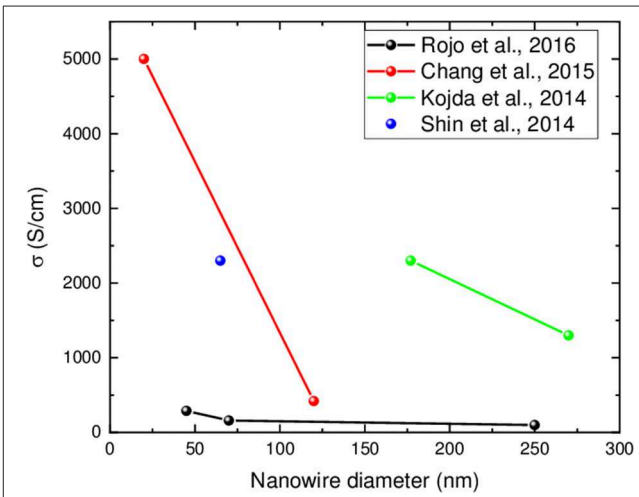

FIGURE 7 | Electrical conductivity as a function of nanowire diameter extracted from different works. They have been measured using different techniques. The values shown are at room temperature. Only data for stoichiometric Bi_2Te_3 nanowires oriented along [110] direction are compiled in this graph.

from $4.2{\cdot}10^2$ to $5{\cdot}10^3$ S/cm for 120 to 20 nm nanowires diameter, respectively (Chang et al., 2015); or from 10^2 to $2.9{\cdot}10^2$ S/cm for 250 to 45 nm nanowires diameter, respectively (Muñoz Rojo et al., 2016); or from $1.3{\cdot}10^3$ to $2.3{\cdot}10^3$ S/cm for 270 to 177 nm nanowires diameter, respectively (Kojda et al., 2014).

One possible explanation for the increase in electrical conductivity upon nanowire diameter reduction can be due to the presence of the surface states since, as it was mentioned

before, bismuth telluride nanowires are topological insulators (Gooth et al., 2015; Muñoz Rojo et al., 2016). Although, these topological states must be further studied by theoretical models to better comprehend the underlying physics, their presence in all the stoichiometric Bi_2Te_3 nanowires will help to understand the increment of the electrical conductivity. Nevertheless, other explications are also plausible.

The variation in the electrical conductivity between the different works shown in **Figure 7** could be also explained taking into account the lack of metrology to calibrate the systems at the nanoscale. Another possible reason, when using microchips to measure single nanowires, can be the presence of an oxide shell in the outer part of the nanowires that is formed upon dissolving the template and by air exposure. In these measurements, another source of error can be the different type of electrical and thermal contacts used in the different studies. There is a wide variety of ways to contact the nanowires some examples are using Pt-carbon, 10 nm (Kojda et al., 2014) Ni/100 nm Al (Shin et al., 2014), 5 nm Cr/250 nm Au (Chang et al., 2015), or Au/tungsten (Muñoz Rojo et al., 2016). This contact resistance has a strong influence on the final values. Other possible reason can be the different sources of the reagents used to grow the nanowires. For example, the tellurium sources have been shown to have an important effect on the electrical conductivity in stoichiometric Bi_2Te_3 films (Manzano et al., 2018), since different companies have different impurities which can dope the semiconductor. The different tellurium sources used have been Te 99.999% from Fluka (Kojda et al., 2014), TeO_2 (the purity was not specified) from Across organic (Shin et al., 2014), Te 99.7% from Prolabo (Chang et al., 2015) and Te 99.99% from Sigma Aldrich (Muñoz Rojo et al., 2016). All of these sources have different types of impurities that affect the final conductivity of the semiconductor, no matter the purity of the precursors (Manzano et al., 2018).

With respect to the Seebeck coefficient (see **Table 2**), maintaining the focus on stoichiometric Bi_2Te_3 nanowires with the appropriate orientation, there is not a clear correlation between the diameter and the Seebeck coefficient in the literature so far. The accurate measurements of the thermal gradient applied to the nanowires (which is not an easy task) and the recorded electrical voltage can be greatly affected by the way of measuring and usually the error is not reported. Then, in a very general way, it is found that the Seebeck coefficient in bismuth telluride nanowires is of the same order of magnitude in all the cases. For instance, in the largest diameters, 177 nm and 270 nm, a Seebeck coefficient of −45 and −41 μV/K was measured, respectively (Kojda et al., 2014). For smaller diameter nanowires of 50 nm, the Seebeck coefficient was measured, −55 μV/K (Lee et al., 2010b). By comparing those measurements one can think that there is a slight increase in the Seebeck upon size reduction. But the only measurement found of the Seebeck coefficient for nanowires of 40 nm in diameter (the smallest mentioned in the literature for Seebeck coefficient measurements) was found to be −30 μV/K (Jongmin et al., 2008), which is also in the same order of magnitude as the previous ones. Moreover, a value of −70 μV/K, for nanowires of 60–70 nm in diameter was measured, which is slightly higher than the previous values reported for nanowires. In another work, a reduction in the Seebeck coefficient (from −70 to −57 μV/K) was observed when the number of twins in the structure was increased (Shin et al., 2014). The use of different sources of the reagents that can dope the semiconductor, as demonstrated for bismuth telluride films (Manzano et al., 2018) affects the doping level and, thus, the Seebeck coefficient. This type of discrepancy in the Seebeck coefficient is also found in literature for electrodeposited Bi_2Te_3 films oriented along [110] direction, as it can be seen for example in the Seebeck coefficient measured for equivalent electrodeposited films, where the authors found a value of −40 μV/K in one case (Fleurial et al., 1999) and −70 μV/K in another work (Li et al., 2008). In any case, one should not forget the lack of metrology at the nanoscale, as another source of discrepancy between different works, as already mentioned before. Then, it can be concluded that the Seebeck coefficient values observed are within the same order of magnitude and no clear trend with the nanowire diameter has been found. Actually, taking into account the theory that predicted an increase of the Seebeck coefficient upon decreasing the dimensionality of the thermoelectric materials, it would be necessary to reach smaller diameters to see the effect of nanostructuration in the case of Bi_2Te_3. For the future, it will be interesting to have a work in which different diameters with stoichiometric nanowires are fabricated using the same reactants and measured in the same kind of system in other to draw experimental conclusions about the Seebeck coefficient trend.

Finally, when the thermal conductivity is analyzed taking only into account stoichiometric Bi_2Te_3 highly oriented nanowires along [110] direction, a reduction in this magnitude is found when the diameter of the nanowire is decreased. For instance, it has been observed a reduction in thermal conductivity of nanowires when their diameter gets smaller, from 1.6 to 0.8 W/m·K for 120 to 40 nm nanowires diameter, respectively. Most probably, this is due to phonon scattering at the surface of the nanowire, given that the smaller the diameter, the higher the surface to volume ratio (Zhou et al., 2005). Moreover, when the crystallite size decreases in stoichiometric Bi_2Te_3 nanowires oriented along [110], the thermal conductivity is reduced from 2.3 to 1.9 W/m·K (Shin et al., 2014). More recently, Martin-Gonzalez's group reported that the thermal conductivity decreased from 1.78 to 0.52 W/m·K for 300 to 25 nm nanowires diameter, respectively (Muñoz Rojo et al., 2017). In that particular work, the Kinetic-Collective model was used to understand such reduction. The main conclusion of this study is that, upon nanowire diameter reduction, the alteration of the mean free path of the low-frequency acoustic phonons is higher. When comparing this model with actual measurements, the agreement was quite remarkable, and thus the reduction in the thermal conductivity of the nanowires can be explained in terms of an increment of phonon scattering in the framework of the Kinetic-Collective model. Finally, **Figure 8** shows the thermal conductivity as a function of nanowire diameter for stoichiometric Bi_2Te_3 nanowires oriented along [110] direction measured in different works.

Other studies with non-stoichiometric nanowires may lead to different conclusions with respect to the thermal conductivity, if not read with enough detail. For instance, Hill's group

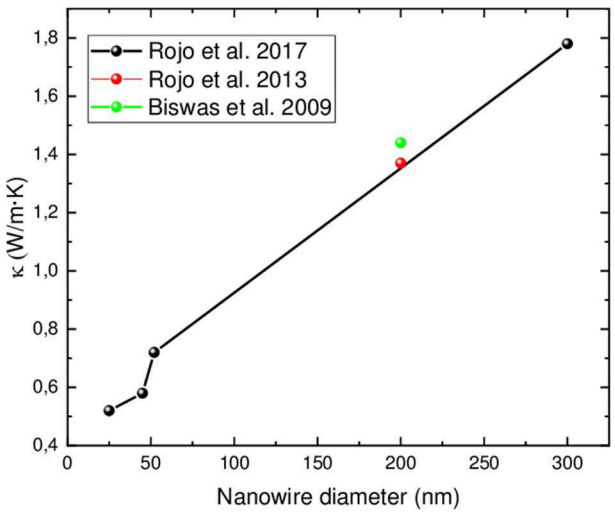

FIGURE 8 | Thermal conductivity as a function of nanowire diameter. Only data for stoichiometric Bi_2Te_3 nanowires oriented along [110] direction are compiled in this graph.

observed the opposite tendency, with an increase in the thermal conductivity from 0.1 to 2.4 W/m·K for 40 to 10 nm nanowires diameter, respectively (Ryan et al., 2017). As it is explained in this manuscript, this variation is not due to the size reduction, but to the different stoichiometry of the nanowires (from $Bi_{11}Te_3$ to Bi_4Te_5), and thus this is not comparable with any other study mentioned above.

In summary, by comparing the different works where stoichiometric nanowires oriented in the same direction [110] have been measured, it can be concluded that the electrical conductivity seems to increase as the nanowire diameter decreases. The Seebeck coefficient does not seem to change much when the nanowire diameter decreases, at least with the results reported in the literature and taking into account that the smallest diameter that has been measured so far has been 40 nm. In consequence, it can be concluded that the power factor should increase as the nanowire diameter decreases, at least in the range measured. Finally, it has been confirmed that the thermal conductivity decreases as the nanowire diameter decreases, as it should be expected from the increase in the phonon scattering. Therefore, in a whole, it could be concluded that there is an increase in the figure of merit upon the reduction on the nanowire's diameter.

Ternary Compounds

Bi_2Te_3 can behave as an *n-type* or *p-type* semiconductor depending on its stoichiometry, being a *p-type* semiconductor (positive Seebeck coefficient) for bismuth-rich compositions and an *n-type* semiconductor (negative Seebeck coefficient) for tellurium-rich stoichiometries. Furthermore, it is well known that Bi_2Te_3 can turn its *n-type* or *p-type* semiconductor response if it is doped with Se and Sb, respectively. The thermoelectric properties are highly improved in these cases. The optimal composition for (Bi-Te-Se) is close to $Bi_2Te_{2.5}Se_{0.5}$. The ternary compounds of bismuth antimony telluride (Bi-Sb-Te) exhibit a high positive Seebeck coefficient and low thermal conductivity, especially for the compositions close to $Bi_{0.5}Sb_{1.5}Te_{3.0}$.

Electrodeposition of Se-Doped Bi-Te Nanowires

In 2003, Stacy's group (Martín-González et al., 2003b) published the first study referent to the electrodeposition of bismuth telluride selenide nanowires. These nanowires were grown at constant potential using AAO templates with two different pore diameters, 50 nm and in commercial Whatman templates (around 200 nm). The composition of the wires was $Bi_{2.1}Te_{2.4}Se_{0.5}$ with a filling ratio of 75% and they were polycrystalline. In that work, the overall electrochemical reaction was described.

The next study in this material appeared in 2009 by Sima's group (Sima et al., 2009) reporting $Bi_2Te_{2.7}Se_{0.3}$ nanowires obtained at a constant potential in a commercial Whatman template. In 2010, nanowires with a composition of $Bi_2Te_{2.7}Se_{0.3}$ were obtained inside commercial AAO templates (Whatman) and ulterior thermal annealing in Ar atmosphere at 300°C was tested (Li et al., 2010). In 2011, Bi_2Te_2Se/Te multilayer nanowires arrays were published. In this case, 60–85 nm diameter and 20 μm length nanowires were obtained by pulsing between BiTeSe and Te reduction potentials (Li X. L et al., 2011). TEM and EDS were performed in the multilayer nanowires in order to confirm both compounds, Bi_2Te_2Se and Te.

One year later, $Bi_2(Te_{0.95}Se_{0.05})_3$ nanowires on 100 nm W/20 nm Ti/Si substrate using AAO templates with 75 nm diameter were electrodeposited (Limmer et al., 2012). **Figure 9** shows a temporal line of the most relevant achievements of bismuth telluride selenide nanowires grown since 2003.

In 2013, Nielsch's group (Bäßler et al., 2013) reported pulsed electrodeposition and thermal annealing in Te atmosphere in thermoelectric nanowires of single bismuth telluride selenide nanowires. The pulsed deposition was performed between two potentials using similar pulses than in a previous work for bismuth telluride nanowires (Jongmin et al., 2008). The composition and diameter of the nanowires were $Bi_{1.9}Te_{2.75}Se_{0.35}$ and 200 nm, respectively. As selenium concentration increases, the power factor increases. The Seebeck coefficient and power factor for as prepared nanowires were found to be −115 μV/K (n-type semiconductor) and 2,660 $\mu W/K^2 \cdot m$, respectively. After annealing in Te atmosphere, the Seebeck coefficient and power factor were found to be −115 μV/K and 2,820 $\mu W/K^2 \cdot m$, respectively, for the composition aforementioned. After thermal annealing, the Seebeck coefficient does not change, while the power increases due to the increase of electrical conductivity. In 2015, Bourgault's group published a study about the electrodeposition of polycrystalline $Bi_2Te_{2.7}Se_{0.3}$ nanowires with 60 nm in diameter (Khedim et al., 2015). In this work, a strong dependence on chemical composition and morphology with the reduction potential was observed. The Seebeck coefficient measured was −75 μV/K.

In 2017, Nielsch's group (Kumar et al., 2017) reported a study of Bi (Te, Se)$_3$ nanowires (ranging from 70 to 325 nm) using

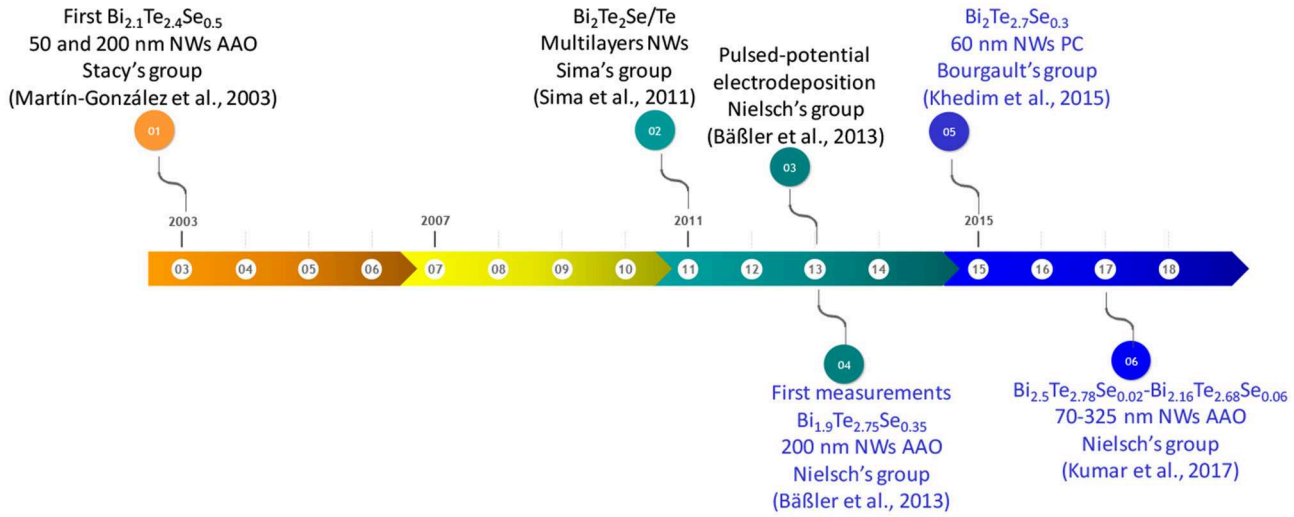

FIGURE 9 | The temporal line of the most relevant achievements of bismuth telluride selenide nanowires grown since 2003. In blue are shown the studies where thermoelectric measurements were performed.

similar pulsed conditions as previously (Bäßler et al., 2013). The electrical conductivity is higher for 70 nm than for 325 nm, the smallest Seebeck coefficient was observed for 85-100 nm and the maximum power factor was obtained for 70 nm nanowires. The thermoelectric measurements were performed in a single nanowire. The thermoelectric measurements of Se-doped BiTe nanowires from the literature are collected in **Table 3**.

From the thermoelectric properties of bismuth telluride selenide nanowires (see **Table 2**), the conclusion that can be extracted is that as nanowire diameter decreases, electrical conductivity slightly increases, similarly as in the case of Bi_2Te_3 nanowires (Kumar et al., 2017). No thermal conductivity measurement of these nanowires could be found in literature, so far.

Electrodeposition Sb-Doped Bi-Te Nanowires

A historical review on the most relevant results obtained in bismuth antimony telluride nanowires is summarized in the temporal line shown in **Figure 11**. The temporal line starts in 2003 when Stacy's group (Martín-González et al., 2003a) published for the first time the electrodeposition of polycrystalline $Bi_{0.5}Sb_{1.5}Te_3$ nanowires inside 40 and 200 nm pore diameter AAO templates at a constant potential, describing the general electrochemical reaction. After thermal annealing, the nanowires were textured along [110] direction. Two years later, in 2005, Myung's group (Lim et al., 2005) reported the growth at a constant current density of n-type (Bi_2Te_3) and p-type (BiSbTe) nanowires in the same template (43 nm in diameter) in order to develop a thermoelectric device. The composition and crystallographic orientation of the nanowires were not mentioned in the manuscript. **Figure 10** shows the thermoelectric nanowire-based fabrication process. **Figures 10A–D**, show alumina templates, b) Bi_2Te_3 nanowires electrochemically deposited, c) Sb-doped BiTe nanowires electrodeposited and d) Finished thermoelectric device.

In 2007, the same group (Feng et al., 2007) published the electron transport properties of $(Bi_{1-x}Sb_x)_2Te_3$ nanowires using polycarbonate membranes of 30–60 nm in pore diameter. When the nanowires were Bi-rich they were preferentially oriented along [110] direction, while in the Sb-rich nanowires the orientation observed was [015]. In 2009, White's group (Li et al., 2009) reported the growth of $Bi_{0.5}Sb_{1.5}Te_3$ nanowires oriented along [110] direction growth at a constant voltage in 80 nm pore diameter PC membranes.

In 2010, Nielsch's group reported the electrodeposition of BiSbTe nanowires of 50 nm in diameter with different compositions (the crystallographic orientation of the nanowires was not mentioned in the manuscript) inside AAO templates, using a non-aqueous solution of ethylene glycol. In 2011, Sima's group (Sima et al., 2011) described $(Bi,Sb)_2Te_3$ nanotubes grown at current pulse plating inside PC membranes performing electrochemical impedance spectroscopy. Two years later, in 2013, Nielsch's group (Bäßler et al., 2013) reported pulsed electrodeposition to fabricate thermoelectric nanowires of $Bi_{0.75}Sb_{1.45}Te_{2.8}$ with 30 nm diameter. The Seebeck coefficient and power factor were found to be 156 μV/K (p-type semiconductor), the highest reported value for these nanowires to date, and 1750 $\mu W/K^2 \cdot m$, respectively. In 2014, Li's group (Li et al., 2014) reported the reduction of thermal conductivity as diameter decreases of $Bi_{0.5}Sb_{1.5}Te_3$ nanowires oriented along [110] direction. The thermal conductivity (0.7-0.89 W/m·K) was measured in a single wire using the 3ω method; these values were lower than that of the bulk material (1.4 W/m·K). The same year, Yen's group (Kuo et al., 2014) reported a work based on pulsed electrodeposition of $Bi_{0.2}Sb_{1.6}Te_{3.2}$ grown inside AAO templates. Different ratios between t_{on} and t_{off} were studied, as well as different diameters and length.

TABLE 3 | Thermoelectric measurements of Se-doped BiTe nanowires found in the literature.

Composition and orientation	Nanowire diameter (nm)	Templates	σ (S/cm)	S (μV/K)	PF (μW/K^2 · m)	References
$Bi_2Te_{2.7}Se_{0.3}$ [1 0 10] and [110]	60	AAO	–	−75	–	Khedim et al., 2015
Bi-rich $Bi_{2.5}Te_{2.78}Se_{0.02}$-$Bi_{2.16}Te_{2.68}Se_{0.06}$ Preferential [110]	70–325	AAO	$2.7{\cdot}10^3$–$1.9{\cdot}10^3$	−60 – (−60)	$1{\cdot}10^3$–$0.7{\cdot}10^3$	Kumar et al., 2017
TeSe-rich $Bi_{1.9}Te_{2.75}Se_{0.35}$ Orientation is not mentioned	200	AAO	$2.2{\cdot}10^3 \pm 0.4{\cdot}10^3$	−115 ± 2	$2.8{\cdot}10^3$	Bäßler et al., 2013

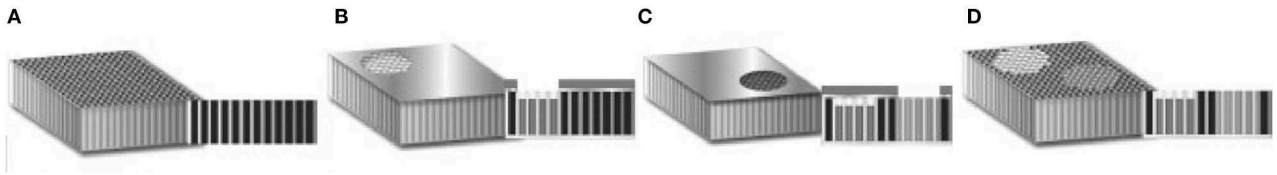

FIGURE 10 | (A) alumina templates, **(B)** Bi_2Te_3 nanowires electrochemically deposited, **(C)** BiSbTe nanowires electrodeposited and **(D)** Finished thermoelectric device. Reproduced with permission from Lim et al. (2005). Copyright 2005 Advanced Materials.

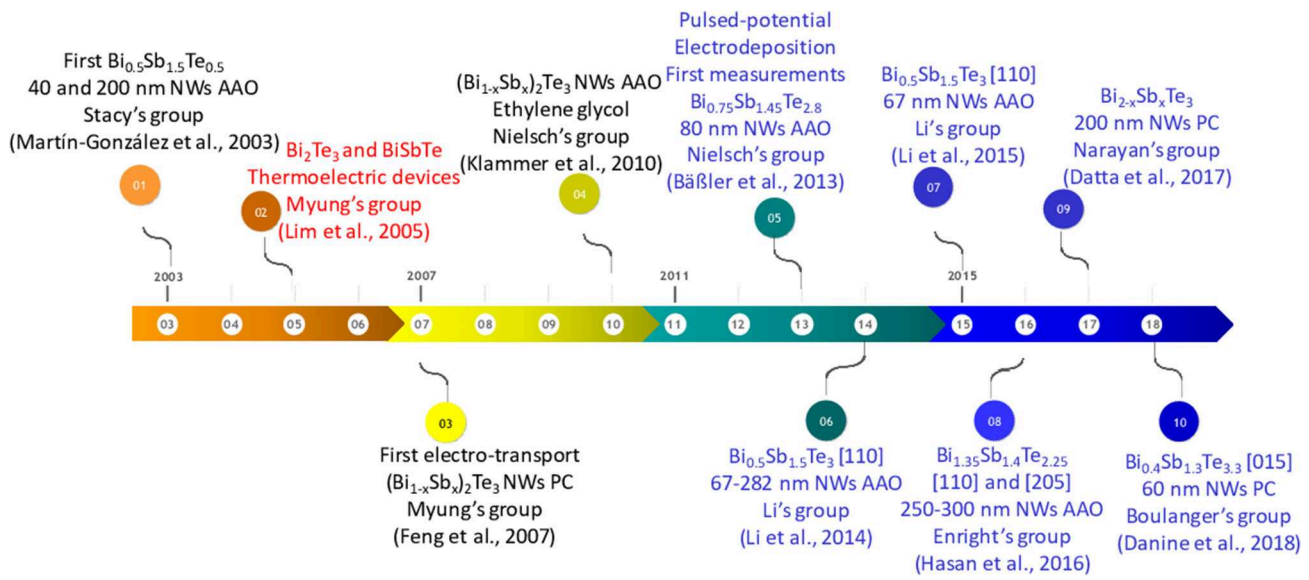

FIGURE 11 | The temporal line of the most important achievements of bismuth antimony telluride nanowires. In blue the studies where thermoelectric measurements were performed is shown. In red is shown the first thermoelectric device based on nanowires.

Choa's group (Ng et al., 2014) published a study based on electrodeposition of polycrystalline $Bi_xSb_yTe_3$ nanowires obtained with different compositions changing the reduction potential. In 2015, Li's group (Li et al., 2015) reported an improvement of Seebeck coefficient (150 μV/K), reaching similar values than the best previously reported, and electrical conductivity (480 S/cm) when $Bi_{0.5}Sb_{1.5}Te_3$ nanowires with 67 nm in diameter and oriented along [110] direction were grown via pulsed electrodeposition. Moreover, the thermal conductivity was found to be 0.2–0.3 W/m·K, lower than the only other work that had measured it for similar nanowire diameters. The Seebeck coefficient was measured in the nanowires embedded inside the AAO, the electrical conductivity using a four-probe system and the thermal conductivity by the 3ω method.

In 2016, Enright's group (Hasan et al., 2016) published the enhancement of the electrical conductivity (2.5 times higher than bismuth telluride) of $Bi_{1.35}Sb_{1.4}Te_{2.25}$ nanowires grown via

pulsed electrodeposition. The nanowires were highly textured along [110] and [205] directions using AAO templates with 250–300 nm pore diameter. In 2017, Narayan's group (Datta et al., 2017) reported a very low Seebeck coefficient (6.5 μV/K) of polycrystalline $Bi_{2-x}Sb_xTe_3$ nanowires grown at constant potential in polycarbonate membranes of 200 nm. In 2018, Boulanger's group (Danine et al., 2018) published 60 nm diameter $Bi_{0.4}Sb_{1.3}Te_{3.3}$ nanowires grown at constant potential inside polycarbonate membranes oriented along [015] direction. In those nanowires, which presented 60° twins, electrical resistivity, and Seebeck coefficient were measured with values of 128 μΩ·m and 138 μV/K, respectively. The thermoelectric measurements found in the literature of BiSbTe nanowires are collected in **Table 4**.

From the thermoelectric properties of bismuth antimony telluride nanowires (see **Table 3**), the conclusions that can be extracted are that the Seebeck coefficient does not change much with nanowire diameter. The thermal conductivity slightly decreased from 0.84 to 0.7 W/m·K for 282 to 67 nm nanowires diameter, respectively (Li et al., 2014). These measurements were performed in $Bi_{0.5}Sb_{1.5}Te_3$ nanowires oriented along [110] direction using AAO templates for the electrodeposition.

Other V-VI Thermoelectrics

Another V-VI compound studied is Sb_2Te_3. This material also presents anisotropic behavior in its properties. The figure of merit of bulk antimony telluride single-crystalline in the direction parallel to the *c-axis* of the structure was determined by Antonova et al. (Antonova and Looman, 2005) and it was found to be $zT_{//c} = 0.48$, with Seebeck coefficient, electrical conductivity, and thermal conductivity values of 92 μV/K, 0.31 $(\mu\Omega\cdot m)^{-1}$, and 1.63 W/m·K, respectively (Antonova and Looman, 2005). Contrariwise, when the crystal structure was oriented perpendicular to the *c-axis,* the values of the Seebeck coefficient, electrical conductivity, and thermal conductivity were 63 μV/K, 0.82 $(\mu\Omega\cdot m)^{-1}$, and 7.47 W/m·K, respectively, corresponding to a much lower figure of merit of $zT_{\perp c} = 0.13$ (Antonova and Looman, 2005).

The first report on electrodeposition of Sb_2Te_3 nanowires can be found in 2008 by Oh's group (Kim et al., 2008). They reported the electrodeposition of polycrystalline Sb_2Te_3 nanowires inside commercial AAO template (200 nm pore diameter) using different constant current densities. One year after, the same group published a second paper with similar nanowires, where the power output was measured with a value of $4.8\cdot10^{-10}$ W (Kim et al., 2009). In 2009, Sb_xTe_y nanowires with different composition were electrodeposited at constant potential using 200 nm pore diameter AAO templates (commercially available Whatmann filters). As reduction potential increases, Te content increases; the length of the wires was ∼5–10 μm (Park et al., 2009). **Figure 12** shows a temporal line of the most relevant achievements of antimony telluride nanowires.

In 2010, Nielsch's group (Klammer et al., 2010) reported the electrodeposition of antimony telluride nanowires grown in an organic solvent (ethylene glycol) using constant current density and 50 nm pore diameter alumina. The Seebeck coefficient was found to be 21 μV/K. In 2011, Devireddy's group (Pinisetty et al., 2011) published the electrodeposition of nanowires and nanotubes grown inside polycarbonate membranes. Nanowires with 400 nm in diameter and nanotubes with 100 nm in diameter were obtained using different current densities, 10 and 5.5 mA/cm^2, respectively. The Seebeck coefficient was found to be 359 and 332 μV/K for nanowires and nanotubes, respectively. These values were measured using Harman's technique in nanowires embedded in the membrane. The last study of antimony telluride nanowires grown by electrodeposition can be found in 2015 by Myung's group. In this work, the electrodeposition of amorphous Te-rich antimony telluride ($Sb_{1.6}Te_{3.4}$) nanowires with 250 nm diameter using different reduction potentials was carried out. After thermal annealing at 100–200°C, the nanowires were polycrystalline with an increase in the crystallite size from 23 to 28 nm (Kim et al., 2015). The carrier concentration and Seebeck coefficient were found to be $1.1\cdot10^{-9}$ cm^{-3} and 318 μV/K, respectively. The thermoelectric measurements of SbTe nanowires are collected in **Table 5**.

From the available thermoelectric properties of antimony telluride found in the literature (see **Table 5**), the only conclusion that can be extracted is that the Seebeck coefficient is slightly higher for nanowires than for nanotubes and that an increase in the figure of merit was observed between nanowires (0.09) and nanotubes (0.2) (Pinisetty et al., 2011).

INTERCONNECTED 3D NANOWIRE NETWORK

One of the latest landmarks in the fabrication of Bi_2Te_3 nanowires by electrodeposition is devoted to the fabrication of 3D-interconnected nanowire networks. The first study which reports the electrodeposition of a Bi_2Te_3 3D-interconnected nanowire network was published in 2014 by Martin-Gonzalez's group. In this work, a 3D interconnected network of Bi_2Te_3 nanowires was obtained by pulsed electrodeposition inside 3D AAO templates (Martín et al., 2014). The nanowire diameters are around 52 nm. In 2018, the same group studied the influence of pulsing (between an applied potential during t_{on} and current equal to 0 during t_{off}) in the morphology, crystallographic orientation, and composition of the network electrodeposited at 0°C. The crystallographic orientation was controlled changing the reduction potential, and stoichiometric bismuth telluride 3D-nanowires oriented along [110] direction (Ruiz-Clavijo et al., 2018) were fabricated. In order to obtain both the stoichiometric composition and the [110] crystallographic orientation, pulsed current-voltage electrodeposition was applied between a density current of 0 mA/cm^2 for 0.1 s and difference potential for 1s. **Figure 13** shows cross-sectional SEM images of 3D-Bi_2Te_3 NW embedded into the AAO template (**Figure 13A**) and the free-standing structure, after selectively removing the AAO template (**Figure 13B**). Additionally, the thermal conductivity of stoichiometric bismuth telluride 3D-nanowires oriented along [110] direction and 52 nm in diameter was measured by Martin-Gonzalez's group (Abad et al., 2016b). A value of 0.58 ± 0.22 $W\cdot m^{-1}K^{-1}$ was found, which

TABLE 4 | Thermoelectric measurements of Sb-doped BiTe nanowires found in the literature.

Composition and orientation	Nanowire diameter (nm)	Template	σ (S/cm)	S (μV/K)	PF (μW/K^2 · m)	k (W/m·K)	References
$Bi_{0.4}Sb_{1.3}Te_{3.3}$ [015] and 60° twins	60	PC	$7.5{\cdot}10^1$	138	142.8	–	Danine et al., 2018
$Bi_{0.5}Sb_{1.5}Te_3$ [110]	67	AAO	$4.8{\cdot}10^2$	150	1,080	0.2–0.3	Li et al., 2015
$Bi_{0.75}Sb_{1.45}Te_{2.8}$ It is not mentioned	80	AAO	$(7.2 \pm 6.4){\cdot}10^2$	156 ± 3	$(1.7 \pm 0.07){\cdot}10^3$	–	Bäßler et al., 2013
$Bi_{0.5}Sb_{1.5}Te_3$ [110]	67–282	AAO	–	–	–	0.7-0.84	Li et al., 2014
$Bi_{2-x}Sb_xTe_3$ Polycrystalline	200	PC	–	6.5	–	–	Datta et al., 2017
$Bi_{1.35}Sb_{1.4}Te_{2.25}$ [110] and [205]	250-300	AAO	$2.4{\cdot}10^3$	–	–	–	Hasan et al., 2016

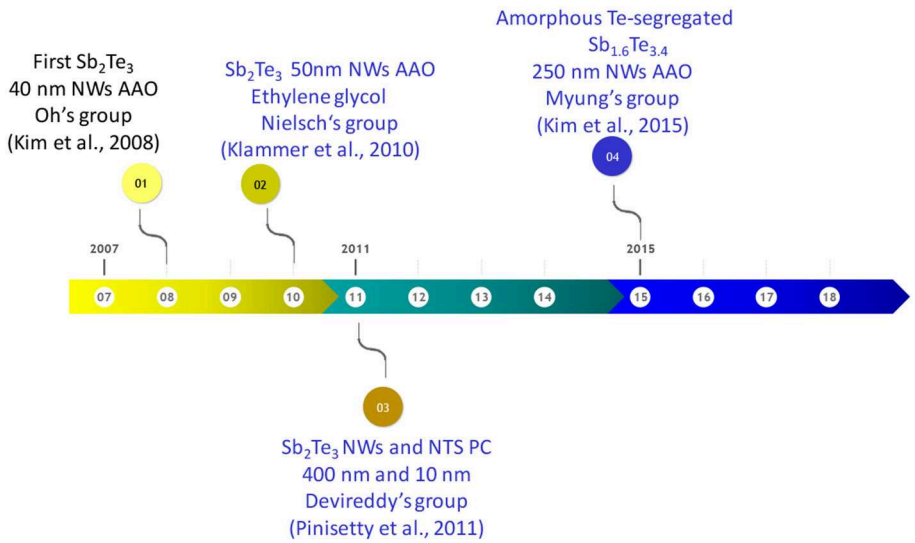

FIGURE 12 | The temporal line of the most relevant achievements of antimony telluride nanowires. In blue are shown the studies where thermoelectric measurements were performed.

shows a reduction in the thermal conductivity value, with respect to 1D nanowires of the same diameter (0.72 ± 0.37 $W{\cdot}m^{-1}K^{-1}$) (Muñoz Rojo et al., 2017). One may think that the reduction in the thermal conductivity between the 3D vs. the 1D could be due to a possible effect of phononic crystal, because of the internal structure of the 3D network. But, before reaching that conclusion, further experiments need to be done.

In 2016, Toimil-Molares's group reported a Sb 3D network inside 3D-PC membranes with 100 nm in diameter and 30 μm in length using pulsed-potential deposition. Although this material is not a V-VI compound, we consider the work of high importance to be mentioned here. These nanowires presented two crystallographic directions, [110] and [104] (Wagner et al., 2016). Furthermore, in this study, thermoelectric measurements using a cross-plane steady-state method was performed in a 3D network with 30 μm in length. The effect of the interconnectivity of the nanowires network is shown. **Figures 13C,D** show SEM images of 3D-Sb NW network free-standing.

The principal differences between both networks are that the vertical spacing of 3D-AAO nanostructures can be controlled very accurately since it is proportional to the time of the pulses applied during their fabrication, so they can be tailored as desired. The wires are perpendicular to the template surface and they have horizontal interconnections at 90 degrees to the vertical channels (see **Figures 13A,B**). These interconnections are perfectly aligned and form a plane of interconnections. This 3D-AAO can also be obtained in non-planar surfaces like in cylinder or wires (Resende et al., 2016). In addition, these 3D-AAO nanostructures could be considered phononic crystals, due to the periodic structures that can be produced inside the membranes. These phononic crystal nanostructures would allow the reduction of the thermal conductivity thanks to a new approach for changing the thermal transport based on the concept of nanophononic metamaterials

TABLE 5 | Thermoelectric measurements of SbTe nanowires found in the literature.

Composition and orientation	Nanowire diameter (nm)	Template	σ (S/cm)	S (μV/K)	PF (μW/K^2 · m)	zT	References
Sb_2Te_3 It is not mentioned	50	AAO	–	21	–	–	Klammer et al., 2010
$Sb_{1.6}Te_{3.4}$ Polycrystalline	250	AAO	–	318	–	–	Kim et al., 2015
Sb_2Te_3 NWs and NTs Polycrystalline	400–100	PC	–	359-332	–	0.09–0.2	Pinisetty et al., 2011

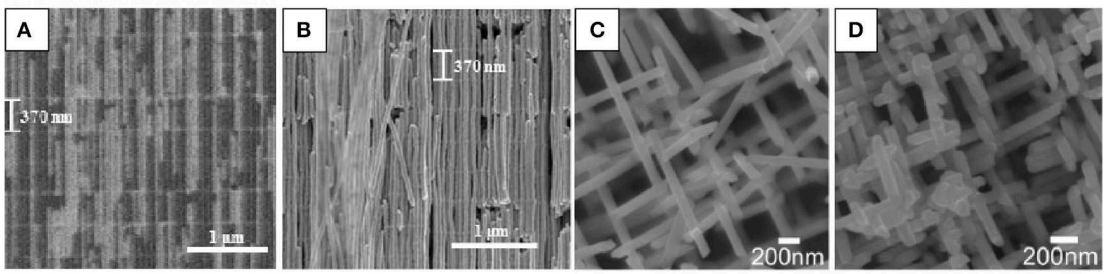

FIGURE 13 | (A) Cross-sectional SEM micrograph images of 3D-Bi_2Te_3 NW with backscattered electrons; **(B)** SEM micrograph of free-standing 3D Bi_2Te_3 nanowire network after AAO template removal. Exhibiting the high degree of interconnectivity and the capacity of being free-standing without the alumina template. Reproduced with permission from Ruiz-Clavijo et al. (2018). Copyright 2018 Nanomaterials. **(C,D)** SEM images of a free-standing 3D network of Sb NWNWs with wire diameters ∼100 nm, exhibiting their well–controlled degrees of interconnectivity. Reproduced with permission from Wagner et al. (2016).

(NPMs) by introducing nanoscale local resonators. In this case, the interconnections distances could be adjusted to enable unique subwavelength properties and killing the propagation of certain phonon wavelengths.

In the case of 3D-PC nanostructures, this spacing cannot be controlled since the ion irradiation is a random process. Only the average density of nanowires, the relative angle with the surface and the pore diameter can be controlled by the influence of the ions during the template fabrication and the etching time during the opening of the pores. In this case, the 3D-PC the nanowires are oriented 45 degrees from the template surface and not complete planes of interconnected nanowires were obtained as can be seen in **Figures 13C,D**.

These 3D-AAO and the 3D-PC membranes open a new avenue to obtain macroscopic hierarchical 3D nanowire networks that will have all the benefits of the nanowires in a macroscopic system that can be handled with tweezers and without any of the drawbacks of having the template in the structure.

CONCLUSIONS

In this review, it has been shown that stoichiometric Bi_2Te_3 nanowires oriented along [110] direction have been grown by electrodeposition with different diameters (25–400 nm) up to date. The smallest nanowire diameter of these nanowires was found to be ∼15 nm. Moreover, all the thermoelectric properties (electrical conductivity, Seebeck coefficient, and thermal conductivity) have been measured for different diameters. The electrical conductivity seems to increase in the different works as nanowire diameter decreases for stoichiometric Bi_2Te_3 nanowires oriented along [110] direction. The change in the Seebeck coefficient can be explained by other factors than by nanowire diameter reductions. And the thermal conductivity decreases as nanowire diameter decreases. Additionally, in the case of Se-doped BiTe, higher electrical conductivity and Seebeck coefficient than Bi_2Te_3 have been reported. And, in the case of Sb-doped BiTe, higher Seebeck coefficient and lower thermal conductivity have been published.

In summary, the most important conclusion is that the nanowires should be grown with small diameter (20–25 nm), given that the electrical conductivity seems to increase for smaller diameters and the thermal conductivity decreases as the diameter decreases. It is worth to note that the different studies found in the literature were done using different tellurium sources and that this can explain the variations on the Seebeck coefficients measured more than the effect on the size reduction.

Regarding the measurements, it is important to highlight that there is a lack of metrology at the nanoscale, even though many different phenomena (electrical contacts, accurate temperature gradient measurement at the nanoscale, stoichiometry of the nanowires, crystalline orientation, tellurium source used, the number of twins, etc.) play an important role in the dispersion of the measurements. Each article uses their own system to measure at the nanoscale and no round-robin experiments between the different setups have been made to date.

Recently, the development of 3D network nanowires has opened a new field to investigate the thermoelectric properties of these nanostructures. These 3D network nanowires are the future to develop more efficient thermoelectric materials.

Nevertheless, different questions are still open in the field. One open question that it is necessary to gain understanding on is the reason why the electric conductivity increases as the diameter decreases, when the theory predicts that this behavior only should be observed in quantum confinement regimes (for nanowire diameters lower than 5–10 nm). Another open question is what will be the value of the Seebeck coefficient for nanowires with a diameter smaller than 40 nm, because in theoretical studies performed to date some phenomena, which will be relevant at such diameters, were not included, such as Dirac superficial phenomenon. Or, the fabrication of a phononic crystal, to cite some.

Therefore, the research in thermoelectric nanowires is nowadays a hot topic in many ways. They provide a more than reasonable way of improving the current performance of thermoelectric materials, but they need a great research effort in three main directions to exploit all their potential: in their fabrication techniques, to go to lower diameters with stoichiometric and properly oriented materials; in the characterization techniques, to asses an accurate way of measuring transport properties in nanostructures and better metrology at the nanoscale; and in the theoretical understanding of the phenomena taking place in these nanostructures.

AUTHOR CONTRIBUTIONS

All authors listed have made a substantial, direct and intellectual contribution to the work, and approved it for publication.

ACKNOWLEDGMENTS

The authors would like to acknowledge partial financial support from MAT2017-86450-c4-3-r and Intramural Infante 201550E072 project. CM acknowledges financial support from Juan de la Cierva Incorporación grants from the Ministerio de Ciencia, Innovación y Universidades.

REFERENCES

Abad, B., Borca-Tasciuc, D. A., and Martin-Gonzalez, M. S. (2017). Non-contact methods for thermal properties measurement. *Renew. Sustain. Energy Rev.* 76, 1348–1370. doi: 10.1016/j.rser.2017.03.027

Abad, B., Maiz, J., and Martin-Gonzalez, M. (2016a). Rules to Determine thermal conductivity and density of Anodic Aluminum Oxide (AAO) Membranes. *J. Phys. Chem. C* 120, 5361–5370. doi: 10.1021/acs.jpcc.6b00643

Abad, B., Maiz, J., Ruiz-Clavijo, A., Caballero-Calero, O., and Martin-Gonzalez, M. (2016b). Tailoring thermal conductivity via three-dimensional porous alumina. *Sci. Rep.* 6:38595. doi: 10.1038/srep38595

Abad, B., Rull-Bravo, M., Hodson, S. L., Xu, X., and Martin-Gonzalez, M. (2015). Thermoelectric properties of electrodeposited tellurium films and the sodium lignosulfonate effect. *Electrochim. Acta* 169, 37–45. doi: 10.1016/j.electacta.2015.04.063

Ali, A., Chen, Y., Vasiraju, V., and Vaddiraju, S. (2017). Nanowire-based thermoelectrics. *Nanotechnology* 28:282001. doi: 10.1088/1361-6528/aa75ae

Antonova, E. E., and Looman, D. C. (2005). "Finite elements for thermoelectric device analysis in ANSYS" in *International Conference on Thermoelectrics, ICT, Proceedings*, 200–203. doi: 10.1109/ICT.2005.1519922

Bäßler, S., Böhnert, T., Gooth, J., Schumacher, C., Pippel, E., and Nielsch, K. (2013). Thermoelectric power factor of ternary single-crystalline Sb 2Te3- and Bi2Te3-based nanowires. *Nanotechnology* 24:495402. doi: 10.1088/0957-4484/24/49/495402

Biswas, K. G., Sands, T. D., Cola, B. A., and Xu, X. (2009). Thermal conductivity of bismuth telluride nanowire array-epoxy composite. *Appl. Phys. Lett.* 94:223116. doi: 10.1063/1.3143221

Borca-Tasciuc, D.-A., Chen, G., Prieto, A., Martín-González, M. S., Stacy, A., Sands, T., et al. (2004). Thermal properties of electrodeposited bismuth telluride nanowires embedded in amorphous alumina. *Appl. Phys. Lett.* 85, 6001–6003. doi: 10.1063/1.1834991

Boulanger, C. (2010). Thermoelectric material electroplating: A historical review. *J. Electr. Mater.* 39, 1818–1827. doi: 10.1007/s11664-010-1079-6

Caballero-Calero, O., Borca-Tasciuc, D. A., Martínez-Moro, R., Gorog, A., Mohner, M., Borca-Tasciuc, T., et al. (2018). Improvement of Seebeck coefficient in as-grown $Bi_2Te_{3-y}Se_y$ electrodeposited films by the addition of additives and bath optimization. *Electrochim. Acta* 269, 490–498. doi: 10.1016/j.electacta.2018.03.025

Caballero-Calero, O., Díaz-Chao, P., Abad, B., Manzano, C. V., Ynsa, M. D., Romero, J. J., et al. (2014). Improvement of Bismuth Telluride electrodeposited films by the addition of Sodium Lignosulfonate. *Electrochim. Acta* 123, 117–126. doi: 10.1016/j.electacta.2013.12.185

Caballero-Calero, O., and Martín-González, M. (2016). Thermoelectric nanowires: a brief prospective. *Scr. Mater.* 111, 54–57. doi: 10.1016/j.scriptamat.2015.04.020

Chang, T., Cho, S., Kim, J., Schoenleber, J., Frantz, C., Stein, N., et al. (2015). Individual thermoelectric properties of electrodeposited bismuth telluride nanowires in polycarbonate membranes. *Electrochim. Acta* 161, 403–407. doi: 10.1016/j.electacta.2015.02.105

Chen, C., He, S., Weng, H., Zhang, W., Zhao, L., Liu, H., et al. (2012). Robustness of topological order and formation of quantum well states in topological insulators exposed to ambient environment. *Proc. Natl. Acad. Sci. U.S.A.* 109, 3694–3698. doi: 10.1073/pnas.1115555109

Chen, C.-L., Chen, Y.-Y., Lin, S.-J., Ho, J. C., Lee, P.-C., Chen, C.-D., et al. (2010). Fabrication and characterization of electrodeposited bismuth telluride films and nanowires. *J. Phys. Chem. C* 114, 3385–3389. doi: 10.1021/jp909926z

Chen, I. J., Burke, A., Svilans, A., Linke, H., and Thelander, C. (2018). Thermoelectric power factor limit of a 1D nanowire. *Phys. Rev. Lett.* 120:177703. doi: 10.1103/PhysRevLett.120.177703

Danine, A., Schoenleber, J., Ghanbaja, J., Montaigne, F., Boulanger, C., and Stein, N. (2018). Microstructure and thermoelectric properties of p-type bismuth antimony telluride nanowires synthetized by template electrodeposition in polycarbonate membranes. *Electrochim. Acta* 279, 258–268. doi: 10.1016/j.electacta.2018.05.071

Datta, A., Sangle, A., Hardingham, N., Cooper, C., Kraan, M., Ritchie, D., et al. (2017). Structure and thermoelectric properties of $Bi_{2-x}Sb_xTe_3$ nanowires grown in flexible nanoporous polycarbonate templates. *Materials* 10:553. doi: 10.3390/ma10050553

Delves, R. T., Bowley, A. E., Hazelden, D. W., and Goldsmid, H. J. (1961). Anisotropy of the Electrical Conductivity in Bismuth Telluride. *Proc. Phys. Soc.* 78:838. doi: 10.1088/0370-1328/78/5/329

Deyu, L., Prieto, A. L., Yiying, W., Martin-Gonzalez, M. S., Stacy, A., Sands, T., et al. (2002). "Measurements of Bi_2Te_3 nanowire thermal conductivity and Seebeck coefficient," in *Proceedings of Twenty-First International Conference on Thermoelectrics,* 333–336. doi: 10.1109/ICT.2002.1190333

Domínguez-Adame, F., Martín-González, M., Sánchez, D., and Cantarero, A. (2019). Nanowires: a route to efficient thermoelectric devices. *Phys. E* 113, 213–225. doi: 10.1016/j.physe.2019.03.021

Dresselhaus, M. S., Chen, G., Tang, M. Y., Yang, R. G., Lee, H., Wang, D. Z., et al. (2007). New directions for low-dimensional thermoelectric materials. *Adv. Mater.* 19, 1043–1053. doi: 10.1002/adma.200600527

Elyaagoubi, M., Najih, Y., Khadiri, M., Mabrouki, M., Oueriagli, A., and Outzourhit, A. (2017). Electrochemically deposited bismuth-telluride

nanowires in nanoporous alumina membranes. *J. Mater. Environ. Sci.* 8, 2070–2075.

Erickson, K. J., Limmer, S. J., Yelton, W. G., Rochford, C., Siegal, M. P., and Medlin, D. L. (2017). Evolution of microstructural disorder in annealed bismuth telluride nanowires. *ECS J. Solid State Sci. Technol.* 6, N3117–N3124. doi: 10.1149/2.0181703jss

Feng, X., Bongyoung, Y., Kyu-Hwan, L., and Nosang, V. M. (2007). Electro-transport studies of electrodeposited $(Bi_{1-x}\ Sb_x)_2Te_3$ nanowires. *Nanotechnology* 18:335203. doi: 10.1088/0957-4484/18/33/335203

Fleurial, J. P., Borshchevsky, A., Ryan, M. A., Phillips, W. M., Snyder, J. G., Caillat, T., et al. (1999). Development of thick-film thermoelectric microcoolers using electrochemical deposition. *Mater. Res. Soc.* 545, 493–500. doi: 10.1557/PROC-545-493

Fleurial, J. P., Gailliard, L., Triboulet, R., Scherrer, H., and Scherrer, S. (1988). Thermal properties of high quality single crystals of bismuth telluride—Part I: experimental characterization. *J. Phys. Chem. Solids* 49, 1237–1247. doi: 10.1016/0022-3697(88)90182-5

Frantz, C., Stein, N., Gravier, L., Granville, S., and Boulanger, C. (2010). Electrodeposition and characterization of bismuth telluride nanowires. *J. Electr. Mater.* 39, 2043–2048. doi: 10.1007/s11664-009-1001-2

Frantz, C., Stein, N., Zhang, Y., Bouzy, E., Picht, O., Toimil-Molares, M. E., et al. (2012). Electrodeposition of bismuth telluride nanowires with controlled composition in polycarbonate membranes. *Electrochim. Acta* 69, 30–37. doi: 10.1016/j.electacta.2012.01.040

Goktas, N. I., Wilson, P., Ghukasyan, A., Wagner, D., Mcnamee, S., and Lapierre, R. R. (2018). Nanowires for energy: a review. *Appl. Phys. Rev.* 5:041305. doi: 10.1063/1.5054842

Goldsmid, H. J. (1961). Recent studies of bismuth telluride and its alloys. *J. Appl. Phys.* 32, 2198–2202. doi: 10.1063/1.1777042

Gooth, J., Gluschke, J. G., Zierold, R., Leijnse, M., Linke, H., and Nielsch, K. (2015). Thermoelectric performance of classical topological insulator nanowires. *Semicond. Sci. Technol.* 30:015015. doi: 10.1088/0268-1242/30/1/015015

Greenaway, D. L., and Harbeke, G. (1965). Band structure of bismuth telluride, bismuth selenide and their respective alloys. *J. Phys. Chem. Solids* 26, 1585–1604. doi: 10.1016/0022-3697(65)90092-2zl

Hasan, M., Gautam, D., and Enright, R. (2016). Electrodeposition of textured $Bi_{27}Sb_{28}Te_{45}$ nanowires with enhanced electrical conductivity. *Mater. Chem. Phys.* 173, 438–445. doi: 10.1016/j.matchemphys.2016.02.035

Hasan, M. Z., and Kane, C. L. (2010). Topological insulators. *Rev. Mod. Phys.* 82, 3045–3067. doi: 10.1103/RevModPhys.82.3045

Jacquot, A., Farag, N., Jaegle, M., Bobeth, M., Schmidt, J., Ebling, D., et al. (2010). Thermoelectric properties as a function of electronic band structure and microstructure of textured materials. *J. Electr. Mater.* 39, 1861–1868. doi: 10.1007/s11664-009-1059-x

Jin, C., Xiang, X., Jia, C., Liu, W., Cai, W., Yao, L., et al. (2004). Electrochemical fabrication of large-area, ordered Bi2Te3 Nanowire Arrays. *J. Phys. Chem. B* 108, 1844–1847. doi: 10.1021/jp036133z

Jongmin, L., Shadyar, F., Jaeyoung, L., Laurent, C., Roland, S., Ulrich, G., et al. (2008). Tuning the crystallinity of thermoelectric Bi_2Te_3 nanowire arrays grown by pulsed electrodeposition. *Nanotechnology* 19:365701. doi: 10.1088/0957-4484/19/36/365701

Jun, S. W., Lee, K. Y., and Oh, T. S. (2006). Effects of hydrogen annealing on the thermoelectric properties of electrodeposited Bi_2Te_3 for nanowire applications. *J. Korean Phys. Soc.* 48, 1708–1712. doi: 10.3938/jkps.50.670

Khedim, M. B., Cagnon, L., Serradeil, V., Fournier, T., and Bourgault, D. (2015). Thermoelectric nanowires based on bismuth telluride. *Mater. Today* 2, 602–609. doi: 10.1016/j.matpr.2015.05.082

Kim, J., Lim, J. H., Bosze, W., and Myung, N. V. (2015). Optimizing thermoelectric property of antimony telluride nanowires by tailoring composition and crystallinity. *Mater. Res. Express* 2:085006. doi: 10.1088/2053-1591/2/8/085006

Kim, M. Y., Oh, T. S., and Kim, J. S. (2007). Annealing behavior of Bi_2Te_3 thermoelectric semiconductor electrodeposited for nanowire applications. *J. Korean Phys. Soc.* 50, 670–676. doi: 10.3938/jkps.50.670

Kim, M. Y., Park, K. W., and Oh, T. S. (2008). Thermoelectric characteristics of the Sb_2Te_3 compound semiconductor electrodeposited for nanowire applications. *J. Korean Phys. Soc.* 53, 266–270. doi: 10.3938/jkps.53.266

Kim, M. Y., Park, K. W., and Oh, T. S. (2009). Fabrication process and power generation characteristics of the micro thermoelectric devices composed of n-type Bi-Te and p-type Sb-Te nanowires. *J. Korean Inst. Metals Mater.* 47, 248–255.

Klammer, J., Bachmann, J., Töllner, W., Bourgault, D., Cagnon, L., Gösele, U., et al. (2010). Electrochemical route to thermoelectric nanowires via organic electrolytes. *Phys. Status Solidi Basic Res.* 247, 1384–1392. doi: 10.1002/pssb.200945549

Kojda, D., Mitdank, R., Mogilatenko, A., Töllner, W., Wang, Z., Kröner, M., et al. (2014). The effect of a distinct diameter variation on the thermoelectric properties of individual $Bi_{0.39}Te_{0.61}$ nanowires. *Semicond. Sci. Technol.* 29:124006. doi: 10.1088/0268-1242/29/12/124006

Kok, K. Y., Ng, I., Thye Foo, C., Saidin, N., and Abdullah, Y. (2016). Electrochemical synthesis and characterisation of BiTe-based nanowire arrays as thermoelectric. *Nanogenerators* 840, 271–275. doi: 10.4028/www.scientific.net/MSF.840.271

Koukharenko, E., Li, X., Nandhakumar, I., Schiedt, B., Trautmann, C., Speed, J., et al. (2008). Development of nanostructures for thermoelectric microgenerators using ion-track lithography. *Electron. Lett.* 44, 500–501. doi: 10.1049/el:20080111

Koukharenko, E., White, N., Li, X., and Nandhakumar, I. (2015). Ion-track etched templates for the high density growth of nanowires of bismuth telluride and bismuth antimony telluride by electrodeposition. *ECS Trans.* 64, 9–14. doi: 10.1149/06435.0009ecst

Krieg, J., Giraud, R., Funke, H., Dufouleur, J., Escoffier, W., Trautmann, C., et al. (2018). Magnetotransport measurements on Bi_2Te_3 nanowires electrodeposited in etched ion-track membranes. *J. Phys. Chem. Solids*. 128, 360–366. doi: 10.1016/j.jpcs.2018.02.002

Kuleshova, J., Koukharenko, E., Li, X., Frety, N., Nandhakumar, I. S., Tudor, J., et al. (2010). Optimization of the electrodeposition process of high-performance bismuth antimony telluride compounds for thermoelectric applications. *Langmuir* 26, 16980–16985. doi: 10.1021/la101952y

Kumar, P., Pfeffer, M., Peranio, N., Eibl, O., Bäßler, S., Reith, H., et al. (2017). Ternary, single-crystalline Bi2 (Te, Se)3 nanowires grown by electrodeposition. *Acta Mater.* 125, 238–245. doi: 10.1016/j.actamat.2016.11.057

Kuo, C.-G., Hsieh, Y.-T., Yang, C.-F., Huang, C.-H., and Yen, C.-Y. (2014). Growth of anodic aluminum oxide templates and the application in fabrication of the BiSbTe-based thermoelectric nanowires. *Int. J. Photoenergy* 2014:7. doi: 10.1155/2014/978184

Lee, J., Berger, A., Cagnon, L., Gösele, U., Nielsch, K., and Lee, J. (2010a). Disproportionation of thermoelectric bismuth telluride nanowires as a result of the annealing process. *Phys. Chem. Chem. Phys.* 12, 15247–15250. doi: 10.1039/c0cp00749h

Lee, J., Kim, Y., Cagnon, L., Gösele, U., and Nielsch, K. (2010b). Power factor measurements of bismuth telluride nanowires grown by pulsed electrodeposition. *Phys. Status Solidi Rapid Res. Lett.* 4, 43–45. doi: 10.1002/pssr.200903368

Lee, W., Ji, R., Gösele, U., and Nielsch, K. (2006). Fast fabrication of long-range ordered porous alumina membranes by hard anodization. *Nat. Mater.* 5, 741–747. doi: 10.1038/nmat1717

Lee, W., and Park, S. J. (2014). Porous anodic aluminum oxide: anodization and templated synthesis of functional nanostructures. *Chem. Rev.* 114, 7487–7556. doi: 10.1021/cr500002z

Li, L., Jin, C., Xu, S., Yang, J., Du, H., and Li, G. (2014). Thermal conductivity of a single $Bi_{0.5}Sb_{1.5}Te_3$ single-crystalline nanowire. *Nanotechnology* 25:415704. doi: 10.1088/0957-4484/25/41/415704

Li, L., Xu, S., and Li, G. (2015). Enhancement of thermoelectric properties in Bi-Sb-Te alloy nanowires by pulsed electrodeposition. *Energy Technol.* 3, 825–829. doi: 10.1002/ente.201500071

Li, S., Soliman, H. M. A., Zhou, J., Toprak, M. S., Muhammed, M., Platzek, D., et al. (2008). Effects of annealing and doping on nanostructured bismuth telluride thick films. *Chem. Mater.* 20, 4403–4410. doi: 10.1021/cm800696h

Li, W.-J., Yu, W.-L., and Yen, C.-Y. (2011). Pulsed electrodeposition of Bi_2Te_3 and Bi_2Te_3/Te nanowire arrays from a DMSO solution. *Electrochim. Acta* 58, 510–515. doi: 10.1016/j.electacta.2011.09.075

Li, X., Koukharenko, E., Nandhakumar, I. S., Tudor, J., Beeby, S. P., and White, N. M. (2009). High density p-type $Bi_{0.5}Sb_{1.5}Te_3$ nanowires by electrochemical

templating through ion-track lithography. *Phys. Chem. Chem. Phys.* 11, 3584–3590. doi: 10.1039/b818040g

Li, X. L., Cai, K. F., Li, H., Yu, D. H., Wang, X., and Wang, H. F. (2010). Alumina template-assisted electrodeposition of $Bi_2Te_{2.7}Se_{0.3}$ nanowire arrays. *Superlattices Microstructures* 47, 710–713. doi: 10.1016/j.spmi.2010.03.009

Li, X. L., Cai, K. F., Yu, D. H., and Wang, Y. Y. (2011). Electrodeposition and characterization of thermoelectric Bi_2Te_2Se/Te multilayer nanowire arrays. *Superlattices and Microstructures* 50, 557–562. doi: 10.1016/j.spmi.2011.09.001

Liang, L., Youwen, Y., Xiaohu, H., Guanghai, L., and Lide, Z. (2006). Pulsed electrodeposition of single-crystalline Bi_2Te_3 nanowire arrays. *Nanotechnology* 17, 1706–1712. doi: 10.1088/0957-4484/17/6/027

Lim, J. R., Whitacre, J. F., Fleurial, J.-P., Huang, C.-K., Ryan, M. A., and Myung, N. V. (2005). Fabrication method for thermoelectric nanodevices. *Adv. Mater.* 17, 1488–1492. doi: 10.1002/adma.200401189

Limmer, S. J., Yelton, W. G., Siegal, M. P., Lensch-Falk, J. L., Pillars, J., and Medlin, D. L. (2012). Electrochemical deposition of $Bi_2(Te,Se)_3$ Nanowire arrays on Si. *J. Electrochem. Soc.* 159, D235–D239. doi: 10.1149/2.084204jes,

Mannam, R., Agarwal, M., Roy, A., Singh, V., Varahramyan, K., and Davis, D. (2009). Electrodeposition and thermoelectric characterization of bismuth telluride nanowires. *J. Electrochem. Soc.* 156, B871–B875. doi: 10.1149/1.3139011

Manzano, C. V., Abad, B., and Martín-González, M. (2018). The effect of electrolyte impurities on the thermoelectric properties of electrodeposited Bi2Te3 Films. *J. Electrochem. Soc.* 165, D768–D773. doi: 10.1149/2.1131814jes

Manzano, C. V., Abad, B., Muñoz Rojo, M., Koh, Y. R., Hodson, S. L., Lopez Martinez, A. M., et al. (2016a). Anisotropic Effects on the thermoelectric properties of highly oriented electrodeposited Bi2Te3 Films. *Sci. Rep.* 6:19129. doi: 10.1038/srep19129

Manzano, C. V., Best, J. P., Schwiedrzik, J. J., Cantarero, A., Michler, J., and Philippe, L. (2016b). The influence of thickness, interpore distance and compositional structure on the optical properties of self-ordered anodic aluminum oxide films. *J. Mater. Chem. C* 4, 7658–7666. doi: 10.1039/C6TC01904H

Manzano, C. V., Martín, J., and Martín-González, M. S. (2014). Ultra-narrow 12 nm pore diameter self-ordered anodic alumina templates. *Microporous Mesoporous Mater.* 184, 177–183. doi: 10.1016/j.micromeso.2013.10.004

Manzano, C. V., Rojas, A. A., Decepida, M., Abad, B., Feliz, Y., Caballero-Calero, O., et al. (2013). Thermoelectric properties of Bi_2Te_3 films by constant and pulsed electrodeposition. *J. Solid State Electrochem.* 17, 2071–2078. doi: 10.1007/s10008-013-2066-7

Martín, J., Manzano, C. V., Caballero-Calero, O., and Martín-González, M. (2013). High-aspect-ratio and highly ordered 15-nm porous alumina templates. *ACS Appl. Mater. Interfaces* 5, 72–79. doi: 10.1021/am3020718

Martín, J., Manzano, C. V., and Martín-González, M. (2012). In-depth study of self-ordered porous alumina in the 140-400 nm pore diameter range. *Microporous Mesoporous Mater.* 151, 311–316. doi: 10.1016/j.micromeso.2011.10.018

Martín, J., Martín-González, M., Francisco Fernández, J., and Caballero-Calero, O. (2014). Ordered three-dimensional interconnected nanoarchitectures in anodic porous alumina. *Nat. Commun.* 5:5130. doi: 10.1038/ncomms6130

Martín-González, M., Caballero-Calero, O., and Díaz-Chao, P. (2013). Nanoengineering thermoelectrics for 21st century: energy harvesting and other trends in the field. *Renew. Sustain. Energy Rev.* 24, 288–305. doi: 10.1016/j.rser.2013.03.008

Martín-González, M., Prieto, A. L., Gronsky, R., Sands, T., and Stacy, A. M. (2003a). High-Density 40 nm Diameter Sb-Rich $Bi_{2-x}Sb_xTe_3$ nanowire arrays. *Adv. Mater.* 15, 1003–1006. doi: 10.1002/adma.200304781

Martín-González, M., Snyder, G. J., Prieto, A. L., Gronsky, R., Sands, T., and Stacy, A. M. (2003b). Direct electrodeposition of highly dense 50 nm $Bi_2Te_{3-y}Se_y$ nanowire arrays. *Nano Lett.* 3, 973–977. doi: 10.1021/nl034079s

Martín-González, M. S., Prieto, A. L., Gronsky, R., Sands, T., and Stacy, A. M. (2002). Insights into the Electrodeposition of Bi_2Te_3. *J. Electrochem. Soc.* 149, C546–C554. doi: 10.1149/1.1509459

Masuda, H., and Fukuda, K. (1995). Ordered metal nanohole arrays made by a two-step replication of honeycomb structures of anodic alumina. *Science* 268, 1466–1468. doi: 10.1126/science.268.5216.1466

Mavrokefalos, A., Moore, A. L., Pettes, M. T., Shi, L., Wang, W., and Li, W. (2009). Thermoelectric and structural characterizations of individual electrodeposited bismuth telluride nanowires. *J. Appl. Phys.* 105:104318. doi: 10.1063/1.3133145

Menke, E. J., Li, Q., and Penner, R. M. (2004). Bismuth telluride (Bi2Te3) nanowires synthesized by cyclic electrodeposition/stripping coupled with step edge decoration. *Nano Lett.* 4, 2009–2014. doi: 10.1021/nl048627t

Muñoz Rojo, M., Abad, B., Manzano, C. V., Torres, P., Cartoix, X., Alvarez, F. X., et al. (2017). Thermal conductivity of Bi2Te3 nanowires: How size affects phonon scattering. *Nanoscale* 9, 6741–6747. doi: 10.1039/C7NR02173A

Muñoz Rojo, M., Grauby, S., Rampnoux, J. M., Caballero-Calero, O., Martin-Gonzalez, M., and Dilhaire, S. (2013). Fabrication of Bi2Te3 nanowire arrays and thermal conductivity measurement by 3ω-scanning thermal microscopy. *J. Appl. Phys.* 113:054308. doi: 10.1063/1.4790363

Munoz Rojo, M., Romero, J. J., Ramos, D., Borca-Tasciuc, D. A., Borca-Tasciuc, T., and Martin Gonzalez, M. (2015). Modeling of transient thermoelectric transport in Harman method for films and nanowires. *Int. J. Thermal Sci.* 89, 193–202. doi: 10.1016/j.ijthermalsci.2014.10.014

Muñoz Rojo, M., Zhang, Y., Manzano, C. V., Alvaro, R., Gooth, J., Salmeron, M., et al. (2016). Spatial potential ripples of azimuthal surface modes in topological insulator Bi2Te3 nanowires. *Sci. Rep.* 6, 19014–19018. doi: 10.1038/srep19014

Naylor, A. J., Koukharenko, E., Nandhakumar, I. S., and White, N. M. (2012). Surfactant-mediated electrodeposition of bismuth telluride films and its effect on microstructural properties. *Langmuir* 28, 8296–8299. doi: 10.1021/la301367m

Ng, I.-K., Kok, K.-Y., Rahman, C. Z. C. A., Saidin, N. U., Ilias, S. H., and Choo, T.-F. (2014). Electrochemically deposited BiTe-based nanowires for thermoelectric applications. *AIP Conf. Proc.* 1584, 125–128. doi: 10.1063/1.4866117

Ng, I. K., Kok, K. Y., Rahman, C. Z. C. A., Choo, T. F., and Saidin, N. U. (2016). Bismuth telluride based nanowires for thermoelectric power generation. *Mater. Today* 3, 533–537. doi: 10.1016/j.matpr.2016.01.086

Park, K., Xiao, F., Yoo, B. Y., Rheem, Y., and Myung, N. V. (2009). Electrochemical deposition of thermoelectric SbxTey thin films and nanowires. *J. Alloys Compd.* 485, 362–366. doi: 10.1016/j.jallcom.2009.05.106

Peranio, N., Leister, E., Töllner, W., Eibl, O., and Nielsch, K. (2012). Stoichiometry controlled, single-crystalline Bi 2Te 3 nanowires for transport in the basal plane. *Adv. Funct. Mater.* 22, 151–156. doi: 10.1002/adfm.201101273

Picht, O., Müller, S., Alber, I., Rauber, M., Lensch-Falk, J., Medlin, D. L., et al. (2012). Tuning the geometrical and crystallographic characteristics of Bi2Te3 nanowires by electrodeposition in ion-track membranes. *J. Phys. Chem. C* 116, 5367–5375. doi: 10.1021/jp210491g

Pinisetty, D., Gupta, M., Karki, A. B., Young, D. P., and Devireddy, R. V. (2011). Fabrication and characterization of electrodeposited antimony telluride crystalline nanowires and nanotubes. *J. Mater. Chem.* 21, 4098–4107. doi: 10.1039/C0JM01969K

Prieto, A. L., Sander, M. S., Martín-González, M. S., Gronsky, R., Sands, T., and Stacy, A. M. (2001). Electrodeposition of Ordered Bi2Te3 Nanowire Arrays. *J. Am. Chem. Soc.* 123, 7160–7161. doi: 10.1021/ja015989j

Proenca, M. P., Rosmaninho, M., Resende, P. M., Sousa, C. T., Ventura, J., Araújo, J. P., et al. (2017). Tailoring Bi-Te based nanomaterials by electrodeposition: morphology and crystalline structure. *Mater. Design* 118, 168–174. doi: 10.1016/j.matdes.2017.01.020

Qi, X.-L., and Zhang, S.-C. (2011). Topological insulators and superconductors. *Rev. Mod. Phys.* 83, 1057–1110. doi: 10.1103/RevModPhys.83.1057

Resende, P., Sanz, R., Ruiz-De Clavijo, A., Caballero-Calero, O., and Martín-González, M. (2016). Cylindrical three-dimensional porous anodic alumina networks. *Coatings* 6:59. doi: 10.3390/coatings6040059

Resende, P. M., and Martín-González, M. (2019). Sub-10 nm porous alumina templates to produce sub-10 nm nanowires. *Microporous Mesoporous Mater.* 284, 198–204. doi: 10.1016/j.micromeso.2019.04.020

Rodríguez-Fernández, C., Manzano, C. V., Romero, A. H., Martín, J., Martín-González, M., Morais De Lima, M. J., et al. (2016). The fingerprint of Te-rich and stoichiometric Bi_2Te_3 nanowires by Raman spectroscopy. *Nanotechnology* 27:075706. doi: 10.1088/0957-4484/27/7/075706

Rojo, M. M., Calero, O. C., Lopeandia, A. F., Rodriguez-Viejo, J., and Martín-Gonzalez, M. (2013). Review on measurement techniques of transport properties of nanowires. *Nanoscale* 5, 11526–11544. doi: 10.1039/c3nr03242f

Rostek, R., Stein, N., and Boulanger, C. (2015). A review of electroplating for V–VI thermoelectric films: from synthesis to device integration. *J. Mater. Res.* 30, 2518–2543. doi: 10.1557/jmr.2015.203

Rowe, D. M. (1995). *Handbook of Thermoelectrics*. (New York). doi: 10.1201/9781420049718

Rowe, D. M. (2012). *Materials, Preparation, and Characterization in Thermoelectrics*. CRC Press.

Ruiz-Clavijo, A., Caballero-Calero, O., and Martín-González, M. (2018). Three-dimensional Bi2Te3 networks of interconnected nanowires: synthesis and optimization. *Nanomaterials* 8:345. doi: 10.3390/nano8050345

Ryan, D. R., Leigh, A. C., Gregory, E. C., and Justin, J. H. (2017). Thermoelectric property enhancement via pore confinement in template grown bismuth telluride nanowire arrays. *Nanotechnology* 28:505401. doi: 10.1088/1361-6528/aa9733

Sander, M. S., Gronsky, R., Sands, T., and Stacy, A. M. (2003). Structure of bismuth telluride nanowire arrays fabricated by electrodeposition into porous anodic alumina templates. *Chem. Mater.* 15, 335–339. doi: 10.1021/cm0207604

Sander, M. S., Prieto, A. L., Gronsky, R., Sands, T., and Stacy, A. M. (2002). Fabrication of high-density, high aspect ratio, large-area bismuth telluride nanowire arrays by electrodeposition into porous anodic alumina templates. *Adv. Mater.* 14, 665–667. doi: 10.1002/1521-4095(20020503)14:9<665::AID-ADMA665>3.0.CO;2-B

Sapp, S. A., Lakshmi, B. B., and Martin, C. R. (1999). Template synthesis of bismuth telluride nano wires. *Adv. Mater.* 11, 402–404.3

Selvan, K. V., Hasan, M. N., and Mohamed Ali, M. S. (2019). Methodological reviews and analyses on the emerging research trends and progresses of thermoelectric generators. *Int. J. Energy Res.* 43, 113–140. doi: 10.1002/er.4206

Shin, H. S., Jeon, S. G., Yu, J., Kim, Y.-S., Park, H. M., and Song, J. Y. (2014). Twin-driven thermoelectric figure-of-merit enhancement of Bi2Te3 nanowires. *Nanoscale* 6, 6158–6165. doi: 10.1039/C4NR00191E

Sima, M., Vasile, E., and Sima, M. (2009). Electrochemically deposited thermoelectric Bi2(Se, Te)3 nanowires. *Optoelectr. Adv. Mater. Rapid Commun.* 3, 539–542.

Sima, M., Vasile, E., and Sima, M. (2011). Study of electrodeposition of (Bi,Sb) 2Te 3 nanowires by voltammetric methods and electrochemical impedance spectroscopy. *J. Optoelectr. Adv. Mater.* 13, 1597–1602.

Sousa, C. T., Leitao, D. C., Proenca, M. P., Ventura, J., Pereira, A. M., and Araujo, J. P. (2014). Nanoporous alumina as templates for multifunctional applications. *Appl. Phys. Rev.* 1:031102. doi: 10.1063/1.4893546

Swinkels, M. Y., and Zardo, I. (2018). Nanowires for heat conversion. *J. Phys. D Appl. Phys.* 51:353001. doi: 10.1088/1361-6463/aad25f

Trahey, L., Becker, C. R., and Stacy, A. M. (2007). Electrodeposited bismuth telluride nanowire arrays with uniform growth fronts. *Nano Lett.* 7, 2535–2539. doi: 10.1021/nl070711w

Tritt, T. M., and Subramanian, M. A. (2006). Thermoelectric materials, phenomena, and applications: a bird's eye view. *MRS Bull.* 31, 188–198. doi: 10.1557/mrs2006.44

Wagner, M. F. P., Völklein, F., Reith, H., Trautmann, C., and Toimil-Molares, M. E. (2016). Fabrication and thermoelectrical characterization of three-dimensional nanowire networks. *Phys. Status Solidi (a)* 213, 610–619. doi: 10.1002/pssa.201532616

Wang, W.-L., Wan, C.-C., and Wang, Y.-Y. (2006). Investigation of Electrodeposition of Bi2Te3 Nanowires into nanoporous alumina templates with a rotating electrode. *J. Phys. Chem. B* 110, 12974–12980. doi: 10.1021/jp061362h

Wilson, A. A., Muñoz Rojo, M., Abad, B., Perez, J. A., Maiz, J., Schomacker, J., et al. (2015). Thermal conductivity measurements of high and low thermal conductivity films using a scanning hot probe method in the 3ω mode and novel calibration strategies. *Nanoscale* 7, 15404–15412. doi: 10.1039/C5NR03274A

Xiao, F., Hangarter, C., Yoo, B., Rheem, Y., Lee, K.-H., and Myung, N. V. (2008). Recent progress in electrodeposition of thermoelectric thin films and nanostructures. *Electrochim. Acta* 53, 8103–8117. doi: 10.1016/j.electacta.2008.06.015

Zhang, H., Liu, C. X., Qi, X. L., Dai, X., Fang, Z., and Zhang, S. C. (2009). Topological insulators in Bi2Se3, Bi2Te3 and Sb2Te3 with a single Dirac cone on the surface. *Nat. Phys.* 5, 438–442. doi: 10.1038/nphys1270

Zhang, T., Cheng, P., Chen, X., Jia, J. F., Ma, X., He, K., et al. (2009). Experimental demonstration of topological surface states protected by time-reversal symmetry. *Phys. Rev. Lett.* 103, 266803–266804. doi: 10.1103/PhysRevLett.103.266803

Zhou, J., Jin, C., Seol, J. H., Li, X., and Shi, L. (2005). Thermoelectric properties of individual electrodeposited bismuth telluride nanowires. *Appl. Phys. Lett.* 87:133109. doi: 10.1063/1.2058217

Conflict of Interest Statement: The authors declare that the research was conducted in the absence of any commercial or financial relationships that could be construed as a potential conflict of interest.

Advantages of publishing in Frontiers

OPEN ACCESS
Articles are free to read for greatest visibility and readership

FAST PUBLICATION
Around 90 days from submission to decision

HIGH QUALITY PEER-REVIEW
Rigorous, collaborative, and constructive peer-review

TRANSPARENT PEER-REVIEW
Editors and reviewers acknowledged by name on published articles

Frontiers
Avenue du Tribunal-Fédéral 34
1005 Lausanne | Switzerland

Visit us: www.frontiersin.org
Contact us: info@frontiersin.org | +41 21 510 17 00

REPRODUCIBILITY OF RESEARCH
Support open data and methods to enhance research reproducibility

DIGITAL PUBLISHING
Articles designed for optimal readership across devices

FOLLOW US
@frontiersin

IMPACT METRICS
Advanced article metrics track visibility across digital media

EXTENSIVE PROMOTION
Marketing and promotion of impactful research

LOOP RESEARCH NETWORK
Our network increases your article's readership